Magnetic domain wall dynamics and spin transport in confined geometries

Dissertation

zur Erlangung des Grades

"**Doktor**

der Naturwissenschaften (Dr. rer. nat.)"

am Fachbereich 08 - Physik

der Johannes Gutenberg-Universität

In Mainz, Deutschland

Mohamad-Assaad Mawass

geboren in Tripoli, Libanon

Mainz, Mai 2016

Mohamad-Assaad Mawass

Magnetic domain wall dynamics and spin transport in confined geometries

1. Berichterstatter: Aus Datenschutzgründen entfernt / Removed due to data privacy

2. Berichterstatter: Aus Datenschutzgründen entfernt / Removed due to data privacy

Datum der mündlichen Prüfung: 15. August, 2016

Vorsitzender der Prüfungskommission: Aus Datenschutzgründen entfernt

Mitglieder der Prüfungskommission: Aus Datenschutzgründen entfernt

Protokollführung: Aus Datenschutzgründen entfernt

Johannes Gutenberg-Universität Mainz
AG Kläui
Institut für Physik
Staudingerweg 7
55128, Mainz

Max Planck Institut für Intelligent Systems
Schütz Dept. – Magnetization Dynamics Group
Heisenbergstr. 3
70569, Stuttgart

Magnetic domain wall dynamics and spin transport in confined geometries

Dissertation submitted

for the degree award of the title

"**Doctor**

of Natural Sciences (Dr. rer. nat.)"

to the Faculty-08 of Physics

of Johannes Gutenberg University

In Mainz, Germany

Mohamad-Assaad Mawass

Born in Tripoli, Lebanon

Mainz, May 2016

This PhD was carried out in a joint project

between the

Institut für Physik, Johannes Gutenberg-Universität

Mainz, Germany

and the

Max-Planck-Institut für Intelligente Systeme

Stuttgart, Germany

Dedication

To my parents, who have always encouraged and supported me.

Abstract

In this work we study the controlled propagation of magnetic domain walls in ferromagnetic nanowires made of Permalloy ($Ni_{80}Fe_{20}$), including curved geometries, with varying width (asymmetric rings). Two types of motion were studied, firstly field driven domain wall motion via fast rotating magnetic field pulses, and secondly the automotive domain wall propagation in nanoscale spintronic devices. In the first experimental approach, we directly observed domain wall spin structure transformations during motion and quantitatively determined the contribution of the spatially varying potential landscape to its propagation. An angular dependence of the domain wall velocity has been observed and explained by the interplay between the domain wall spin structure and relevant forces that act on the vortex wall. However, in contrast to symmetric ring systems, the interplay between these forces leads to distortion-free domain wall motion. Therefore, using this varying domain wall potential landscape, we are able to control spatially the internal domain wall spin structure transformation and synchronization of the domain wall velocities in ring geometries, even above the Walker breakdown. For the second experimental approach, we report a direct dynamic experimental visualization of spontaneous domain wall propagation in asymmetric ferromagnetic rings, with different widths in the narrowest part. Surprisingly, we observed domain wall automotion with an average velocity of about ~ 60 m/s, which is a significant speed for spintronics devices. We show that the domain wall inertia and the stored energy allow the walls to overcome both the local extrinsic pinning and the topological repulsion between domain walls. Our observation can be explained based on the minimization of the magnetostatic and exchange energies. In order to provide more device functionality we went beyond the propagation of one or two walls and managed to achieve a major breakthrough in the development of methods of information processing in spintronics, by demonstrating a scheme to induce synchronous motion of multiple in-plane domain walls in ferromagnetic nanowires using perpendicular field pulses. This paradigm shifting achievement provides the required functionality for nonvolatile domain wall-based shift register devices. The direct visualization of the domain wall spin structure in all experiments was performed employing time resolved scanning transmission X-ray microscopy, which combines the requisite temporal and lateral resolution needed in our measurements.

Finally in order to investigate the influence of miniaturization for ultra-small devices we studied magnetic nanocontacts in order to understand the interaction between spin polarized charge carriers and magnetization on the nanoscale. In particular we studied the evolution of the domain wall magneto-resistance in electromigrated ferromagnetic nanocontact fabricated in ultra-high vacuum conditions. We find that the domain wall pinning strength increases on decreasing the contact cross section. Moreover, we measured the depinning field's angular dependence and symmetry in order to determine the complete domain wall pinning potential in a device with a narrow constriction. The work presented here paves the way for the development of a new generation of non-volatile spintronic components, which could be implemented in a wide range of applications for logic, sensing as well as data storage devices based on the reliable manipulation of domain walls.

Table of Contents

Chapter 3: Synchronous precessional motion of multiple domain walls in a ferromagnetic nanowire by perpendicular field pulses

Chapter 6: Domain wall pinning in ultra-narrow electro-migrated constriction

Preface

One of the current research aims in the field of magnetism is to enable the continued realization of Moore's law by using new concepts and methods to build spintronic devices with feature sizes on the nanoscale. In this context, geometrically confined magnetic domain walls in magnetic nanostructures have recently become the focus of intense scientific interest. Due to the geometrical constraints of the magnetic nanostructure, different types of domain walls can occur in comparison with the bulk and continuous films. The spin structure of such domain walls, e.g. 180° head-to-head walls, is usually dominated by the geometrical environment rather than by the material properties as is the case for bulk material.

This field of research constitutes a new sub-disciplinary field of condensed matter physics which looks to realize a new generation of electronic devices, where not only the charge of the electrons is considered but also their spins. Some such spintronic devices have the potential for vastly reduced energy consumption and offer data processing speeds that overcome the velocity limit of electric charge.

Furthermore one particular class of nanoscale spintronic technologies which are intensely investigated in order to develop novel, smaller, reliable and faster magnetic devices are based on controlled domain wall motion, with examples including magnetic memory/storage, sensing and logic device. In general, different approaches have been suggested in order to control the motion of the magnetic domain walls either via a magnetic field, by varying geometry or using charge and spin currents. The global aim from the study of these systems is to develop a competitive device based on magnetic materials which combines the advantages of the spintronic devices such as non-volatility with the benefits of the existing options.

However, spintronic devices which use magnetic domain walls as functional elements rely on the precise control of the domain wall propagation in various nanowires, including curved geometries, therefore the fundamental physical mechanisms underpinning the domain wall dynamics in nanoscale magnetic wires need to be controlled and understood. Since domain walls can be treated as quasi-particle with an effective mass, when a force is applied the domain wall undergoes oscillations in the external potential (created by the force), leading to domain wall inertia resulting from the domain wall energy stored during the displacement. This is very important for the understanding of the propagation of domain walls. For instance, the deformation of the domain wall spin structure during the propagation influences the wall dynamics. Moreover in the simplest

case the domain wall can be described by one single coordinate, for example, the vortex core position of the domain wall (as described in the one-dimensional model). By investigating and engineering the domain wall propagation, for instance via tailoring the potential landscape, the performance of spintronics devices can be significantly improved.

Despite the many achievement in the field of spintronics, much things still need to be understood before a reliable and commercially viable performance of these devices is achieved. In this thesis we report our contribution on the road to supply the understanding and improve the performance of these systems with a precise control of both the domain wall position and velocity. We are able to unravel the physical mechanisms behind the domain wall spin dynamics by employing time resolved scanning transmission X-ray microscopy (STXM) which combine the requisite temporal and lateral resolution for our experiments. Furthermore we discuss the evolution of domain wall pinning in an ultra-narrow ferromagnetic junction narrowed by electromigration. The work presented here paves the way for the development of a new generation of non-volatile spintronic components, which could be implemented in a wide range of applications for logic, sensing as well as data storage devices based on the reliable and reproducible manipulation of the domain wall.

The thesis is organized as follows:

Chapter 1 introduces the theoretical background to our experiments such as the theory of micromagnetism in ferromagnetic nanowires. This chapter describes magnetization dynamics driven by a magnetic field including the equation of motion of the domain wall in both one-dimensional and two collective coordinate approximations, in various geometries.

Chapter 2 describes in detail the sample fabrication and patterning techniques based on electron beam lithography. In addition, an overview of the experimental methods used in this work is given including the description of the time resolved dynamic acquisition scheme (pump and probe) using time-resolved STXM, which is used to directly observe the magnetization dynamics on the nanoscale.

Chapter 3: We demonstrate a radically different domain wall propagation scheme using out-of-plane field pulses which combines the efficiency of field-induced motion with the ability to move multiple walls synchronously. This is achieved for in-plane magnetized transverse domain walls of the same chirality through the application of asymmetric field pulses to a wire which incorporates regularly spaced pinning sites. The experimental observations showed a qualitative agreement with our analytical and numerical results, which confirms and demonstrates the viability of our proposed novel mechanism approach for domain wall motion.

Chapter 4: We report local control of the domain wall velocity and position by engineering the geometry of ring structures, leading to a tailored domain wall potential landscape. By employing time-resolved STXM we directly observed domain wall spin structure transformations during motion driven by rotating magnetic field pulses and quantitatively determine the contribution of the spatially varying potential landscape to the domain wall propagation. This result is qualitatively in good agreement with our micromagnetic simulations.

Chapter 5: We report direct dynamic experimental visualization of spontaneous domain wall propagation in asymmetric ferromagnetic rings, with different widths in the narrowest part, without the existence of an external driving magnetic field. Surprisingly, even at zero external magnetic field, we observed domain wall automotion with an average velocity of about ~ 60 m/s, which is a significant speed for spintronic devices based on domain wall dynamics. Our experimentally obtained angular dependencies of spontaneous domain wall velocities can be explained based on the minimization condition of the magnetostatic and exchange energies. We demonstrate that both simulation and experimental results are qualitatively consistent with one another.

Chapter 6: We discuss the evolution of domain wall pinning in an ultra-narrow ferromagnetic (Permalloy) junction narrowed by electromigration. The magnetic junction was fabricated and eventually tailored in-situ in clean ultra-high vacuum conditions. By using the advantage of a controlled in-situ electromigration process, which is able to tailor the nano-contact's width, we are able to probe the nanostructure device at different constriction widths. In agreement with the wall energy, which is reduced in narrower constrictions, we find that the domain wall pinning strength is increased on decreasing the contact width. Moreover, we measured the depinning field's angular dependence and symmetry in order to determine the complete domain wall pinning potential in a device with a narrow constriction.

Summary and Outlook: The conclusions of the work are presented as well as suggestions for potential avenues for future study.

Part of this work has been published in peer reviewed journals. A list of publications is given at the end.

Chapter 1

Introduction and theoretical background

I. Micromagnetic theory of ferromagnetic nanostructures

The origin of the ferromagnetism, as well as magnetism in general, was explained to be a quantum-mechanical effect. The Bohr-van Leeuwen theorem states that there is no total magnetization, **M**, at a finite thermal equilibrium, in the classical system, and in the absence of an external field [1]. All classical approximation failed to explain the magnetic phenomena.

Currently, it is known that ferromagnetism is mainly obtained by two contributions or models whose depends on the system. In the case of highly localized electrons materials, ferromagnetism is described by the exchange interaction theory, which leads to a coupling of neighbor atomic moment at a short range. These couplings are due to the Pauli's exclusion principal and the overlapping of the neighbor wave functions. However for the weakly localized 3d-electrons metals or classical ferromagnetic material such cobalt, iron, nickel and their alloys the band model [1] proved to be a useful theory to describe magnetic effects.

The most characteristic property of ferromagnets is that once exposed to a magnetic field they retain their magnetization even when the field is removed. The retention of magnetization distinguishes ferromagnets from paramagnets which, although they acquire a magnetic moment in an applied magnetic field, cannot maintain the magnetization after the field is removed.

The most common way to represent the magnetic properties of a ferromagnetic material is by the plot of the magnetization, **M**, against the applied magnetic field, **H**. The magnetization of a ferromagnetic material exhibits a hysteretic behavior as a function of the applied magnetic field (Figure 1.1).

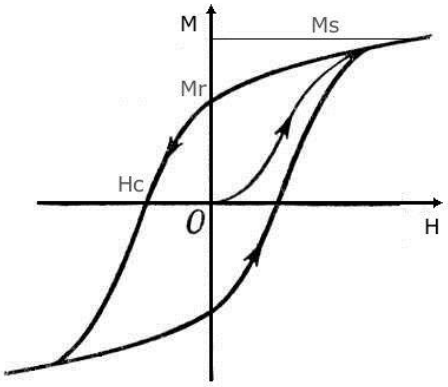

Figure 1.1: schematic of a basic hysteresis loop for a ferromagnetic material. H_c , M_s and M_r are the coercive field, the saturation magnetization and the remnant magnetization, respectively.

The main quantities which determines the hysteresis loop are the coercive field H_c, the remnant magnetization M_r and the saturation magnetization M_s. The area within the hysteresis loop is proportional to the work that has to be done in order to switch the magnetization from one direction into the opposite direction: $E = V\mu_0 \int \mathbf{H}\, d\mathbf{M}$.

The great differences between ferromagnetic material behavior and other material such as paramagnetic are:

(a) In a ferromagnet the magnetization depends on the history of the magnetic field treatment.

(b) A non-zero magnetization can be achieved in ferromagnets even in zero magnetic fields.

(c) In general, small magnetic fields of the order of 10^3 - 10^4 A/m can induce in ferromagnets large magnetizations of the order of 10^6 A/m.

I.1. Magnetic domains & domain walls

As definition, a magnetic domain is an area within a magnetic material which has uniform magnetization direction. This means that each individual atom in one domain exhibit a magnetic moments aligned one to each other in the same direction.

Historically, in 1907 Pierre Weiss introduced the two following postulates [2, 3] in order to explain some ferromagnetic properties:

(1) A molecular field H_m exists within the ferromagnetic material that orders the magnetic moments against the thermal motion. It is so large that the ferromagnet can be saturated even without an external magnetic field. At above T_C (so-called Curie temperature) the ferromagnetic

order is lost, the thermal energy (which disorders the system) and the magnetic energy (which orders the system) should be of the same order of magnitude: $k_B T_C \approx \mu_0 \mu_B H_m$. For instance with a T_C of 1043 K for iron (Fe) one finds $H_m \approx 10^9$ A/m.

(2) In the demagnetized state of a ferromagnetic material, i.e. $M_r = 0$, the material is divided into some small regions, so-called magnetic domains. The magnetization within a single domain is saturated, but the magnetization directions in different domains are different.

In bulk ferromagnetic samples the given coercive fields are substantially lower, usually by a factor of 10, than those found in the *uniform rotation* model [4]. The origin of this difference is the existing of another magnetization-reversal mechanism that can occur via notably lower energy expenditure. This mechanism is based on the nucleation of domains, the growth of reversed domains and the motion of domain walls.

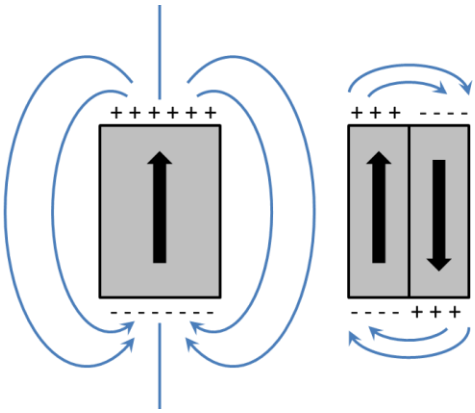

Figure 1.2: shows two hypothetical domain configurations. The magnetic field energy ($\propto \int H^2 \, dV$) is decreased by the creation of magnetic domains.

In the schematic domain configurations represented in Figure 1.2, the exchange energy is minimal because all moments are aligned as well as the anisotropy because the magnetization axis is an easy axis.

However, the demagnetizing energy is not minimal. Many uncompensated magnetic "poles" are presented at the surface of the ferromagnetic sample. This energy contribution can be decreased by including domains as it is shown in the right configuration of the figure 1.2. However, a transition region at the interface of the two domains has been created in such a way that the moments are not collinear to each other. Moreover, the moments in the region between the two domains are not anymore parallel to the easy axis. Thus, both the exchange and the anisotropy energy are larger than in the left configuration. Nevertheless, the total energy in massive ferromagnets is lower than in the single domain state, because the number of moments involved in increasing the exchange and the anisotropy energy are relatively small.

In bulk materials (often in soft magnetic material) and continuous films the existence of the domains is attributed to defects, whereas in nanoscale patterned structures the situation is radically different. In this case, the lowest energy state of the magnetization configuration is usually a multi-domains state with domain walls, since the stray field (dipole interaction) tends the magnetization to be parallel to the edges of the element. This results in an inhomogeneous magnetization distribution or domains. Where the ferromagnetic properties of an element start to strongly given by the shape of the element and not only by the intrinsic properties of the materials. This later dependence on the geometry helps to tailor the magnetization configuration by engineering the geometry [5, 6].

I.1.1. Magnetic domain walls in nanowires

The boundary between two domains, consist a domain wall. In past domain walls has been researched. The most common examples are the Neel and the Bloch wall types, which take place in continuous thin films [7, 8]. Nowadays the arrival of the high resolution imaging method allowed us to be able to image the nanoscale domain wall spin structure. In addition to the possibility of the time resolved imaging spin structure relaxation as well as the dynamics on a very short time scales (few picoseconds). In this section the spin structures of the domain walls will be presented for only the case of the soft magnetic materials and ignoring the materials with a strong anisotropy where the magnetization is out-of-plane. The soft magnetic materials such Permalloy ($Ni_{80}Fe_{20}$) represents the main material studied in this work. This materials exhibit two basic domain wall configurations (the vortex and the transverse domain wall which are discussed below) and important in this thesis.

I.1.2. Theory of head-to-head domain wall spin structures in soft magnetic materials

The related spin structures and domain wall types can be theoretically understood by considering the energy terms which the reason of the wall formation. At the nanoscale the head-to-head spin structure types is in general the consequence of the energy minimization the Landau free energy (the appropriate thermodynamic potential) [9, 10]. Since in the case of the soft magnetic material the anisotropies are neglected and in the absence of any applied fields, the main two energy terms are the exchange and the stray field terms of magneto-static energy (the results of the dipole interaction of the spins).

Qualitatively speaking in the case where the exchange energy dominates, this lead to a very wide wall, because a small angle between adjacent spins is needed to minimize the exchange energy. In the opposite case where the magneto-static energy dominates, lead to a narrow wall, since the spins keep collinear as much as possible to the edge structure.

Beyond the qualitative, micromagnetic simulations are a keys of further mechanism understanding. Such simulation was carried by McMichael and Donahue in 1997 [11]. Two

types of wall spin structures were predicted to happen: vortex walls see figure 1.3b and transverse walls see figure 1.3a.

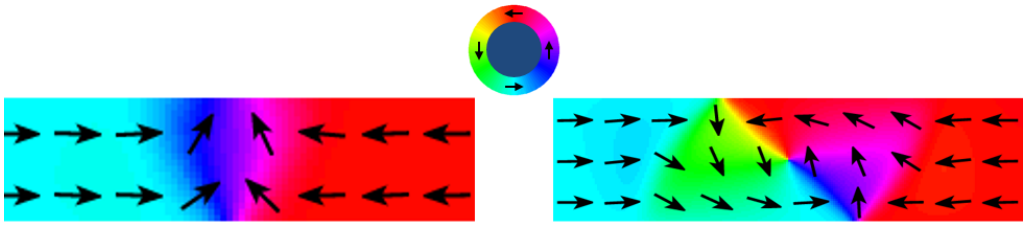

(a) Transverse wall (b) Vortex wall

Figure 1.3: Micro-magnetic simulation (Performed by Dr. J. -S. Kim) of two domain walls spin structure configuration in nanowires using OOMMF **(a)** Transverse wall and **(b)** Vortex wall configuration.

Transverse wall

In the transverse wall case the spins rotate in the plane of the wire.

In the case of narrow and thin nanowires, the transverse wall minimizes the energy where the spins rotate in the plane, see Figure 1.3a.

Vortex wall

In the case of vortex wall the spins rotate around the vortex core. The magnetization of the vortex core is pointing out of the plane. This vortex core is created to prevent the large increase in the exchange energy, in way that the magnetization turns out of plane, which depends on the vortex core polarity up or down. This was predicted initially by Feldkeller and Thomas [12].

This lead to four folds energetically degenerate states. When the rotations of the in plane magnetization are counter-clockwise or clockwise and the out of plane vortex-core points either down or up.

At the wire edges, up and down, and at the boundary of the vortex wall there is two half anti-vortices and forming 90°-Néel domain wall boundaries [13].

Phase diagram

The Phase diagram of the domain wall configuration in nanowires, where firstly investigated by *McMichael and Donahue*. They calculated the energies of both wall types as a function of geometry [11].

A refined calculation showed that there are two types of transverse wall, the symmetric and asymmetric transverse wall (ATW) [14]. Each domain wall type are stable at a certain width-thichness configuration as it is shown in Figure 1.4a.

Thus, by tuning the thickness and the width the magnetic structure will affect the preference of vortex or transverse domain walls.

Furthermore an experimental phase diagram was studied previously by our group as described in [14]. In this study an arrays of 5x5 polycrystalline Permalloy and Co rings with different thicknesses and width were fabricated. The experimental phase diagram for Permalloy rings is shown in Figure 1.4b

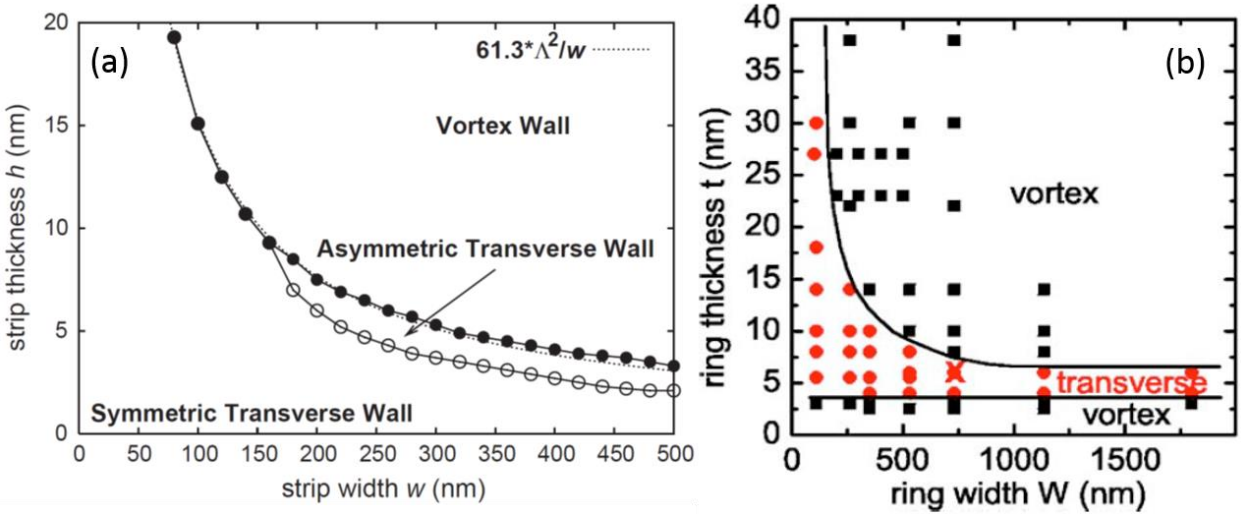

Figure 1.4: (a) Phase diagram of the domain wall types established by numerical calculations in nano-strip from reference [14] and **(b)** experimental phase diagram (adapted from [15]). The ring thickness t is plotted versus the ring width W, in nanometers scale. Regions where a vortex wall is preferred are presented by the black squares, and regions where a transverse wall is more favorable in the ring are shown by the red discs.

I.2. Micromagnetic description and Landau free energy

The smallest nano-magnets consist of a wide number of atoms, the calculation of their properties cannot be determined only using the quantum-mechanics theory. Therefore ones need to apply a semi-classical theory which is called micromagnetism.

The theory of micromagnetism was developed in the 1930s and 1940s in way to fill the gap between the quantum theory, based on atoms, and the classical Maxwell theory.

Micromagnetism describes the magnetic properties ferromagnets at the nano-scale, where the size and the shape of the structure determine the magnetic configurations, whereas in bulk magnets are not the case.

At the nanoscale two competing interactions take place, the exchange interaction and the dipole-dipole interaction, the results of these interactions determines the magnetism in soft ferromagnetic materials, since the magneto-crystalline anisotropy is negligible. In ferromagnets, the dipole-dipole interaction favors to minimize to zero the net magnetic moment by closed magnetic loops or in another word to minimize the stray field. While the exchange interaction favors or tend to align the neighbors magnetic moments in parallel in a short scale.

The dipole-dipole interaction usually can be in competition with the exchange interaction only at sizes larger than the so-called exchange length, defined as ($l_{ex} = \sqrt{A/\mu_0 M_S^2}$), and not possible below that length since the dipole interaction is weaker and has a long range properties (proportional to $1/r^2$). The resulting interplay between this two interactions lead to the actual magnetization configurations, depending on the shape, materials and size of the ferromagnetic nanostructures. Finally we could say that the micromagnetic theory describe the magnetization configuration in magnetic materials as a continuous vectors **M(r)** at each position **r**. This approach is only valid length scale larger than the exchange length which is usually in order of few nanometers [16].

In summary, and due to the recent computational power, it is possible to solve numerically non-linear micromagnetic equations. Thus, the possibility of solving the spin structures of the magnetic ground state of multidomain configurations. Moreover to the magnetization dynamics can be determined.

The energy of the magnetic system is obtained by the thermodynamical Gibbs potential free energy:

$$G_L(\mathbf{H}, T, \mathbf{m}) = U(T, \mathbf{m}) - TS - \mu_0 \int \mathbf{m} \cdot \mathbf{H}$$

Where $\boldsymbol{H}$ is the fixed external field and temperature T, with U the internal energy, S the entropy and $\mathbf{m} = \mathbf{M}/M_s$ the normalized magnetization by the saturation magnetization M_s. In the following we neglected the entropy by considering the open system case at $T = 0$. After this assumption the Gibbs free energy is expressed by the Landau free energy, which is calculated for each elementary volume [17].

In ferromagnetic body or in micromagnetism there are four important energy terms which contribute to the Landau free energy: the stray field or demagnetization field/magneto-static energy, the exchange energy, the magnetocrystalline anisotropy energy and the Zeeman energy.

The equilibrium ferromagnetic configurations for a given structure are obtained by minimizing the Landau free energy [18].

I.2.1. Magnetostatic energy

The interaction energy of the magnetic moments in the dipolar field defines the magnetostatic energy which is created by magnetic body itself [6]. This energy is associated with the stray field created by the magnetic moment or called, as well, the demagnetization field $\mathbf{H}_d$ which minimize the global magnetization of a system. To derive the stray field energy we start from the Maxwell's equation $\nabla \cdot \mathbf{B} = \nabla \cdot (\mu_0 \mathbf{H} + \mathbf{M}) = 0$. This leads to a definition of the demagnetization field, the field generated by the divergence of the magnetization:

$$\nabla \cdot \mathbf{H}_d = -\nabla \cdot \mathbf{M}$$

The sources of the magnetization act like negative and positive "magnetic charges" for the stray field, see figure 1.5. We can then calculate the field as equivalence to an electrostatics field generated from the electrical charges. However the magnetic charges never appear isolated in contrast to the electrical charges. The magnetostatic energy connected to the stray field and assumed as an external field is:

$$E_d = -\frac{\mu_0}{2} \iiint \mathbf{M} \cdot \mathbf{H}_d \, dV$$

We note that the dipole fields in a continuous magnetization distribution, may be presented as due to the magnetic pseudo-charges with a surface density $\sigma_m = \mathbf{n} \cdot \mathbf{M}$, where $\mathbf{n}$ is the normal to the surface, and a volume density $\rho_m = -\nabla \mathbf{M}$. If we assume a uniform magnetization, then the surface only carry some pseudo-charges. In this case the demagnetizing field is determined by the number of pseudo-charges.

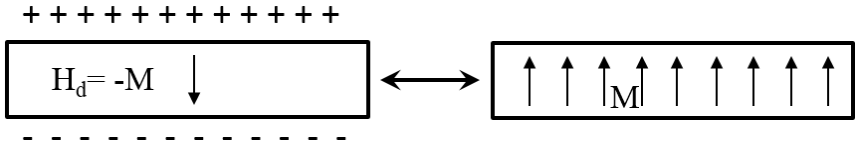

Figure 1.5: Thin film sample with magnetization out-of-plan, where a pseudo-charges appearing on the upper and the bottom surface. The results of the demagnetizing field is H_d is – M.

I.2.2. Exchange energy

The exchange interaction is the origin of the alignment of the spin system since it is the largest magnetic interaction which is one of the main origins of ferromagnetism. In order to derive the energy we start from the modified Heisenberg model [19].

$$H_{Hei} = -J \sum_{i \neq j, n.n.} \mathbf{S}_i \cdot \mathbf{S}_j$$

Where J is the exchange integral for all pairs of nearest neighbors (n.n.) are the same and constant. One can assume that the angle difference $\theta_{i,j}$ between two adjacent spins is small therefore the exchange interaction can be written as:

$$E_{ex} = -JS^2 \sum_{ij} \cos^2 \theta_{ij}$$

Obviously the exchange energy is minimal when the n.n. spins are perfectly aligned ($\theta_{i,j} = 0$). For a magnetic systems ones use the associated magnetic moment **m** = **M**/Ms. Since the magnetic material could be considered as an assembly of a single magnetic moments, as continuum approximation, the exchange energy is as the following:

$$E_{ex} = A \int |\nabla \mathbf{m}|^2 \, dV$$

Where A is called the exchange stiffness, which indicate the strength of the exchange interaction. $|\nabla \mathbf{m}|^2 = (\nabla m_x)^2 + \left(\nabla m_y\right)^2 + (\nabla m_z)^2$ is the squared gradient of the magnetization.

I.2.3. Anisotropy energy

In the solid state the crystal lattice are coupled with the electron orbitals of the atoms, which results a particular orientation of the electron orbitals with respect to the crystalline axes. The spin angular momentum (**S**) is coupled orbital angular momentum (**L**) through the spin-orbit interaction ($E_{so} = \xi \mathbf{L} \cdot \mathbf{S}$) the orbitals orientation forces the spin magnetic moments in one or more particular direction, the so-called *easy axes* of the magnetization

The magneto-crystalline energy must reflect the lattice symmetry therefore it depends only on the magnetization with respect to the easy axes [6]. Usually the anisotropy energy is expressed in a power series of trigonometric functions of the angle (θ_i) which is the angle between the magnetization and the easy axes of the crystal [18].

Indeed, there is no general equation for the anisotropy energy, however for each specific crystallographic geometries case, we can present an equation. For the sake of ease, we consider the case where the existence of one easy axes **(***uniaxial anisotropy)*, the energy density is thus expanded into the first important term:

$$\varepsilon_{ani} = K_1 \sin^2(\theta)$$

Where θ is the angle between the magnetization and the easy axes, and K_1 is the anisotropy constants with a unit of (J/m^3).

Therefore anisotropy energy is obtained as the following:

$$E_{ani} = \int \varepsilon_{ani}(\mathbf{m})\, dV$$

In the out of plane magnetized thin films the easy and hard axes are determined by the sign of K_1. In real system, it exhibit a much more complex anisotropy, with many other anisotropies contributions. For instance beside the magneto-crystalline anisotropy, which is mainly due to the spin-orbit interaction, there is the magnetostriction which is not in the framework of this thesis.

I.2.4. Zeeman Energy

In the presence of an external field $\mathbf{H}_{ext}$ the Zeeman energy is the energy contribution of this external field on the local magnetic moments, thus the energy equation is:

$$E_Z = -\mu_0 \int \mathbf{M}(\mathbf{r}) \cdot \mathbf{H}_{ext}(\mathbf{r}) dV$$

For a uniform applied magnetic field, the Zeeman energy is minimal when the angle θ between the external field and the magnetic moment is minimal so that: $E_Z = -\mu_0 \int \mathbf{M}\,|\mathbf{H}_{ext}| dV$.

This energy is independent from the sample shape or particular domain configuration and only depend on the average magnetization [6].

I.2.5. Landau free energy and Brown's equation

By combining the above four energy contribution to the micromagnetism, the final Landau free energy would be expressed as the following:

$$E_{tot} = E_d + E_{ex} + E_{ani} + E_z$$

In equivalence to the Zeeman energy derivation, where the external applied magnetic field is considered, here we consider the effective field $\mathbf{H}_{eff}$, resulting from the four contributions as an applied field. This effective field can be calculated from the total energy density ε_{tot} with the help of the Brown equation [20]:

$$\mathbf{H}_{eff} = -\frac{1}{\mu_0} \frac{\delta \varepsilon_{tot}}{\delta \mathbf{M}}$$

Therefore the total energy can be written as:

$$E_{tot} = -\mu_0 \int \mathbf{M}(\mathbf{r}) \cdot \mathbf{H}_{eff}(\mathbf{r}) dV$$

And intuitively, this total energy is minimal when the local equilibrium magnetization distribution, $\mathbf{M}_{eq}$ is aligned with $\mathbf{H}_{eff}$.

For complex systems, $\mathbf{M}_{eq}$, have to be solved numerically in a quasi-equilibrium state however for simple systems, it is determined using the Brown equations [20], which suggest a parallel alignment of the spins to the effective field $\mathbf{H}_{eff}$.

$$\mathbf{M} \times \mathbf{H}_{eff} = 0$$

II. Field induced magnetization dynamics and domain wall motion in various geometries

When $\mathbf{M} \times \mathbf{H}_{eff} \neq 0$, the equilibrium is not anymore the case in the system and will evolve in time according to some adequate equation of dynamics. Originally the equation was proposed by Landau and Lifshitz and which is mostly used for the magnetization dynamics description. The main idea which the equation is based on is that in ferromagnetic system a precession of the local magnetization **M** (**r**, *t*) is induced by the effective field $\mathbf{H}_{eff}$, and it has the following form:

$$\frac{d\mathbf{M}}{dt} = -\gamma\left(\mathbf{M} \times \mathbf{H}_{eff}\right)$$

Where $\gamma = |e|g_e/2m_e > 0$ the *gyromagnetic ration* associated with the electron spin (for simplicity). This later determines the rate of the precession, and *g* is the *Landé factor*.

In the dynamics, described in the latter equation, is such that the length (magnitude) of the magnetization |**M**| is conserved and thus ($\cdot \mathbf{H}_{eff}$), which mean that the total energy of the system is conserved as well ($E_{tot} = -\mu_0 \int \mathbf{M}(\mathbf{r}) \cdot \mathbf{H}_{eff}(\mathbf{r}) dV$). While $\mathbf{M} \nparallel \mathbf{H}_{eff}$the magnetic moment precesses around $\mathbf{H}_{eff}$ under the Lamor frequency with the following equation:

$$\omega = \gamma\left|\mathbf{H}_{eff}\right|$$

In a more realistic system and due to the magnetization interaction with the thermal bath, which should dissipate the dynamics of the system, thus the equilibrium approach is not described in this dynamics equation. Therefore the above dynamics description is non dissipative.

Later, Landau and Lifshitz [21], considered the relaxation energy by introducing an additional phenomenological term proportional to $\mathbf{H}_{eff}$ which represent the damping force and it is perpendicular to magnetization. This damping tries to align the magnetization vector **M** with the $\mathbf{H}_{eff}$ (see figure 1.6). The most used Landau-Lifshitz equation in literature is:

$$\frac{d\mathbf{M}}{dt} = -\gamma_L(\mathbf{M} \times \mathbf{H}_{eff}) - \frac{\alpha\gamma_L}{M_s}\mathbf{M} \times (\mathbf{M} \times \mathbf{H}_{eff})$$

Where γ_L is a different gyromagnetic constant than γ. While α is the damping constant (dimensionless) which determine the damping strength.

The magnetization dynamics was described by another equation introduced by Gilbert [22] this equation is, now known as, the Landau-Lifshitz-Gilbert (LLG) equation:

$$\frac{d\mathbf{M}}{dt} = -\gamma_G(\mathbf{M} \times \mathbf{H}_{eff}) + \frac{\alpha}{M_s}\mathbf{M} \times \frac{d\mathbf{M}}{dt}$$

This equation can be written in the following form:

$$\frac{d\mathbf{M}}{dt} = -\gamma_G\mathbf{M} \times \left(\mathbf{H}_{eff} - \frac{\alpha}{\gamma_G M_s}\frac{d\mathbf{M}}{dt}\right)$$

we can clearly remarks in the latter equation that we subtract a damping-term which is proportional to the magnetization derivative from the $\mathbf{H}_{eff}$.

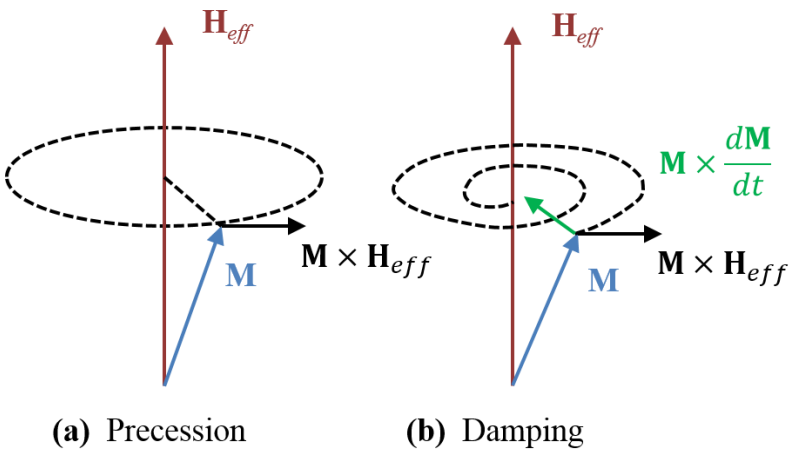

Figure 1.6: (a) Schematic of the precession of the magnetization without damping and **(b)** with the damping term (Green) (always perpendicular to M) of the LLG equation.

The domain wall can be driven by an external applied field at different geometries (planar [23] or ring nanowires [24]). The main origin of the motion is the minimization of the Zeeman energy. The latter is reduced when the domain wall is moved in the direction of growing the domain size where the spins are, somehow, parallel to the applied field while the opposite domain size is reduced. This dynamics can be happed easily, at small fields, in the absence of pinning cites.

The theory behind the domain wall propagation, under an applied field, shows that its motion is not similar to a classical particle driven inside a nanowire. Some of these forces are not all along the wire direction. Some of the spins inside, a transverse or a vortex, wall are perpendicular to the applied field $\mathbf{H}_a$. This yields to a torque, which forces the local magnetic moment out-of-plane, (Figure 1.7).

For sake of simplicity in the analytical treatment we assume a transverse wall using the well-known 1-D model (see subsection II.1 and [25]). In this approximation, the magnetic moment **m**, with an orientation (θ, φ), **m** rotates from **-X** to **+X** ($0 < \theta < \pi$) along the so-called domain wall width (Δ), tilted from the easy plane the angle φ.

In order to move the wall, a torque on θ is needed to align the magnetic moments along the external field $\mathbf{H}_a$. The applied field $\mathbf{H}_a$ toward **–X** generates a torque which tilt the wall spins out-of-plane and intuitively generates a demagnetizing field $\mathbf{H}_d$ perpendicular to the plane. The latter creates a demagnetizing torque in the applied field direction, $\gamma\mathbf{M} \times \mathbf{H}_d$, which tilts the wall spins along the applied field. Finally, therefore only this torque moves the domain wall along the external field (figure 1.7b). By consequence this leads to complex mathematical equations due to the coupling between the linear propagation and the out-of-plane motion [23].

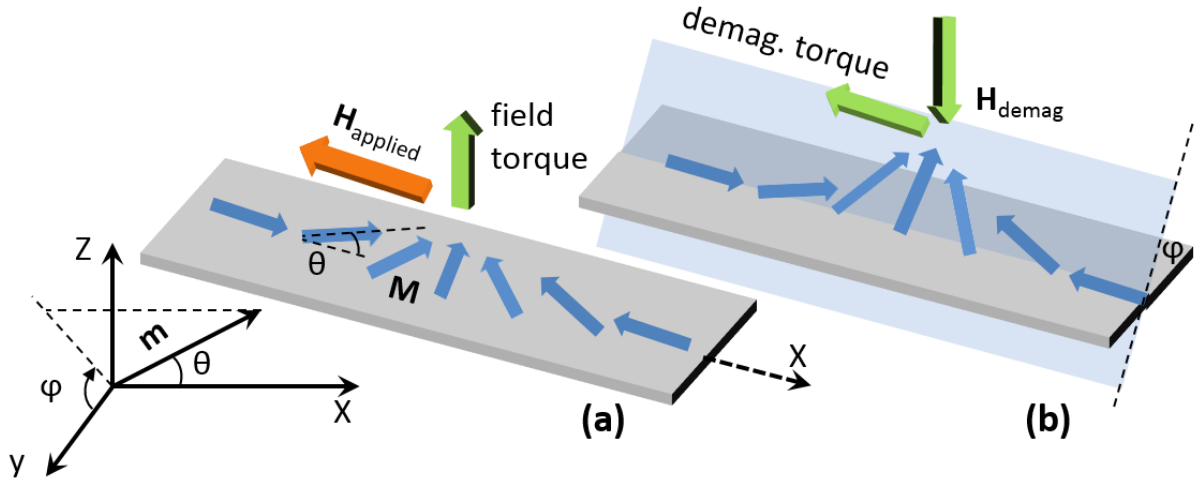

Figure 1.7: Schematic of the field induced domain wall motion in the 1-D models approach. The involved torques in the domain wall motion is also represented: **(a)** the external field (orange) applies a torque (Green) on the domain wall spins (blue) and thus tilting them out-of-plane. **(b)** This yield to a demagnetization (demag.) field and its torque (Green). As a result the domain wall moves in the direction of the field.

II.1. One dimensional (1D) collective coordinate domain wall model

Domain walls driven by an external field at low fields in nanowires are discovered to be well explained by the 1D collective coordinates model. This model describes the domain wall by their azimuthal angle and position. The magnetization configuration used in this limit is mainly the Bloch-wall profile in the presence of a strong uniaxial anisotropy. Moreover, the profile is more general and can be compared with the vortex and transverse wall configuration [26]. However, in the case of the vortex wall, one needs to expand the model to a two coordinates model in order to described more specifically.

Analytically, in the case of a tail to tail Bloch-wall profile, the magnetization components m_x (transverse) and m_y (longitudinal) as the following:

$$m_x = \tanh(x/\Delta) \;\; ; \;\; m_y = 1/\cosh(x/\Delta)$$

Δ, represents the domain wall width.

In order to exanimate the field induced domain wall dynamics in the 1D limit, one should derive the 1D analytical model of the magnetization profile, starting from the Landau-Lifshitz-Gilbert (LLG) equation:

$$\frac{d\mathbf{m}}{dt} = \gamma_0 \mathbf{H}_{eff} \times \mathbf{m} + \alpha \mathbf{m} \times \frac{d\mathbf{m}}{dt}$$

while, $\mathbf{H}_{eff} = -\frac{1}{\mu_0 M_s}\frac{\delta E}{\delta \mathbf{m}}$ is the micromagnetic effective field with $\mathbf{m}$ is the normalized magnetization and E represent the total Landau free energy described above. $\gamma_0 = \mu_0|\gamma|$ the gyromagnetic ratio. It is easier in the present case to use the spherical coordinate system: where θ represent the polar magnetization angle (the wire axis is the polar axis), and φ the azimuthal angle, the magnetization angle in the **Y-Z** plan (see Figure 1.7). In this sense we can write the LLG equation as the following:

$$\dot{\theta} + \alpha \sin\theta \dot{\varphi} = \gamma_0 H_{\varphi},$$

$$\alpha\dot{\theta} - \sin\theta \dot{\varphi} = \gamma_0 H_{\theta},$$

Where both effective field components are:

$$\mathbf{H}_{\theta} = -\frac{1}{\mu_0 M_s}\frac{\delta E}{\delta \theta} \;\; ; \;\; \mathbf{H}_{\varphi} = -\frac{1}{\mu_0 \sin(\theta) M_s}\frac{\delta E}{\delta \varphi}$$

The one dimensional profile (180° Bloch wall profile) can be described as well by the following three parameters: q (the domain wall center position), ϕ (the domain wall magnetization angle or non-local azimuthal angle) and Δ (the domain wall width). By using this parameter the non-local domain wall magnetization profile description become:

$$\theta(x,t) = 2\tan^{-1} exp\left(\frac{x-q(t)}{\Delta(t)}\right); \qquad \varphi(x,t) = \phi(t).$$

We note that *θ(x,t)* represent, here, a head-to-head walls (one has to add π to *θ* to get our tail-to-tail profile). The 1D dynamic equation can be obtained by using a Lagrange framework and by inserting *θ(x,t)* and *φ(x,t)* into the LLG equation which result to following effective equations of motion:

$$\alpha\frac{\dot{q}}{\Delta} + \dot{\phi} = \gamma_0 H_a$$

$$\frac{\dot{q}}{\Delta} - \alpha\dot{\phi} = \gamma_0 H_K \frac{\sin 2\phi}{2}$$

Where $\boldsymbol{H}_a$ is the applied field and H_K is the effective anisotropy field ($H_K = 2K/\mu_0 M_s$) represent the transverse anisotropy field with *K* is the effective transverse anisotropy constant.

In order to understand better the basis of the 1D wall dynamics it is enough to use the time derivative equation of the azimuthal angle, which can be obtained by eliminating the domain wall position q from both previous equations:

$$\dot{\phi} = \frac{\gamma_0}{1+\alpha^2}\left(H_a - \frac{\alpha}{2}H_K \sin 2\phi\right)$$

There are two situations which can be discussed:

1) The first situation is when no transverse anisotropy is presented ($\boldsymbol{H}_K$ = 0). By replacing this condition in the previous equation it becomes:

$$\dot{\phi} = \frac{\gamma_0 H_a}{1+\alpha^2}$$

Which mean that the azimuthal angle precesses under the fixed applied field $\boldsymbol{H}_a$ at a constant precession. Obviously this yields to a linear dependence of the wall velocity with the external field strength.

$$\dot{q} = \gamma_0 \Delta_0 H_a \frac{\alpha}{1+\alpha^2}$$

Where $\Delta_0 = \sqrt{\frac{A}{K_1}}$ is the equilibrium Bloch domain wall width ($\theta = \pi/2$), with A is the exchange stiffness constant and K_1 the anisotropy constant for a uniaxial anisotropy parallel to the Z-axis (Figure 1.7). This is because we assume the domain wall width, $\Delta(t)$, is always in equilibrium, because it relaxes relatively fast towards the equilibrium domain wall width. Therefore $\Delta(t) = \Delta_0(\theta)$ where,

$$\Delta_0(\theta) = \sqrt{\frac{A}{K_l + K\cos^2\theta}}.$$

We note that K_l is the effective longitudinal anisotropy constant which correspond to K_1 in materials with perpendicular magnetic anisotropy, while in thin film $K = 0$.

2) The second situation where transverse anisotropy is presented, the dynamics is quite different than the previous case where the wall velocity is now proportional to the external field H_a respecting the so-called *Walker field*, H_W, introduced by *Walker* in his 1D solution [27].

$$H_W = \frac{\alpha H_K}{2}$$

If the absolute value of the external field $|H_a| < H_W$, a constant domain wall velocity, which scales linearly with the external field, with the existence of a new equilibrium value of azimuthal angle (ϕ^*):

$$\dot{q} = \gamma_0 \Delta^*(\phi^*) H_a/\alpha$$

In this regime we observe a steady state domain wall motion. We note that the velocity is constant but higher in comparison with the zero transverse anisotropy case, since the damping parameter α is presented in the denominator when assuming a small value of α. Therefore from the previous equation the *Walker velocity* (v_W) is defined as the following:

$$v_W = \frac{\Delta_0 \gamma_0}{\alpha} H_W = \frac{\Delta_0 \gamma_0}{2} H_K$$

Clearly this velocity is independent of the damping parameter α. The field-velocity relation is shown in figure 1.8 (blue curve).

At the Walker field, the existing equilibrium between the demagnetizing/damping torque and the driving field torque which keep ϕ constant is no-longer presented. The wall velocity reach it maximum for a $\phi = \pi/4$ in the linear low field regime [28]. In the case where $|H_a| > H_W$ no equilibrium value of ϕ is presented, as well, and exercising a no-linear precession or oscillatory dynamics, due to the periodic nature of the torque term with respect to ϕ and because of the variation of the domain wall width [26], therefore a complex dynamics happen. This required the need of the numerical calculation of the wall velocity or position. This results a deep domain wall velocity decrease take place above the *Walker velocity* (Walker breakdown) see Figure 1.8.

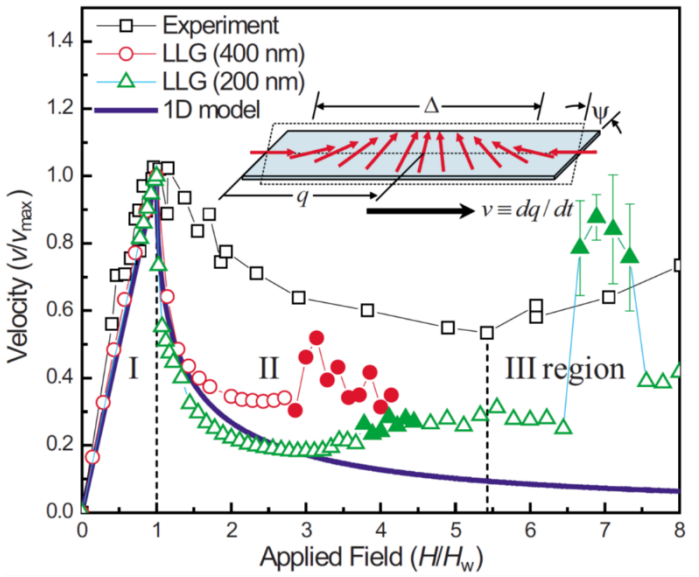

Figure 1.8: experimental and simulated domain wall velocity in straight Py nanowires as a function of an external field. The linear velocity increase for low fields (**region I**) and reach the maximum velocity, $v_{max} = v_W$, whereas the velocity drop at the Walker field H_W (**region II**). From Ref. [29].

II.2. Two collective coordinates approximation

We could demonstrate above that the experimental Walker breakdown observation for a transverse wall can be explained by the one dimensional approach for a Bloch-wall profile. However in the opposite case where the nanowire exhibit a vortex wall spin structure the dynamics become more complex due to the wall configuration. The spin structures of vortex domain wall consist of three topological defects: two half-antivortices at both edges and a vortex in the center of the nanowire [30]. Although, the occurrence of the Walker breakdown for a vortex wall still can be described.

In general the collective-coordinate model uses the soft modes of the system, in order to describe the vortex core dynamics in more details. In the present case (vortex wall) the softest modes are the (X, Y) coordinate of the vortex core, where X is along the wire axis and Y the transverse coordinate across the width of the wire [30].

In contrast to the 1D model for the transverse wall, where only the x-direction is considered. The azimuthal angle ϕ is not anymore the rotation of spins inside the wall however, it represent the vortex core position in the y-direction. We note that for $\phi > \pi$ the vortex core is expelled from the wire. For a given applied field in the wire axis direction, ones expect four different vortex core displacement possibilities (see Figure 1.9). A *y* motion means that the vortex core could be expelled from the wire edge depending on the resulting forces strength acting on it.

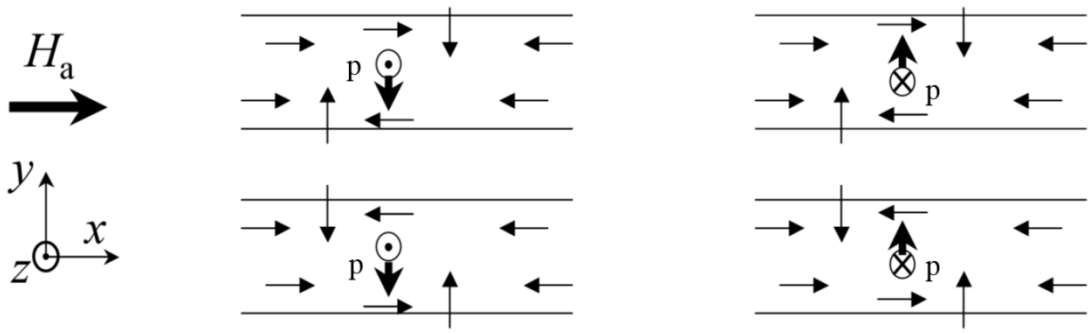

Figure 1.9: spin structure configuration of four different head-to-head vortex wall lateral displacement possibilities (along y) driven by the same external applied field direction. The vortex core polarities (p) inside the wall are shown. Adapted from [26].

The dynamics of the core are equivalent to the core precession. In this new model, the equation of motion for the domain wall dynamics could be derived from the LLG equation; more details can be found in reference [30]. By analyzing of this equation of motion of the vortex core, it can lead to a four different regimes: (A) low field, (B) critical field, (C) high field and (D) a very high field regime. These regimes (A - D) are illustrated in the figure 1.10. The figure presents a schematic curvature of the vortex core velocity in function of the applied field $\mathbf{H}_{\boldsymbol{a}}$.

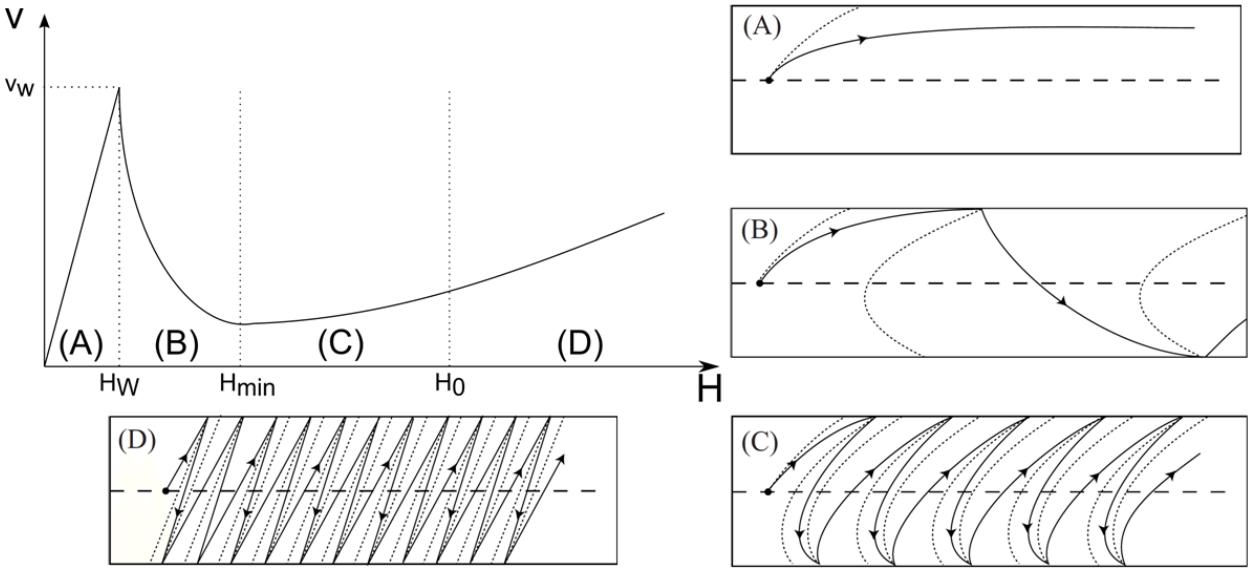

Figure 1.10: the graph represent the domain wall velocity V(H) curve due to an external field. The domain wall trajectories (solid line) and equipotential line (dotted) at different regimes are illustrated as well. Adapted from [30].

(A) Low field regime:

At the metastable state of the vortex wall it is more favorable that the core is sitting in the wire center, this mean there is a restoring force which opposite the *y* motion of the core. Therefore at low fields and below a critical field H_W the vortex domain wall move in a viscous motion, with a high mobility $\mu = dV/dH$. However the domain wall trajectory includes a small core offset in the *y*-direction after reaching an equilibrium azimuthal angle (Figure 1.10).

(B) Critical field regime:

Above the critical field, H_W, the transverse equilibrium position of the vortex core is not anymore inside the strip, thus the vortex core is expelled out of the wire and the wall will transform to a transverse wall. This transition from vortex wall to transverse wall is called Walker breakdown and occurs with a velocity decrease. Therefore above the Walker threshold the viscous motion is replaced by an underdamped oscillation propagation followed by small drift of the wall. The oscillated domain wall velocity is related to the periodic transformation of the domain wall spin structures. The domain wall precessions happen when the vortex core is crossing the wire width periodically as illustrated in figure 1.10. We note that the Walker velocity (V_W) increases linearly with the thickness of the strip.

(C) Small dissipation or high field regime:

At this regime, the vortex core with polarity *p* switch its polarity to *-p* each time the vortex core is expelled from the nanowire edge and re-nucleate at the same position as the schematic of the trajectory shows. Thus, the vortex domain wall propagates between the wire edges and switches its polarity *p* once it expelled from the edge. However in contrast to this simulated result in straight nanowire, we recently demonstrate experimentally, in nano-rings structure, that the vortex core then re-injected with the same vortex-core polarity.

(D) Very high field regimes:

At much higher fields an increase of the wall velocity by increasing of the applied field strength since the motion is dominated by the Zeeman energy however the mobility is far away than in the low field regime. Therefore the vortex core trajectory showed in figure 1.10-**(D)** almost follows the equipotential line. The transformation frequency between vortex wall to transverse wall and vice versa is the highest as illustrated [26, 30].

Chapter 2

Sample fabrication and experimental setup

Abstract

The first step towards a successful experiment with magnetic micro- and nanostructures, is the careful fabrication of the sample with the desired properties. For reliable nanofabrication it is crucial to work in a clean environment and in a well-controlled manner. To this end, there are several parameters to consider such as the patterning method, the nanostructure design, substrate, magnetic materials, electric contact and many other factors. In this chapter the experimental techniques necessary to fabricate the samples as well as the characterization methods to perform the magnetization dynamics imaging and spin transport measurement on the nanoscale are presented. We note that most studied samples in this thesis were produced using a newly bought electron-beam lithography (EBL) system at our institute (Institute of Physics - Johannes Gutenberg-Universität Mainz), therefore quite a long time was invested for the sample fabrication optimization process. Some samples have been prepared in collaboration with the Nanostructuring Center at TU Kaiserslautern. Various shapes and sizes of ferromagnetic nanowires have been studied. The direct observation of the field induced magnetization dynamics was achieved by employing time resolved scanning transmission X-ray microscopy (STXM) at MAXYMUS Beamline, Helmholtz Zentrum Berlin, BESSY II.

This chapter is arranged as follows. The sample fabrication by electron-beam lithography is discussed in Section II. We describe here the basic sample fabrication process step-by-step. The magnetic imaging is based on recording the X-ray transmission through the magnetic sample, where the magnetic contrast depends on the local orientation of the magnetization with respect to the incident X-ray photons, as described in Section III. Furthermore in this section we discuss the generation of the required spatially coherent and X-ray light with a well-defined energy and the functionality of the used STXM microscope. The time evolution of the magnetization dynamics is recorded stroboscopically by employing a pump/ probe technique, as discussed in Section IV, in addition to the periodic electronic signal generation and acquisition.

I. Magnetic material

The main magnetic material used in our studies (spin transport and magnetization dynamics), is the polycrystalline permalloy (Py), which is an Iron-Nickel alloy ($Ni_{80}Fe_{20}$). This material exhibit a very weak crystalline anisotropy [31], hence the shape anisotropy dominate in determining the magnetization configuration in nanostructres. Permalloy has a relatively high tunneling spin polarization ~ 45 % at the Fermi level E_F [32, 33] and a high magnetic susceptibility. Moreover, permalloy exhibit low damping due to its low coercitive field, which is important for the magnetization dynamics studies. Due to these properties permalloy is described as a soft magnetic material.

These advantageous properties make permalloy an ideal candidate to study magnetization dynamics using relatively small fields, which are required from the technological application point of view in order to limit the energy consumption. Furthermore the resistivity of permalloy is quite low in comparison with other alloys [34], and its anisotropic magnetoresistance (AMR) is high [35]. This latter effect is critical to detect changes of the spin structure electrically. Finally what is also important is that both nickel and iron have a strong X-ray magnetic circular dichroism (XMCD) signal at the L_3-absorption edges for the soft X-ray energies, 852.7 eV and 706.8 eV, respectively [36], thereby providing a contrast mechanism for the magnetic imaging.

II. Sample fabrication and preparation

In this section the single steps of the sample fabrication process in addition to all needed materials for the sample preparation and verification will be explained.

II.1. Electron Beam Lithography

One of the most established techniques to produce nanostructures with lateral dimensions down to a few tens of nanometers is Electron Beam Lithography (EBL). The system consists of an electron gun with an emission source and includes the needed optics for controlling and focusing the electron beam. Therefore one of the factors limiting the spatial resolution is the optical system quality.

Electron beam lithography is based on the exposure of a sample, which is covered in a electron sensitive resist, to a desired pattern of an electron beam. After the exposure, the molecular properties of the exposed areas of the resist are changed. These properties changes lead to the exposed area being either more or less soluble in a given developer, depending on the resist type. In general there are two categories of resist, either positive or negative resists. The difference between them is that the electron exposed area is removed for the positive resist while in the case of the negative resist the unexposed area will be dissolved after development [37]. However all the fabricated sample in my work used a positive resist such as methyl methacrylate/methacrylic acid (MMA/MAA) and polymethyl methacrylate (PMMA). This technique is similar to optical lithography, where the optical resists are irradiated by photons instead of electrons.

In general with electron beam lithography, the required design is produced by scanning the sample surface and exposing the desired area with an electron beam, in analogy with the scanning electron microscope (SEM) working principle. In order to obtain a high precision during the exposure the scan of the electron beam can be done electronically by deflecting the beam within a small area, which is called a *stitching field*. In the case that the structure geometry is bigger than the *stitching field*, then the exposure is split into several stages. These pieces have to be "stitched" together, therefore the sample stage, is moved during the exposure in such a way that these divided parts match together. The precise matching of *stitching fields* is very important in the fabrication of nanostructures. Therefore, successful electron beam lithography requires firstly a high a high precision and good alignment of the beam deflection within the exposed areas (so-called *write-field alignment*), and secondly a very precise and stable sample stage motion. One of the main advantages of the specialized electron beam lithography systems is that they employ a laser interferometer system to provide the required positioning precision.

Most of the EBL in this work was performed using the commercial Raith *PIONEER* system. It is characterized by its thermal field emission technology (TFE), sub 20 nm lithography resolution, high resolution imaging and pattern inspection and laser interferometer controlled stage with modular rotation and tilt with a precision error less than 50 nm [38].

There are some basic important parameters have to be chosen for any EBL which are the acceleration voltage of the electrons, *U*, and the electron beam current, *I*. In our system any value between 0 kV and 30 kV can be chosen for *U*. In addition the aperture sizes for the electron beam can be selected (e.g. 7.5 μm, 10 μm, 15 μm, 20 μm etc.). The bigger the size of the aperture, the higher the resulting beam currents are. Using a GDSII-editor within the *PIONEER* software, one can design the pattern layout for any desired two-dimensional structures. Within the layout it is possible to indicate a rectangular sub-area which then will be considered for the electron beam exposure. This zone is called the working area and is usually divided into specific *stitching fields* depending on the desired *write-field* size, taking into account the exposure time and the desired finest structure resolution. Before starting any exposure it is crucial to calibrate the system to perform a precise transformation of the stage's X,Y-coordinate system to the sample layout's system with coordinates U,V, in addition to having a good focus of the electron beam on the sample. Therefore the first lithography step is dedicated to making markers which become vital for positioning the nanostructure in relation to the contact pads which are usually made in a different lithography step. The markers are incorporated in the design layout, hence, their location and the distances between them are well known. Therefore it is necessary that the system reads in the associated X,Y-coordinates and the input is used by the software in order to calculate the transformation matrix between these two coordinate systems. In the final step before launching the automatic exposure, one needs to set appropriate exposure parameters such step-size, *s*, and dosage, *D*. These parameters are chosen from previous exposure tests which are performed before starting any real sample fabrication. For instance, for good exposure results, the step-size should be chosen to be smaller than $1/5$ of the smallest feature size of the exposed structure.

Using the following equation:

$$D = \frac{I \cdot \tau}{s^2}$$

where τ represents the dwell time, the system can estimate the expected exposure time of the whole pattern layout inside the indicated *working area* [38].

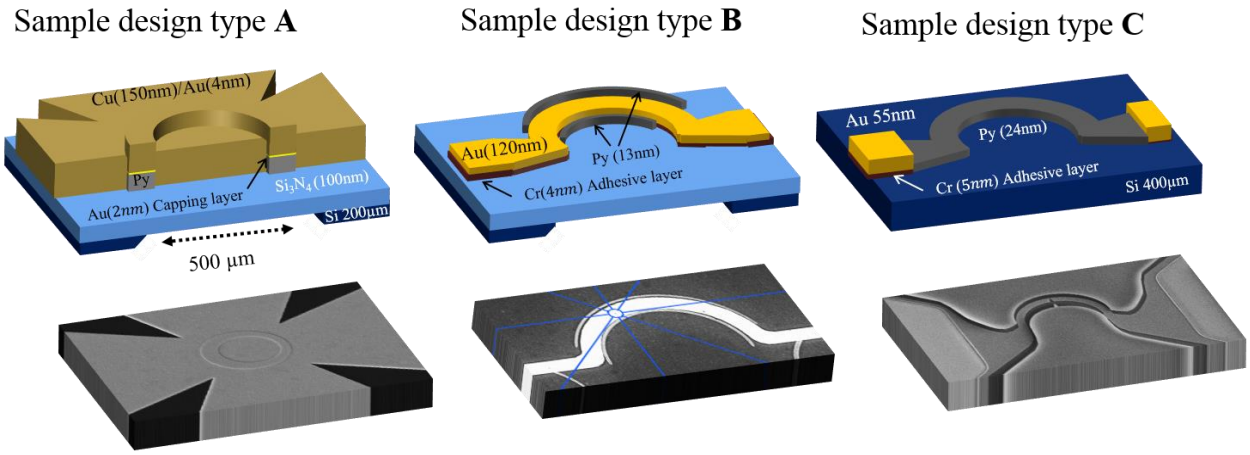

Figure 1.1: Top schematic illustration of three sample designs on Si and Si_3N_4 substrates. **(A)** Crossed copper stripline on top of permalloy rings (diameter 5 µm, thickness 30 nm), **(B)** two curved permalloy nanowires (thickness 13 nm, width ~150 nm) surrounding a curved gold stripline with a width of 1.1 µm and **(C)** contacted permalloy nanocontact half-ring. Samples **(A & B)** are both fabricated on top of Si_3N_4 substrate (500 µm windows size), whereas sample **(C)** is structured on top of a Si (100) substrate. **Bottom:** SEM images showing the real shape of the fabricated samples for each sample design.

II.2. Substrates

A preliminary step for sample fabrication is the choice of a suitable substrate, depending on the experiment needs. In this thesis there are two main different classes of measurement which in turn need substrates with different properties, explained as follows:

The first sets of measurements are the magnetotransport measurements of magnetic nanostructures (see chapter 6). For these studies it is important to have a rigid and insulating layer to ensure a fixed support of the nanocontact and to prevent any current shunting through the substrate during the measurement, respectively. Therefore we used a naturally oxidized, un-doped (n-type) silicon Si (100) substrate with the following specifications: 375 µm thickness with a high electric resistivity (> 1000 Ωcm).

In the second project we directly image the magnetization in magnetic nanostructures by detecting and recording the transmitted X-ray photons, therefore we need to fabricate our sample on substrate with sufficient X-ray transparency (discussed in chapter 3, 4 and 5). To this end we fabricate our sample on top of 100 nm thick silicon nitride (Si_3N_4) membranes. These are

commercially available from (Silson Ltd.). One substrate chip is $23.5\,mm \times 23.5\,mm$ and consists of 200 µm thick, high resistivity, silicon Si (111) including an array of 4×4 membrane frames ($0.5\,mm \times 0.5\,mm$). The front side of the chip is covered by 100 nm thick Si_3N_4 layer, which is freestanding at the frames. Single frames are schematically shown in figure 2.1.

II.3. Positive electron beam resists and sample coating

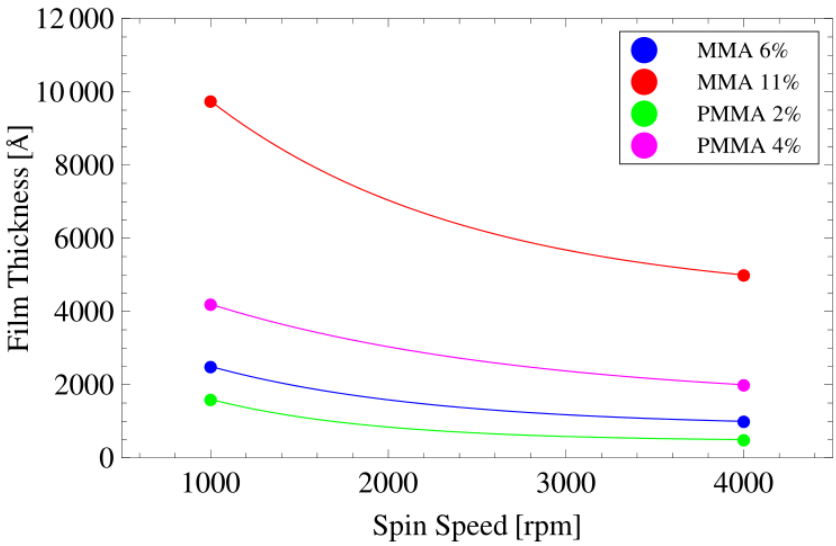

Figure 2.2: Spin curves for the main electron beam resists employed in this work: polymethyl methacrylate (**PMMA**) for two different concentrations percent **(2% and 4%)** in Anisol with a molecular weight of **950 k** and methyl methacrylate/methacrylic acid (**MMA/MAA**) for two different concentrations percent **(6% and 11%**) in ethyl lactate. From Ref. [39].

Before any electron beam exposure or pattern transfer one needs to prepare the substrate. Following on initial cleaning of the substrate, the electron beam resist layers have to be coated on top. In general electron beam resists are either organic or inorganic molecules which are dissolved in a solution and can be coated on top of substrate by using a so-called spin-coater. By fixing the substrate into the spin-coater on top of a substrate holder, *the chuck*, (either using a vacuum in the case of a rigid substrate such as Si, or using clamps in the case of the Si_3N_4 membranes) the resist can be dropped onto the center of the substrate using a pipette. Subsequently the sample is rotated, with relatively high speeds, which removes the excess resist and providing a well-defined homogenous resist thickness (excluding the substrate corner where the resist is a bit thicker). The thickness is controlled by the following parameters: spinning speed of the chuck, spinning time, substrate material/sizes and the used resist with its specific concentration and molecular weight. Typical spin curves presenting the resist thicknesses for different spin speed for different resists and solvent concentrations, are shown in figure 2.2. In

this work the used electron beam resist stack consists of (MMA/MAA) and (PMMA) as mentioned above. Both are common positive resists.

The used resist coating procedure is presented in the following and partially schematically illustrated in figure 2.3 for the case of the Si_3N_4 membrane as substrate (sample type **(A)** shown in figure 2.1:

1) Pre-cleaning procedure of the substrate:
   A complete immersion of the substrate in Acetone "$(CH_3)_2CO$" Isopropanol followed by "$(CH_3)_2CHOH$", for about ~ 1 min in each case and subsequently blow dry using a nitrogen gas gun.

2) MMA/MAA 6% coating layer:
   The spin coater is programed to initially pre-spin with a spin speed of 500 rpm for 5 s, in order to initially spread the resist on the whole sample, followed by the main spin at 4000 rpm for 60 s.

3) MMA/MAA 6% baking using hotplate:
   The substrate is placed on a hotplate at a temperature of 180 °C for 90 s. Hereby the solvent will be evaporated and the resist will be transformed from a polycrystalline to an amorphous phase, leading to a smooth surface.

4) PMMA 4% coating layer:
   In this step we repeat step (2) using the same speed spin and timing.

5) PMMA 4% baking:
   Repeat of the third step (3) with the same parameters.

We note that the above resist coating procedure is the same for both the Si_3N_4 membranes (sample type (A) & (B)) and the Si substrate (sample type (C)), shown in figure 2.1, and for each of the electron beam exposures for the different lithography steps. However the resist recipe (solvent characteristics and thickness) is different depending on whether the nanostructures or contact pads are patterned, since different steps require different resist sensitivity, resolution and materials deposition thicknesses. Thus, the above resist recipe is specifically for the first electron beam step to produce alignment markers as discussed below.

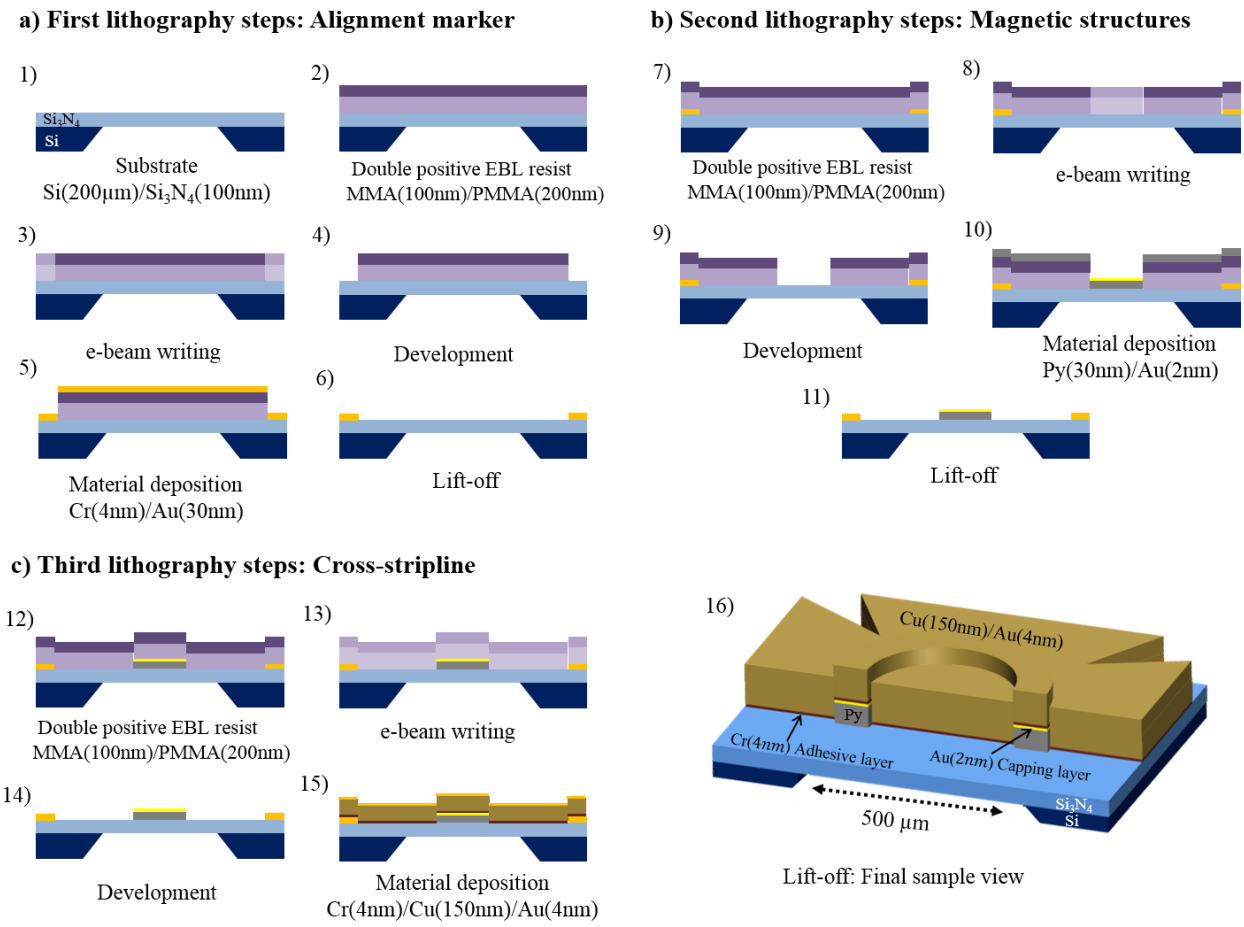

Figure 2.3: Step-by-step process for positive electron beam lithography, for the sample design **(A)** presented in figure 2.1, on commercial pre-structured Si_3N_4 membranes.

II.4. Pattern transfer steps with positive resists

As mentioned above, the characteristic of the positive resists is that the area exposed by the electron gun will be dissolved in a solvent, whilst the unexposed area remains. The electron sensitivity of the resists is proportional to the thickness, molecular weight and the concentration. In this section we are going to describe the step-by-step sample fabrication using 100 nm thick silicon nitride (Si_3N_4) membranes (as described above in section II.2) for the sample design **(A)** Figure 1.2. A typical sample preparation process is discussed below and schematically presented in figure 2.3:

a) First lithography steps: Alignment markers

One of the extremely important issues during the whole sample fabrication process is the precise alignment of different exposures and specifically between the magnetic structures and the contact pads and/or striplines. Therefore the first lithography steps consist of pattering alignment

markers, which are typically $10 \times 10\ \mu m^2$ crosses of Cr (4 nm)/ Au (30 nm) as shown in figure 2.4. Thus this first lithography steps consist as follows:

1 – 2) These steps are the same cleaning and spin coating steps described in the subsection II.3.

3) After loading the sample into the EBL system and preparing the exposure data, the crossed alignment markers are patterned into the resist.

4) After the e-beam writing with a sufficiently high energy to penetrate the whole resists thickness, the exposed resists become soluble in a special solvent. In this step the sample is developed (by complete immersion) in Methyl-iso-butlyl-ketone (MIBK) solution mixed with Isopropanol (IPA) in a composition of 1:3 MIBK:IPA for 40 s.

5) At this step the material, Cr (4 nm)/ Au (30 nm), is deposited using the sputter machine (described below).

6) After deposition the resist is lifted-off, taking with it the undesired metal on top, by a complete immersion in NEP (N-ethyl pyrrolidone) at 130 °C for ~ 30 min to 60 min. Since we are dealing with very thin substrates (100 nm (Si_3N_4) membranes) it is not advisable to use the ultra-sonic bath in order to accelerate the lift-off process, therefore we used NEP which showed more efficiency than the more conventional approach using Acetone.

b) Second lithography steps: Magnetic structures:

7) Repeat step number **2),** using the same resists.

8) Similar to step **3)**, however different exposure parameters are used in order to provide high resolution for the smallest magnetic structures.

9) Repeat of step **4)**.

10) Magnetic material (Py) deposition of ~ 30 nm thickness and capped with 2 nm gold (Au).

11) Repeat of step **6)**. We note that the lift-off process at this stage is the most difficult, in particular for the inner part of the ring. For this reason we initially used a double resist layer with different sensitivity MMA/PMMA (MMA more sensitive to IPA than the PMMA) which provides a small undercut, thus helping with the lift-off process. Furthermore an array of the magnetic nanostructure (rings) is patterned. The success of the lift-off of each individual nanostructure is checked by scanning electron microscopy (SEM) (figure 2.4) in order to pattern, in the next step, the cross-strip lines on top of a well lifted nanostructure.

c) Third lithography steps: Cross-stripline:

12) Repeat of step **2)**.

13) Repeat of step **3)**, however different exposure parameters are used to reduce the exposure time, since the cross-strip lines are quite big in comparison to the magnetic structure (few hundred of μm) which means that an over-night exposure is needed for the whole chip (16

membranes). One of the main parameters which dramatically increase the exposure speed is the use of big apertures (e.g. 120 µm) and larger step-sizes. This can safely be done since the roughness of the stripline has little influence on the measurement.

14) Repeat step **4)**.

15) The material, Cr(4 nm)/Cu(150 nm)/Au(4nm), is deposited via sputtering.

16) Repeat step **6)**.

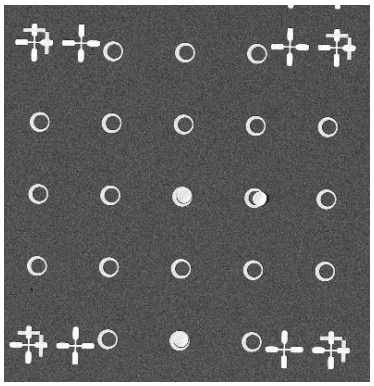

Figure 2.4: SEM image after the second lithography step following lift-off, for the sample design **(A)** (shown in figure 2.1). It shows an array of asymmetric rings with 5.5 µm diameter. The filled rings represent the unsuccessful lift-off. The crosses are the alignment markers used to guarantee a precise registry between different exposures steps. The distance between the centers of two rings is 20 µm.

II.5. Pattern transfer steps with shadow lithography

These samples are prepared to be measured *in-situ*, directly after the magnetic material deposition, without breaking the vacuum, since one of the main aims of this experiment is to ensure the cleanest possible nanocontacts, see chapter 6. For that reason we fabricate a resist shadow mask as shown in figure 2.5. Here we use a double layer resist similar to the previous case, however in this case the MMA buffer layer is thicker, i.e. MMA(500 nm)/ PMMA(200 nm). MMA is a copolymer that is chemically very similar to PMMA, however more soluble in IPA. This allows for the creation of a tunable undercut by varying the time in IPA during the developing stage. The lithography steps are similar to the previous method; however the main difference is that the Au contact pads are exposed at the first lithography step together with the alignment markers, and re-exposed in the third lithography step.

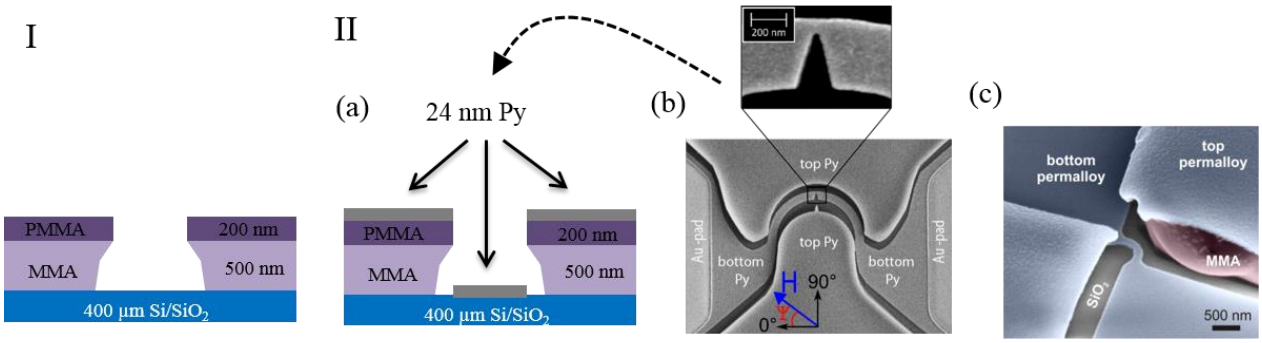

Figure 2.5: Nanocontact sample illustration (Sample type **(C)**): **(I)** Schematic side view of sample before deposition. A MMA/PMMA shadow mask formed of resists of different sensitivities is patterned via e^--beam lithography. The structure is a notched half-ring. The undercut at the edges of the resist ensures the subsequently deposited ring and pads are electrically isolated from ground. **(II)** Sample after deposition: **(a)** Schematic side view; **(b)** SEM image of the sample (top view); **(c)** Colored SEM image of the sample (oblique view). The material is evaporated in an UHV chamber with in-situ characterization subsequently performed at 80 K, without breaking the vacuum allowing the highest contact purity. The MR is measured in low-magnetorestrictive materials ($Ni_{80}Fe_{20}$), with rigidly attached substrates to reduce magnetostriction.

II.6. Material deposition

In this work the material deposition was done using DC-sputtering, for the contact pads and alignment markers and electron beam evaporation in ultra-high vacuum (UHV) for the magnetic material deposition.

II.6.1. Electron beam evaporation

The main advantage of the electron beam evaporation is the achievement of a high thin film quality. This deposition method requires a good UHV during the deposition in order to ensure the cleanest possible film quality. The material evaporator consists of a target metal, such (Py, Ni, Au,..), next to a tungsten (W) filament and oriented towards the sample position. The material evaporation take place by heating the metal by connecting the target to a high voltage (~1000 V) and thus accelerating the electrons emitted from the tungsten filament. The deposition rate is controlled by the applied voltage to the evaporator and the applied current to the filament.

II.6.2. DC-sputtering

Sputter deposition is a physical vapor deposition (PVD) method for thin film deposition. The basis of this method is that the atoms of a target material are evaporated when momentum exchange takes place between ionized gas atoms and target atoms [40]. Therefore during the deposition the chamber is filled with inert Argon (Ar) gas to a deposition pressure of 5×10^{-2} mbar. The deposition works as follows, the ionized gas atoms are accelerated into the metal target

under the influence of a created electric field. The metal atoms are thereby sputtered and reach the sample surface. It was found that the angular emission of the sputtered atoms has a cosine distribution [41]. One of the main advantages of the sputtering technique is that the deposition rate is much higher than using electron beam evaporation technique.

III. Imaging magnetization dynamics

Nowadays, a wide range of high resolution magnetic imagining techniques are available, which all have various advantages and disadvantages.

Some of them do not require synchrotron radiation. For instance, scanning electron microscopy with polarization analysis (SEMPA), magnetic force microscopy (MFM) and Lorentz transmission electron microscopy (LTEM) or spin polarized scanning tunneling microscopy (STM). However all these techniques do not offer good temporal resolution and are therefore only efficient for static magnetic configuration imaging. On the other hand, using femtosecond laser pulses in magneto-optical Kerr microscopy (MOKE) provides time information with a high resolution (less than a few tens of femtoseconds). However, the lateral resolution of the resulting image is limited by the wavelength of the laser radiation, which is usually not enough to image the spin structure within the domain wall in ferromagnetic nanostructures. For more details on different magnetic imaging techniques, a thorough overview can be found in Ref. [17, 42].

A breakthrough, in magnetic microscopy the discovery of the X-ray magnetic circular dichroism (XMCD) [43] effect which has been used as a magnetic contrast mechanism with synchrotron light based microscopy techniques. This was rapidly implemented, years ago, with proof of concept on scanning transmission X-ray microscopy (STXM) at the Advanced Light Source (ALS) facility [44]. This was shortly followed by studies of magnetic systems using Transmission X-ray Microscopes (TXM) [45] and Photoelectron Emission Microscopy (PEEM) [46]. The X-ray magnetic circular dichroism techniques provide a direct probe of the magnetic configuration independent of the stray field, thus it can be bulk sensitive as well as surface sensitive. Moreover these are sensitive techniques due to the strong advantages of the XMCD effect as will be discussed below, section III.1. Therefore the X-ray microscopy has significant advantage over the other mentioned magnetic imagining techniques due to its relatively high probing depth and its spectroscopic benefits. X-ray microscopy is supported by the development of the synchrotron radiation sources, which provide X-ray radiation with a high brilliance and other advantages in comparison to laboratory sources, as shown in section III.2.

Regarding the direct imaging of the magnetization dynamics, in the framework of this thesis, we used the synchrotron based magnetic imaging technique time-resolved scanning transmission X-ray microscopy (STXM). This technique provides us high temporal and spatial resolutions, temporally by taking the advantage of the pulsed nature of synchrotron radiation and spatially due to the use of the XMCD effect as the magnetic contrast mechanism which requires circularly polarized X-rays exhibiting a wavelength of just a few nanometers. One of the strongest

advantages of STXM is the scanning feature in combination with the fast photon detector, which allows for fast single photon counting and uses directly the whole synchrotron radiation capacity. This is a great advantage in comparison to other synchrotron based magnetic imaging techniques such as coherent X-ray holography [47] or PEEM, which employ a full-field charge-coupled device (CCD) detector, instead of a photon detector, in order to integrate the image signal.

In the following we present general background information for synchrotron radiation and STXM, including the optical devices.

III.1. X-ray magnetic circular dichroism (XMCD)

There are several techniques used to measure the magnetic properties of materials. However most of them are sensitive to the total magnetization of the measured system and cannot distinguish between the contributions of different atoms in alloys or multilayers system, or between their angular moment and its spin. Furthermore, the low quantity of material present in many samples, which exhibit interesting technological effects such as magnetic nanostructures, requires a high sensitive method of measurement. One of the most powerful approaches to achieve sensitive, elemental specific, probing of magnetic properties employs X-ray magnetic circular dichroism.

The magnetic dichroism effect is driven by the symmetries of the magnetization distribution created by unpaired electrons. For example, materials with a net moment (ferro- or ferri-magnets) may exhibit magnetic circular dichroism, where the absorption depends on the relative orientation of the photon helicity and the magnetic easy axis. XMCD is the absorption difference, for a magnetic material, between the left & right circularly polarized X-rays at the resonant excitation from the core level of the materials. This absorption difference can be related to the magnetic moment of the atoms which is involved in the absorption processes [48].

In the resonant absorption of the X-rays, the atom absorbs a photon, which leads to an electron transition from the core level to an empty valence state above the Fermi level (Figure 2.6). Each element has its characteristic absorption energy edges. The dipolar selection rules define the final level probed by the transition [49].

Nowadays, due to the intense and coherent X-rays obtained from synchrotron facilities, the XMCD techniques are developed in the fields of spectroscopy and microscopy in order to quantify the magnetization configuration of the studied systems.

The easiest way to describe the X-ray absorption spectra is through the one electron model. In this model, one electron is excited from the core level and transmitted to an unoccupied state at the valence level of the system. According to Fermi's golden rule [17], in the first approximation, it is possible to determine the transmission probability per unit time or in other words the transition rate from the initial to the final level, which can be written as follows:

$$\omega_{abs} = \frac{2\pi}{\hbar}|\langle k|P|c\rangle|^2 \rho_f[h\upsilon - (E_k - E_c)]$$

Where $|\langle k|P|c\rangle|$ is the absolute value of the matrix elements of the interaction operator "P" of the electromagnetic field with the electron of the absorber atom between the core level $|c\rangle$ and the valence level $|k\rangle$. For example, in our study it represents the following transition: $2p \rightarrow 3d$ level. In the electrical dipolar approximation $P = p \times \hat{e}$, where p is the electron momentum operator and $\hat{e}$ represent the circular polarization vector left (+) or right (-). ρ_f is the valence density states at an energy E_k above the Fermi level. We therefore deduce that, according to the photon circular polarization, the transition leads to spin polarized final states. For magnetism, the most interesting absorption edges are those where the final level is that which contributes most to the magnetization of the probed element, for instance the empty states in the d orbital level in the transition metals. The transition usually happens as follows: $2p \rightarrow 3d$.

The quantum numbers representing the core level $|c\rangle$ (initial state) and the valence level $|k\rangle$ (final state) are the electronic states in the atom, $|n, l, m_l, s, m_s\rangle$, where n is the main quantum number, l is the orbital quantum number, m_l the magnetic quantum number, $s = 1/2$ represents the electron spin and $m_s = \pm 1/2$ represents the orientation of the electron spin. This representation of the initial and final states with the electronic states in the atom leads to the dipole selection rules as follows:

$\Delta l = \pm 1$, due to the angular momentum conservation, the total angular momentum change corresponds to the total spin of the photon $\hbar$.

$\Delta m_l = \pm 1$: The magnetic quantum number changes for circular polarized light. While $\Delta m_l = 0$, for linear polarized light.

$\Delta m_s = 0, \Delta s = 0$: The photon is a multiple of the electron spin, therefore there is no change in the electron spin.

By considering the dipole selection rules, it is possible that an electron at the $2p$ core level is excited into an empty $3d$ state at the Fermi level. However it is not allowed that the electron spin switches during this transition.

An intuitive manner to understand the presence of circular dichroism in the X-ray absorption spectra in magnetic materials is by way of the so-called *two steps mechanism* proposed by *Stöhr* and *Wu* [50] as depicted in Figure 2.6.

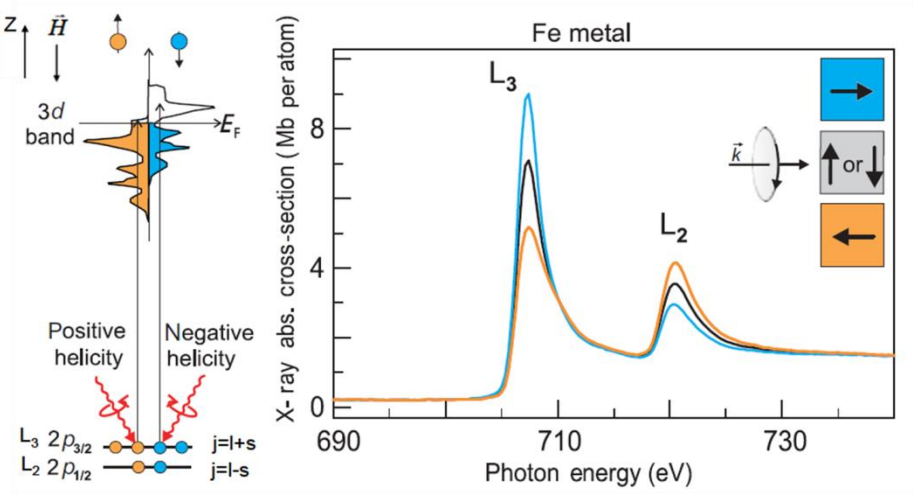

Figure 2.6: Adapted from Ref. [17]. **Left:** band model with the core 2*p* levels and the 3*d* valence band. In the first step, the spin polarized electrons are excited from the 2*p* level and the polarization depends on the absorption edge (L_3 or L_2) and the polarization of the absorbed light. In the second step (final state), the 3*d* band acts as a spin detector, depending on the number of the empty states available for the electron spins. **Right:** illustration of the XMCD effect for the absorption at the core level for Fe $L_{2,3}$. The color code of the X-ray absorption spectra (XAS) corresponds to the magnetization orientation inside magnetic domains as reproduced schematically right of the XAS, relative to the helicity and the incidence wave-vector *K* of the light for the given external magnetic field.

In this model, the first step describes the excitation of the core electrons by the circularly polarized light. For example, left circularly polarized light propagating in the +z, gives rise to a transition $\Delta m_J = +1$ (-1 for right circular polarization). Here, for simplicity, we discuss only the transition $2p \rightarrow 3d$. During the photon absorption process, the photon's angular momentum is completely transmitted to the electron $\Delta m_J = +1$ (ou -1) due to the angular moment conservation. In the second step, the $3d$ band reacts as a spin detector, depending on of the number of available empty states for the spins.

In a simple model the electrons in the initial $2p$ state are split into two levels because of the spin-orbit coupling ($2p_{3/2}$ & $2p_{1/2}$): spin parallel and anti-parallel to the magnetization orientation ($3d$). The transitions $2p_{3/2} \rightarrow 3d$ correspond to the "L_3" absorption edge, whereas transitions $2p_{1/2} \rightarrow 3d$ correspond to the "L_2" absorption edge. The electron spin in the final state depends on the helicity of the absorbed X-ray photon and on the spin-orbit coupling ($j = l + s$ for the "L_3" absorption edge; $j = l - s$ for the "L_2" absorption edge) [42]. Thus, the spin polarization of the excited electrons depends on the initial state (core level) and on the photon helicity.

The excitation probabilities are given by the Clebsch-Gordon coefficients [17] without taking into account the amount of the unoccupied final states. For instance the excitation probabilities at

the "L_2" absorption edge with a right (negative helicity = -1) circularly polarized photon are 25% for spin down and 75% for spin up electrons. At the L_3 edge, 37.5% spin up and 62.5% spin down electrons are excited with right circular polarized light. Left circular polarized light does the opposite. Intuitively in a non- magnetic material the total transition intensities of electrons (spin up and down) are the same for both circular light polarizations. The imbalance in the number of available empty spin up and down states, in magnetic materials, causes this difference in the absorption of the both circular light polarizations. This differences is opposite at the L_3 and L_3 absorption edges [51].

The importance of the spin-orbit coupling in this description which provides the spin sensitivity of the transition could be understood as follows:

The spin sensitivity of the final state, resulting from the transition rate calculation according to the two different circular polarizations of the incident flux, is not directly due to the transition characteristics. Indeed, the selection rules tell us that such transitions keep the spin invariant.

In order to understand this particular sensitivity, it is indispensable that the initial states of the transition (in our case the $2p$ states) are spin split by spin-orbit coupling. Therefore the good quantum numbers describing these states are thus j and m_j and no longer $\{l, m_l, s, m_s\}$. The $2p$ states are described in the basis of $\{j; m_j\}$. Therefore, when the $2p$ states are decomposed according to their radial and angular parts, a basis transformation is performed. The $2p$ states are written in the basis of $\{l, m_l, m_s\}$. In this case the $2p$ states are a linear combination of spin up and down states. This transformation is a specific example of the more general transformation between functions in different coupling schemes given by the Clebsch–Gordon [17, 52, 53].

Thus, the sensitivity to the spin of the final state transitions caused by the interaction between an X-ray beam and the sample is due to spin-orbit coupling of initial states.

The magnetic properties of our sample (Permalloy) are mainly related on the electronics states in the 3d band. In ferromagnetic materials, according to the Stoner model, the exchange interaction between the spins of the electrons gives rise to an energy difference between the majority and the minority spin bands in the metals at the 3d band level (the exchange splitting). This results in an asymmetry in the density of states at the Fermi level. In the case of the strong ferromagnetic materials such as "Ni, Co,.." there are more minority spin empty states than majority at the Fermi level. This results in a difference in the X-ray absorption depending on the spin densities of states in the corresponding final state according the circular polarization of the light, see Figure 2.6.

Experimentally, the XMCD signal of a ferromagnetic layer is obtained by taking the difference between the two absorption spectra measured using right (-) and left (+) circular polarized light, corresponding to the angular momentum absorption $L_{ph} = q\hbar$ $(q = -1)$ and $(q = +1)$. In an equivalent way we are able to obtain the XMCD signal by making the difference between two spectra taken with a fixed helicity, however with opposite magnetization directions.

The intensity of the dichroism effect, for a given system, depends on three important parameters:

- P_{circ} the circular light polarization in degrees.
- $\langle m \rangle$ the magnetization of the 3*d* orbital level of the materials.
- θ, the angle between the direction of the photon angular momentum $L_{ph} = q\hbar$ and the magnetic moment, *m*.

This results in an angular dependence of the XMCD intensity according to the angle, θ, between the incident photon direction and the magnetization [17],

$$I_{XMCD} \propto P_{circ}\, m\,.\; L_{ph} \propto\; P_{circ}\, \langle m \rangle \cos\theta.$$

A given systems (Fe, Co, Ni,...) involves a specific electronic structure (Fermi level) which determines the magnetic circular dichroism amplitude of the chemical element. Therefore for a particular system (e.g. Ni) the maximum XMCD effect is observed when the spin photon direction is parallel or (anti-parallel) to the magnetization directions of the system, as indicated on the right side of Figure 2.6.

By denoting the transmitted intensity for left/right circularly polarized light as I_+/I_-, respectively, the pure magnetic dichroic contrast is defined as $I_{XMCD} = (I_+ - I_-)/(I_+ + I_-)$. However in our presented work it was sufficient to obtain the resulting STXM-XMCD images by dividing the two absorption images taken at the same photon energy but with opposite light polarization I_+/I_- in order to eliminate all non-magnetic contrast.

III.2. Synchrotron radiation

Our measurement using STXM requires circularly polarized X-rays with a high brilliance, which are only available at synchrotron facilities e.g. BESSY II. In general synchrotrons are basically a type of charged particle accelerator first developed in 1947. They consist of a storage ring accelerator where electrons are accelerated using magnets, to velocities close to the speed of light. Through bending magnets, undulators, and wigglers, these electrons undergo a modification in their trajectory. This change in trajectory, and therefore in the momentum of the electrons, results in a loss in energy in the form of photons (light). This electromagnetic radiation is characterized by a broad distribution of wavelengths, going from the infrared up to the hard x-ray range for high electron energies.

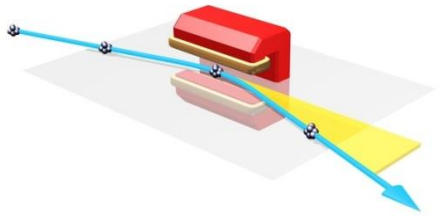

Figure 2.7: Schematic of bending magnet. The tangential emitted radiations is depicted in yellow. Adapted from [54].

In the case of the use of the so-called bending magnet insertion device, tangential radiation is emitted due to the magnetic field (inside the small cone), which at the same time, keeps the electron bunches on the circular trajectory. This is due to the Lorentz force which changes the direction of the electrons which leads to a loss of energy in the form of dipole radiation along the tangent to the trajectory when they change their direction, see figure 2.7.

The energy spectrum of this radiation is broad. This spectrum is defined by a so-called characteristic energy, E_c, which is the central energy value of the spectrum [53]:

$$E_c = \frac{3e\hbar B\gamma^2}{2m} = \hbar\omega_c$$

where m is the electron rest mass, e the electrical charge of the electron, B the magnet field strength of the bending magnet, and γ the Lorentz factor

$$\gamma = \frac{1}{\sqrt{1-\frac{v^2}{c^2}}} = \frac{E_e}{mc^2} = 1957E_e[Gev]$$

E_e is the energy of the storage ring, c speed of the light and v the velocity of the electrons. For electrons traveling close to the speed of light with a total energy, E_c, the tangential emitted radiation cone becomes narrow with an opening angle $\approx \gamma^{-1}$. We note that the amount of generated radiation scales with the electron flow, i.e. the electrical current in the storage ring.

In third generation synchrotron facilities (modern synchrotrons), other insertion devices such as undulators are also used. Such devices are composed of periodic NdFeB magnets, which create periodically alternating and circular magnetic fields forcing electrons to undulate as shown in figure 2.8. Using such devices it is possible to generate monochromatic circular and linear polarized X-rays.

For instance, circularly polarized light can be generated by shifting two rails of magnets relatively to each other, by approximately 90 degrees as shown in figure 2.8a. This leads to a magnetic field which forces the electron beam into a helical trajectory inside the undulator, which creates both circularly polarized lights (positive/ negative). However for a zero degree shift, the electrons oscillate, creating linearly polarized light with both polarizations (linear horizontal/ vertical), see figure 2.8b. The intensity of the radiation emitted will increase at each period of the electron oscillation (for the case of linear polarization) and at each circular period (for the case of circular polarization) due to constructive interference, resulting in a high light brilliance (photon flux per unit solid angle).

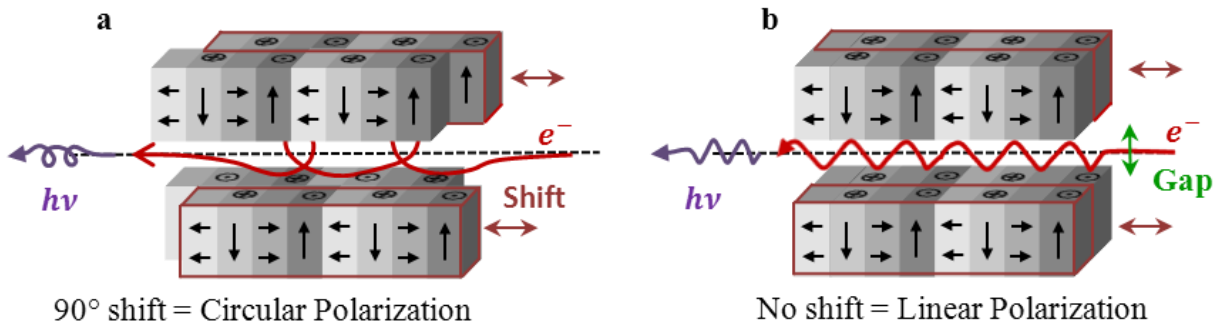

Figure 2.8: Schematic illustration of an undulator. It consists of both top and bottom rails of periodic permanent magnets decomposed into two parts, with the ability to create shifts between each other (dark red arrows). The generated magnetic field forces the electrons into an undulating motion. A 90° rail shift leads to circularly polarized X-rays **(a)**, while zero shift result in the emission of horizontal/vertical linear polarized X-rays **(b)**. The gap (green arrow) can be adjusted in order to select different energy values.

Without destroying the intensity of the photon flux a variable magnetic field is applied to the electrons by changing the gap between the upper and lower two magnets in order to change the wavelength of the photons obtained by following this equation:

$$\lambda = \frac{\lambda_u}{2\gamma^2}\left(1 + \frac{K^2}{2} + \gamma^2\theta^2\right).$$

K is a dimensionless parameter proportional to the undulator period, λ_u, and the magnetic field, B_0.

$$K = \frac{eB_0\lambda_u}{2\pi mc} = 0.9337B_0[T]\lambda_u[cm].$$

For a further increase of the energy resolution, the synchrotron radiation is focused, after the undulator, onto a plane grating monochromator (PGM) which selects precisely the energy of the light by rotating the grating with respect to the exit pinhole, as shown in figure 2.9.

The main properties of the synchrotron light are as follows:

- The photon energy is tunable
- High brilliance of the source
- High photon flux in the spectrum region going from the far IR into the hard X-ray.
- Light polarization can be tuned.
- Time structure for time resolved measurements.

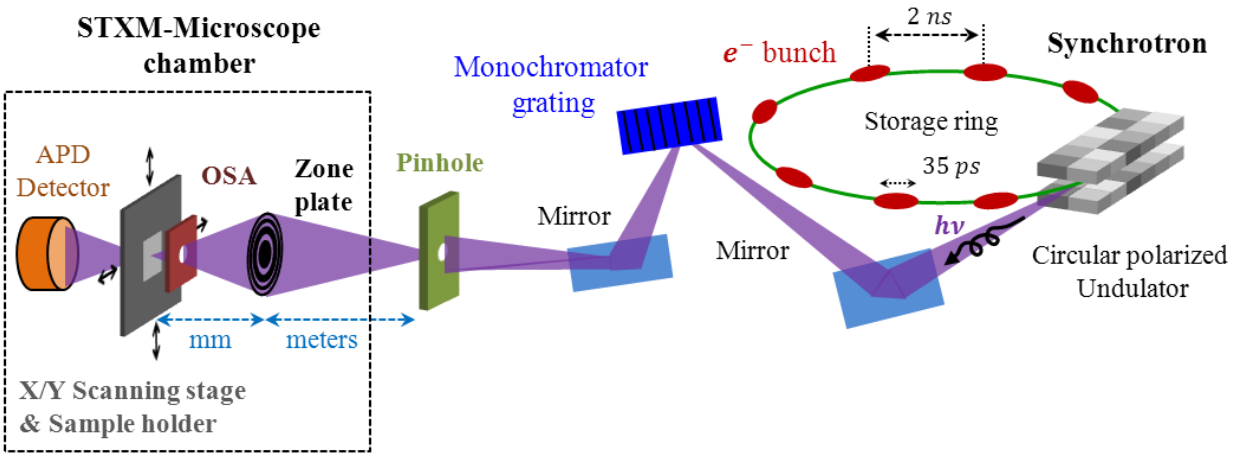

Figure 2.9: Schematic of the optical components of a scanning transmission X-ray microscope. Within the storage ring at the synchrotron, the electron bunches are separated by 2 ns and the width of each bunch is ~ 35 ps. A circular polarized undulator mode is used to generate circularly polarized X-rays in the relevant energy range between 700 – 900 eV. Monochromatic and spatially coherent X-ray light is generated using a pair of deflection mirrors and a monochromator grating and pinhole apertures of typically 20 µm. The X-rays illuminate the zone plate several meters away, which creates a focal spot in the sample with focal lengths in the mm range. Depending on the zone plate type, the light is then focused to a spot of typically 25 nm in diameter, which strongly dominates the spatial resolution of the microscope. The sample mounted on the scanning stage is then scanned across the focused X-ray beam, while the transmitted signal intensity is recorded at each scanned point.

III.2.1. Synchrotron BESSY II properties and time structure

In the synchrotron storage ring a bunch of electrons is evenly spaced, in so-called buckets. The distance separating them is 60 cm, corresponding to a bucket frequency:

$$f_{ring} = \frac{c}{60\ \text{cm}} \approx 499.654\ \text{MHz}.$$

The synchrotron storage ring has a perimeter of 240 m. Taking into account the separation distance between buckets, this leads to 400 buckets traveling in a circular trajectory, since the circumference of the ring has to be on exact multiple of the bucket spacing. These electron bunches are accelerated up to E_e = 1.72 GeV (different energies can be used as well). The total storage ring current is ~300 mA when operated in a "Top-up" mode. The constant temporal separation between two buckets is 2 ns, as schematically shown in figure 2.9. The typical length of the electron bunch inside the buckets in the normal synchrotron operation is around 35 ps [55], which determines the limit of the temporal resolution of STXM.

III.3. Scanning transmission X-ray microscopy

A magnetic Scanning transmission X-ray microscope (STXM) [56] employs the XMCD effect to image the magnetization configuration with high spatial resolution. It is one of the most interesting synchrotron light based microscopy techniques. Due to the scanning nature of the technique, STXM does not require a 2D detector. Instead, the sample stage is moved through a fixed narrow x-ray spot the light absorption is measured for each point, in order to build up a full image of the sample (see figure 2.9). Better methods of X-ray focusing have become possible since the development of synchrotron radiation sources. Historically, the first focusing way of the synchrotron light was achieved using a glancing incidence mirror directed on a pinhole, which leads to a spatial resolution in the order of the pinhole diameter [57].

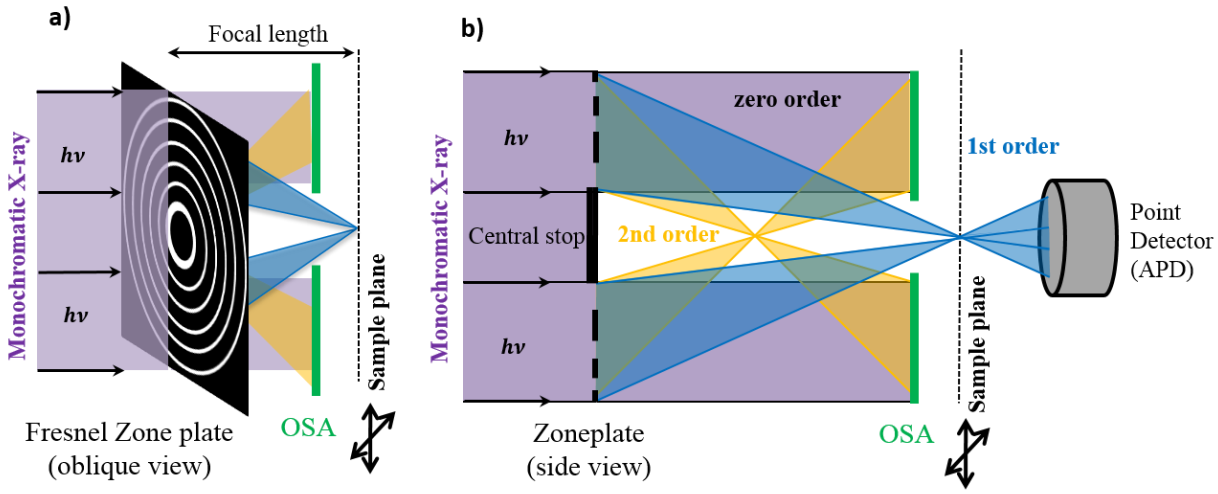

Figure 2.10: Microscope optics. Schematic illustration of the zone plate lens in combination with the OSA to focus only the 1st order light onto the sample plane, in oblique **(a)** and side view **(b)**. The zero order diffraction light is absorbed by the central stop of the zone plate, while higher diffracted orders are absorbed by the OSA.

Nowadays, Modern STXM use a Fresnel zone plate lens which build images by scanning the focal spot over an object in the focal plane of the zone plate [58]. Hence the mono-energetic photon beam is focused to a small spot on the sample, using a Fresnel zone plate lens in combination with an order selecting pinhole, the so-called *Order Sorting Aperture* (OSA). This latter prevent light from unwanted diffraction orders to be penetrated in addition to the center stop of the zone plate, especially the zero-order light passing through the zone plate. The OSA has to be introduced between sample and zone plate (figure 2.9 & 2.10). The Fresnel zone plate consists of concentric (alternating transparent and absorbing) rings such that coherent light traveling through the plate constructively interferes at a central spot (figure 2.10).

A STXM image is constructed by scanning the sample in the horizontal and vertical direction via a high accuracy laser interferometer stage which can compensates vibrations in the microscope [59]. The transmitted intensity is detected at each position with a photo diode placed behind the

sample (figure 2.10). With this avalanche photo diode (APD) single photons are detected. The avalanche photo diode is operated with a reverse bias voltage at a rate of 500 MHz, corresponding to each individual electron bunch at 2 ns temporal spacing at BESSYII in Berlin. The lateral resolution of this technique is limited by the focus of the zone plate in addition to the size of the pinhole (figure 2.9). Under the normal experimental conditions, the spatial resolution is about 20 – 30 nm [60].

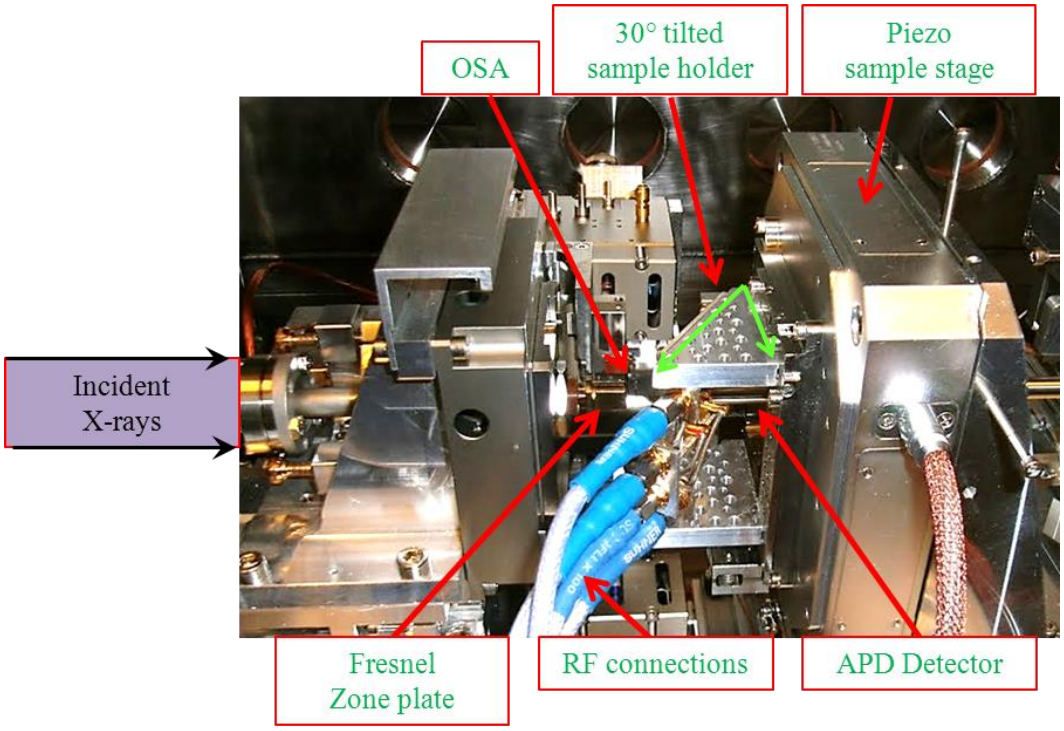

Figure 2.11: View from the inner part of the STXM, with the Fresnel zone plate, the order selecting aperture (OSA) and the 30° tilted sample holder with the RF-connections.

All the experimental magnetic images presented in this work were taken at the UE46-PGM2 Beamline (MAXYMUS end-station) at BESSYII in Berlin [61]. An image of the inner part of STXM at MAXYMUS is shown in figure 2.11. The in-plane magnetization component was imaged by tilting the sample surface normal by 30° with respect to the incident light direction. The contrast of the image is based on the X-ray magnetic circular dichroism (XMCD) effect [43].

IV. Time resolved dynamics acquisition (Pump and Probe scheme)

In addition to the high spatial resolution, scanning transmission X-ray microscopy offers the ability of time resolved imaging which is implemented at different synchrotron sources. This is accessible due to the pulsed nature of synchrotron light, which consists of a rapid succession of very intense and short X-ray flashes (< 100 ps). This unique feature can be used for stroboscopic imaging. In this work we used the pump-and-probe principle. In a general *pump-and-probe*

scheme, the pump represents any type of periodic and regular excitation of the sample, whereas the probe is performed by measuring the system response at different times after the pump.

In our case, the pump consists of a repetitive external magnetic field excitation of the magnetic nanostructures. This excitation is usually a short unidirectional (~20 ns) or rotating magnetic field pulse (~500 ns) with a few hundreds of Kilo-Hertz (~832 KHz) repetition rate, created by periodic current pulses through micro-striplines. The electronic excitation signal can be either a subsequent burst pulse using one stripline or two continuous sinusoidal signals, 90° phase shifted, which pass simultaneously through the two ends of crossed striplines (see chapter 4 and 5). The magnetic response is probed employing the regular X-ray pulses of the synchrotron with a repetition rate of 500 MHz.

After the signal from the APD has been detected and amplified, the signal has to be evaluated. For such time resolved imaging technique it is necessary to be able to record individual x-ray photons in a time-resolved manner. For instance to be able to attribute each detected photon to its corresponding synchrotron bucket and then sorts them within an appropriate time channel. Moreover, more importantly, the excitation must be precisely synchronized with the synchrotron operation frequency.

In the following subsections, the time structure of the pump-and-probe technique and how we determine the absolute timescale of the excitation with respect to the photon flashes is explained in detail.

IV.1. Time-structure of the measurement technique

As explain previously, the operation frequency of the storage ring at BESSYII is 500 MHz, which corresponds to 400 electron buckets equally separated by 2 ns. The time resolution of the imaging technique is determined and limited by the electron bunch width which is limited to 35 ps. However, depending on the operation mode of the synchrotron, the buckets are filled differently and their intensity may vary for technical reasons. For instance, in "multibunch" operation mode all buckets are filled with an average amount of electrons, expect 50 empty buckets where one *camshaft* buckets in between contains a much higher current in comparison with the other filled buckets.

In order to accommodate the 500 MHz input rate, a so-called FPGA (Field Programmable Gate Array) system has been implemented (electronic board). This allows for full rate photon detection up to 500 MHz and sorts the photons into different individual channels "N". The number of channels can be chosen arbitrarily (up to a few thousand), and the FPGA cycles through the channels at the 500 MHz rate of the synchrotron buckets. Later each channel will represent one frame in the constructed time resolved images.

At the Maxymus Beamline, this is done via a custom counting unit based on a FPGA (up to 2048 individual channels), which can be programmed concerning the photon sorting and binning, depending on the experiment needs. The counting principal of the photon detection in this system is based on a simple threshold comparison where the input signal (photons detection) measured

by the APD is compared to a defined voltage level, and if it exceeds this threshold, the flip-flop generates a "1" state. This is transmitted to the FPGA and internally added as a count to the corresponding time channel (a photon is recorded). This comparison is implemented into the FPGA board, which is wired to compare the input APD signal.

This procedure runs until the control software of the microscope indicates the end (dwell time) of the measurement at the individual scan position (individual pixel). Afterwards, all the recorded counts for the different time channels for each pixel are transmitted to the control software of the STXM, and the time channels contents are reset to zero. This whole process continues until the control software finishes the scan by taking a complete two-dimensional image with a vector of time channels for each pixel, resulting in three dimensional information (a time resolved magnetic image). By synchronizing the detection electronics to the synchrotron we are able to allocate the single photons detected and counted by the APD to the N individual counting time channels. Moreover all electronic devices which generate the excitation signal (pulses) are synchronized to the 500 MHz ring clock signal of the synchrotron storage ring.

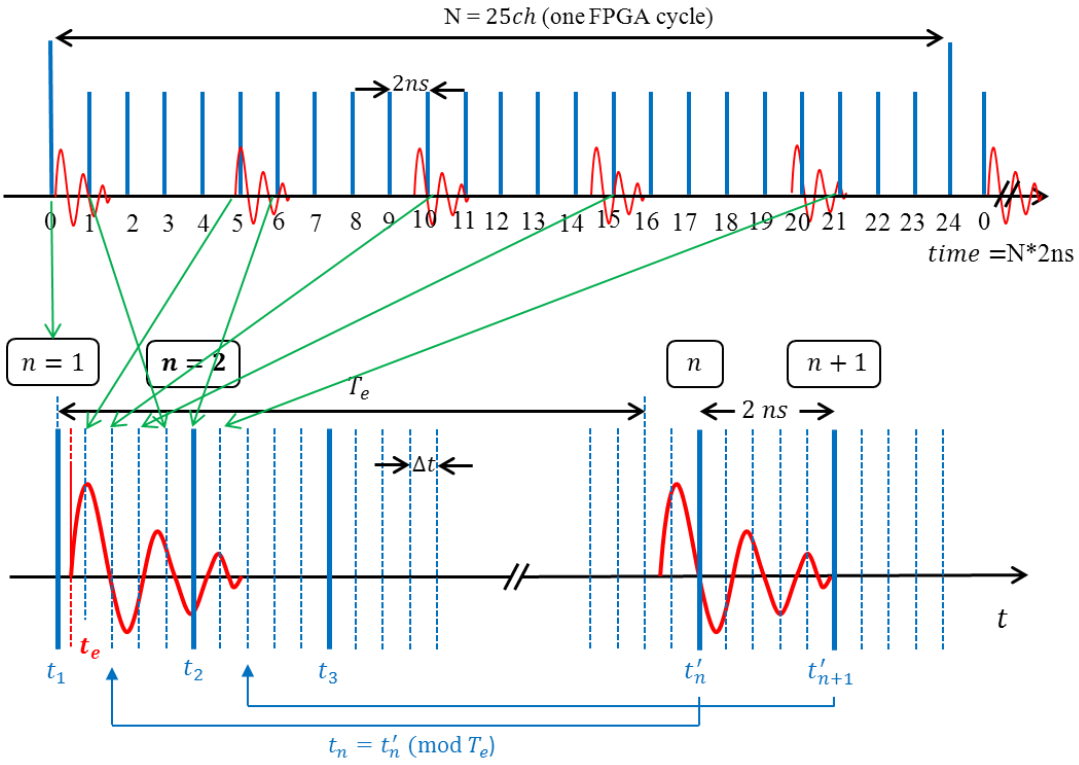

Figure 2.12: Illustration of the stroboscopic nature of the imaging technique. **Top:** Pump-probe technique, where the magnetic sample is excited periodically with a pump signal (in red), whereas the magnetization dynamics is probed stroboscopically with fast X-ray flashes, each 2 ns in duration (blue). It also show one FPGA cycle for *N* = 25 channels including 5 pump signals, since in this case *M* = 5. **Bottom:** The asynchronous acquisition measurement after re-ordering the recorded data. Each time resolved image *n* is associated with a time $\boldsymbol{t_n = t'_n (\mathrm{mod}\ T_e)}$ with respect to the excitation period. The time resolution of the measurement in this case is $\boldsymbol{\tau = 0.4}$ on re-ordering the recorded data.

Due to the regular spacing of the synchrotron flashes, the intuitive pump-and-probe setup would use the same number of acquisition channels as the number of buckets in the synchrotron ring. The basic operation mode is that each FPGA channel corresponds one-to-one to a synchrotron bucket, leading to N = 400 time channels with a fixed spacing time of 2 ns. This FPGA configuration means that the same channel is addressed after each ring orbit.

This *synchronous acquisition* operation mode is not ideal since, as we mentioned above, the synchrotron buckets are filled differently and their intensity may vary for technical reasons. Hence, the intensity of the individual time frames will be modulated by the amount of current in each bucket. Thus, there will be significant differences between the acquired intensity in each time channel due to the presence of the empty buckets in the gap of the filling pattern in the synchrotron.

IV.2. Asynchronous acquisition

In this work the asynchronous excitation operation mode is used. This scheme assures that all image frames are recorded with the same intensity, which constitutes one of the main important differences from the previous method. Here FPGA configurations no longer require that the same channel is addressed after each ring orbit. This gives us more freedom to choose an acquisition scheme. Within this operation mode, we are able to record thousands of channels, and, hence, the acquisition cycle of FPGA only needs to repeat after a large number of ring orbits. This allows for a very wide range of excitation frequencies and time steps.

The acquisition scheme is defined by two integer parameters: the number of recording channels, *N*, and the number of excitation periods, *M*, which are applied during the time $N \times 2\,ns$. The repetition rate or the excitation frequency, *f*, is then:

$$f = \frac{M}{N} \cdot 500\ \text{Mhz}.$$

Furthermore, *N* and *M* should not have a common prime factor. For instance, when we choose excitation periods $M = 3$ during the recording of $N = 120$ channels, it is then better to apply $M = 1$ excitation periods during $N = 40$ channels. This is just in order to prevent recording the same excitation cycle a number of times in succession.

The time period for of different numbers of channels ($N \times 2\,ns$) must be a multiple, *M*, of the period, T_e, of the pump excitation signal:

$$N \cdot 2\,ns = M \cdot T_e; \qquad M \in \mathbb{N}$$

As a result, a desired time resolution, τ, is given by the excitation period, T_e, divided by the number of channels, *N*, or equivalently the time spacing between channels divided by the number of excitation periods, *M*:

$$\tau = \frac{2\,ns}{M} = \frac{T_e}{N}.$$

Each time channel has *n* buckets contributing to it, where *n* is calculated as follows:

$$n = \frac{\mathrm{lcm}(N, N_B)}{N},$$

with *N* the number of the time channels, N_B the number of buckets in the synchrotron (N_B = 400) and lcm is the lowest common multiple of the two numbers. For example, for 200 channels only 2 buckets contribute to each channel. However, in order to eliminate the unwanted effect of intensity variations in the electron buckets, *N* should not share prime factors with the number of electron buckets in the synchrotron (N_B) or in another word *N* must not be divisor of N_B. In this case every bucket will contribute to each time channel, which is the case for any number of channels, *N*, ending in 1, 3, 7 or 9. This latter case is the ideal case, since the intensity of the buckets is equally distributed over all of the time channels, which facilitates the detection of real dynamic contrast. Thanks to this asynchronous acquisition setup it is possible to choose a random number of channels *N*. However due to technical restrictions of the electronic devices one should choose a possible combination of the multiple, *M*, numbers of excitation periods and of channels numbers *N*, by taking into account these electronic restrictions and the time structure of the synchrotron.

IV.3. Time resolved movies

In our stroboscopic measurement technique a resulting time resolved movie of the magnetization dynamics, consists of a set of *N* (time channels number) time resolved images with an equal time spacing, corresponding to the time resolution, τ. Each image $n \in [1,2,\dots,N-1,N]$ corresponds to a relative time t_n with respect to the excitation period, T_e, which must be smaller than T_e as shown in figure 2.12. However in the case where M > 1, it could be the case that the real time t_n' is bigger than the product $M \cdot T_e$, which is the multiple of the excitation periods. Therefore the relative time t_n with respect to the excitation period will replace the real one t_n', and is defined as following:

$$t_n = t_n' (\mathrm{mod}\, T_e),$$

where the operation $x(\mathrm{mod}\, y)$ result remainder of the division of *x* by *y*. In this manner the obtained time resolved images have to be sorted with respect to the excitation period, T_e, and be correlated with its t_n. In this way we obtained our magnetization dynamics movies. In addition one needs to determine the absolute *time-zero* ($t_0 = t_e - t_1$), the time difference between the starting time of the excitation and the time of the first channel.

IV.4. Acquisition statistics

In our experimental method employing time resolved STXM it is possible to control the acquisition statistics by choosing the specific constant acquisition time, the so-called *dwell-time*, for each scanned pixel. However, like any experimental technique, high acquisition statistics lead to a longer waiting time for each completed image.

The scanning operation mode of the sample also influences the scanning speed, leading to different resulting image quality. There are two frequently used scanning operation modes, which are *point-by-point* and *line-at-once* scanning modes.

Point-by-point scanning is the basic scanning mode of STXM. In this case the defined scanning area is decomposed into a regular grid of coordinates and each point or pixel of the grid is individually scanned with the X-ray beam. Each point of this coordinate is illuminated for a predefined dwelling time, before the X-ray beam is moved to the next point. The photon counting happens only when the sample is at rest. However, in the *line-at-once* scanning mode, instead of stopping on each pixel during the scanning, each line is scanned at one constant predefined velocity. The use of this mode increases the scanning speed in comparison with the point by point scan. However the acquisition does not happen at a well-defined pixel, thus the contrast is integrated over the full scanned line, leading to image distortions. One can switch between these operation modes through the STXM software depending on experimental needs.

For a constant dwell time and excitation period T_e, the acquisition time for a time resolved set of images, *N*, scales inversely proportionally to the time resolution, τ, ($\tau = \frac{2\ ns}{M} = \frac{T_e}{N}$.)

Usually one need to set a fixed excitation period T_e, in order to keep a minimum *duty cycle, D,* the ratio between the pulse duration and the excitation period (T_e) of a rectangular waveform

$$D = \frac{pulse\ duration}{T_e} \cdot 100\%$$

Due to the limited heating dissipation in the striplines, otherwise electromigration will otherwise start to happen and by consequence the striplines will be damaged. For good imaging results and statistics most of our time resolved movies presented in this thesis (see chapter 4 & 5) used an acquisition time of 100 ms per pixel where *N* = 601 and image size of 150 × 163 pixels corresponding to 6 × 6.5 µm. The time required to acquire such a movie is about 30 min. Thus one XMCD movie takes ~ one hour, since one needs at least to record two movies for the two different circular polarizations of the X-rays.

IV.5. Time calibration of the excitation with respect to the synchrotron flashes

The time calibration of the excitation signal with respect to the synchrotron probe flashes, arriving on the sample, can be determined by determining the *time-zero*, the absolute time difference introduced above ($t_0 = t_e - t_1$). It can be determined by measuring this time difference of the excitation signal with respect to the synchrotron flashes. A simple way would be by assuming an instantaneous response of the magnetic system to the excitation and imaging this response of the magnetization. In this case t_0, is therefore the time when the event takes place in the time resolved movie for $t_1 = 0$. However this simple method is not accurate, since it is based on assumptions which are not always correct. For instance, magnetic domain wall motion shows a delayed response to a fast rise time external field pulse, which corresponds to the domain wall

inertia [62]. The delay time in the system's response is proportional to the strength of the pinning potential for the domain wall, due to the external pinning fields created by the geometry of the magnetic nanostructures.

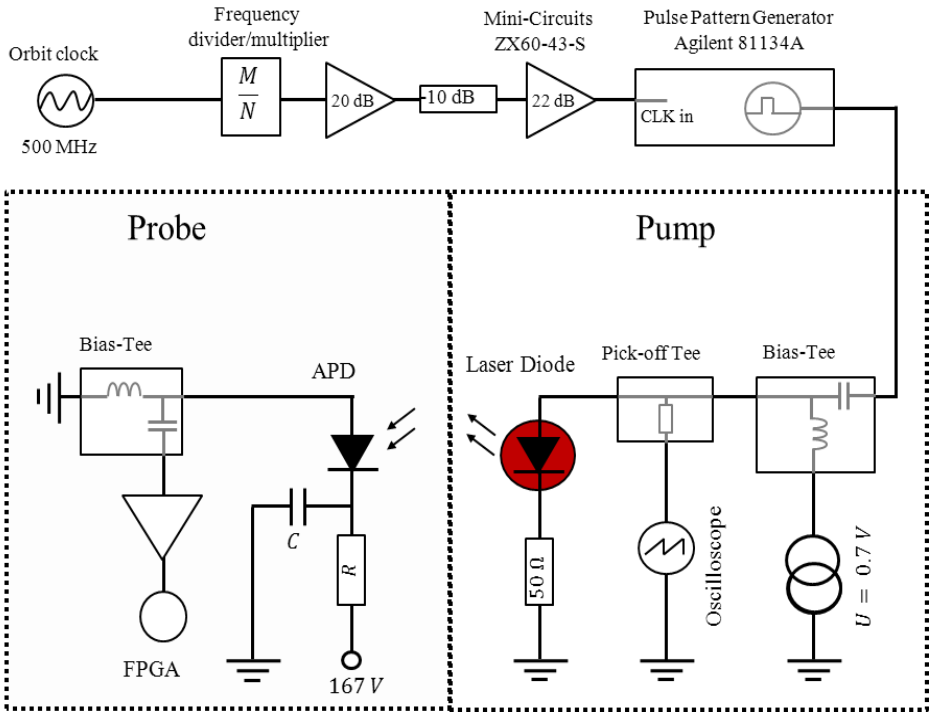

Figure 2.13: Schematic of the electronic set-up which is used to calibrate the excitation signal with respect to the electronic detection procedure by measuring the time delay between the two events. The laser diode (red) emits light flashes once the excitation signal, generated from the pulse pattern generator, reaches the diode. The emitted light is detected by the APD and recorded by the FPGA.

A second and more precise method is usually used to determine the *time-zero* electrically. This method consists of mounting a laser diode onto the STXM sample stage and connecting it using the same electrical connection and electronic set-up as used for the sample (pump and probe), where the diode is triggered by a fast pulse which lead to an emission of flashes. The emitted light is detected by the APD. Hence, the time delay can be measured as the time difference between the pulse signal triggering the laser diode (pump) and the signals detected by the detector and recorded by the FPGA (probe). A schematic of the electronic set-up is shown in figure 2.13.

V. Controlling domain wall velocities using rotating magnetic fields

On injecting a current through a micro stripline, a magnetic field is generated on a micrometer size length scale following Ampére's law [63]. In this work using ferromagnetic ring-shaped nanostructure, which are magnetized in-plane, it is necessary to produce in-plane rotating magnetic fields. This is achieved by pattering a crossed-stripline on top of the magnetic nanostructure (figure 2.14. left).

In this study we investigate ferromagnetic ring structures made of permalloy, where the ground state of the magnetic configuration is the "vortex" state [24]. On relaxation of the magnetization from saturation in an external magnetic field, the magnetic configuration is transformed to the "onion" state, which consists of two opposite domain walls (a tail-to-tail and a head-to-head domain wall) [64-66]. On applying an external field, $\mathbf{B}_{rot}$, to the ring, the Zeeman energy depends on the angle, $\Delta\theta$ between the direction of the applied field and the line connecting the two domain walls [67], see figure 2.15. The lowest energy is found when the applied field is aligned with both domain walls, $\Delta\theta = 0°$, whereas for non-zero values of $\Delta\theta$, the domain walls experience a restoring torque towards the minimum of the potential landscape created by the applied field. Thus the domains wall positions can be controlled. If now the external field rotates in the plane of the nanoring:

$$\mathbf{B}_{rot}(t) = B \cdot [\sin(2\pi f t)\,, \cos(2\pi f t)\,, 0],$$

the Zeeman energy potential landscape dynamically moves around the ring, and hence the position of two energy minima also rotate, dragging the domain walls around the nanoring in a circular motion.

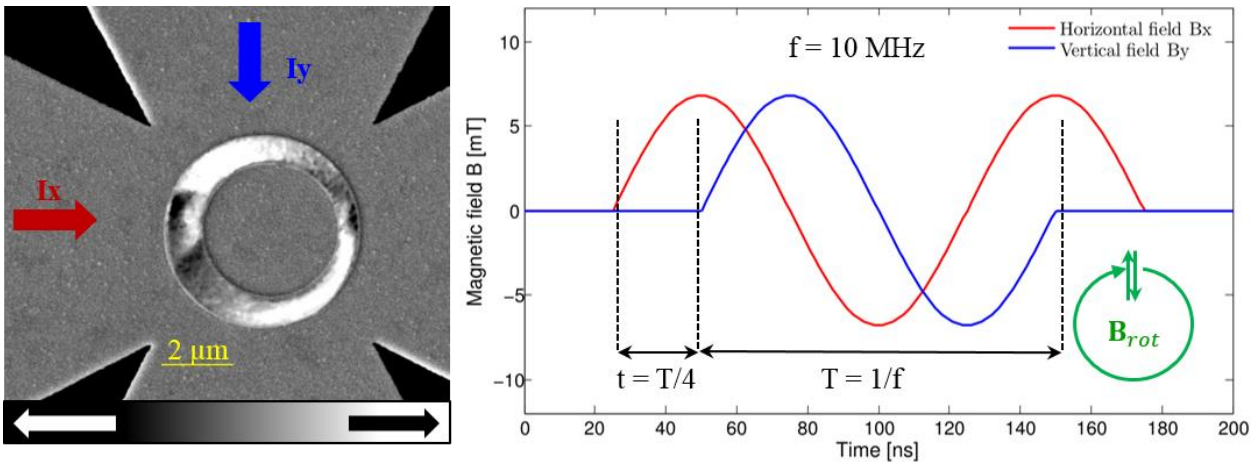

Figure 2.14: Left: merged XMCD image of an asymmetric ring structure with an SEM image of the sample. The red and blue arrows represent the direction of the injected sinusoidal current bursts with a 90° phase shift, injected in the horizontal and vertical crossed stripline. A rotating magnetic field is generated. **Right:** the in-plane rotating magnetic field pulse $\mathbf{B}_{rot}$ (in green) is generated by the superposition of the generated sinusoidal fields in vertical, B_y, and horizontal direction, B_x. the resulting sense of rotation is clockwise and the rotation frequency f = 10 MHz. the maximum field amplitude of B ~ 6.8 mT is constant during the rotation period T = 100 ns (50 - 150 ns).

This means that the domain wall propagation can be controlled by both the field amplitude, *B*, and the field rotation frequency, *f*, providing an extra degree of control compared to straight wires where the field strength and angle controls the domain wall propagation.

As discussed in chapter 1, the one-dimensional collective coordinate model represents the simplest model which can describe field driven domain wall motion, through the LLG equation. It uses two co-ordinates to describe the domain wall, q is the domain wall position and ϕ the polar angle. In the following the domain wall propagates in ring structures of radius, *r*, hence the domain wall position is periodic, $(q,t) \equiv (q + 2\pi r, t)$. Moreover, the tangential field component of the rotating field, $B_t = B \sin\theta$, represents the domain wall driving field (see figure 2.15b).

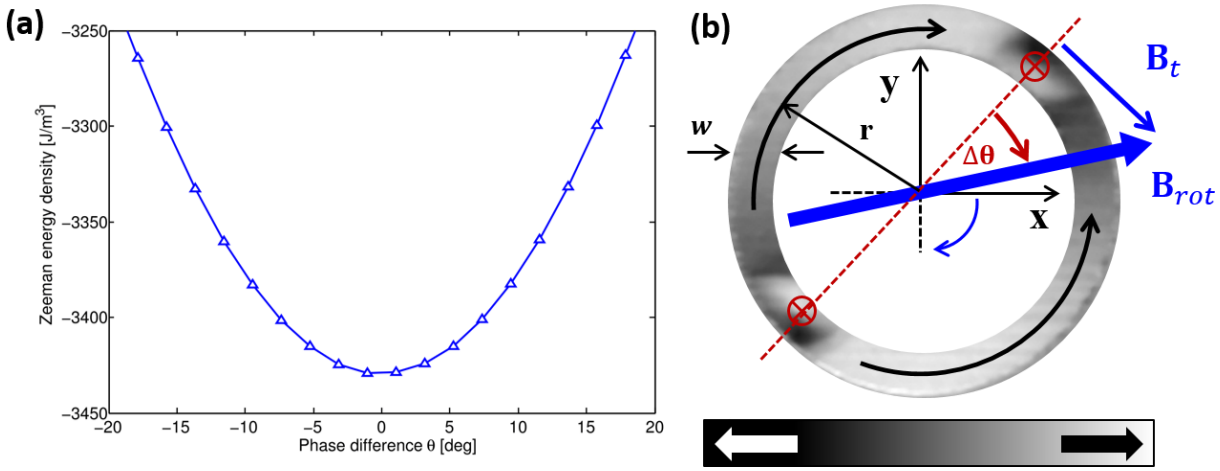

Figure 2.15: Controlling domain wall velocities using rotating magnetic fields. **(a)** Plot of the Zeeman energy of the system during the magnetic field rotation as a function of the phase difference, $\Delta\boldsymbol{\theta}$. The calculated energy for a symmetric permalloy ring structure (thickness 30 nm, w = 500 nm, *r* = 2 μm and field amplitude *B* = 6.8 mT) (this calculation has been performed by Dr. A. Bisig after Ref. [67]). **(b)** Adapted XMCD image illustrating the dimensions of the ring structure. The red arrows represent the rotating magnetic field, $\mathbf{B}_{rot}$, and its tangential component, $\mathbf{B}_t$ (driving field). The red dashed line is the line connecting both domain walls. The black and white scales indicate the magnetization direction.

Firstly we consider the case where the tangential field strength, B_t, is smaller than the Walker field, $H_W = \alpha H_K/2$, (see chapter 1 – subsection II.1). In this case the domain wall propagates with a viscous motion and the domain wall velocity is proportional to B_t [26]:

$$v_{dw} = \frac{\Delta_0 \gamma_0}{\alpha} B_t \,.$$

For $\theta = \pi/2$, the domain wall velocity reaches its maximum, since in this case $B_{t(max)} = B$. From this one can define the critical field rotation frequency for the domain wall to track the field,

$$f_c = \frac{v_c}{2\pi r} = \frac{\Delta_0 \gamma_0 B}{2\pi r \alpha},$$

where r is the radius of the ring structure and v_c the domain wall velocity for $B_t = B$. When the rotating field frequency, $f < f_c$, the domain wall lags behind the position of the rotating field (for $0 < \theta < \pi/2$) and the domain wall velocity grows until it matches the field rotation speed $v_{dw} = 2\pi f r$. Theoretically, in the framework of the one-dimensional model, in this velocity regime the domain wall velocity is constant without any precession of the polar angle ϕ (steady-state motion). However, in our previous experimental study (on symmetric ring structures) we demonstrate that this is not always the case and we showed, for the first time, oscillations of the domain wall velocity driven by rotating field amplitudes below the Walker field [24]. We demonstrate that this new regime of oscillating vortex domain wall motion, even below the Walker breakdown, results from intrinsic effects such as oscillating domain wall spin structure transformations, due to different forces acting on the domain wall, and extrinsic pinning due to imperfections in the nanowires.

If the rotating field frequency is larger than the critical field rotation frequency, $f > f_c$, the domain wall will no longer follow the external rotating magnetic field, $\mathbf{B}_{rot}$.

On the other hand when the tangential field strength is larger than the Walker field, H_W, ($B_t > H_W$), the domain wall velocity becomes smaller than the Walker velocity ($v_W = \Delta_0 \gamma_0 H_K/2$) [26], since above the Walker threshold the viscous motion is replaced by an underdamped oscillatory propagation. Thus, linear dependency between the domain wall velocity and the driven field is not valid anymore.

V.1. Creation of high frequency rotating field pulses within the ring structure

In this study we directly observe the magnetization dynamics employing time-resolved scanning transmission X-ray microscopy, which is a stroboscopic technique (pump and probe). The pump consists of a repetitive external magnetic field excitation of the magnetic nanostructures. The magnetic response is probed employing the regular X-ray pulses of the synchrotron. This technique relies on reliable and reproducible control of the magnetization dynamics, as discussed above. In this section we discuss the experimental set-up employed to create the high frequency (HF) rotating field pulses, using crossed-striplines patterned on top of the magnetic nanostructures.

V.1.1. Device properties and design

The sample design and properties were carefully chosen in order to fit the imaging technique and magnetic rotating field generation.

Magnetic structure:

The width and thickness of the rings was defined such that the vortex domain wall spin structure is the lowest energy magnetic configuration [15]. In order to minimize extrinsic and intrinsic pinning effects, we maximized the ring width, since the pinning strength scales inversely

proportionally to the ring width [68]. Furthermore, the thickness was chosen to provide an optimum XMCD contrast at the Ni - L_3 absorption edge. The ring radius was defined to be larger than the ring width ($r \geq 4w$) such that the onion state was a local stable state after relaxation from saturation. We also note the ring radius is one of the key parameters, along with the rotation frequency, that defines the domain wall velocity (figure 2.16).

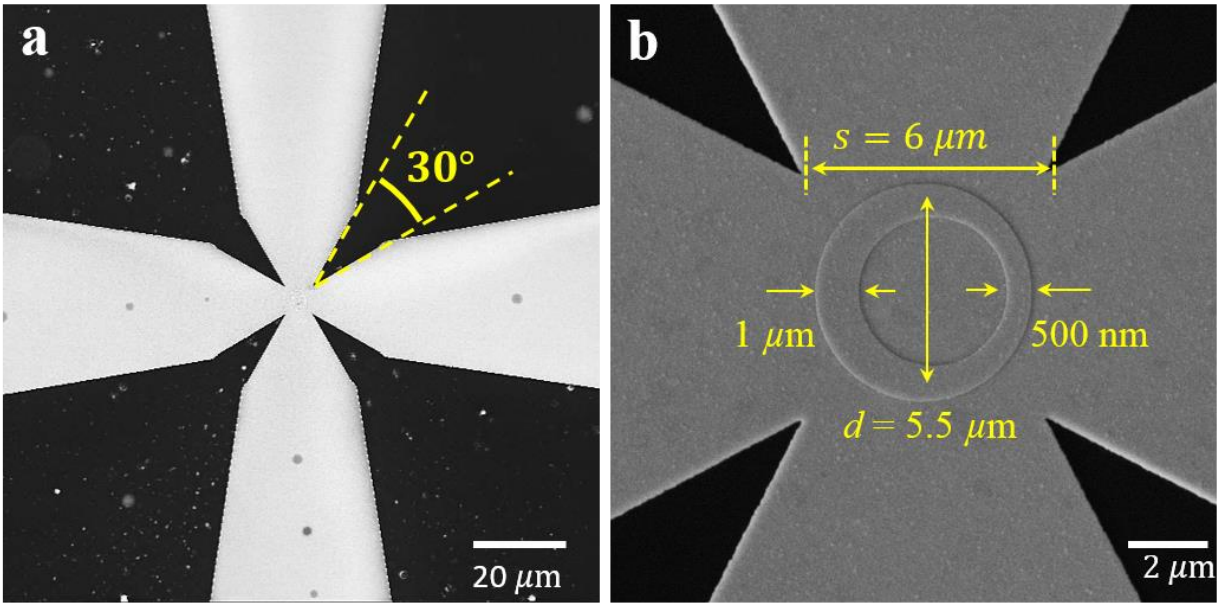

Figure 2.16: Scanning electron micrograph (SEM) images of the sample design for two different scales **(a)** and **(b)**. The dimensions and sizes are marked in yellow.

Crossed stripline structure:

The crossed stripline geometry has been developed by "Max-Planck-Institut für Intelligente systeme (MPI-IS)" to generate rotating field [69]. The two most important parameters for the crossed stripline geometry are the size of the overlap region, *s*, and the angle at the edge of the stripline. The first parameter is chosen as a compromise between having a high degree of field homogeneity, which is provided by a large value of *s* compared to the outer diameter of the ring structure, and having a large maximum magnetic field strength, *B*, which is provided by the smallest possible values of *s*, since $B = \mu_0 I/2s$, is inversely proportional to *s* [69]. In the other hand, the 30° angle at the edge of the crossed stripline helps the field homogeneity and heat conductivity (see figures 2.16 & 2.17). The material used for the striplines is copper, since it has a relatively good heat and electrical conductivity. It is capped by a thin layer of gold in order to prevent degradation of the copper in air. Furthermore the copper has a relatively low X-ray absorption in comparison to gold at the Ni L_3 edge. This is necessary for an optimum XMCD contract, which depends on the transmitted X-rays through the whole sample. In order to keep the resistance relatively low (higher *I* and lower Joule heating) the striplines should be thicker than 100 nm.

The ring structures are patterned below the striplines directly, on top of the flat SiN membrane, in order to prevent large surface roughness and thus preventing strong extrinsic pinning.

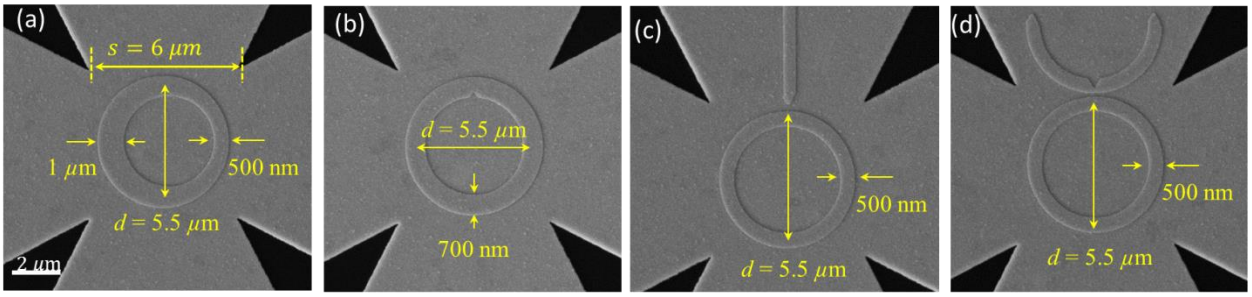

Figure 2.17: SEM images of different ring geometry. (a) Asymmetric ring, **(b)** symmetric ring with a small notch in the upper part of the ring, **(c)** symmetric ring with a neighboring nanowire above, **(d)** symmetric ring with a neighboring notched half-ring. These samples have all been prepared in the scope of this thesis, however only the asymmetric ring samples are discussed here.

V.1.2. Generation of the pump signal

In our study, the pump consists of a repetitive external magnetic field excitation of the magnetic nanostructures which can be either unidirectional or a rotating magnetic field pulse with a few hundreds of Kilo-Hertz (~832 KHz) repetition rate, created by periodic current pulses through crossed micro-striplines.

For the unidirectional magnetic field pulse, the electronic excitation signal can be either burst pulses through one or both striplines, depending on the desired magnetic field orientation. Injection of a current pulse through one of these striplines can result in two magnetic field orientations, depending on the sense of the current, following Biot-Savart law. However, using both striplines and injecting simultaneously two burst pulses, leads to a magnetic field pulse with a different orientation depending on the amplitude difference between the pulses.

The generated rotating in-plane magnetic field consists of the superposition of orthogonal sinusoidal fields:

$$B_x(t) = C \cdot B\sin(wt), \qquad B_y = B\cos(wt).$$

Where $C = \pm 1$ determines the sense of field rotation (counter-clockwise or clockwise) and $w = 2\pi f$ is the angular frequency. We obtained an in-plane rotating magnetic field by simultaneously injecting, 90° phase shifted, radio frequency (RF) currents through the two ends of orthogonal crossed striplines. The starting angle of the rotating field can be set by both the sense of the injected current and by switching between the two orthogonal sinusoidal signals through the striplines. Such in-plane rotating field burst pulses were previously discussed by Curcic *et al.* [69]. We note that the decoupling of the RF-currents flowing in the *x*- and *y*-directions, even

without electrical isolation, is realized by two symmetric sources for the two RF-currents. This will maintain the center of the striplines at virtual ground, which eliminates the need for sample impedance matching with the electronics impedance ($\mathrm{Re}[Z] = 50\,\Omega$), since the Ohmic resistances of our striplines are usually, $R_s \approx 11\,\Omega$. These symmetric RF burst pulses or differential signals are provided by 180°-power splitters with a bandwidth of 1-500 MHz.

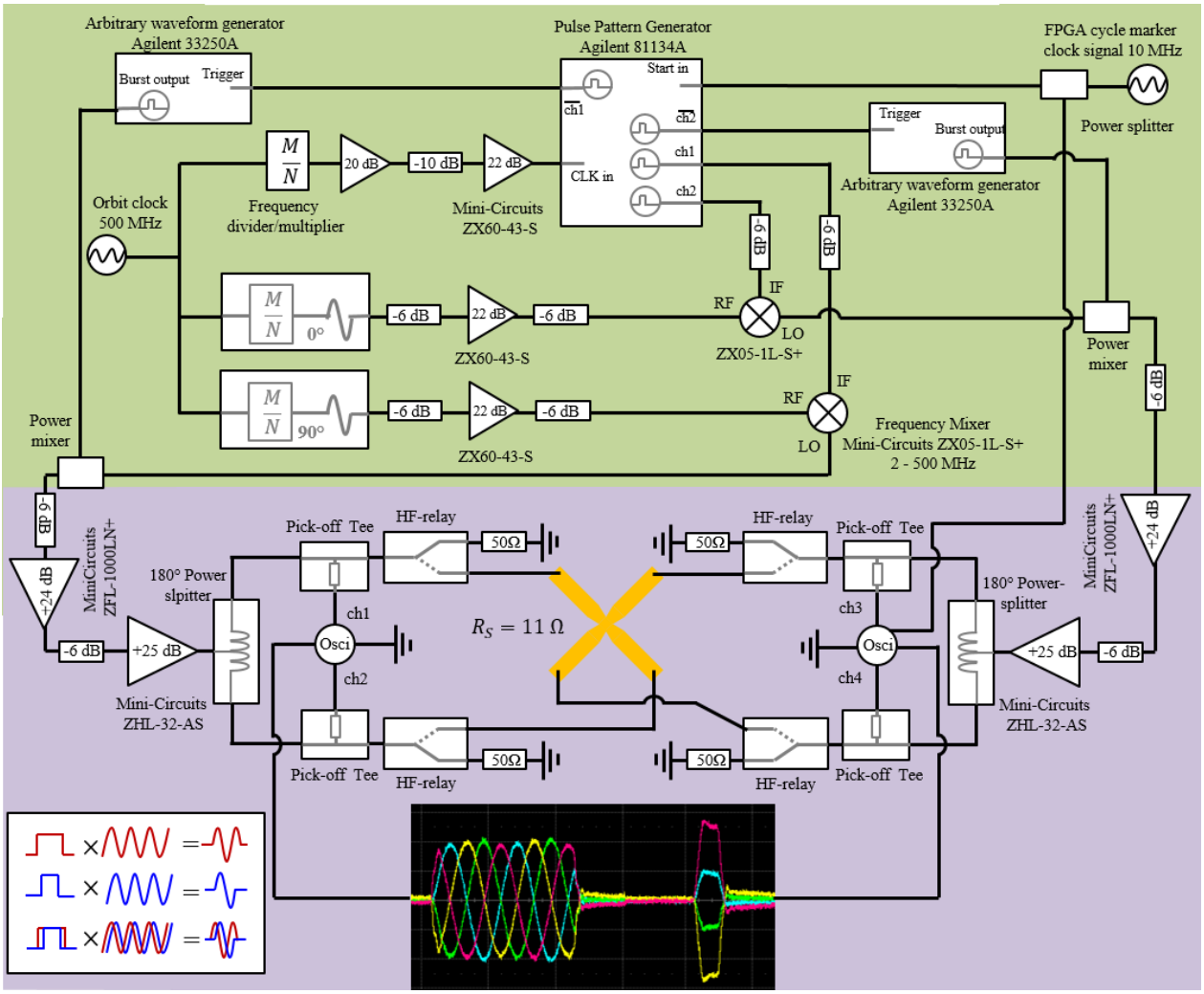

Figure 2.18: Schematic drawing of the experimental setup (electronic circuit). The setup is decomposed into two parts: **the first part (green region)**, consist of the synchronization and signal generation and mixing, whereas **the second part** (**light violet region)**, consist of the driver electronics to amplify and produce the differential electronics for the four ends of the striplines. The **bottom left inset**, shows the creation of the burst pulse. The first two lines describe the pulse for the horizontal and vertical striplines (red and blue) and the third line shows the mixed and final pulse shape. A real pulse shape is shown in the **bottom middle inset** which illustrates the differential burst pulse to generate a burst pulse for two rotations of the magnetic field (sinusoidal signal), mixed with a uni-directional nucleation pulse (squared signal). This image represents an oscilloscope screenshot presenting the four oscilloscope channels. The setup has been developed in collaboration with the group of Dr. H. Stoll and Prof. G. Schütz.

In order to generate the differential pump signal, either uni-directional for nucleation magnetic of field pulse bursts or for the rotating magnetic field pulse bursts or combining both pulses together, we use the experimental setup illustrated in figure 2.18. This circuit is synchronized with the probe flash light of the synchrotron.

The first part of the circuit, shown in figure 2.18, consists of the generation of the burst pulse and the synchronization electronics. The two sinusoidal signals are generated directly from the synchrotron orbit clock signal using a frequency divider (M/N), which is synchronized with the number of excitation periods, *M*, within one cycle of counting channels *N*. Such signal generation reduces the jitter from the electronics. In order to select the pulse length and hence the number of rotations of the magnetic field, the orthogonal sinusoidal signals with 90° phase difference are then mixed with two rectangular pulses with a time delay $\delta t = 1/4f$ and two different length $1/f$ and $3/2f$. This results in a burst pulse of one rotation of the magnetic field, see figures 2.14b & 2.18. In our case, the repetition rate or the excitation frequency of the pump pulses was (~832 KHz), chosen taking into consideration the requirement for heat dissipation in the striplines, since the Joule heating of the stripline will influence the efficiency of the continuous RF-excitation. Therefore, the number of the counting channels is N = 601, and the number of excitation periods, M = 1, since the time resolution is $\tau = 2\ ns$.

The second part of the circuit, shown in figure 2.18, consists of the driving electronics to generate and amplify the differential pulses. The maximum signal amplitude used in this experiment for the rotating magnetic field pulse was $\pm 5\ V$, whereas $\pm 8\ V$ was used for the nucleating field pulse. The phase and amplitude of all signals are measured by the oscilloscope by picking off 1 % of the signal using a "Pick-off Tee" placed just before the HF-relay which has been used to protect the samples. The field strength and homogeneity of the generated magnetic field in the center of the striplines was previously calculated by Curcic *et al.*. Therefore, approximatively, the maximum total field strength B_{max} at $U = \pm 5\ V$, for our RF-signal in our sample is:

$$B_{max} = \frac{\mu_0\, U}{2s\ \mathrm{Re}[Z]} f_0(0,0) = 6.8\ \mathrm{mT}\ .$$

Where $\mathrm{Re}[Z] = 50\ \Omega$ and $f_0(0,0) = 0.65$ which is the form factor value at the center of the sample, numerically calculated by Curcic *et al.* [69].

We note that the pulse amplitude $U = 5\ V$, corresponds to a maximum current density of $j \approx 10^{11}\ A/m^2$, which is relatively high, and at the limit before damage of our sample. In order to prevent such damage we performed the measurement, with a Helium atmosphere in the microscope chamber and using pulses with a duty cycle of less than 25 %.

On the other hand, In order to generate the asymmetric out-of-plane field pulses as a differential pump signal, which we employed in the study discussed in chapter 3, we use the experimental setup illustrated in figure 2.19. This circuit is synchronized with the probe flash light of the synchrotron.

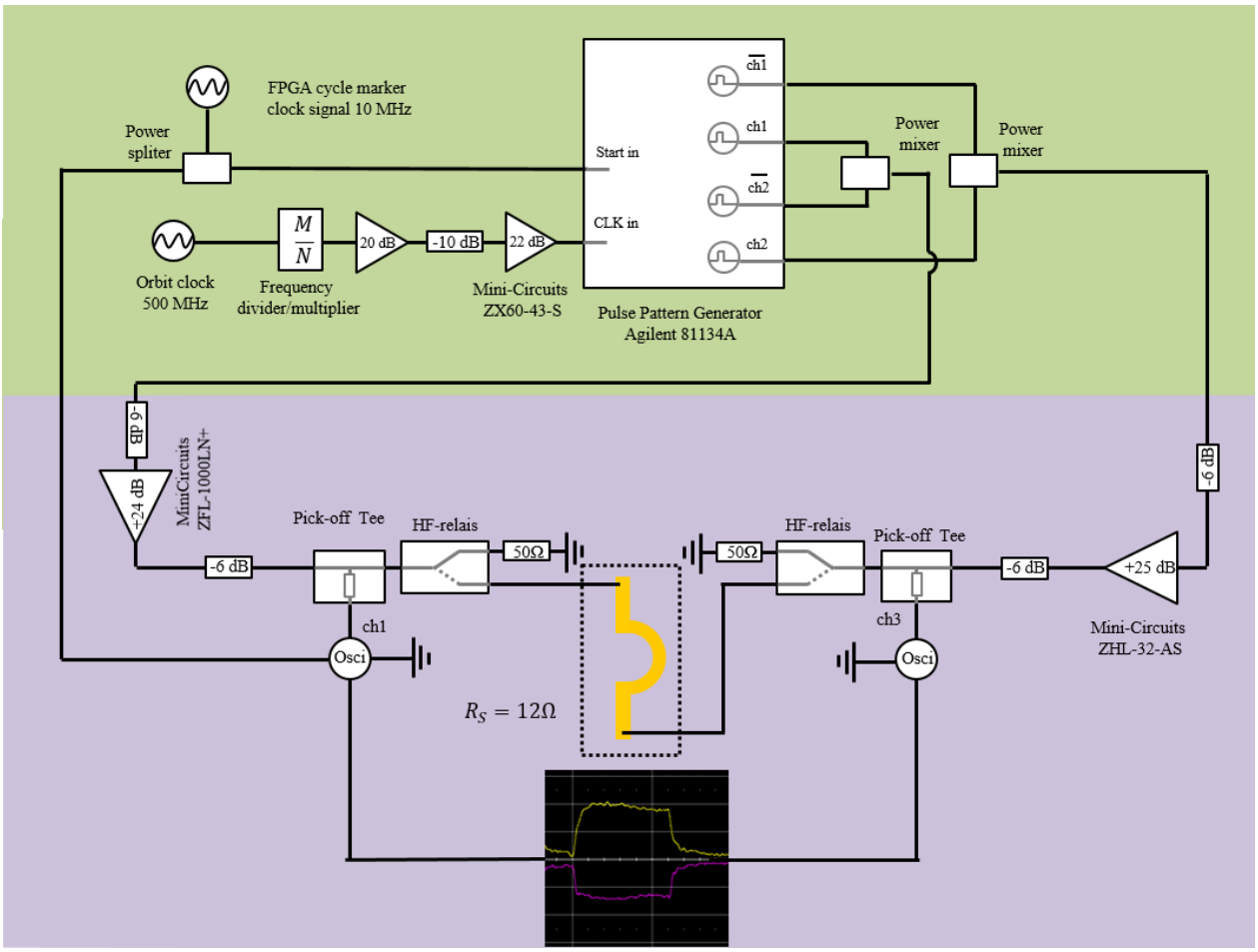

Figure 2.19: Schematic drawing of the experimental setup (electronic circuit). The setup is decomposed into two parts: **the first part (green region)**, consist of the synchronization and signal generation and mixing, whereas **the second part** (**light violet region)**, consist of the driver electronics to amplify and produce the differential electronics for the two ends of the micro-coil. A real pulse shape is shown in the **bottom middle inset** which illustrates the differential burst pulse to generate the out-of-plane field pulse. This image represents an oscilloscope screenshot presenting the two oscilloscope channels. The setup has been developed in collaboration with the group of Dr. H. Stoll and Prof. G. Schütz.

The first part of the circuit, shown in figure 2.19, consists of the generation of the burst pulse and the synchronization electronics. The time resolution of the experiment can be defined using a frequency divider (M/N), which is synchronized with the number of excitation periods, M, within one cycle of counting channels N. This results in a burst asymmetric out-of-plane field pulse, see figure 2.19 and figure 3.5a. The second part of the circuit, shown in figure 2.19, consists of the driving electronics to generate and amplify the differential pulses. The maximum signal amplitude used in this experiment for the out-of-plane magnetic field pulse is $j = 2.6 \times 10^{12} Am^{-2}$. This value results is a maximum out-of-plane magnetic field amplitude, at the center of both nanowires, of $B_\perp = 114$ mT.

Chapter 3

Synchronous precessional motion of multiple domain walls in a ferromagnetic nanowire by perpendicular field pulses

Abstract

Conventional domain wall manipulation approaches via in-plane magnetic fields are not suitable for the synchronous propagation of multiple in-plane magnetized domain walls in a single wire, as required for memory devices, since adjacent walls have opposite spin-orientations and hence move in opposing directions, which leads to a loss of data when the domain walls annihilate. An alternative is the use of current driven domain wall motion, which does facilitate synchronous domain wall motion, yet requires large current densities, which can make the implementation challenging. Here we demonstrate a radically different domain wall propagation scheme using out-of-plane field pulses which combines the efficiency of field-induced motion with the ability to move multiple walls synchronously. This is achieved for in-plane magnetized transverse domain walls of the same chirality through the application of asymmetric field pulses to a wire which incorporates regularly spaced pinning sites. An analytical model is developed to describe the system which reveals that the force on the domain wall is independent of the wall orientation but crucially depends on the time derivative of the applied magnetic field. It is therefore possible to tailor the force on the domain wall by choosing the pulse rise and fall times and by applying asymmetric field pulses to achieve net domain wall motion. This scheme is modelled in a realistic geometry using micromagnetic simulation. Finally, the concept is experimentally demonstrated using scanning transmission X-ray microscopy.

In this chapter I outline a paradigm shifting scheme for synchronous domain wall motion using a perpendicular field geometry and tailored pulse shapes, which has been published with me as second author [70]. The work in this chapter was carried out in collaboration and with the contribution of several people who I acknowledge. The idea was developed by Dr. J. -S. Kim and studied using micromagnetic simulation. As an experimentalist my main contribution was dedicated to the experimental part and to the corresponding data analysis where I am the first author. I was responsible for the innovation and realization of an experimental approach to demonstrate the micromagnetically predicted behavior. Therefore my biggest contribution was in the following: samples fabrication, the X-ray microscopy measurement including the beamtime preparation at the STXM-Beamline (MAXYMUS), at BESSYII synchrotron in Berlin, data analysis and finally the contribution to the preparation of the manuscript.

I. Introduction

A wide range of proposed spintronic memory, logic and sensing devices require the ability to reliably control the motion of magnetic domain walls [71-75]. Field induced domain wall motion was achieved, where the domain wall exhibits high velocities [76-78]. Moreover this method is attractive for many applications, due to the simplicity of the device structure fabrication since there is no need for electrical connection and direct contact writing to the sample.

However, the established realization of field driven domain wall using an applied field collinear to the magnetization orientation in the domain shrinks or extends the domains and therefore in the presence of multiple domains, this leads to a collapse, and thus annihilation, of these domains [79]. Furthermore, in-plane magnetized nanowires (e.g. made of Permalloy) required a lateral homogenous in-plane field for the domain wall motion, which is quite unrealistic. Some approaches to overcome this were suggested, however they lead again to a very complex device architecture, which has not been realized commercially [80]. Another approach suggested using out-of-plane (OOP) magnetized materials and engineering a domain wall ratchet in order to move the domain walls in the same direction [81]. However this fails in the case of in-plane magnetized samples and yet again leads to a complicated design for applications.

Synchronous motion of multiple domain walls, can be achieved by the spin polarized current driven domain wall motion, independently of the magnetization orientation in the domains. This can be achieved due to the spin transfer torque [82-84]. Therefore this constitutes an alternative method to manipulate the spin structure in new devices. However, it lead to a Joule heating problem due to the necessity of high currents [85, 86]. In addition there are the contributions of other effect such as spin Hall and Rashba effects which make the dynamics more difficult to manipulate [87-89]. Consequently, no present device or method, so far, provides high domain wall velocities at low-current densities.

Recently it was shown that by applying a supplementary constant perpendicular magnetic field the Walker breakdown can be pushed to higher fields and current values and thus the domain wall velocity can be increased [79, 90, 91]. These applied fields, for symmetry reasons, do not lead to a final domain wall motion. Therefore it cannot lead to a synchronous motion of multiple in-plane domains. In this chapter we studied a radically different approach: out-of-plane magnetic field pulses used to move in-plane domains combining the efficiency of field driven domain walls with the ability to have synchronous motion of domain walls in the same direction.

This is achieved for in-plane magnetized transverse domain walls of the same chirality through the application of asymmetric OOP field pulses. The sense of the motion depends only on two parameters, the chirality of the transverse wall and the field direction [70].

II. Theoretical Results

By making use of the transient domain wall dynamics that depend on the wall chirality, we introduce a new mechanism to move multiple domain walls in the same direction using magnetic fields perpendicular to the in-plane spin orientation in the domains and domain walls, which was previously deemed impossible. This can be an alternative to current induced domain wall motion. The OOP magnetic field pulse can be created by an electrical pulse through a microstrip placed very close, adjacent to the nanowire (few nanometers). In order to explain the force resulting from the OOP field and how the OOP field pulses can be used to move domain walls analytically, we extend the 1D collective coordinates model [70] and include this generated torque. This latters exhibit a similar behaviour to the adiabatic spin transfer torque (STT).

We begin with the Landau-Lifshitz-Gilbert equation (LLG) [6,92,93] which represent the general description of the magnetization dynamics induced by the spin polarized electron flow and fields:

$$\frac{\partial \mathbf{M}}{\partial t} = -\gamma' \mathbf{M} \times \mathbf{H}_{\text{eff}} + \frac{\gamma' \alpha}{M_S} \mathbf{M} \times (\mathbf{M} \times \mathbf{H}_{\text{eff}}) - \frac{1+\alpha\xi}{1+\alpha^2} (\mathbf{u} \cdot \nabla)\mathbf{M} + \frac{\xi - \alpha}{(1+\alpha^2)M_S} \mathbf{M} \times (\mathbf{u} \cdot \nabla)\mathbf{M}, \qquad (1)$$

where $\mathbf{M}$ is the local magnetization, $\gamma' = \gamma/(1+\alpha^2)$ represent the gyromagnetic ratio and α is the viscous Gilbert damping parameter. The first two terms represent the precession of the magnetization around the effective magnetic field $\mathbf{H}_{\text{eff}}$ and the damping term, respectively. The 3rd term or the so-called adiabatic term describes, the momentum transfer from the spin polarized current to the local magnetization adiabatically [92-94]. Here $\mathbf{u} = \mathbf{j}_e P \mu_B / e M_S$ is the spin drift velocity, $\mathbf{j}_e$ is the electron current and P is the spin polarization of the conduction electrons. The last term represents the non-adiabatic spin transfer torque which describes all remains torques, where ξ is the non-adiabaticity constant. As a reminder the in-plane domain walls, in the case of the 1D model, are represented by two parameters, the angle ϕ which describes the rotation of the domain wall around the wire axis, and the domain wall center position q [93] as shown in figure 3.1a. (See chapter 1 – subsection II.1).

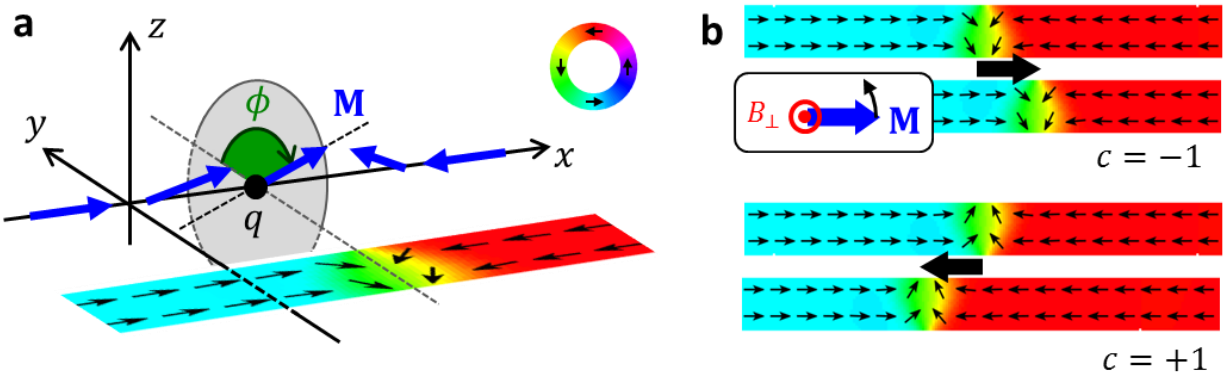

Figure 3.1: (a) Schematic illustration of the one dimensional domain wall geometry to describe an in-plane transverse wall by two collective coordinates, the domain wall position q and the polar angle φ (green). **(b)** A head-to-head transverse wall with negative (positive) chirality is displaced to the right (left) by the application of an OOP field $B_\perp$ = +50 mT along the +z-direction, which can be understood from the acting torques [70].

By introducing the 1D domain wall profile into the LLG equation, the following two equations are obtained which describe the domain walls dynamics in terms of the two collective coordinates,

$$\mathrm{cp}\lambda\dot{\phi} + \alpha\dot{q} = cp\gamma\lambda H_{\parallel} + \xi u - \frac{\lambda\gamma}{2S\mu_0 M_s}\left(\frac{\partial E}{\partial q}\right), \quad (2)$$

$$\alpha\lambda\dot{\phi} - cp\dot{q} = \frac{\pi}{2}\gamma\lambda H_{\perp}\cos(\phi) - cpu - \gamma\lambda\frac{K_{\perp}}{\mu_0 M_S}\sin(2\phi), \quad (3)$$

where $K_{\perp}$ is the effective transverse shape anisotropy which forces the spins in the plane of the structure and λ is the domain wall width. The external driving fields $B_{\parallel} = \mu_0 H_{\parallel}$ in-plane parallel (along the x-direction) and $B_{\perp} = \mu_0 H_{\perp}$(along the z-direction) OOP perpendicular. The parameter p distinguishes whether the orientation of the transverse magnetization component in the center of the static transverse wall, points in the direction of the + *y* axis ($p = +1$, figure 3.1b top) or in - *y* direction ($p = -1$, figure 3.1b bottom).

In the ground state of the domain wall $p = \cos(\phi)$. In equation (2), the first two terms on the right hand side represent an equivalence of the resulting torque due to the in-plane parallel field $H_{\parallel}$ and the non-adiabatic STT term. The last term in (2) identifies the position-dependent potential energy E, due to of the extrinsic pinning. *S* represents the nanowire cross-section [95].

The resulting torque due to the OOP field pulse, $H_{\perp}$, and in particular its orientation depends on the spin direction inside the transverse wall, and therefore the first term in equation (3) representing the latter torque is proportional to $\cos(\phi)$. Thus for transverse walls in nanowires with a strong in-plane anisotropy and below the Walker breakdown (where the polar angle ϕ is small and $\cos\phi \approx \pm 1$), the torque arising from $H_{\perp}$ is equivalent to the adiabatic spin transfer torque. The direction of the motion depends on the domain wall type, in the case of in-plane field driven domain wall dynamics. In our model the domain wall type, i.e. head-to-head or tail-to-tail is determined by the domain wall handedness $cp = +1$ or $cp = -1$, respectively.
The magnetization rotation when passing from left to right within the domain wall, is defined by the chirality ($c = +1$) for a counter clockwise and ($c = -1$) for a clockwise rotation.

$$c = \frac{1}{\pi}\int_{-\infty}^{\infty}\left(\mathbf{m} \times \frac{\partial \mathbf{m}}{\partial x}\right)\hat{\mathbf{e}}_z \, dx = \pm 1, \quad (4)$$

where *x* is the nanowire direction, and $\mathbf{m} = \mathbf{M}/M_S$ is the normalized magnetization. As an example, in the case of head-to-head domain walls where $\phi = 0$ ($p = -1$) and thus $cp = -1$ it has a negative chirality ($c = -1$) as shown in figure 3.1b. Therefore the non-equilibrium transverse wall motion driven by the OOP field, and the direction of the motion depends on the chirality *c* of the transverse wall, see figure 3.1b.
The equation of motion for the domain wall quasiparticle is obtained. By separating the two first order differential equations of the 1D model and obtaining a second order equation for the position q only. By ignoring any in-plane field parallel to the wire and since no currents are

present, from our extended 1D domain wall model we could find the following equation of motion:

$$F = m\ddot{q} = -cH_{\perp}\frac{\pi m\gamma\lambda}{2(1+\alpha^2)} - \frac{\delta E}{\delta q} - m\frac{\dot{q}}{\tau_d}\left(\frac{\alpha^2\tau_d^2}{m(1+\alpha^2)}\frac{\delta^2}{\delta q^2} + 1\right), \quad (5)$$

Where $m = \frac{S\mu_0^2 M_s^2(1+\alpha^2)}{\gamma^2 K_{\perp}\lambda}$ is the domain wall mass and $\tau_d = \frac{\mu_0 M_s(1+\alpha^2)}{2\gamma\alpha K_{\perp}\lambda}$ represents the relaxation time.

We can clearly infer from equation (5) that the amplitude of the force depends on the time derivative of the OOP field $\dot{H}_{\perp}$, which means the rise and fall time of the OOP field pulse. Moreover, the force strength depends on the domain wall velocity and on the potential landscape arising from the extrinsic pinning $\left(\frac{\delta E}{\delta q}\right)$. Since the Zeeman energy remains constant w transverse wall hen the domain wall is moved by an OOP field, it would be not expected that the OOP magnetic field can move the in plane domain wall. In other words, a continuous displacement driven by static OOP magnetic fields is not possible from the energetically point of view.

However there is a small, transient, displacement which happens during the short time pulse, as we can infer from the dynamic forces applied on the transverse wall, revealed in equation (5). When the pulse is over and thus the OOP field is switched off, the domain wall moves back to its original position since it relaxes to its ground state [70]. In order to understand better let us take as an example the case of a transverse wall with a positive chirality ($c = +1$) and a positive OOP applied field (in the direction of $+z$). The precession term or the resulting torque of the field pulse rotates the in-plane spin structure of the transverse wall counter-clockwise, in analogy to the precessional switching in Ref. [96]. The transverse wall moves along the wire axis the + *x* direction during the pulse until a new equilibrium between the OOP field torque and the arising demagnetization torque (which compensate the effect of the applied field) is reached and the domain wall displacement is stopped. The demagnetization field is resulting from the damping term which tilts the spins OOP (in the direction of $+z$). This means in the absence of any pinning sites, the domain wall moves a finite distance, and the transient displacement is expressed by:

$$q(t) = q_f\left(1 - e^{-\frac{t}{\tau_d}}\right), \quad (6)$$

$$q_f = -cH_{\perp}\frac{\lambda\gamma\pi\tau_d}{2(1+\alpha^2)}. \quad (7)$$

This equation can be obtained by solving equation (5). Equation (6) describes the displacement of the domain wall from the initial position ($q = 0$) to the final equilibrium position q_f during the OOP field pulse $H_{\perp}$. Equation (7) shows that the displacement is inversely proportional to the damping parameter, whereas the direction of the motion depends on the chirality *c*. After the applied field pulse is turned off, the transverse wall moves back to its initial position $q = 0$. Such domain wall displacement occurs only on the time scale of the non-equilibrium dynamics. This

transient motion is similar to the resulting acting torques in the case of purely adiabatic domain wall motion below the Walker breakdown ($\xi = 0$), where the net domain wall displacement is zero [93].

The backward motion when the OOF field is switched off can be suppressed to achieve a net transverse wall motion as the follows:

In the presence of periodically arranged artificial pinning sites along the nanowire, and by using a short (on the timescale of the non-equilibrium dynamics) and asymmetric OOP field pulse with tailored its rise and fall time, we can tailor the acting forces on the transverse wall. The resulting forces on the transverse wall, when the field pulse is applied, can then depin the transverse wall from its initial position which will get pinned at the next pinning potential site when the pulse is turned off.

Experimentally, such a pinning landscape is preexisting and can be geometrically designed using notches, since the nanowire edge-roughness leads to little change in the shape anisotropy [97]. Next, in order to check, in a realistic nanowire geometry, the validity of our model and the efficiency of this new domain wall driven mechanism, we performed some micro-magnetic simulations. One of the most interesting point to check is the dependence of the domain wall motion, e.g. the displacement distance and velocity, with different damping parameters, since this can be tuned in a real system by appropriate choice of material or doping.

III. Micromagnetic simulations Results

III.1. Single transverse wall displacement

In this section we present the simulation results of the transverse wall motion driven by the OOP field pulses as a function of the field amplitude and the damping values. In the simulation we assume the following, as an example: a negative chirality ($c = -1$) head-to-head transverse wall is introduced at the center of a nanowire and an OOP magnetic field pulse ($B_\perp$) is applied along the +z direction. The field pulse characterized as follows ($B_\perp = 60 \sim 100$ mT, pulse duration = 5 ns, rise and fall time ~100 ps). These values were chosen in such a way so as to be accessible.

In figure 3.2a we show the plot of the transverse wall displacement q as a function of the time for different pulse amplitude, $B_\perp$. In agreement with our analytical model, q_f scales linearly with the pulse amplitude and the transverse wall position reaches its maximum displacement. Moreover, as predicted, after the field is turned off the transverse wall moves back to its initial position. The obtained transverse wall displacement, for $B_\perp$= 100 mT, calculated analytically (the black dashed line) using our 1D domain wall model, is also plotted in figure 3.2a, and shows excellent agreement with the simulated results.

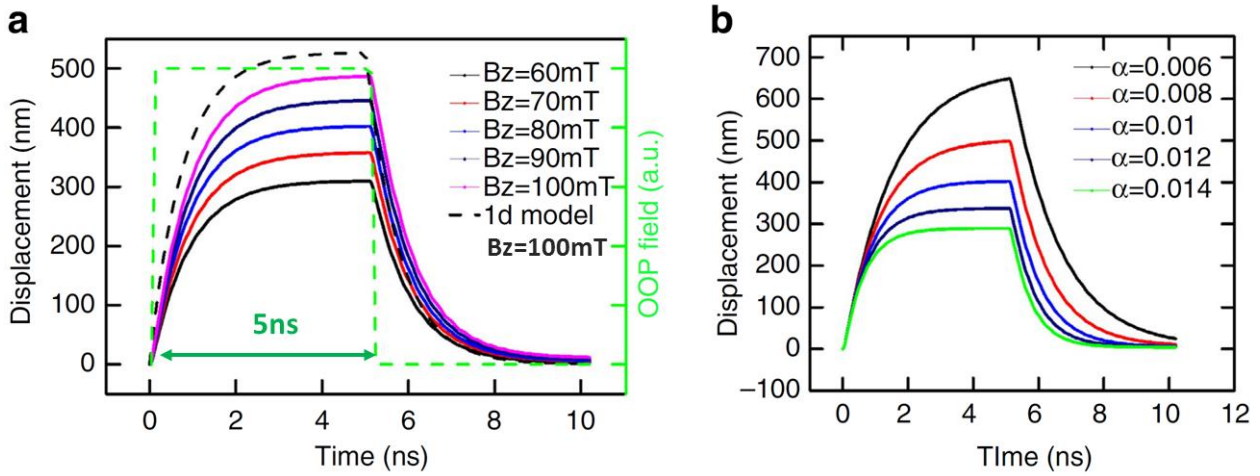

Figure 3.2: transverse wall displacement by symmetric OOP field pulses. (a) Transverse wall displacement as a function of the time (pulse rise time = 100 ps, pulse duration = 5 ns, and fall time = 100 ps) for various OOP field amplitudes. The dashed line indicates the shape of the OOP field pulse, with Bz = 100 mT. **(b)** Dependence of the displacement on the damping constants (α = 0.006 ~ 0.014) [70].

To optimize the displacement, we study the magnetic damping constant dependence of the motion. From the one dimensional model (Eq. (2) and (3)), we see that the damping constant plays a key role and so in figure 3.2b we show the plots of the transverse wall displacement as a function of time for different damping values, α ($0.006 < \alpha < 0.014$). Experimentally these damping parameters can be easily obtained by rare earth ion doping [98]. As we can clearly see from the graph, the plot that displays the highest displacement, q_f, of $\sim 650\, nm$ corresponds the smallest damping value ($\alpha = 0.006$), since it takes longer for the system to reach its new equilibrium state, allowing for a larger displacement. As a consequence we showed that the biggest displacement q_f scales inversely with the damping. It also means that by extending the pulse length to larger durations, larger displacements can be obtained and thus the displacement can be tailored by the pulse height as well as the pulse length, in addition to the material properties.

In order to prevent the backward motion of the transverse wall when the OOP field is turned off, we introduce a square notch ($5 \times 5\, nm^2$) as an extrinsic pinning site with a distance of 400 nm from the center of the nanowire which is the initial position of the transverse wall before the pulse. We chose the 400 nm distance since it was the biggest displacement distance of the transverse wall for a field strength of $B_\perp = 80$ mT.

Intuitively the torques are expected to be symmetric for a symmetric square pulse, thus the transverse wall moves back afterward however it is possible to tune the torques by tuning the rise and fall times by way of making an asymmetric field pulse [99].

We show in Figure 3.3a the transverse wall displacement as a function of time (solid black line) due to an asymmetric pulse (red solid line). This pulse has the following characteristics: the rise time, pulse duration, and fall time are 100 ps, 3 ns, and 3 ns, respectively.

Figure 3.3b, shows a head-to-head transverse wall with negative chirality ($c = -1$) which is displaced along the +x wire direction until it reaches the notch is kinetically pinned [24, 100, 101]. This effect is shown additionally in figure 3.3a with the damped oscillations of the domain wall displacement (black line) at the notch, which creates an attractive potential well for the domain wall [24, 66, 100-102].

After 3.1 ns (rise time + pulse width), the OOP field is slowly decreased over 3 ns since the slower the fall time is, the smaller the dynamic torques, thus the wall is permanently trapped at the notch, as is also illustrated as well in figure 3.3b where the lower and the upper images show the final and the initial spin structure configurations of the nanowire. We then can calculate the average velocity for the domain wall motion which yields ~ 65 m/s.

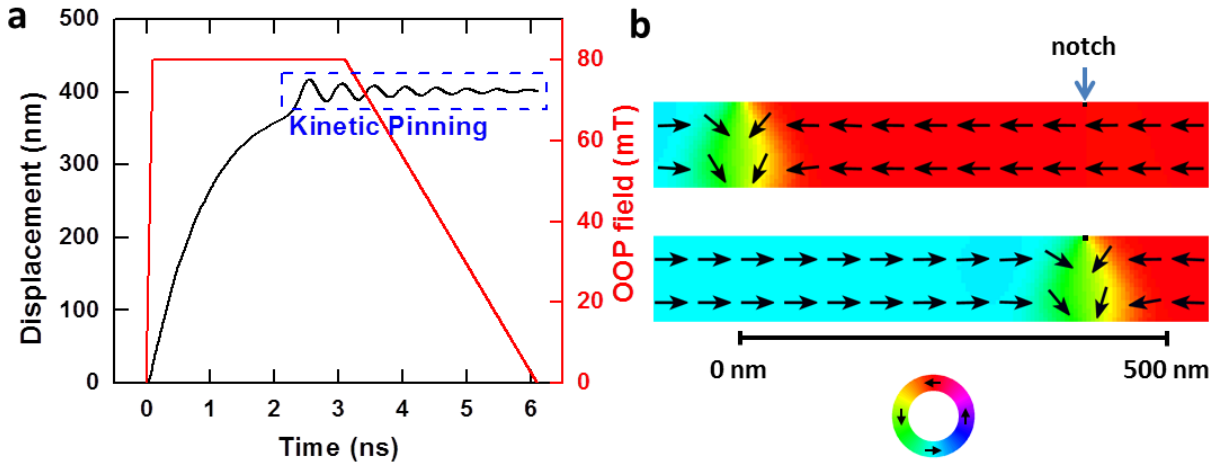

Figure 3.3: Transverse wall motion to a square notch by an asymmetric OOP field pulse [70]**. (a)** Motion of a transverse wall in a wire with a notch by an asymmetric OOP field pulse (rise time = 100 ps, pulse duration = 3 ns, and fall time = 3 ns). **(b)** The initial (up) and final (down) spin configurations of the transverse wall motion. The notch is located at a position 400 nm to the right of the center of the nanowire (only part of the wire is shown). A head-to-head transverse wall with down chirality is placed at the center of the wire. After the wall has moved, it is trapped at the notch position by kinetic pinning. The color ring indicates the direction of the magnetization.

III.2. Synchronous motion of multiple transverse walls

The synchronous displacement of multiple domain walls is an essential key for applications such as domain wall logic devices [74] or racetrack memory devices [73]. We show in figure 3.4 the

synchronous motion of multiple transverse walls induced by successive OOP field pulses. The simulated nanowire consists of Py with 10 nm thickness, 5 µm length and 100 nm width. We introduced an experimentally realistic triangle constriction geometry (10 nm height × 15 nm base) with 100 nm spacing. Figure 3.4 illustrates the displacement of two (a) and three (b) transverse walls, of varying type (tail-to-tail and head-to-head), however all transverse walls exhibit a negative chirality ($c = -1$). In to order prevent any interaction between the domain walls, we initially introduced the transverse walls in such a way that the distance between two successive transverse walls was 600 nm for the case of two and three transverse walls. We use the same asymmetric field pulse shape as was shown in figure 3.2a in order to depin and move the transverse walls with $B_{\perp} = +110$ mT. The walls then relaxed and become pinned at the pinning centers during the fall of the pulse. Therefore as a result the transverse walls displace synchronously from one constriction to next due to the subsequent OOP field pulses which move always the transverse walls is the same direction by the distance of one notch spacing.

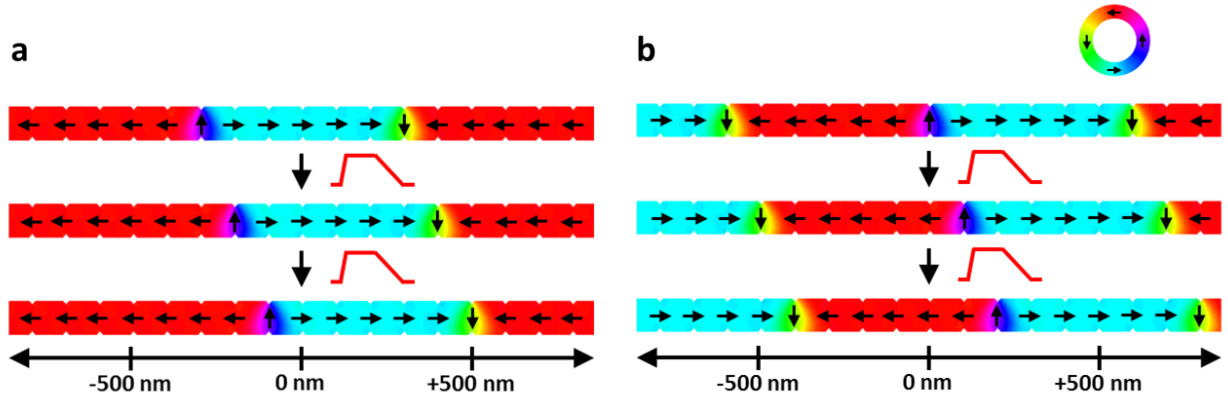

Figure 3.4: Multiple synchronous transverse wall motion by an OOP field (Bz = 110 mT) [70]. Successive triangular notches (100 nm spacing) are introduced and transverse walls are nucleated 600 nm spacing for both case of transverse walls. **(a)** Motion of two transverse walls with successive OOP pulses (rise time = 100 ps, duration = 3 ns, and fall time = 3 ns). **(b)** Synchronous Motion of three transverse walls with successive OOP pulses. The color ring indicates the direction of the magnetization.

IV. Direct imaging of the domain wall displacement

The proposed scheme for synchronous domain wall displacement seems to be a very promising attentive to existing solutions, with good agreement shown between the analytical model and the micromagnetic simulation of the system. So far, however, the demonstrations of the principles have only been theoretical. Therefore in order to test the theoretical predictions I set out to try to verify the mechanism experimentally and thereby assess the functionality and efficiency of the approach. In this section I outline the related sample fabrication and experiment design and execution, which constitutes my major own contribution to the project.

It was decided to initially test the scheme in the simplest possible geometry, which consists of simple nanowires. Not the exact device-like architecture of the simulated model, including the patterned notches. In this case pinning sites are naturally provided due to unavoidable defects and edge roughness from the fabrication process. An impedance matched gold curved stripline was designed to allow the generation of the required fast-rise time field pulses, with two adjacent Py wires patterned to allow the simultaneous measurement of the displacement for opposite field polarity. Curved magnetic nanowires are chosen for ease of domain wall positioning. Since curved element proven to be a useful geometry for the investigation of domain walls because of its high element symmetry, thus the walls can be easily created and positioned by applying an external uniform magnetic field.

The best way to directly confirm the expected domain wall displacement is by direct magnetic imaging. Here the scanning transmission X-ray microscopy (STXM) is a suitable technique since it provides a high spatial resolution of less than (30 nm). Furthermore we are expert, in our group, in combining this technique with the time resolved imaging (see chapter 4 & 5). Whilst the dynamics imaging capabilities have not been directly used in this study, the setup is already optimized for the generation of the required short/fast, asymmetric pulses (see chapter 2 - subsection VI.2 and figure 2.19).

IV.1. Sample preparation

The devices fabrication was done through three lithography steps:

The first step consists of patterning an array of alignment markers from Au, in order to use them into the upcoming steps as a reference and in order to allow perfect alignment from one lithography step to another. These markers play a very important role since our device fabrication is very challenging and requires state of the art fabrication processes due to the need for the smallest possible structure separation without any overlapping at two different steps, for instance between the stripline and magnetic nanowires.

The second step consists of the fabrication of the magnetic structures, which in our case are half rings with two different widths and the same thickness. The dimensions of the nanowires are chosen such that the transverse wall is the ground state [66]. We note that the small different widths of both nanowires are not required, but allow us to check the behavior in a range of conditions.

The third and final step consist of the gold (Au) curved stripline fabrication. This stripline is going to be used for the generation of the OOP magnetic field pulse by the injection of electrical pulses. The material and the dimensions of the stripline were chosen to provide us with the maximum field strength possible, which is in this case ~120 mT, before electromigration effect starts to take place due to the high current density which is proportional to the pulse amplitude.

All samples was prepared on top of a 100 nm thick silicon nitride membrane. We fabricated two permalloy $Ni_{80}Fe_{20}$ (Py) (13 nm)/Au (2 nm) thickness next to curved Cr (6 nm)/Au (100 nm) striplines which were 1.1 µm wide. The curved nanowires were chosen to have two different widths, 170 nm and 140 nm at the top and bottom of the stripline respectively, as it is illustrated in figure 3.5.

All the structures geometry were prepared with lift-off processing using a PMMA/MMA positive resist mask, following electron exposure using the electron-beam lithography system at our institute. The Permalloy was deposited by molecular beam evaporation (MBE) in ultra-high-vacuum (UHV) and the gold was thermally evaporated in order to provide the highest fabrication quality and best resolution (more details can be found in chapter 2 - section II).

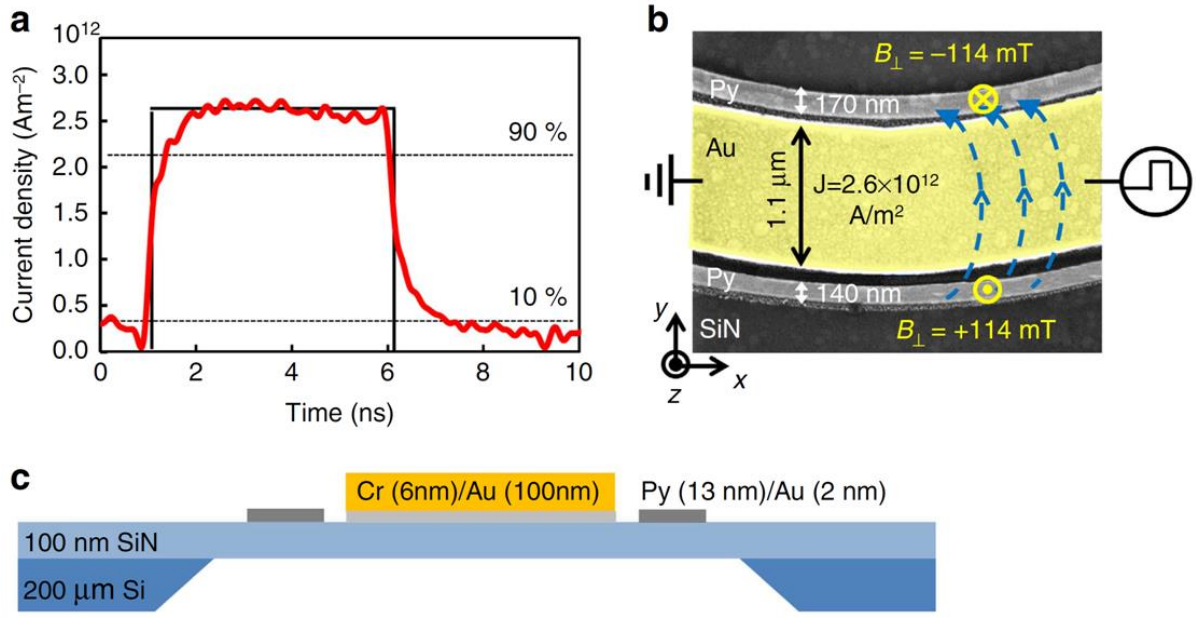

Figure 3.5: Sample layout and generation of the OOP field. (a) The current density, J, in the Au microstrip is plotted as a function of time. The pulse duration is 5 ns, the pulse amplitude is $\mathbf{j = 2.6 \times 10^{12}\ Am^{-2}}$ and the pulse is asymmetric, as the rise time of 700 ps is more than 50% faster than the fall time of 1,100 ps. **(b)** False color scanning electron micrograph of two curved Permalloy nanowires fabricated next to a gold microstrip (yellow). The magnetic field, generated by the current pulse injected through the microstrip, is perpendicular to the plane and opposite in direction at the position of the nanowires on top and on the bottom of the microstrip, as indicated by the blue arrows. **(c)** Schematic illustration showing the cross-section of the device on top of a silicon nitride (SiN) membrane [70].

IV.2. Experimental measurements:

By using an in-plane static magnetic field perpendicular to the nanowires, we saturate the spin structure and after switching off the field a head-to-head or tail-to-tail, (depending on the field

orientation, - *y* or + *y* direction), transverse wall is formed at the center of the half ring, as shown in figure 3.6a. As mentioned above, the transverse domain wall type is formed due to fact that the dimensions of the magnetic structures are chosen such that the transverse wall is the ground state, by considering the experimental domain wall phase diagram respecting the width and the thickness of the wire [66].

In order to move the transverse walls, we injected asymmetric current pulses through the Au curved microstrip, employing the experimental setup illustrated in figure 2.19. This creates OOP magnetic field pulses as illustrated in figure 3.5a & b. The pulse is asymmetric with a 5 ns duration. The asymmetry of the pulse come from the fact that the pulse rise time of 700 ps is about 50 % faster than the fall time of 1100 ps, corresponding to average slew rates of 1.64×10^{10} V/s and 1.05×10^{10} V/s, respectively. The current density of the pulse through the corresponding stripline is $j = 2.6 \times 10^{12}$ A/m^2. This value results is a maximum out-of-plane magnetic field amplitude, at the center of both nanowires, of $B_{\perp} = 114$ mT. In general the generated out of plane field component from the stripline decays inversely proportionally to the distance from the edge of the stripline (as r^{-1}). However, since the widest nanowire is 170 nm, we are able to assume that the OOP field is constant along the transverse direction of the wire axis, with an error smaller than ±20 %. Moreover, the created field should be homogenous along the magnetic nanowires, since the curvature of the nanowires follows the curvature of the Au mico-stripline. This means that the distance separating the stripline and the nanowires is a constant distance along the nanowires, which is corresponds to of ~ 40 nm (see figure 3.5).

The transverse wall moved either to the right or left after the injection of a positive or negative asymmetric burst pulse, respectively in the case where the chirality of the transverse wall is negative ($c = -1$). The in-plane spin structure configuration was imaged by scanning transmission X-ray microscopy (STXM) with a lateral resolution of less than 30 nm, where the sample is tilted by 60° with respect to the X-ray beam. The magnetic contrast of the images is provided by the X-ray magnetic circular dichroism (XMCD) [43], more details can be found chapter 2 – subsection III.1. The data is recorded at the Ni L_3-absorption edge (852.7eV). The XMCD images of the two transverse walls position were statically imaged before and after the application of the magnetic OOP field pulses.

IV.3. Direct observation

The initial magnetization configuration of both head-to-head transverse walls in figure 3.6b is schematically illustrated in figure 3.6a. Both transverse walls exhibit a negative chirality ($c = -1$) after the nucleation due to the curvature of the wire and the direction of the initializing field. The transverse wall positions before and after five successive magnetic OOP field pulses are shown in figure 3.6b and figure 3.6c, respectively. We can clearly observe that the generated two opposite OOP field directions led to net domain wall displacements in the two opposite directions for the two transverse walls presented in the nanowires above and below the microstrip. The displacement of the upper transverse wall was 840 ± 20 nm from position (1) to position (3),

whereas the lower domain wall moved a total distance of 940 ± 20 nm from position (2) to position (4) as shown in figure 3.6b-c.

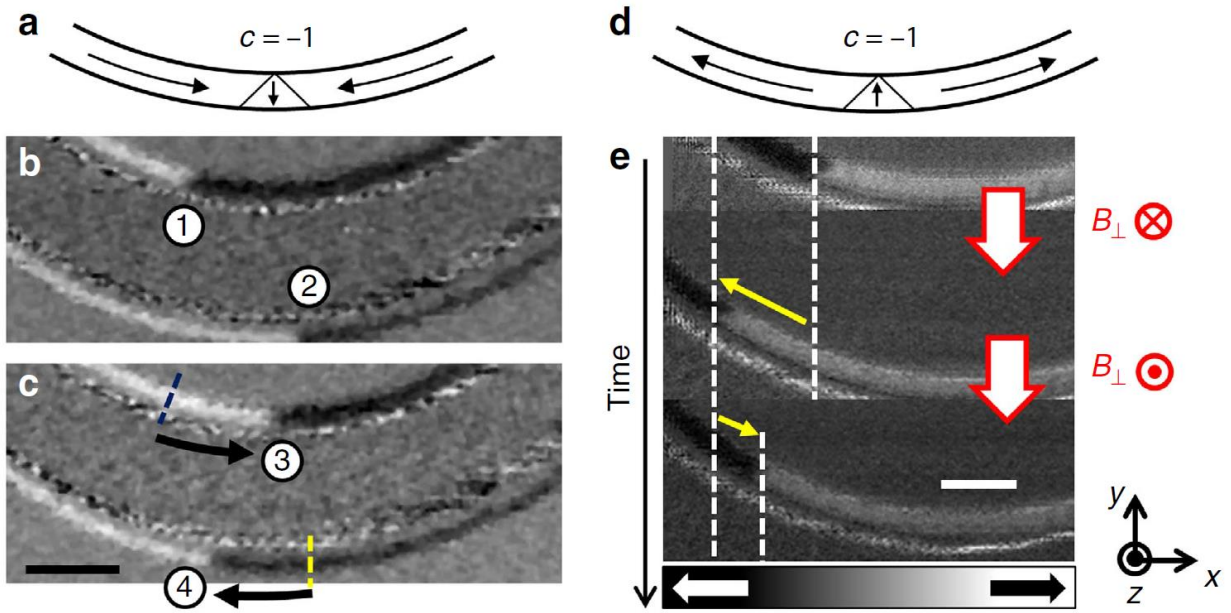

Figure 3.6: OOP field induced transverse wall motion [70]**. (a)** The initial transverse wall configuration ($\mathbf{p = 1}$ and $\mathbf{c = -1}$) of the transverse wall o transverse walls in **(b)** and **(c)** is schematically illustrated. (**b, c**) Grey scale X-ray magnetic circular dichroism (XMCD-STXM) images showing the magnetic contrast of the domains and two head-to-head transverse walls with negative chirality before **(b)** and after **(c)** the injection of five subsequent pulses through the stripline. The OOP field pulse is positive (negative) on top (at the bottom) of the stripline. The upper transverse wall moved a distance of $\mathbf{840 \pm 20\ nm}$ from position **(1)** to position **(3)**, while the lower transverse wall travelled $\mathbf{-940 \pm 20\ nm}$ from position **(2)** to position **(4)** Scale bar, 1 µm. **(d)** The initial transverse wall configuration ($\mathbf{p = -1}$ and $\mathbf{c = -1}$) of the transverse wall in **(d)** is schematically illustrated. **(e)** A XMCD-STXM image series showing a tail-to-tail transverse wall with negative chirality before and after the injection of two subsequent and opposite in direction OOP field pulses. The transverse wall travelled $\mathbf{720 \pm 20\ nm}$ to the left (in negative x-direction) after the application of a negative OOP field pulse $\mathbf{B_\perp = -114\ mT}$. In contrast, the transverse wall moved $\mathbf{340 \pm 20\ nm}$ to the right (in positive x-direction) after the application of a positive OOP field pulse $\mathbf{B_\perp = +114\ mT}$. In all images, white (black) contrast corresponds to magnetization pointing to the right (left). White scale bar, 500 nm.

OOP magnetic field pulses, and we imaged the upper transverse wall position before and after each pulse injection. The initial spin structure configuration of the transverse wall in the upper nanowire is shown in figure 3.6d schematically where the domain wall is a tail-to-tail transverse wall with a negative chirality. We show in figure 3.6e, a series of three XMCD images which

have been taken before and after the injection of two successive and inverted polarity OOP field pulses. As we expected, we could clearly see that after the injection of a negative OOP field pulse direction ($B_\perp = -114$ mT), the transverse wall moved in the –x direction with a distance of 720 ± 20 nm. However, the transverse wall travelled along the + x direction (to the right) with a value of 340 ± 20 nm after the subsequent injection of a positive OOP field pulse direction ($B_\perp = +114$ mT). In this current experimental work, we are making use of the fact that the wires exhibit some edge roughness or other defects, i.e. some natural pinning sites, which are of course uniform the same along the wire. This can easily explain the differences in the displacement after the application of the opposing OOP fields with the same field strength. First of all, in order to reproduce completely the displacement the driving field pulse should provide sufficiently strong forces to overcome the natural pinning which is always present in real systems. In addition with the artificial pinning sites (notches), which are much stronger than the natural pinning, this will lead to more reproducible motion. However in our case it was sufficient to rely on the natural pinning only in order to demonstrate the resulting motion direction, regardless of the reproduction of the displacement distance which would be the topic of future study in optimized device-like geometry, beyond the proof-of-principle demonstration here.

V. Discussion

In order to demonstrate and gauge the applicability of our approach as an alternative to the current induced domain wall motion for applications, this section will discuss the experimentally observed transverse wall displacement and compare them with the theory.

In figure 3.6 we clearly showed by direct imaging experiments, a total net displacement of domain walls resulting from the injection of asymmetric current pulses through the Au stripline in both opposite directions and generating OOP field pulses. These observations confirm quantitatively our predicted analytical model and the micromagnetic simulations where the direction of the domain wall motion is controlled by the orientation of the OOP magnetic field pulses in addition to the transverse wall chirality ($c = \pm 1$). The measured displacement distance is independent of the domain magnetization directions, which is a very important prerequisite in the case of synchronous displacement of many domains. The observed asymmetric motion using identical pulse shapes in both directions is attributed to the asymmetric potential landscape resulting from the non-constant edge roughness due to the imperfection in the real fabrication process, in addition to thermal activation effects.

First, we consider the influences of the materials' parameters and nanowire geometry on the transverse wall displacement in order enhance the performance of a possible device. It was shown that the displacement distance is proportional to the field pulse strength (figure 3.2a) as also explained by the equations (6 & 7). Moreover, the maximum displacement is also proportional to (τ_d) which is the time constant of the transient motion. However, this displacement distance is inversely proportional to the saturation magnetization, M_S, the damping parameter, α and to the transverse $K_\perp$ ratio. All this means, that the transverse wall displacement as well as the domain

wall velocity can be controlled and improved by the use of different materials with a larger saturation magnetization or smaller damping parameter (as demonstrated in figure 3.2b) or by engineering the geometry of the wire in order to decrease the transverse anisotropy ratio. Furthermore, the sensitivity of the device to defects or edge roughness is indeed an important aspect.

In equation (5) we conclude that the effective resulting force exerted on the domain wall (considered as a quasi-particle) strongly depends on the time derivative of the field pulse amplitude. Therefore the displacement and the acting torques on the transverse wall can both be tuned by the shape of the field pulse by changing its rise and fall time. In other words, by tailoring the pulse shape, the needed motion can be obtained for a given pinning strength, spacing sites and edge roughness.

From the applications' point of view, it is important to compare our proposed system (OOP field-induced transverse wall motion) with the alternative common method of synchronous multiple domain wall motion which is current driven domain wall displacement. However it is not easy to make comparison between the transverse wall displacement due to the spin transfer torque effect and the precessional torque responsible of the transverse wall displacement through the OOP field pulses created by the electrical current injection in the gold stripline. Nevertheless, one can compare the energy dissipations for the domain wall motion by both effects.

For instance, one of the experimental transverse wall displacements induced by the OOP field in the case of a Py nanowire (170 nm wide and 13 nm thickness) was ~840 nm using a 5 ns electrical pulse injected through the 1.1 μm wide and 100 nm thick gold microstrip. This corresponds to a current density $j = 2.6 \times 10^{12}\ \mathrm{A}/m^2$. Our micromagnetic simulation shown in figure 3.4 suggests that our proposed system works well for the case of multiple domain walls placed in the nanowire with spacing of 600 nm. Due to the fact that the maximum displacement is linearly proportional to the current density, in order to reach such domain wall displacements during the 5ns pulse width one would need a current density of $j = 1.7 \times 10^{12}\ \mathrm{A}/m^2$. Therefore the dissipated energy in this case is $22\ pJ$ per moved domain wall which can be obtained by considering a specific gold resistivity of $2.44\ \mu\Omega cm$.

On the other hand, in the case of the current induced domain wall motion by the STT effect, we now compare the calculation of the domain wall motion numerically and theoretically [93], since in the case of in-plane magnetized materials, several experimental domain wall velocities measurement were reported [82, 83, 103, 104]. First of all, we suppose the case where the Gilbert damping constant is equal to the non-adiabicity parameter and consider that the spin polarization is 0.4 as in [105]. In addition, the saturation magnetization of Py is $8 \times 10^5\ Am^{-1}$ which results in a maximum current density of $4.2 \times 10^{12}\ Am^{-2}$. Therefore we obtain a dissipated energy for the motion of one domain wall of $46\ pJ$ by considering the specific Py resistivity $40\ \mu\Omega cm$ [106]. However, the specific Py resistivity in devices may be increased due to the high current density in the Py nanowire, which increases the nanowires temperature. As a consequence, the required energy for the displacement of one domain wall would also increase. By comparing the

experimental energy dissipation of our system to the theoretically predicted domain wall motion in a non-defect nanowire by the spin transfer torque one can conclude that our system is more efficient at this scale.

Furthermore, many other advantages of our system are shown in the following:

Although the OOP field pulse shape has a fall time longer than the rise time and long enough to relax the domain wall at the pinning centers, there is still another torque which is directed in the opposite direction and may partly move the transverse wall backwards. This was demonstrated in figure 3.5a where the transverse wall moves backward once the OOP field is tuned off. Hence, the maximum experimental obtained transverse wall displacement of 840 nm may be smaller than the forward traveled distance before the influence of the arising opposite torque. A further advantage is that in our system the precessional torque tends to rotate the transverse wall spin structure components, and does not nucleate any anti-vortex core. Whereas this does occurs above Walker Breakdown for current induced domain wall motion and this negatively influences the motion of the domain wall. Therefore our system using field induced domain wall motion at high current density does not have any disadvantage from the resulting slow velocities due to the Walker breakdown in the case of the STT system. This results from the fact that in our system the current pulses are injected through the Au stripline which can support a higher critical current density than the magnetic nanowires.

VI. Conclusion

To summarize, a radically different approach using OOP field pulses could lead to a paradigm shift to obtain the required synchronous motion of multiple domain walls driven by magnetic fields. This is an efficient alternative to the current induced domain wall motion.

We demonstrate that we can displace transverse walls by OOP magnetic field pulses. This paradigm shifting achievement provides the required functionality for nonvolatile domain wall-based shift register devices. This demonstration was supported by an extended analytical model (based on the 1D model), and by micromagnetic simulations.

The experimental observations showed a qualitative agreement with our analytical and numerical results, which confirm and demonstrate the viability of our proposed novel mechanism approach for domain wall motion. We note that this approach can be also interesting, from the application point of view, in systems where the magnetization of the nanowires is perpendicular to the structure plane and the applied magnetic field pulses are in-plane, since the present mechanism is identical spin under rotation, without any influence to the underlying physics.

The transverse wall motion direction relies only on the chirality ($c= \pm 1$) of the transverse wall and the field direction. Analytically we showed, using the 1D collective coordinate domain wall profile model that the displacement of the transverse wall happens during the non-equilibrium dynamics when the pulse is active. The net transverse wall displacement is obtained over few

hundreds of nm with a high velocity, where the backward motion is suppressed using asymmetric field pulses and including periodic pining centers (notches).

Chapter 4

Local domain wall velocity engineering via tailored potential landscapes in asymmetric rings

Abstract

Magnetic sensing and logic devices based on magnetic domain walls rely on the precise control of the local domain wall propagation in various nanowires, including curved geometries. We report local control of the domain wall velocity and position by engineering the geometry of ring structures, leading to a tailored domain wall potential landscape. By employing time resolved scanning transmission X-ray microscopy (STXM) we directly observed the domain wall spin structure transformations during motion driven by rotating magnetic field pulses and quantitatively determine the contribution of the spatially varying potential landscape to the domain wall propagation. In this chapter, we experimentally demonstrate an angular dependence of the domain walls velocities. We explain this effect by the interplay between the domain wall spin structure and relevant forces that act on the vortex domain wall. The long-range forces which contribute arise from the Zeeman interaction of domain walls with the applied external magnetic field pulse. Secondly there are local forces arising from the domain wall energy changes due to the non-constant ring width. In contrast to symmetric ring systems, the interplay between these forces leads to distortion-free domain wall motion. Therefore, using this varying domain wall potential landscape, we are able to control spatially the internal domain wall spin structure transformation and synchronization of the domain wall velocities in ring geometries, even above the Walker breakdown.

This chapter is arranged as follows. In Section I we motivate and introduce the work. In Section II we present our sample and experimental approach. In section III we present and discuss the experimental results and finally in Sections IV we summarize the work. The work in this chapter was carried out in collaboration and with the contribution of Dr. Kornel Richter and A. Krone who attended part of the experimental beamtimes, which have been dedicated for this study, and helped in the data analysis of the presented results.

I. Introduction:

One key prerequisite for precise control and reproducible propagation of magnetic domain walls in nanowires is a thorough understanding of the mechanisms that lead to variations in the domain wall velocity, as well as to control the dynamics on a local scale. In general, the occurrence of the Walker breakdown [27] limits the steady-state motion of a driven domain wall in straight wires, independently of the driving mechanism (see chapter 1 - subsection II.1). In this regime, above a critical so-called *walker field*, an internal change of the domain wall spin structure takes place, resulting in an oscillation of the domain wall velocity and reducing the reliability and the reproducibility of the dynamics. Conversely for low fields, several studies have confirmed the existence of a stable steady-state domain wall motion regime at low fields in several geometries of different materials, with different driving mechanisms and magnetic anisotropies [23, 28, 77].

However, we recently demonstrated that this steady-state domain wall motion regime at low field does not exist for curved nanowires geometries, where domain walls are driven by rotating magnetic field pulses [24]. In particular, we have reported for the first time, a direct dynamic experimental visualization of oscillating domain walls dynamics induced by rotating field pulses in symmetric ferromagnetic rings. This oscillatory propagation of the vortex domain wall was explained by the interplay between the rotating driving magnetic field and the periodically changing domain wall spin structure due to the off-tangential forces that act on the vortex domain wall during its motion. It was shown that these oscillations could occur even without an accompanying wall transformation into a transverse domain wall and thus below the Walker breakdown. We concluded that this oscillatory behavior of the domain wall velocity occurring above and below the Walker breakdown, is a general feature in application relevant curved geometries, for motion driven by a rotating magnetic field [24].

Theoretically the explanation of the vortex wall dynamics is still complicated to understand, even from just our simple model which describes the relevant forces acting on the vortex domain wall spin structure in Ref. [24]. These complications stem from the complex spin structure of the vortex domain wall. Therefore the interplay between the domain wall velocity and the radial vortex core displacement is not predicted by the analytical description of the one-dimensional model [25, 26] showing that the oscillating domain wall propagation in curved wires above and below the Walker breakdown goes beyond the framework of this simple one-dimensional model. The spin configuration of the vortex domain wall consists of three elementary topological defects, two half-vortices at the edge of the nanowire and one vortex with a vortex core in the center of the domain wall as described in [107]. Hence the excitation of the internal spin structure exhibit extra degrees of freedom during the dynamical motion [30]. In other words the local oscillations of the domain wall velocity directly result from the complex two-dimensional motion of the vortex core even in perfect defect-free systems and not from the domain wall interaction with pinning centers, as we previously reported [24].

Moreover, in ferromagnetic rings both half-vortices of the vortex domain are confined to different edges of the ring and since both edges have different radii, both half-vortices propagate by a different distance after one full field rotation which results in intrinsic instabilities in the wall displacement. This means that, different velocity profiles can be obtained when rotating the domain wall with different start angles in the ring, which is inappropriate for applications [108, 109].

The domain wall dynamics can be controlled locally by introducing notches in the magnetic structure, and thus pinning the wall at this constriction [110]. Several experimental and theoretical studies were able to control statically the domain wall position in this manner since the notches provide a potential well for the domain wall [111]. Such static pinning potentials have been extensively characterized in terms of the potential well global shape [112], curvature [110] and depth [102].

The dynamic interaction of domain walls with pinning potentials exhibits different properties. Theoretical predications explained that the kinetic pinning field of moving domain walls is reduced compared with the static pinning. This was experimentally confirmed by us [24]. However, using notches in magnetic devices based on domain wall motion has showed several disadvantages. For instance the spin structure of a vortex domain wall passing through narrow constrictions can be dramatically deformed by expulsion of the vortex core, which could mean a loss of information.

Moreover, the abrupt changes of the geometry of the notches and the minimum constriction width at the center are not very suitable for down-scaling as precisely controlled narrow constrictions are difficult to fabricate. As result this approach is not deemed very useful for realistic devices. For applications, therefore, alternatives are sought to (i) enhance the dynamic stability of the domain wall spin structure, as much as possible, and (ii) and control its velocity locally.

One approach involving the gradual variation of the domain wall energy landscape (in contrast to abrupt changes at constrictions), for example via geometrical variations (e.g. gradually varying ring width) seems a good concept for a possible local control of the domain wall velocity influenced by the spatially dependent domain wall energy [66]. Although the static properties and the influence of a varying geometry on domain walls in straight wires have been determined theoretically [113], the imaging of the controlled domain wall dynamics as well as the theoretical analysis in curved geometries, as necessary to understand the underlying physics, has not been reported before. For example, the determination of the geometrical influence on the intrinsic dynamic domain wall properties such as inertia and effective domain wall mass [62]. It is highly beneficial to determine such properties directly by experimental imaging in combination with micromagnetic simulations due to the complexity of domain wall dynamics in curved geometry that go beyond the simple one-dimensional framework, as we described above. Overall a full understanding of these properties is crucial for applications due to their influence on the dynamics and performance of magnetic nano-devices [66].

In this chapter, we discuss the dynamics of domain walls in ferromagnetic rings tailored by an inhomogeneous domain wall potential landscape. It is demonstrated that the variation of the ring width, allows for a local control of the resulting spatially dependent domain wall velocity around the ring, with the maximum value obtained in the widest part of the ring nanostructure. We experimentally show, by direct time-resolved imaging, that the global minimum of the domain wall potential landscape in the narrowest part of ring provides a spatial synchronization of the domain wall velocity profile, regardless of the starting angle of the domain wall propagation along the ring. This is a distinct advantage for applications since the local velocity no longer depends on the initial position at which the domain wall is nucleated. Furthermore we show that the resulting forces from the inhomogeneous potential landscape can efficiently suppress and control the radial motion of domain wall. This provides extra stabilization of the local domain wall velocity, since the radial motion of the vortex core is the main origin of the oscillatory behavior of domain wall velocity below Walker breakdown in rings [24]. We note that part of this work has been recently published in Ref. [114].

II. Samples and experimental

We study asymmetric ferromagnetic permalloy rings which consist of an outer diameter of 5.5 µm and non-centered inner diameter of 4 µm, with a thickness of 30 nm. Taking into account the experimental phase diagram discussed in Ref. [15], the geometry of our sample leads to the vortex domain wall spin structure being stable the whole ring width.

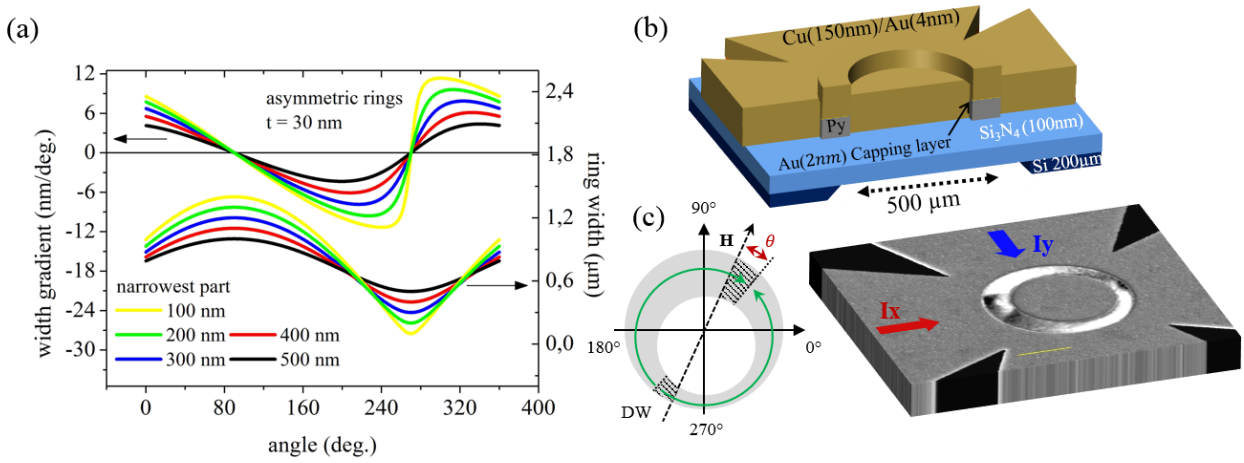

Figure 4.1: Schematic of the sample geometry and design used in our experiment. (a) Sample overview for different magnetic structures with narrowest widths of 100, 200, 300, 400 and 500 nanometers. Sample thickness t = 30 nm [114]. **(b) Top:** schematic illustration of the sample design patterned on Si_3N_4 substrates for the study of domain wall dynamics (crossed copper striplines on top of permalloy rings with a diameter of 5 μm and 30 nm thickness). **Bottom:** merged STXM-XMCD image of an asymmetric ring structure with a SEM image of the sample under investigation. The in-plane magnetic field is generated by the sinusoidal currents, $I_{x,y}$, with a 90° phase shift injected in the crossed stripline. **(c)** Ring schematic ring illustration, where the angle $\boldsymbol{\theta}$ is the phase difference between the field H and the azimuthal vortex core position.

This is crucial in our study because it helps to ensure that the observed dynamics of domain walls driven by the rotating magnetic field are free from any domain wall transformations induced by variations in the ring width. The observed dynamics are therefore purely influenced by the irregular potential landscape. Measurements of a series of samples having different widths in the narrowest part have been carried out in order to disentangle two influences on the domain wall dynamics: the intrinsic material properties, such as the natural roughness or defects resulting from the sample fabrication, and the effect of the inhomogeneous potential landscape. This series of samples provides almost the same range of width gradients, is ranging from -9 nm/deg. to 9 nm/deg., as shown in figure 4.1a.

The permalloy asymmetric rings with a different widths in the narrowest part (300 nm 400nm and 500 nm), were fabricated by a lift-off process using electron beam lithography (EBL) with a substrate of 100 nm thick X-ray transparent Si_3N_4 membranes, with material deposition performed using molecular beam evaporation in a ultra-high vacuum (UHV) chamber. We note that in the following we refer to the widths in the narrowest part as a convention to name and differentiate between different ring structures. The magnetic structure was capped with a 2 nm thick gold (Au) layer in order to prevent oxidation of the permalloy. For the generation of the in-plane rotating magnetic field, a 150 nm thick copper (Cu) crossed stripline, was fabricated on top of the magnetic structure, and capped by a 4 nm thick Au layer protecting the copper from surface degradation (see figure 4.1b,c). The whole sample fabrication process was done through three successive steps, as described in chapter 2 - section II.

The ring dimensions, width and thickness, was defined such that the vortex domain wall spin structure is the lowest energy magnetic configuration [15] after saturation with a uniform external magnetic field [14, 66]. The ferromagnetic rings are then in the onion state [65]. Furthermore the permalloy thickness (30 nm) is chosen as a compromise between four different effects: maximization of the XMCD contrast, ground state domain wall configuration, avoiding the formation of 360° domain walls that can occur in rings of smaller thickness [115] and lastly providing a low depinning field for current and field induced domain wall motion [116].

The time evolution of the magnetization dynamics is recorded stroboscopically employing a pump and probe technique employing time resolved scanning transmission X-ray microscopy (STXM), with a sub 30 nm spatial resolution, at the MAXYMUS endstation, Helmholtz Zentrum Berlin, BESSY II, Germany (see chapter 2 - section IV). The in-plane magnetization component was imaged by tilting the sample surface normal by 30° with respect to the incident light direction. The contrast of the image is based on the X-ray magnetic circular dichroism (XMCD) effect [43]. The data were recorded at the Ni L_3-absorption edge (852.7 eV). The pump, in our case, consists of a repetitive external magnetic field excitation of the nanostructures. This excitation is decomposed into two successive magnetic field pulses. Firstly a uniform magnetic field in order to create the onion state, then the generation of an in-plane rotating magnetic field by simultaneously injecting 90° phase shifted, radio frequency (RF), currents through the two ends of the orthogonal crossed striplines (see chapter 2 - section VI). Thus, the propagation of the domain walls is induced by counter-clockwise rotating magnetic field burst pulses. These, have

the following properties: firstly, the magnetic field amplitude first increases until it reach its maximum, pointing in the initial saturation direction of the onion state, followed by two full counter-clockwise rotations of the in-plane magnetic field, and finally, the field amplitude is decreased, also along the initial saturation direction of the onion state. It is worth mentioning that the experiment is repeated at a repetition rate of 832 kHz and the transmission signal X-ray signal is recorded over more than ten billion subsequent pulse cycles, and hence domain wall propagation events, ensuring a high signal-to-noise ratio and demonstrating the reproducibility and the reliably of our measurement results (as discussed in chapter 2 – section IV).

III. Results:

We experimentally observed that the phase shift, θ, between the local position of domain wall and the field direction of the driven rotating magnetic fields show a large correlation with the inhomogeneous geometry of the ring sample. On relaxation of the magnetization from saturation during the nucleation process, the magnetic configuration is transformed to the onion state. At $t = 0\,ns$ of the rotating field pulse, the system tends to minimize its energy by aligning the position of both domain walls to the magnetic field direction, as shown in figure 4.2a where the phase shifts for both domain wall are almost zero. The initial magnetic configuration and position of both domain walls (head-to-head & tail-to-tail), at $t = 0\,ns$, are schematically shown in figure 4.2d. We note that the domain wall position is defined by the position of the vortex core. The domain walls start to move with $t < 2\,ns$, just after the magnetic field begins to rotate with a counter-clockwise sense of rotation. In this case the head-to-head domain wall propagates from the narrower towards the wider part of ring and vice versa for the tail-to-tail domain wall moving in the opposite part of the half-ring.

For $t < 30\,ns$ the tail-to-tail domain wall propagating from the wider to the narrower part of the ring, overcomes the speed of the rotating field, resulting in a positive phase shift (red curve), as shown in figure 4.2a. conversely the head-to-head domain wall moving from the narrower to the wider part of the ring, exhibits a negative phase shift (black curve), which mean that the wall is always lagging behind the rotating field in this region. We observed that at $t = 30\,ns$, both domain walls cross the symmetry axis of the asymmetric ring, illustrated in figure 4.2b, resulting in a reversal of the phase shift sign. We note that such behavior (sign changes) is repeated each time the domain walls cross the symmetry axis (figure 4.2a). Thus, this constitutes a direct proof that the phase shift oscillations are purely resulting from the geometry changes and determined by the shape of ring.

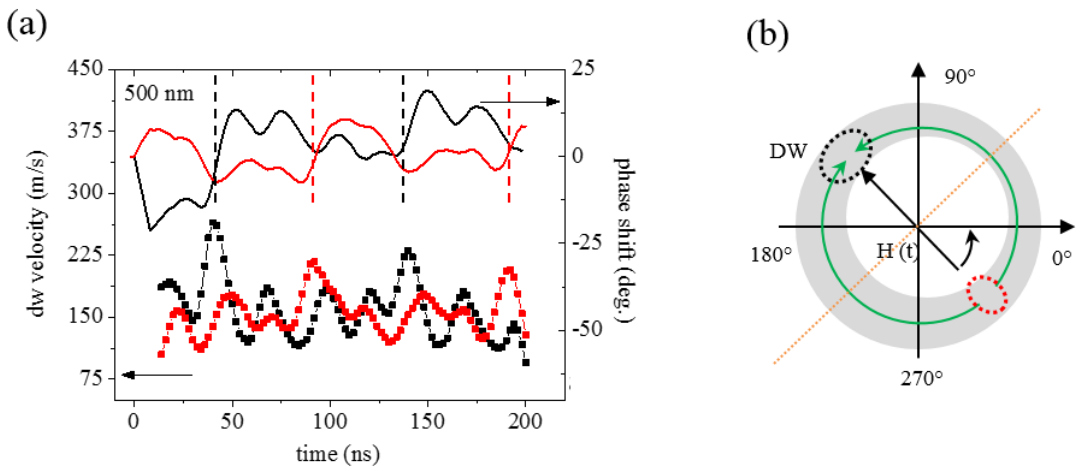

Figure 4.2: Domain walls propagation in an asymmetric ring. The black and red curves correspond to the head-to-head and tail-to-tail vortex domain walls, respectively. The domain walls are driven, from the starting angles ~-45° and ~135°, by a counter-clockwise rotating magnetic field with two rotation cycles. **(a)** Domain wall velocities and phase difference are plotted as a function of time for two counter-clockwise field rotations. The dashed vertical lines represent the time when the domain wall of the corresponding color (head-to-head and tail-to-tail) crosses the widest part of the asymmetric ring [114]. **(b)** Schematic illustrating the ring geometry. The black (red) ellipse represents the initial position of the head-to-head (tail-to-tail) domain wall at t = 0 ns. The yellow dashed line represents the symmetric axis of the ring.

The key to understand the mechanisms of the observed domain wall dynamics is through the quantitative determination of its relevant energetics, which we analyzed. Qualitatively speaking, the oscillating behavior of the phase shift sign can be explained by the interplay between the energy variations of the domain wall, resulting from the position dependent potential landscape, and Zeeman energy. We note that, when an in-plane external magnetic field **B** is applied, the Zeeman energy is minimal when the two domain walls align with the applied field ($\theta = 0°$). Therefore the energy depends on the phase shift, θ, between the field and the azimuthal position of the two vortex domain walls whereas for non-zero values of θ, the domain walls experience a restoring torque towards the minimum of the potential landscape created by the applied field [67]. Thus, when a field is applied to the asymmetric ring in the onion state, the energy of the domain wall can be stored in two reservoirs: While the Zeeman energy is given by the phase shift, the domain wall potential landscape has a spatial dependence due to the exchange and dipolar energy variations in the domain wall spin structure and thus it depends on a local ring width.

In contrast to our previous study in a symmetric ring system [24], the inhomogeneous geometry of the ring structure modulates the Zeeman energy landscape created by the external magnetic field (figure 4.3a). However this modulation of the energy landscape is less than ~ 3 % for any geometry and field direction used in this experimental study see figure 4.3a. Hence, the alternating phase shift cannot only be explained by the latter effect and should result from other effects contributing to the domain wall energy and which better explain the observed results.

Such effects arise from the irregular ring width of the sample, since in addition to the Zeeman energy effect, described above, the irregular ring width modulates the domain wall potential landscape. The inhomogeneous ring width give rise to a spatial energy dependence of the domain wall, *U*, which is expected to be the lowest in the narrowest part of the ring and the highest in the widest part of ring. Such modulations of the domain wall energy lead to an effective local force,

$$\mathbf{F_U} = -grad\ U\ ,$$

which moves the domain wall towards the narrower part. Therefore, in the case where the domain wall is driven with an external field with a counter-clockwise sense of rotation, from the narrowest toward the widest part of the ring, the restoring force is expected to be negative ($\mathbf{F_U} = -grad\ U < 0$) with respect to the sense of motion and in the direction of the minimum of the Zeeman energy (see figure 4.3a). Hence this force may result in a negative phase shift (the domain wall is dragged). However the negative gradient of domain wall energy ($grad\ U < 0$), present in the opposite half of the ring, results in a positive local force in the direction of the domain wall motion (sense of field rotation) and hence leading to a positive phase shift in this area of the ring. As well as in asymmetric rings, the oscillatory behavior of the phase shift sign has been recently observed in symmetric rings, in our group. This was attributed to the competition between the extrinsic and intrinsic pinning (intrinsic domain wall spin-structure oscillations) with the resulting forces dragging of the domain wall and accelerate the domain wall beyond the driving rotation velocity of the magnetic field [24].

It is worth mentioning that the fact that the domain wall overshoots the driving field, resulting in a positive phase difference, represents a direct signature of domain wall motion under its own inertia [117]. However, in the present study the spatial dependence of the phase difference and its alternating behavior are strongly correlated to the variation in the geometrical shape of the ring.

We note that such oscillatory behavior of the phase shift has not only been observed in 500 nm asymmetric rings (figure 4.2a), but also in rings with different widths (e.g. 300 nm and 400 nm) as shown in figure 4.4. In order to check the role of the width gradient, we repeated the experiment by driving domain walls for one full rotation by a rotating magnetic field for 300 and 400 nm rings (figure 4.4). The width gradients for both samples can be seen in figure 4.1a.

The repeatability of the phenomenon for different samples clearly demonstrates that the well-controlled domain wall position with respect to the driving field is not related to extrinsic natural pinning sites, resulting from the sample fabrication, but rather to the inhomogeneous potential landscape created by the ring shape. This is highly advantageous because the extrinsic pinning is usually randomly distributed along the ring.

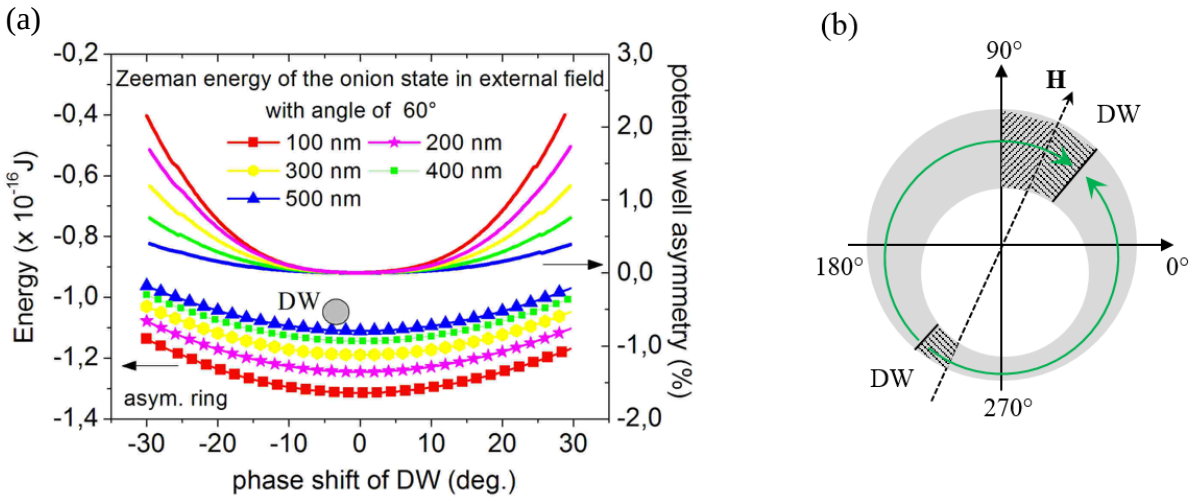

Figure 4.3: (a) Zeeman energy of the onion state in the presence of an external field in the asymmetric rings with different ring widths. The irregular ring width leads to a modulation of the Zeeman energy landscape, resulting in a differences in Zeeman energy values for different phase shift values (positive and negative). This is shown in the potential well asymmetry curves which are calculated as $(\boldsymbol{E(\theta) - E(-\theta)/E(\theta = 0°)})$, where $\boldsymbol{E(\theta)}$ is the Zeeman energy of the onion state as a function of the phase shift $\boldsymbol{\theta}$, after Ref. [114]. **(b)** Schematic of an asymetric ring illustrating the difference in the spin structures (dashed area) for negative and positive phase shift of the head-to-head domain wall, which leads to differences in the Zeeman energy values.

For applications based on domain wall propagation, in addition to the reliable control of the domain wall position, a reproducible and stable domain wall velocity are also required. In figure 4.2a and 4.4 we present a typical experimental domain wall velocity profile for different ring geometries. This velocity is the magnitude of the angular velocity of the vortex core multiplied by the mean radius of the ring structure and is extracted from the measured time resolved movie. By considering Figure 4.5a, where the domain walls are driven by a counter-clockwise field rotation pulse consisting of two rotation in a 500 nm wide asymmetric ring, one could clearly see that both domain walls do not move at a constant velocity despite being driven by a constant field amplitude $(B = 6.8\,mT)$ and fixed rotation frequency $(f = 10\,MHz)$. Both domain wall velocities oscillate between ~ 105 m/s to ~ 270 m/s with an average velocity of ~ 157 m/s, regardless of the vortex wall configuration (i.e head-to-head or tail-to-tail). We note that this average velocity is very close to the critical velocity that we observed in the symmetric ring geometry [24].

By direct observation of the internal spin structure of the domain wall via STXM we see a transformation of the domain wall configuration from a stable vortex domain wall to a metastable transverse domain wall at approximately $-10°$, see figure 4.5, snapshot $t = 78\,ns$. This domain wall spin structure transformation reveals the existence of the Walker breakdown phenomenon in our experiment. Similar to what has been reported in our previous study in symmetric ring

structures, the vortex domain wall transforms into a transverse domain wall by the expulsion and re-nucleation of the vortex core during the periodic change of the spin structure, which can only be observed through direct dynamic imaging [24]. This was shown in figure 4.5b, which consist of a series of snapshots of the domain wall propagation with a 2 ns time resolution. The vortex core is expelled at the outer edge of the ring structure and the vortex domain wall transforms into a transverse domain wall at $t = 78\,ns$. Then, the vortex core is re-nucleated at the same outer edge of the ring structure while conserving the same vortex core polarity.

Furthermore the chirality of the vortex domain wall is conserved during the Walker transformation in curved nanowires with rotating fields, which is in contrast to domain wall propagation above the Walker breakdown in straight nanowires, where both the polarity and the chirality of the transformed vortex wall alternate periodically [26]. The observed chirality conservation of vortex domain walls before and after the Walker breakdown can be explained by the strong correlation between the vortex chirality and sense of rotation. This confirm our previous observation in symmetric rings [118], where the sense of the rotating field controls the domain wall chirality due to the interplay between a dynamic distortion of the vortex domain wall structure and the radial magnetic field. We note that the backward propagation of the domain wall during the Walker breakdown (negative velocity) was not observed in this experiment within our 2 ns temporal resolution. This indicates further differences in behavior between domain wall dynamics in curved structures in comparison with straight nanowires. However, we also see a significant drop in the local domain wall velocity (down to ~ 107 m/s), which is approximatively a global velocity minimum, as highlighted in purple in figure 4.5a. Intuitively, this results in a big phase difference relative to the position of the rotating field vector figure 4.2a.

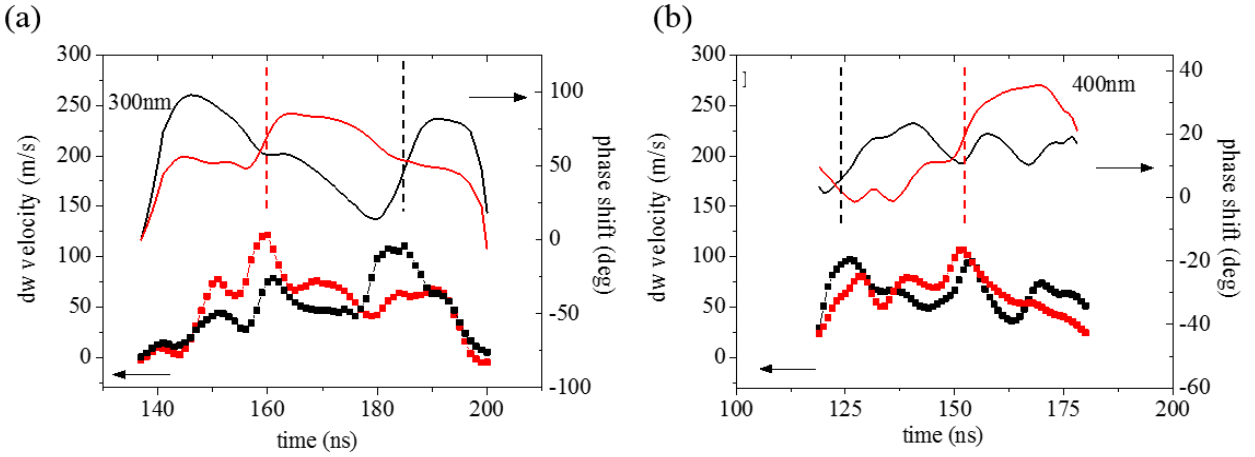

Figure 4.4: Micromagnetic simulation, domain wall velocities and phase differences are plotted as a function of time. The black and red curves correspond to the head-to-head and tail-to-tail vortex domain walls, respectively. The dashed vertical lines represent the time when the domain wall of the corresponding color (head-to-head and tail-to-tail) crosses the widest part of the asymmetric ring. Clockwise field rotation with rotation frequency of 10 MHz in 300 nm sample **(a)** and 8.31 MHz in 400 nm sample **(b)**. Both graphs show a similar behavior to the 500 nm ring presented in figure 4.2a. These calculations has been obtained with the help of Dr. Krüger and Dr. Richter.

III.1. Walker Breakdown influence

By taking into account the inhomogeneity of the domain wall potential landscape, one could explain the existence of the Walker breakdown at the ring position $\sim -10°$, indicated by the purple rectangle in the ring schematic inset in figure 4.5. As described above, the local forces resulting from the spatially dependent domain wall energy roughly scale with the gradient of ring width. Therefore such forces are expected to reach a maximum at the highest ring-width gradient position. We note that this ring position $\sim -10°$ illustrated in the ring schematic inset of figure 4.5 is equivalent to the ring position $\sim -45°(\equiv 315°)$ represented in figure 4.1a, which is characterized by the highest ring width gradient ~ -4.36 nm/deg.. For instance, when the domain wall crosses this region, during propagation along the ring with a counter clock wise sense of rotation, the local forces resulting from the decrease of the of the domain wall energy assist the acceleration of domain wall in such a way the domain wall experiences the Walker breakdown. This is directly observed employing STXM and visualized in the series of snapshots shown in figure 4.5b. As mentioned above, the repetition rate of the stroboscopic experiment was 832 kHz, and the transmission signal was recorded over more than 10^9 consecutive pulse cycles of the motion. Therefore the spatial control of the Walker breakdown by the inhomogeneous potential landscape is highly reliable and reproducible. This process is illustrated in figure 4.5a (purple areas) where domain walls experience the Walker breakdown each time they cross the highest ring-width gradient position ~ $(-10° \equiv 350° \equiv 710°)$ where the local velocity is minimum.

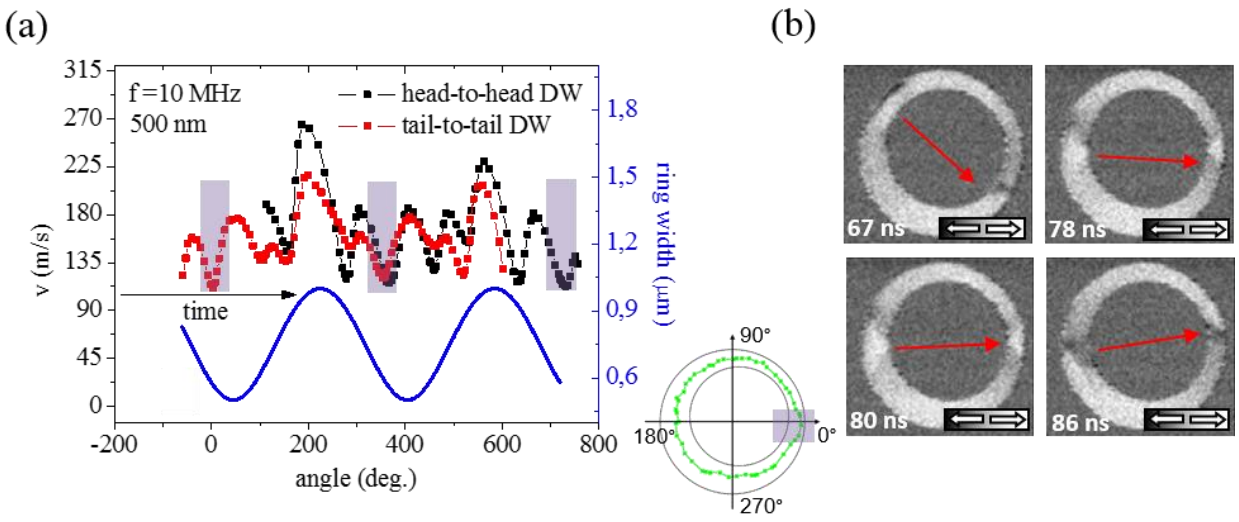

Figure 4.5: (a) Same domain wall velocity profiles as these presented in figure 4.2a, however here they are plotted as a function of the azimuthal angle. Purple rectangle indicates the position of the Walker breakdown. **(b)** A series of time-resolved XMCD-STXM snapshots at $\mathbf{t = 67, 78, 80, 86\ ns}$, visualizing the Walker breakdown during a 10 MHz rotating field burst pulse with an amplitude of $\boldsymbol{B = 6.8\ mT}$. The inset presents a schematic of the ring illustrating the trajectory of the domain wall center, in green, as extracted from the time resolved movie. Adapted from [114].

We note that in domain-wall-based devices the Walker breakdown normally results in irreproducible motion and is detrimental to the performance and functionality of the proposed device. Therefore many efforts and methods has been applied to suppress the breakdown which have been demonstrated in simulation [90, 119] and experiment [120], in order to stabilize the local velocity in straight wires. However in our asymmetric ring system the existence of the Walker breakdown is surprisingly associated with a good reproducibility of the local domain wall velocity, independent of the domain wall type. This is manifested in figure 4.5a at ~ 350°, where the local velocities of both domain walls (tail-to-tail and head-to-head) are roughly the same and perfectly synchronized.

On the other side, when both domain wall types have a vortex spin structure which means that the domain wall propagation is below the Walker breakdown, the difference between their velocities is larger.

III.2. Discussion of the relevant forces leading to velocity oscillation:

These periodic oscillations of domain wall velocity occurring below the Walker breakdown present a general feature of the domain wall propagation in curved geometries, which can be attributed to the two-dimensional motion of a vortex wall, due to different forces acting on it, as well as to extrinsic pinning due to imperfections in the nanowires [24]. However, in contrast to the symmetric ring systems, the amplitudes of oscillations are not constant, but modulated by the geometry as we observe a global maximum domain wall velocity in the widest part of the ring figure 4.5a. The underlying mechanisms of this behavior can be explained by considering the forces that act on the vortex domain wall spin structure.

In general, for non-zero phase difference, θ, during the field driven domain wall motion in asymmetric rings, there are five forces acting on the vortex domain wall spin structure, three of which are radial and the other two are tangential forces, which act as an azimuthal driving force, as schematically illustrated in figure 4.6. The tangential component of the driving rotating field,

$$B_t = B \sin\theta \, ,$$

acts both as an azimuthal driving force moving the wall circularly along the ring structure and as a radial force $\mathbf{F_t}$ on the vortex core [26]:

$$\mathbf{F_t} = c\pi M_S L R_V B_t \hat{\mathbf{e}}_\mathbf{r} \, ,$$

where c is the chirality of the vortex, M_S is the saturation magnetization, R_V is the radius of the vortex spin structure and L its thickness. It is obvious that the radial force, $\mathbf{F_t}$, is proportional to B_t, which in turn depends on the phase shift, θ. A second radially acting force is the gyroforce,

$$\mathbf{G} \times \mathbf{v} ,$$

where **G** is the gyrovector [121, 122] which points anti-parallel to the vortex core polarity, p, and **v** is the velocity vector of the domain wall. In the case of a counter clock wise rotation with a positive phase difference and for $p = +1$, the gyroforce points parallel to $\mathbf{F_t}$, as seen in figure 4.6b. The third radial force that acts on the vortex core is the restoring force, F_{res}, resulting from the shape anisotropy, which pushes the vortex core toward the center of the nanowire and depends on the radial vortex core position as well as the ring width and material. Finally, a fifth force that acts on the vortex domain wall is the force resulting from the asymmetrical shape of our ring structure,

$$\mathbf{F_U} = -grad\ U .$$

This force results from the inhomogeneous potential landscape of the domain wall energy, U, in the asymmetric ring, is as a local force, proportional to the width-gradient of the ring. Thus it is dependent on the angular position of the domain wall (figure 4.6c). We note that the interplay between the domain wall spin structure and these forces leads to oscillating domain wall propagation below the Walker breakdown, as we previously described in reference [24] in symmetric rings.

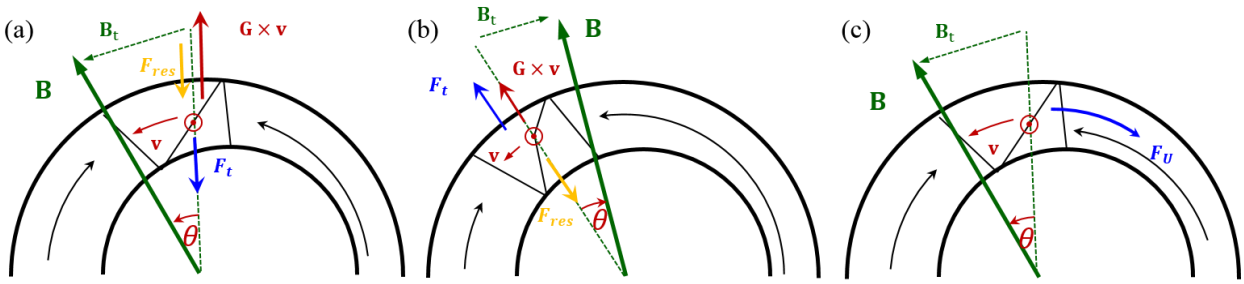

Figure 4.6: Schematic illustration of the relevant forces that act on the vortex domain wall spin structure during counter-clockwise propagation. **(a)** Illustration of the forces acting radially on the vortex wall for a negative phase difference $\boldsymbol{\theta}$. The gyroforce $\mathbf{G} \times \mathbf{v}$ (red), the radial force $\mathbf{F_t}$ (blue) is resulting from the tangential field component of the field $\mathbf{B_t}$ and finally the restoring force $\mathbf{F_{res}}$ (yellow) resulting from the shape anisotropy that pushes the vortex core to the center of the wire. **(b)** Relevant forces in the case of a positive phase difference. **(c)** Illustration of the tangential forces only: The shape force $\mathbf{F_U}$ (blue) resulting from the inhomogeneous potential landscape of the domain wall energy in the asymmetric rings. This force is characterized as a local force proportional to the width-gradient of the ring. Finally the tangential force $\mathbf{B_t}$ driving the wall circularly, resulting from the driving field, which is proportional to the phase difference.

III.3. Vortex Core Trajectory

By direct imaging of the domain wall dynamics we are able to track the time dependent position of the domain wall and extract its complete trajectory. In contrast to the observed domain wall trajectory in symmetric rings, the radial oscillations of the vortex core below the Walker breakdown are surprisingly missing. The domain wall trajectory displays a quite perfect circular shape, as shown in the ring schematic inset in figure 4.5. We note that the trajectory is reproducible for both domain walls and for more than one full domain wall rotation along the ring.

The observed behavior can be in general explained by the radial forces acting on the vortex core, and in particular by the radial force, $\mathbf{F_t}$, which is the only radial force that shows a different behavior than in the symmetric ring system [24]. This is due to the fact that $\mathbf{F_t}$ depends on the well-controlled phase difference, which alternates sign in our system (as discussed above), resulting in a switching of the radial force, $\mathbf{F_t}$, direction. Therefore the observed effect can be explained in terms of a control of the phase shift (figure 4.2a) due to the inhomogeneous shape of our ring sample. This effect seems to be sufficient to prevent the large radial oscillations of the vortex core trajectory seen in symmetric rings [24]. This effect leads to a minimization of the velocity fluctuations and pinning at the natural random defects at edges of the wire, since the trajectory of vortex core is confined to the center. Therefore the suppression of the radial oscillations of the domain wall during its propagation represent a very important result and demonstrate a further step towards the stabilization of local domain wall propagation in nanostructured devices.

However despite the fact that the radial motion of the vortex core is almost eliminated in our measured system, the domain wall velocity exhibits local oscillations. In contrast to the velocity oscillation of the domain wall presented in symmetric rings resulting from intrinsic effects, in our case these oscillations must result from the variation of the ring width which is related to the varying tangential force arising from the non-zero phase difference. This can be easily understood, since the radial motion of the vortex core is suppressed and thus the radial forces acting on the domain wall can be excluded and only the tangential forces are considered. This represents a great result since these latter effects which lead to these domain wall oscillations can be extrinsically tailored and controlled by the geometry of the structure.

For example, as discussed above, when a domain wall propagates from the widest to the narrowest part of ring, the phase shift is positive due to the local tangential force, $\mathbf{F_U}$, resulting from the asymmetrical shape of the ring structure, which assists the driving rotating field in this case. This force results from the inhomogeneous potential landscape of the domain wall energy in the asymmetric ring, which is characterized as a local force, proportional to the width-gradient of the ring. We note that the domain wall continues to increase its velocity by reducing the negative value of the angle, θ, thus has a negative phase difference, because the domain wall is moving faster than the driving field, and reaches its maximum velocity at the moment where the phase shift value is equal to zero, as seen in figure 4.2a (black curve at $t = 46\,ns$ or $t = 138\,ns$). At

this moment where the domain wall has overtaken the rotating field and the phase shift starts to switch to a positive value, the domain wall is moving faster than the driving field, however the driving force starts to decelerate the domain wall as schematically illustrated in figure 4.6b. Therefore one can find a drop in the domain wall velocity after each increase of the positive phase shift value and conversely each drop in the positive phase shift is followed by an increase in the local domain wall velocity. Hence the maximum velocity deceleration is reached, and thus the velocity has a local minimum, when the positive phase difference reaches a local maximum (as seen in figure 4.2a black curve at $t = 52\ ns$ or $t = 150\ ns$).

On the other hand, when the domain wall moves from the narrowest to the widest part, the phase difference is negative and the local tangential force, $\mathbf{F_U}$, is pointing against the driving rotating field. In this case the absolute value of the negative phase shift is increasing since the domain wall velocity is lowest, therefore when the phase difference is largest the driving force is maximal (figure 4.6a). Hence the domain wall accelerates, again leading to an increase of the local velocity of the domain wall. This behavior is directly observed by our time-resolved imaging of the domain wall dynamics, where we were able to extract the velocity profile of the domain wall presented in figure 4.2a. Here one can clearly deduce that the increase of the local domain wall velocity is followed by the increase of the absolute value of the negative phase difference (see figure 4.2a at $t = 96\ ns$).

At the moment where the domain wall crosses the symmetry axis of the ring (i.e. the ring position where the width gradient is equal to zero) the force, $\mathbf{F_U}$, resulting from the inhomogeneous potential landscape becomes zero. Here the stored Zeeman energy is responsible for the acceleration of the domain wall, due to the energy transfer between Zeeman and dipolar energy, which due to the interplay between the dynamic field and the inhomogeneous potential landscape (as visible from the phase shift). We note that in the case where the domain wall is crossing the widest part of the ring, the negative value of the phase shift accelerates the domain wall as discussed above, however here the effect is much stronger than in the other parts of the ring having a negative sign of phase shift. Therefore the domain wall velocity reaches a global maximum (~230 m/s) in the widest part of ring (~ 225° in figures 4.5a and 4.7a). This latter result is in contrast to the intuitive expectation in the case we only considered the local forces resulting from the potential landscape due to the shape variations, since the domain wall energy, *U*, in the widest part is the highest. The global maximum velocity presented in the widest part of the ring demonstrates that it is not only the local forces the resulting from the shape that should be taken into account here, but also the alternating behavior of the phase shift and the fact that in the widest part there is less geometrical confinement in comparison with the narrowest part of the ring.

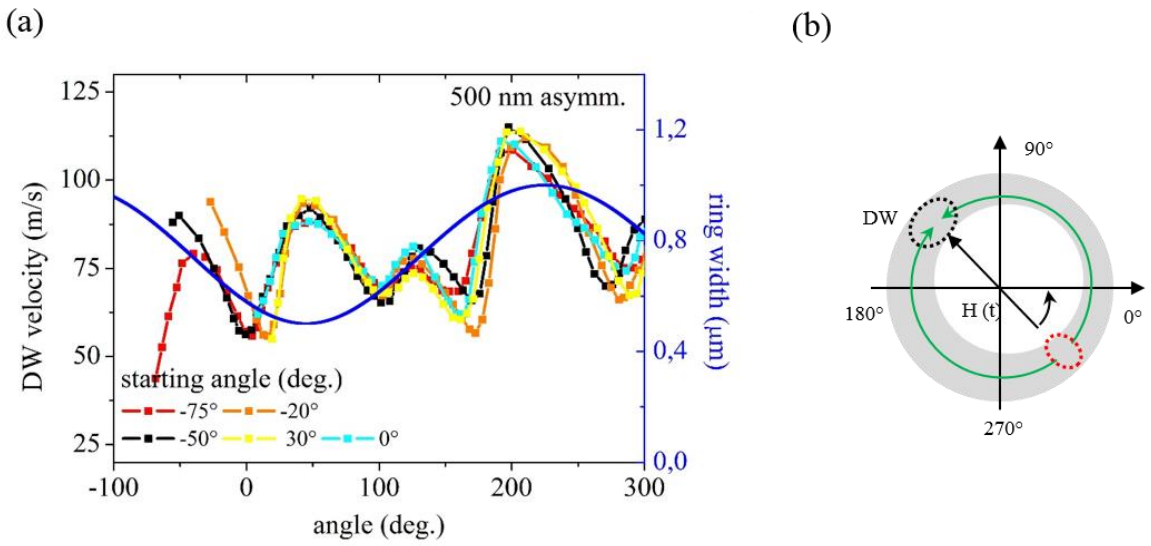

Figure 4.7: (a) Domain wall velocity profile for different starting angles in a 500 nm asymmetric ring plotted as a function of the domain wall azimuthal coordinate illustrated in the figure, recorded for a full field rotation at $f = 10$ MHz with counter clockwise sense of rotation. The blue solid line represents the ring width [114]. **(b)** Schematic illustrating the ring geometry. The black (red) ellipse represents the initial position of the head-to-head (tail-to-tail) domain wall at t = 0 ns.

III.4. Spatial synchronization of domain wall dynamics

We have explained above that in our case the oscillations of the domain wall velocity most likely results from the variation of the ring width which leads to the varying tangential force arising from the non-zero phase difference, and not from the radial motion of the vortex core which is suppressed by the inhomogeneous potential landscape. This can be additionally confirmed here by the observed strong correlation between the local domain wall velocity and the phase difference. This latter proves that the key driving force in our observed dynamics has a tangential direction resulting from the phase difference between the domain wall and the field positions and depends on its relative orientation. We note that the observed velocity profiles of the domain wall shows a good reproducibility between the first and the second subsequent rotation of the magnetic field, as can be inferred from the black curve in (figure 4.2a at 48 ns – 96 ns and 130 – 180 ns).

Furthermore, by plotting the velocity profiles of both tail-to-tail and head-to-head domain walls, propagating in the ring as a function of the angular azimuthal coordinate we can clearly infer that the local domain wall velocities are very similar to each other (figure 4.5a). This observation is in contrast to our obtained results for the same field rotation frequencies (10 MHz) in the symmetric ring systems which have comparable dimensions of our asymmetric ring geometry [24]. Since we have demonstrated that for a driving field with an amplitude of 6.8 mT and rotation frequencies above 7 MHz the domain wall velocity oscillates because of the intrinsic periodic domain wall

spin structure changes, there is no indication of extrinsic pinning. In other words we demonstrated that in this freely and intrinsically oscillating domain wall propagation regime, domain walls propagating for a complete field rotation with different start and stop angles show two different velocity profiles when plotted as a function of the domain wall azimuthal coordinate [24].

Therefore in order to identify the mechanism of such a spatial synchronization of domain wall dynamics, we recorded the local domain wall velocity for a complete field rotation with different start angles, where domain walls are initially nucleated, as shown in figure 4.7. In this figure we observe that initially the velocity profiles are different, however once the domain wall passes through the narrowest part of the ring presented at $\sim -45°$, all local domain wall velocities synchronize spatially and their values become quite similar. This behavior can be explained by the interplay between the forces resulting from the Zeeman energy and the local forces arising from variations of domain wall energy due to the inhomogeneous ring width. We note that these energies represent two reservoirs for the domain wall energy, which interact with each other during the propagation. For instance, when the domain wall crosses the narrowest part of the ring the force, $\mathbf{F_U}$, resulting from the inhomogeneous potential landscape, vanishes. The field continues rotating toward the widest part of the ring, which leads to an increase of the domain wall energy and results in a non-zero value of $\mathbf{F_U}$, oriented against the propagation, as a restoring force toward the narrowest part of the ring. This force will be balanced by another arising opposing force resulting from $\mathbf{B_t}$ (Zeeman energy) due to the rapid increase of the phase shift. Therefore, the stable domain wall propagation in areas of non-constant ring width can be obtained through the presence of these two energy reservoirs. In conclusion the spatial synchronization of domain wall velocities can be engineered by tailoring the potential landscapes in the ferromagnetic rings.

III.5. Micromagnetic simulation results

In order to understand the contribution of the inhomogeneous shape of our ring structure in controlling the domain wall potential landscape that go beyond the simple one-dimensional model framework quantitatively, we performed a series of micromagnetic simulations using MicroMagnum software [123]. The dimensions of the simulated ring are the same as in the experiment which consist of an outer diameter of 5.5 µm and non-centered inner diameter of 4 µm, a permalloy thickness of 30 nm and a cell size of $5 \times 5 \times 30$ nm^3. The material parameters used are typical for permalloy [124]: saturation magnetization, $M_S = 800 \times 10^3$ A/m, exchange stiffness $A = 1.3 \times 10^{-11}$, damping parameter $\alpha = 0.008$, no uniaxial anisotropy.

We note that the proper dimension of the grid size is defined based on the *exchange length*, $l_{ex} = \sqrt{2A/\mu_0 M_S^2}$, which depends on the magnetic properties, for more details see chapter 1. For instance, in our case the *exchange length*, $l_{ex} \geq 5\,nm$, which is typical for permalloy. The exchange length determines the characteristic length scale over which the exchange interaction is dominant. Thus, the magnetization is spatially uniform, over ~ l_{ex}. Therefore, the cell size, in a micromagnetic framework, has to be smaller than l_{ex} and at the same time not too small in order

to reduce the simulation time and be consistent with the mesoscopic approximation of the model [125].

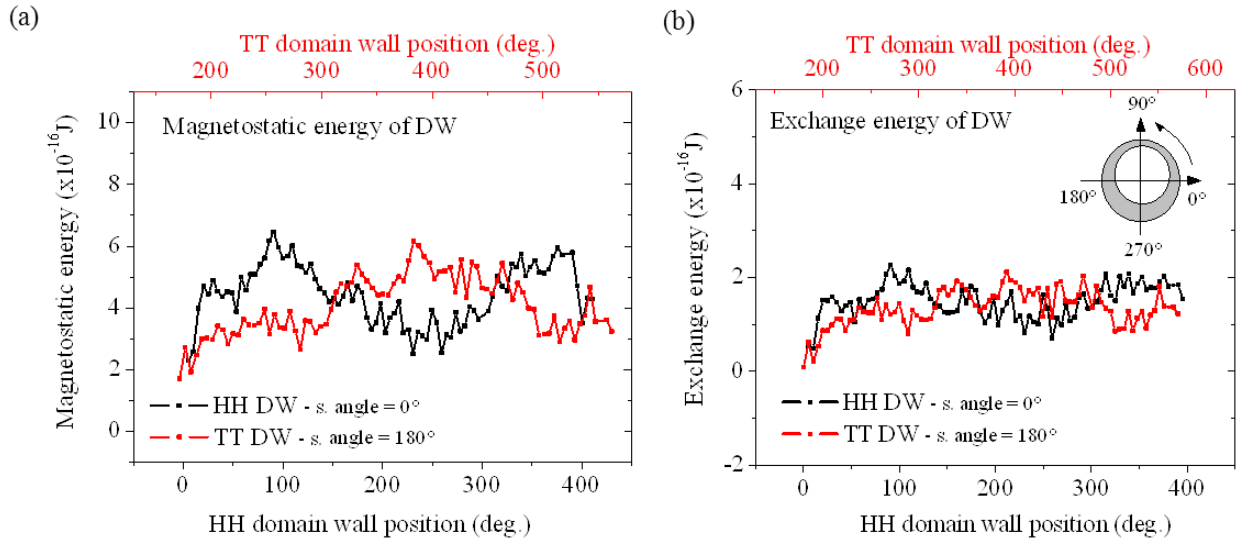

Figure 4.8: contribution to the domain wall energy in asymmetric ferromagnetic rings (500 nm width in the narrowest part) as a function of domain wall position. The black and red curves correspond to the head-to-head (HH) and tail-to-tail (TT) vortex domain wall configuration, respectively. The energies are obtained from micromagnetic calculations, by propagating the domain wall along the ring with a field pointing along different directions with an amplitude of 2600 A/m, which corresponds to the field strength used in the experiment. **(a)** Domain wall exchange energy and **(b)** domain wall magnetostatic energy. Adapted from [114].

Here the domain wall configuration under discussion is the vortex domain wall in the two-dimensional model [126], where the vortex domain wall can be understood as a composite quasi-particle with a central vortex core that is surrounded by a magnetization curling in-plane (see chapter 1). The rotational sense of this in plane component, could be either counter-clockwise or clockwise, defining the vortex chirality $c = +1$ or $c = -1$, respectively [118]. The magnetization component of the vortex core points out of the plane in order to reduce the exchange energy [127], defining the vortex core polarity p, which is either anti-parallel ($p = -1$) or parallel ($p = +1$) to the z-direction. In our case for the two vortex walls in the ring we have $p = +1$, $c = \pm 1$, which means that both domain walls have the same polarity and opposite chirality. The knowledge of the field rotation leads to certain well-defined chirality configurations, as we recently reported in reference [118]. For counter-clockwise (clockwise) the head-to-head domain wall has $c = -1$ ($c = +1$) and the tail-to-tail domain wall has $c = +1$ ($c = -1$). Note that in symmetric onion state, the two diametrically opposed vortex domain walls always have opposite chirality [118]. The rotating magnetic field burst pulses are chosen as in the experiment (counter-clockwise sense of rotation). The field strength is 2600 A/m with a rotation frequency of $f = 10$ MHz. The position of the vortex core was extracted by fitting a Gaussian through the M_Z (out-

of-plane) component of the magnetization. In general, such micromagnetic simulations of curved geometries lead to artifacts due to the cubic discretization of a curved surface that can entail artificial pinning at the edges of the nanoring. Therefore we define a smooth profile of the saturation magnetization along the edges of the nanoring to reduce this pinning.

The contributions to the domain wall energy in asymmetric ferromagnetic rings are plotted as a function of the domain wall position in figure 4.8. The inset shows the ring width at different azimuthal positions for each domain wall during the propagation, which helps to illustrate the correlation between the domain wall energy and the shape of the nanoring during propagation. By considering the magnetostatic energy of the domain wall, we observe a significant difference between the energy values in the widest and narrowest part of the ring (figure 4.8a). On the other hand, a much smaller dependence is seen for the exchange part of the domain wall energy in relation to the ring width (figure 4.8b). This latter is in good agreement with the logarithmic dependence of exchange energy on wire width obtained in similar studied systems [10, 128]. As for a vortex domain wall structure, this is a reasonable result, since the exchange energy contributes roughly 20% of the total domain wall energy, independent from the ring width at the position of domain walls [10].

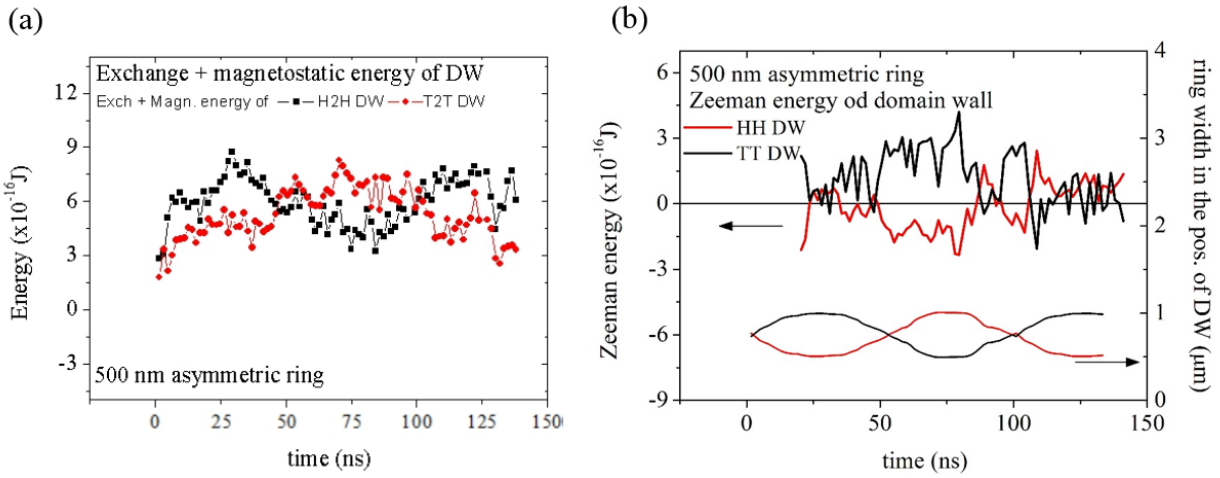

Figure 4.9: Domain wall energetics in an asymmetric ferromagnetic ring (500 nm width in the narrowest part) as a function of time. **(a)** The sum of the domain wall energies, magnetostatic and exchange energy, presented in figure 4.8. **(b)** Zeeman energy of the domain wall generated by the phase difference of the domain wall in the presence of an applied field of 2600 A/m. The curves at the bottom of the graph represent the ring width at the position of the domain wall during the propagation. The alternating behavior between the Zeeman energy and the total domain wall energy represents the energy transfer between both energy reservoirs. These calculations has been obtained with the help of Dr. Krüger and Dr. Richter.

The sum of the magnetostatic and the exchange energies displays a global maximum in the widest part, whereas the total domain wall energy is the lowest in the narrowest part of the nanoring, thus the sum of these energies roughly scales with the ring width (figure 4.9a). This

result is expected since the domain wall size in the widest part is larger than in the narrowest part. This is a direct demonstration that the inhomogeneous potential landscape result from the asymmetrical shape of the ring and the domain wall energy is directly proportional to the variation of the ring width (figure 4.9). Similar qualitative simulation results were obtained for all studied ring geometries. Note that the total domain wall energy shown in figure 4.8a represents the spatial variation of the domain wall energy, U, which lead to the local force, $\mathbf{F_U}$, proportional to the width-gradient of the ring.

On the other hand by considering the performed series of micromagnetic simulations of domain wall dynamics, it is possible to demonstrate whether the spatial control of the phase shift and the correlated domain wall velocity oscillations observed in the experiment, are related to the natural extrinsic pinning sites, or whether they result from the sample fabrication. The obtained micromagnetic simulation results, the phase difference and the velocity profile of the domain wall dynamics in a 500 nm asymmetric ring are presented in figure 4.10. As mentioned above, the rotating magnetic field burst pulse is chosen to be similar to the experiment (counter-clockwise sense of rotation), with a field strength of 2600 A/m and a rotation frequency of $f =$ 10 MHz. The figure shows that the phase shift is strongly correlated to the shape of the ring. This is very similar to the observed result in the experiment, even though the micromagnetic simulation dynamics are performed in defect-free systems, as described above. This simulated result demonstrates that the inhomogeneous potential landscape leads to a maximum domain wall velocity in the widest part of ring, where the sign of the local force is switched, confirming the observation in the experimental results.

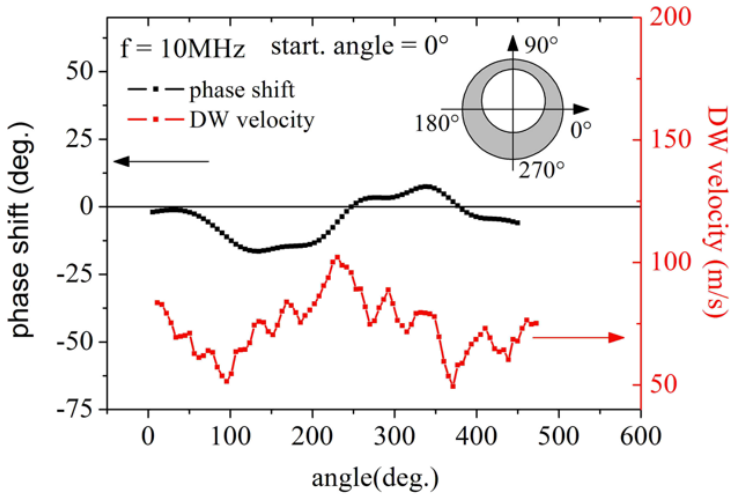

Figure 4.10: Domain wall velocity (red) and phase difference (black) plotted as a function of the domain wall azimuthal coordinate, illustrated in the inset schematic of the ring shape, obtained from micromagnetic simulation of domain wall motion in a 500 nm asymmetric ring [114].

IV. Conclusion

In conclusion, we have directly imaged controlled domain wall propagation in asymmetric ring structure driven by rotating magnetic fields.

The observed periodic oscillations of domain wall velocity occurring below the Walker breakdown present a general feature of the domain wall propagation in curved geometries, which can be attributed to the two-dimensional motion of a vortex core of the vortex wall, due to different forces acting on it. The relevant forces are proportional to the applied field and the geometry of the inhomogeneous ring which leads to a spatially dependent domain wall potential landscape with a minimum domain wall energy, *U*, in the narrowest part of the ring and maximum velocity in the widest part.

The pump and probe experiment of domain wall propagation driven by a rotating magnetic field demonstrates that the observed oscillatory velocity profile can be tailored by the variations of the domain wall potential landscape, leading to a global maximum velocity in the widest part of the ring. This behavior can be explained by the interplay between the forces resulting from the Zeeman energy and the local forces arising from variations of domain wall energy due to the inhomogeneous ring width.

Furthermore, the inhomogeneous domain wall potential landscape stabilizes the radial motion of the vortex core in the domain wall, keeping the internal spin structure constant and leading to the observed circular trajectory of the vortex core. Therefore the oscillations must result from the variation of the ring width which is related to the varying tangential force arising from the non-zero phase difference, since the radial forces acting on the domain wall can be excluded and only the tangential forces should be considered. This is an important result since the latter effects, which in our case lead to these domain wall oscillations, can be extrinsically tailored and controlled by the geometry of the structure. The minimum of the domain wall energy landscape presented in the narrowest part of ring leads to the spatial synchronization of domain wall velocities. This means that even for domain walls starting at different positions, the velocities can be reliably and reproducibly controlled, by tailoring the potential landscapes in the ferromagnetic rings.

Finally, by performing a series of micromagnetic simulations on defect-free systems, we demonstrate that the spatial control of the phase shift and the correlated domain wall velocity oscillations observed in the experiment, are not related to the extrinsic pinning sites, resulting from the sample fabrication. We have demonstrated as well that all micromagnetic simulation results are consistent with the experimental observations and explain the velocity oscillations from the energetics of the asymmetric potential landscape.

Chapter 5

Domain wall automotion induced by geometrical effects in asymmetric ferromagnetic rings

Abstract

In contrast to field- and spin transfer- driven domain wall motion, automotive propagation is the displacement of a magnetic domain wall due to the influence of the demagnetization and exchange energy present in nanoscale spintronic devices. These latter occur without the presence of external stimuli, such as magnetic fields or spin-polarized charge currents, leading to motion which is instead resulting from the topological interaction between domain walls and an energy gradient associated with the spin structure change when the geometry is changing. Thus by relaxing an excited system, the stored energy can move the domain wall, which leads to a new concept of so-called automotive domain wall motion. In this chapter, we report a direct dynamic experimental visualization of spontaneous domain wall propagation in asymmetric ferromagnetic rings, with different widths in the narrowest part, without the existence of an external driving magnetic field. Surprisingly, even at zero external magnetic field, we observed domain wall automotion with an average velocity of about ~ 60 m/s, which is a significant speed for spintronic devices based on domain wall dynamics. We show that the domain wall inertia and the stored energy allow the walls to overcome both the local extrinsic pinning and the topological repulsion between domain walls. Our experimentally obtained angular dependencies of spontaneous domain wall velocities can be explained based on the minimization condition of the magnetostatic and exchange energies. Micromagnetic simulations have been carried out for magnetic rings with different dimensions. In addition to providing visualization of the spin structure for comparison with the experimental results, micromagnetic simulations help to investigate the detailed intrinsic spin structure changes and their contribution to the domain wall dynamics. We demonstrate that both simulation and experimental results are qualitatively consistent with one another.

This chapter is arranged as follows. In Section I we motivate and introduce the work. In Section II we present our sample and experimental approach. In section III we present our experimental and micromagnetic results. All the results is compared and discussed in section IV and finally in Sections V we summarize the work.

I. Introduction:

Geometrically confined magnetic domain walls in magnetic nanostructures have recently become the focus of intense scientific interest. Due to the geometrical constraints of the magnetic nanostructure, different types of domain walls can occur in comparison with the bulk and continuous films. The spin structure of such domain walls, e.g. 180° head-to-head walls, are usually dominated by the geometrical environment rather than by the material properties as is the case for bulk material [64, 129-133]. This indicates that by changing smoothly the geometrical parameters we can easily tailor domain wall properties, which is an alternative to including notches within the nanostructure [133, 134] (see chapter 4). It is well known, from a fundamental physical point of view, that the domain wall types are formed to minimize the energy terms (exchange, magnetostatic, and anisotropy) which govern the magnetization configurations in small magnetic structures (see chapter 1). Therefore, studying the geometrical dependence of the domain wall propagation, allows for a deeper understanding of the interplay between the different energy terms and the resulting propagation of the domain wall**.**

Recently, the study of ferromagnetic nanorings has started to draw the attention of numerous research efforts, due to the promise shown by flux-closure states (vortex states) for spintronics applications due to the potential for high memory densities and their expected stability. In magnetic structures the magnetic configurations are defined by the shape of the edges and are thus very sensitive to edge roughness and shape fluctuations, due to the demagnetization field induced by dipolar interactions close to the edge borders. These effects lead to some complexities in the switching mechanism of these elements. In circular structures, one proposed method to overcome such complications is by using the magnetic flux closure (vortex) state where the edge roughness does not significantly affect behavior. This vortex state has been proposed for use in magnetic random access memories in rings [108]. Asymmetric ferromagnetic nano-rings represent one candidate geometry for such applications because they exhibit a very stable vortex state, where the direction of the spins is aligned with the ring edges, either counterclockwise or clockwise [65, 135]. Furthermore the rings geometry is very useful for the study of domain wall propagation since it allows for a selective positioning of created domain walls by applying a saturated field along different angular directions. On relaxation of the magnetization from saturation, by removing the field, the magnetic configuration is transformed to the onion state with a tail-to-tail and head-to-head wall on opposing sides of the ring at the position defined by the applied field [64-66] (see chapter 2 - section V). This method of creating domain walls results in reproducible domain wall types for certain ring geometries even along different field directions and at room temperature. This simple method to control the domain walls position in rings is in contrast to the case with straight wires, where it is quite difficult to manipulate the domain wall position using an external saturating field.

Whilst the vortex state of the ferromagnetic ring structure has a lower energy than the onion state [136] depending on the geometry, the two states are separated by an energy barrier, resulting in two metastable configurations.

In the vortex state, two-fold degeneracy of the magnetization chirality (clockwise and counterclockwise) can be used to encode binary data bits. Furthermore these bits could be stored densely without any coupling between neighboring structures due to the absence of stray fields. Thus, many studies have been devoted to explore the vortex chirality in rings controlled by a uniform external magnetic field. It has been found that for symmetric rings, the orientation of the vortex cannot be manipulated by a uniform magnetic field [128], since the reversal mechanism from the onion (high-field) state to the flux closure (intermediate-field) state occur via domain wall motion at zero external magnetic field. In this process both domain walls in the ring move to each other and get annihilated, resulting a vortex magnetization state. In contrast in asymmetric rings, it is possible to easily control the vortex chirality by a homogeneous external field [128, 137, 138, 139], due to the interplay between different forces acting on the domain walls which can be found in such geometrical structures.

For instance local forces arise from the domain wall energy changes due to the non-constant ring width and there is the force resulting from the interaction between both domain walls, the so-called topological interaction [140, 141]. Since the head-to-head and tail-to-tail domain walls in magnetic nanowires behave in a similar manner to free magnetic monopoles carrying a single opposite magnetic charge, they attract one another. In the former case, the inhomogeneous ring width gives rise to a spatial energy dependence of the domain wall, U, which is expected to be lowest in the narrowest part of the ring and the highest in the widest part of ring (as discussed in see chapter 4).

To date, most studies have only investigated static properties of the vortex state. The direct observation of the dynamical switching and domain wall, propagation in curved wires is still lacking. Understanding the dynamics of domain walls in curved ferromagnetic geometries has attracted great attention from not only the fundamental point of view but also the technological point of view for spintronic devices based on the controlled motion of domain walls, such as magnetic memory and magnetic logic devices [71, 73, 142, 143]. Therefore numerous studies have been devoted to the understanding of the domain wall motion in ferromagnetic nanowires. So far most of these studies have focused on the domain wall propagation driven by spin torque [144] or by an external field along a straight nanowire [143, 73] and only recently, in curved nanowires [24]. It is worth mentioning that a few studies have reported a presence of automotive domain wall motion in ferromagnetic nanowire at zero applied external magnetic field [145, 146, 147]. As a definition, automotive propagation is the motion of a magnetic domain wall under the influence of the magnetostatic and exchange anisotropy presented in nanoscale spintronic devices, in contrast to external force driven domain wall motion (i.e via external magnetic fields or current induced domain wall motion). This concept attract large interest for the development of magnetic devices, since on the first hand automotion could be used to prevent or assist domain wall pinning at low driving fields [79, 148]. Furthermore it is an avenues for to the needed minimization of the energy consumption in the field of information technology (IT) based on spintronic interconnects where the inertial motion of the domain wall is due to its shape [149].

The domain wall propagation along any ferromagnetic nanowire includes, in principle, this automotion mechanism, since it contributes implicitly to the velocity of the domain wall in all cases, and therefore should not be neglected. Thus, in any experimental domain wall velocity measurement one should carefully analyze the results taking into account the automotive forces, although in the presence of fields, the resulting driving force from the Zeeman energy still constitutes mostly the main driving force.

While a series of theoretical studies predict the existence of the spontaneous domain wall motion at zero external magnetic field in a straight nanowire [146, 149], the experimental observation of this phenomenon has proven difficult due to the strong domination of the demagnetization field, and the natural roughness or defects resulting from the sample fabrication. Moreover, it is still not clear whether the reduction of Zeeman energy can be strong enough to overcome the barrier potential resulting either from the pinning centers or stray fields.

Here, we report a detailed study concerning the direct experimental visualization of the dynamic automotive domain wall motion in asymmetric permalloy rings, with different widths in the narrowest part, without the presence of external driving magnetic fields. Although the micromagnetic simulations provide a quantitative determination of the energy contributions, they are crucial to provide a comparison with the dynamic imaging experiment of the nanoscale spin structure for a better understanding of the involved energy landscape which allows us for the first time to directly check the previously reported predictions. We demonstrate that depending on the size and geometry of the rings, the automotion process occurs during the domain wall relaxation from the higher energy onion state to the energetically favored vortex state, where both domain walls annihilate. Moreover micromagnetic simulations have been carried out for asymmetrical rings with dimensions similar to the experimental systems. In addition the micromagnetic simulation allow us to investigate the intrinsic spin structure changes and their contribution to the domain wall dynamics, such as the topological structures of the vortex domain walls (i.e. the chirality and polarity).

The obtained experimental results of the angular dependencies of automotive domain wall velocities can be understood in terms of the minimization of the total energy of the system. For example, the magnetostatic energy originating from the long-range attractive interaction between walls is minimized since adjacent domain walls attract each other (when spaced further apart than their width) because they always carry opposite topological charges [140, 141]. Moreover, the energy originating from non-constant ring width resulting in a short-range local geometrical forces is also minimized. Finally we note that understanding the automotion process allows us to improve the control of the domain wall motion in the low field regime as well as the high field regime, where domain walls are driven by an external magnetic field since the automotion phenomenon is implicitly included. Hence, understanding the domain wall dynamics in curved nanowires potentially improves the performance of future spintronic devices based on domain wall motion.

II. Samples and experimental

We study asymmetric ferromagnetic permalloy rings which have of an outer diameter of 5.5 µm and non-centered inner diameter of 4 µm, and a thickness of 30 nm. Variation of domain wall potential landscape were introduced to the sample by this non-concentric geometry, where the inner circular cut-off is shifted with respect to the outer circular edge of the ring, making the width of the ring angularly dependent (Figure 5.1a). The ring dimensions, width and thickness, were chosen such that the vortex domain wall spin structure is the lowest energy magnetic configuration within the whole ring width [15]. The onion state was formed after saturation with a uniform external magnetic field [13, 66].

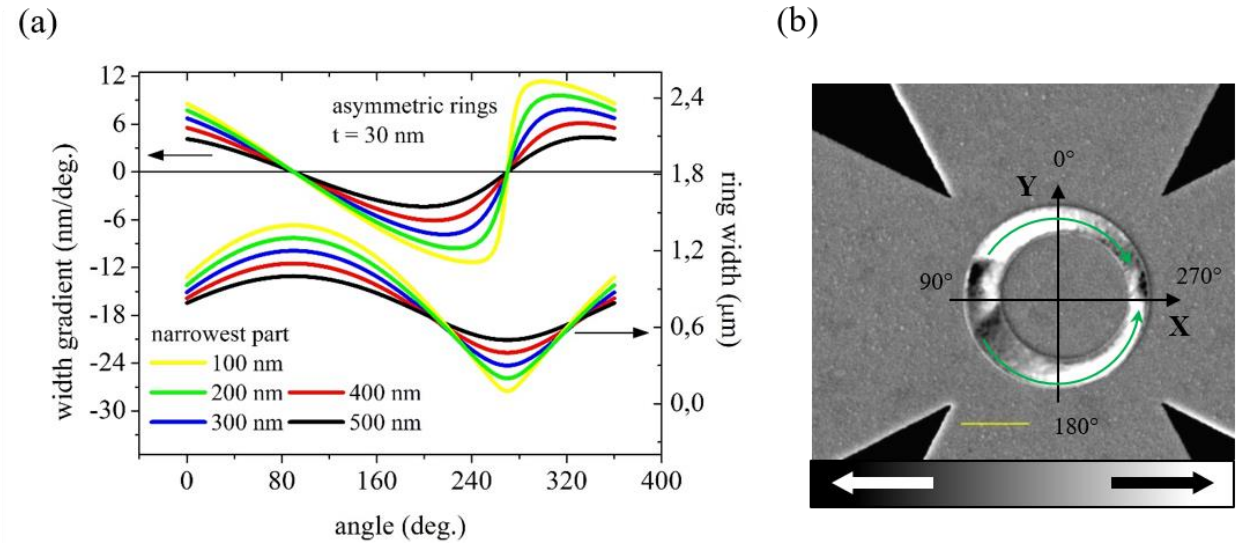

Figure 5.1: Schematic of the sample geometry and design used in our experiment. (a) Sample overview for different magnetic structures with narrowest widths of 100, 200, 300, 400 and 500 nanometers. Permalloy thickness t = 30 nm [114]. **(b)** Merged STXM-XMCD image of an asymmetric ring structure with a scanning electron micrograph image of the sample under investigation. The unidirectional in-plane magnetic field pulse is generated by burst current pulses, $I_{x,y}$, injected through one or both crossed-striplines, depending on the desired magnetic field orientation. Yellow scale bar indicates a distance of 2 µm. Black (white) contrast corresponds to magnetization pointing to the left (right), as illustrated by the green arrows.

Furthermore the permalloy thickness (30 nm) is chosen as a compromise considering four different effects: maximization of the XMCD contrast, ground state domain wall configuration, avoiding the formation of 360° domain walls that can occur in rings of smaller thickness [115] and lastly providing a relatively low depinning field for the domain wall motion [116].

Measurements of a series of samples which consist of permalloy asymmetric rings having different widths in the narrowest part (ranging from 100 nm to 500 nm with 100 nm step size), have been carried out in order to disentangle two influences on the domain wall dynamics: firstly,

the imperfection in the nanowire, such as the natural surface and edge roughness which gives rise to a position dependence of the domain wall energy, resulting in velocity variations because of extrinsic pinning. Secondly the effect of the irregular potential landscape on the domain wall automotion. This series of samples provides almost the same range of width gradients, ranging from -11 nm/deg. to 11 nm/deg. (as shown in Figure 5.1a). We note that here we refer to the widths in the narrowest part as a convention to name and differentiate between different ring structures. The samples were fabricated by a lift-off process using electron beam lithography (EBL) on 100 nm thick X-ray transparent Si_3N_4 membranes, with magnetic material deposition performed using molecular beam evaporation in an ultra-high vacuum (UHV) chamber. For the generation of the in-plane magnetic field pulses, a 150 nm thick copper (Cu) crossed stripline was fabricated on top of the magnetic structure, and capped by a 4 nm thick Au layer protecting the copper from surface degradation (see Figure 5.1b). The whole sample fabrication process was done through three successive steps, as described in chapter 2 - section II.

The time evolution of the magnetization dynamics is recorded stroboscopically via a pump and probe technique employing time resolved scanning transmission X-ray microscopy (STXM), with a sub 30 nm spatial resolution, at the MAXYMUS endstation, Helmholtz Zentrum Berlin, BESSY II, Germany (as described in chapter 2 - section IV). The in-plane magnetization component was imaged by tilting the sample surface normal by 30° with respect to the incident light direction. The contrast of the image is based on the X-ray magnetic circular dichroism (XMCD) effect [43]. The data were recorded at the Ni L_3-absorption edge (852.7 eV).

In this study, the pump consists of a repetitive unidirectional external uniform magnetic field excitation of the magnetic nanostructures, created by periodic current pulses through crossed micro-striplines in order to initialize the onion state [65]. The magnetic field orientation can be defined by the injection of the current pulses through one stripline or injecting simultaneously two burst pulses through the two ends of the orthogonal crossed striplines, see chapter 2 - section VI).

After each unidirectional magnetic field excitation (~20 ns) the ferromagnetic rings are then in the onion state, afterward the magnetic structures are relaxed and switch, through automotive domain wall propagation, to the lowest energy state (vortex state) on a time scale of a few tens of nanoseconds. We note that this annihilation process of the domain walls depends on different physical aspects (as discussed below). It is worth mentioning that the experiment is repeated at a repetition rate of 832 kHz and the transmission signal X-ray signal is recorded over more than ten billion subsequent pulse cycles, and hence domain wall propagation events, ensuring a high signal-to-noise ratio and demonstrating the reproducibility and the reliably of our measurement results.

III. Results

The experimental demonstration of automotion dynamics:

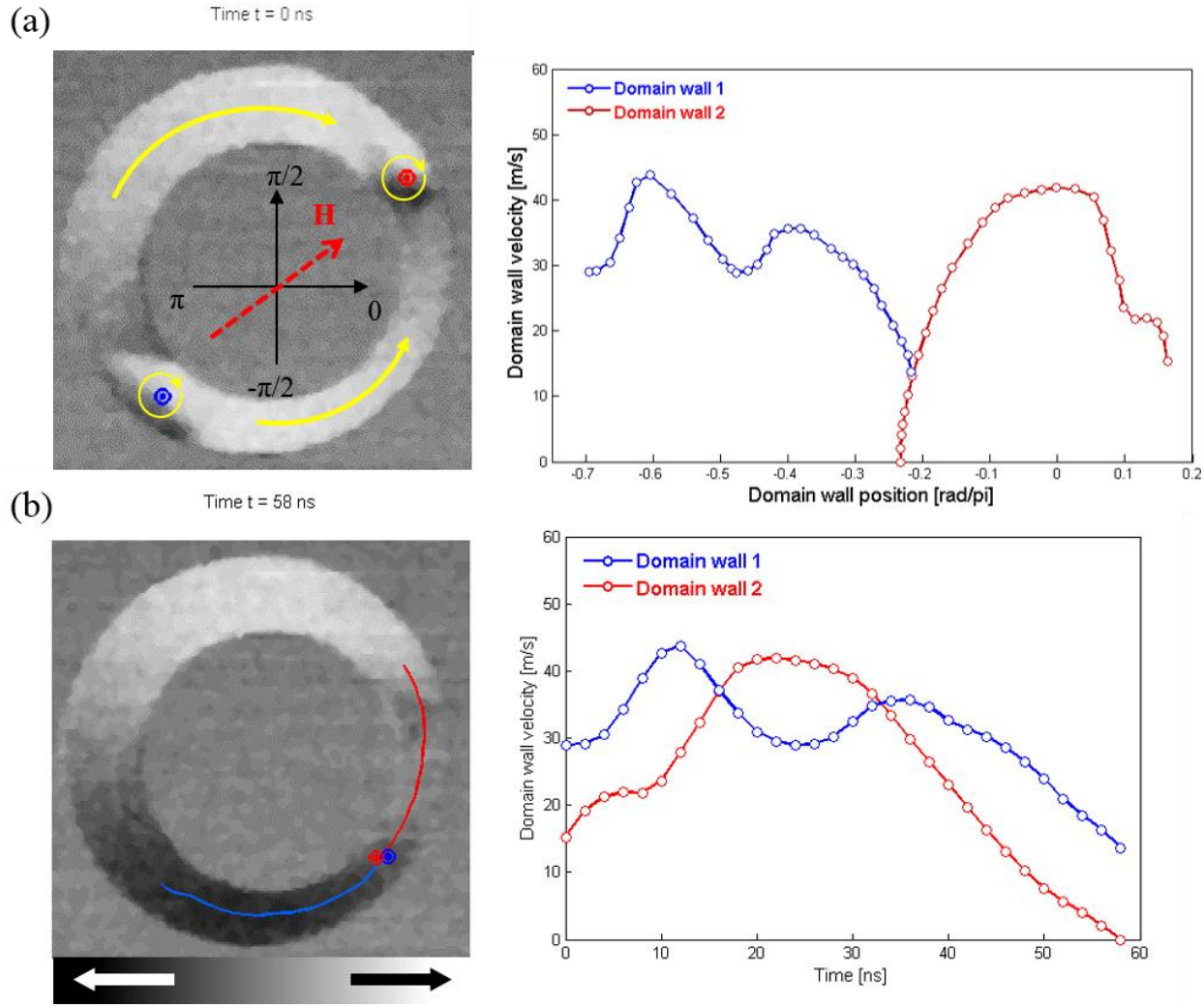

Figure 5.2: Automotive domain wall propagation in an asymmetric ring (500 nm): (a) Left: A time-resolved XMCD-STXM image at **t = 0 ns** showing the relaxed onion state after saturation with a uniform external magnetic field H (red arrow), along the asymmetrical axis of the ring (π/4). The vortex core polarity of both vortex domain walls ($\boldsymbol{p} = +\mathbf{1}$) is indicated in red (head-to-head) and blue (tail-to-tail). This image visualizes the magnetization state just before the start of the automotion process. The yellow arrows indicate the direction of the magnetization. **Right:** Domain wall velocities plotted as a function of the azimuthal angle. **(b) Left:** A time-resolved XMCD-STXM snapshot at **t = 58 ns** showing the vortex state (clockwise) after the annihilation process of the domain walls. Red and blue line illustrates the trajectory of the domain wall center, extracted from the time resolved movie. White (black) contrast corresponds to magnetization pointing to the right (left). **Right:** Domain wall velocities plotted as a function of time.

To investigate the automotion mechanism in detail, we dynamically imaged the propagation of vortex domain walls in a series of samples having different widths in the narrowest part (described above).

As a general description of the experiment, the ferromagnetic rings are initialized in the onion state, following a magnetic field excitation. Afterwards the magnetic structure is relaxed and switched, through automotive domain walls propagation, to the lowest energy state (vortex state) on a time scale of a few tens of nanoseconds. In the asymmetrical ring geometry one can find different types of domain wall automotion depending on the angular position of the initial domain wall with respect to the asymmetrical shape and width gradient of the ring structure. For instance, domain wall automotion of both walls takes place when both domain walls are placed along the perpendicular direction to the symmetrical axis of the ring (i.e. $\pi/4$ axis) (see Figure 5.2a) and move toward each other. A single automotion event of one wall happens when one wall moves toward the second pinned domain wall in the narrowest part of the nanoring, as both domain walls are initially placed along the symmetrical axis of the ring.

We note that the domain wall position is roughly defined by the position of its vortex core. In general, a way to experimentally determine the orientation of the vortex core polarity is by the sense of gyration of the vortex core after the field driven domain wall, as we reported recently in [118]. However, in this experimental study we image domain wall motion at zero field, therefore it is difficult to determine exactly the polarities, in combination with some technical limits (e.g lateral and time resolution of the experiment). Thus, the domain wall polarity in all experimental movies, discussed here, is defined as a positive polarity ($p = +1$) as we observed in Ref. [24, 118].

As is known for all spontaneous and switching mechanisms, the exact evolution depends mainly on the pinning and thermal activation [15, 150] which determine the time for reversal and modifies the evolution, leading to additional blurring of the XMCD-image that is averaged across all repetitions in our experimental imaging technique, as described in chapter 2. Therefore during this switching process, the image contrast of the vortex domain walls is slightly blurred, leading to less accuracy in defining the exact vortex core position during the automotion. In other words, the extracted domain wall position represents the averaged domain wall position (e.g. the wall center).

III.1. Automotive propagation of multiple vortex walls with the same chirality

As a first step, we recorded the magnetic structure after the injection of a short unidirectional uniform magnetic field excitation with field strength of $\mathbf{B} \approx 9$ mT and pulse duration of ~ 25 ns. The Zeeman energy is minimal when both domain walls align with the applied in-plane external magnetic field, thus the two domain walls are roughly positioned along the orientation of the magnetic field pulse, which is in this case the perpendicular direction to the symmetrical axis of the ring (i.e. $\pi/4$ axis), as shown in figure 5.2a. This figure depicts the initial magnetic configuration and position of the two domain walls, at $t = 0\ ns$, for a 500 nm asymmetrical ring structure. In this case, we can clearly see that the chirality of the two domain walls is clockwise

($c = -1$) after a unidirectional magnetic field excitation. This is in contrast to the chirality formed when using a rotated magnetic field excitation, where the two diametrically opposed vortex domain walls always have opposite chiralities after rotation, as we reported in [118].

In the next step, after the onion state nucleation process following the magnetic field pulse, we dynamically imaged the spontaneous domain walls propagation at zero fields. The dynamic domain wall propagation was imaged in a stroboscopic scheme in which a snapshot of the moving domain walls is taken every 2 ns, as described above. The temporal resolution of a single frame is limited by the electronics jitter to ~ 250 ps (see chapter 2 – section IV).

The results of the automotive domain wall propagation of two walls in the asymmetric ring (500 nm in the narrowest part), are shown in figure 5.2. We present the experimental velocity profile for both domain walls plotted as a function of the azimuthal angle around the ring, as well as a function of time. We note that these velocity values are the magnitude of the angular velocity of the vortex core, extracted from the measured time-resolved movie, multiplied by the mean radius of the ring structure. The duration of the full magnetization switching process of the ring, from its initial onion state to vortex state at zero field, is roughly $58 \pm 2\ ns$.

The domain walls start to move at $t < 2\ ns$, just after the unidirectional magnetic field is removed. The velocity profiles in figure 5.2b clearly show that the tail-to-tail wall (in blue) accelerates first and reaches as its maximum velocity at $t = 12\ ns$, whereas the maximum velocity of the head-to-head wall (in red) is reached at $t = 20\ ns$. This can be easily explained by the fact that the initial position of the tail-to-tail domain wall is slightly closer to the highest width gradient of the ring than the head-to-head wall, since the onion state is not perfectly aligned with the perpendicular direction of the symmetrical axis of the asymmetric ring. Thus, the influence of shape of the sample on the domain wall resulting from the highest width gradient is highest at the beginning for the tail-to-tail wall. The velocity of this wall oscillates slightly during the propagation, possibly due to a pinning center naturally occurring due to unavoidable defects and edge roughness from the fabrication process. This pinning effect may lead to some stochasticity in the spin structure configuration of the vortex domain wall, in turn leading to additional blurring of the domain images resulting from the thermal activation. At $t = 34\ ns$ the tail-to-tail wall increases its velocity, which is smaller than the first acceleration as the wall has already passed the highest width gradient position (see figure 5.1a), and is now closer to the narrowest part (zero width gradient) where both domain walls annihilate. On the other side, the head-to-head domain wall starts to decrease it velocity at $t = 34\ ns$. We note that the global velocity maximum of both domain walls are roughly equal ($\sim 45\ m/s$).

We also note that a small effect of the domain wall inertia can be observed during the annihilation process of both domain walls. This can be concluded from the fact that the domain walls slightly overshoot the narrowest part of the ring, which represent the global minimum of the domain wall potential landscape, by getting relatively much slower. However this effect is relatively small, since the domain wall velocity and at this region is the lowest.

III.2. Automotive propagation of multiple vortex walls with opposite chirality

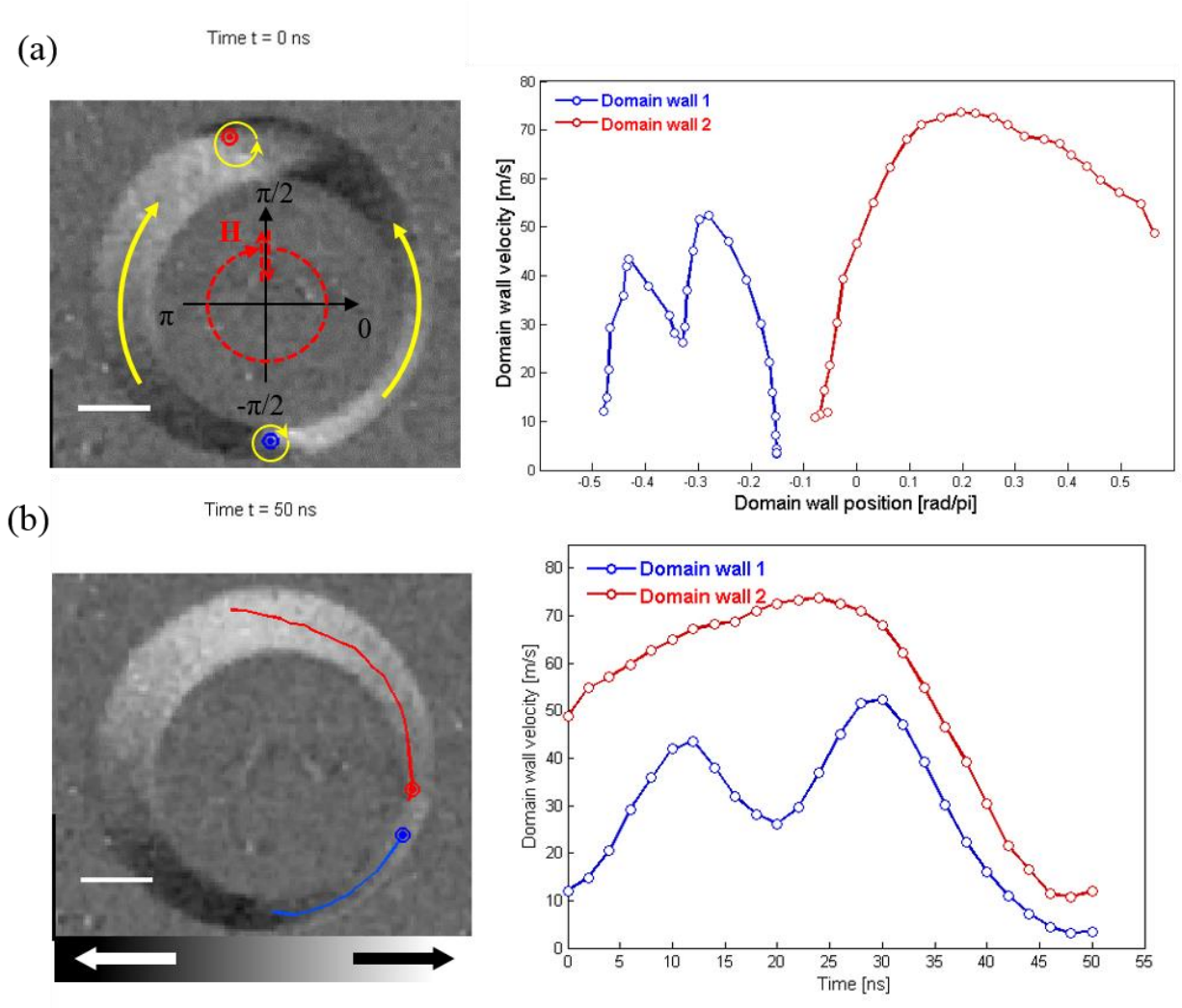

Figure 5.3: Automotive domain wall propagation in an asymmetric ring (400 nm): (a) Left: A time-resolved XMCD-STXM image at **t = 0 ns** of the onion state after one full rotation of the magnetic field H (red arrow). The vortex core polarity for both vortex domain walls ($\boldsymbol{p = +1}$) is indicated in red (head-to-head) and blue (tail-to-tail). This image visualizes the magnetization state just before the start of the automotion process. The yellow arrows indicate the magnetization directions. **Right:** Domain wall velocities plotted as a function of the azimuthal angle. **(b) Left:** A time-resolved XMCD-STXM snapshot at **t = 50 ns** showing the vortex state after the annihilation process of both domain walls. Red and blue lines illustrate the trajectory of the domain wall center extracted from the time resolved movie. White (black) contrast corresponds to magnetization pointing to the right (left). White scale bar indicates a distance of 1 µm. **Right:** Domain wall velocities plotted as a function of time.

In order to investigate the automotive vortex domain wall dynamics in terms of the topological character of the walls (chirality), we now study the approach of two vortex walls of opposite chirality. This provides us with a comparison to the previous approach of two vortex domain walls of the same chirality.

Here we discuss the experiments that dynamically image the magnetic structure of vortex domain wall propagation at zero field after the injection of a clockwise rotating magnetic field pulse. This latter, consists of two rotations with a constant field strength of $\mathbf{B} \approx 6.8$ mT and fixed rotation frequency ($f = 10\ MHz$). The sample is a 400 nm wide asymmetric ring. The rotating magnetic field pulse is used instead of the unidirectional field, discussed above, in order to define opposite chiralities ($c = \pm 1$) for the two vortex domain walls. This nucleation process is highly reproducible, meaning that the domain wall chirality can be set with high fidelity, as reported in Ref. [118]. We note that the shape anisotropy for both this and the previous asymmetrical ring structure (i.e. 400 nm and 500 nm) are very similar, as we can infer from the width gradient plotted in figure 5.1 where the differences in value can be easily neglected. Thus as a first approximation we can consider that both ring structures have the same geometrical contribution to the magnetization dynamics.

The Zeeman energy is minimal when both domain walls align with the applied in-plane external magnetic field, thus the relaxed domain walls are positioned along the orientation where the rotating magnetic field pulse is abruptly switched off, which is in this case along the ~ $\pi/2$ direction, as shown in figure 5.3a. This figure depicts the initial magnetic configuration and domain wall positions for the onion state (at $t = 0\ ns$) after a full rotation of the magnetic field in the clockwise direction.

We can clearly observe that the two vortex domain walls have opposite chiralities, with the head-to-head and tail-to-tail domain walls having counter-clockwise ($c = +1$) and clockwise ($c = -1$) chirality, respectively. This is in agreement with our reported results in symmetric ring systems where the two vortex domain walls always have opposite chiralities, following a full rotating field pulse [118].

In the next step, we dynamically image the automatic domain wall propagation at zero field. The results of the automotive propagation of multiple domain walls in the asymmetric ring are shown in figure 5.3. The domain walls move towards the narrowest part during the annihilation process. This figure presents the experimental velocity profile for both domain walls plotted as a function of the azimuthal angle around the ring, as well as a function of time. The duration of the full annihilation process of the domain wall is roughly $50 \pm 2\ ns$. It is worth mentioning that the duration of the full magnetization switching process of the ring, from its initial onion state to vortex state at zero field in this case occurs sooner than in the previous case, shown in figure 5.2 where the two walls have the same chirality.

The walls continue to move spontaneously, after the external magnetic field is removed. The velocity profiles in figure 5.3b clearly show that the head-to-head domain wall (in red) starts with a high velocity and continues to accelerate slowly in time until reaching its maximum velocity at

$t = 24\ ns$, which represents roughly the highest width gradient position for this wall. Afterwards the wall starts to decelerate and continues moving to the narrowest part of the ring, where the local forces, resulting from the spatially dependent domain wall energy, are expected to reach a minimum, before being annihilated with the tail-to-tail wall (in blue). This can be explained by the fact that the head-to-head domain wall is rotating and has just passed the widest part of the ring before the driving rotating magnetic field pulse is removed. In chapter 4 we have explained, in a similar ring structure, that the oscillations of the domain wall velocity must result from the variation of the ring width which leads to the varying tangential force arising from the non-zero phase difference. Thus, the phase shift is strongly correlated to the shape of the ring structure. At this part of the ring the negative value of the phase difference (i.e. the angle between the field, **H**, and the azimuthal vortex core position) is largest, thus the driving force is maximal and hence the domain wall was accelerating and its velocity has reached a global maximum. Therefore once the rotating field is removed and the automotion process began, the wall velocity was higher.

On the other hand the tail-to-tail wall was rotating during the field pulse for $t < 0\ ns$, towards the widest part of the ring which leads to an increase of the domain wall energy and results in a non-zero value of the local force $\mathbf{F_U} = -grad\ U$ (where U is the local domain wall energy), oriented against the propagation, as a restoring force toward the narrowest part of the ring. Therefore the wall at $t < 2\ ns$, starts with a lower velocity. However, since the wall was initially placed very close to the highest width-gradient position ($-0.42\ \mathrm{rad}/\pi$), it accelerates and reaches a local high velocity at this position ($t = 12\ ns$), which is lower than the head-to-head wall since the influence of the shape of the sample on the domain wall resulting from the highest width gradient is lower as well. Equivalent to the effect observed for the head-to-head domain wall, the tail-to-tail starts to decelerate after crossing the highest width-gradient area.

At $t = 22\ ns$ the tail-to-tail wall again increases its velocity since both domain walls are moving closer to each other. At this position there are three attractive forces acting on the walls, which are oriented in the propagation direction. Thus the second velocity increase can be easily explained by these forces, as discussed below in section IV. However, contrary to the previous case (i.e. vortex walls with the same chirality), the short-range interaction force arising and resulting from the detailed topological nature of the walls, is an attractive force since the topological vortex defects of both walls have opposite winding number. Therefore we observe a global maximum velocity ($\sim 53\ m/s$) at $t = 32\ ns$. This is maximum in the velocity constitutes a direct demonstration of the short-range attractive force when we compare with the former case discussed above where the second maximum velocity is lower.

The tail-to-tail wall velocity oscillation is explained by the interplay between the relevant forces that act on the wall and the local pinning potential resulting from extrinsic effects, such as defects and imperfection in the nanowires. These are expected to give rise to a spatially varying energy landscape for domain walls [151], and the interaction of the moving domain walls with the local pinning potential is expected to result in velocity variations due to extrinsic pinning. This effects impacts slow domain walls whereas fast walls are able to overcome the extrinsic pinning due to the stored magnetostatic energy which scales linearly with the wall velocity and behaves as an

energy reservoir, leading to a domain wall inertia [24, 62]. This is clearly observed in the results presented in figure 5.3 where there is an indication of extrinsic pinning for the head-to-head wall exhibiting a maximum automotive velocity roughly equal to $\sim 75\ m/s$. Finally, the walls move towards each other until they annihilate at $t = 50 \pm 2\ ns$.

III.3. Automotive propagation of a single vortex domain wall

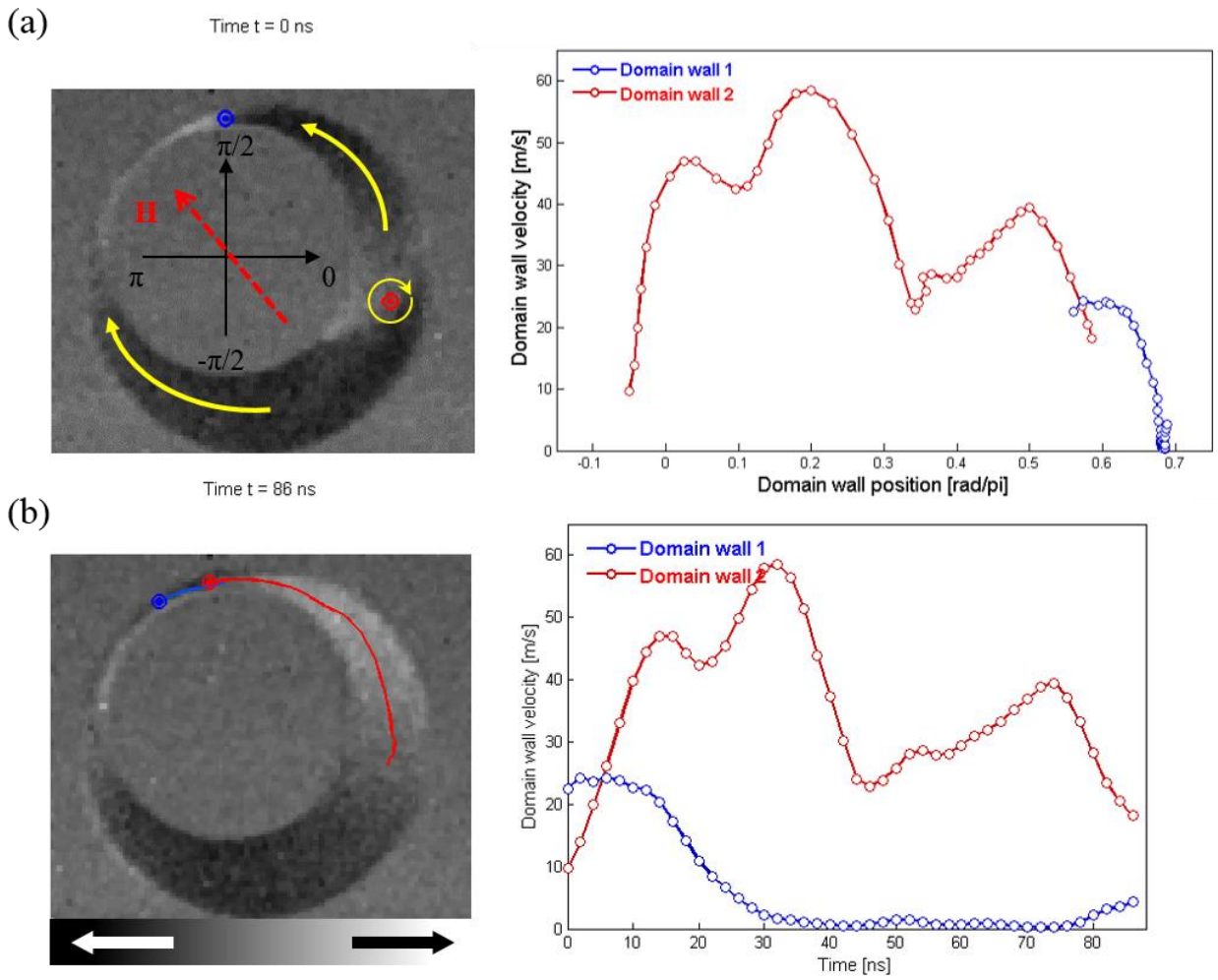

Figure 5.4: Automotive domain wall propagation in an asymmetric ring (100 nm): (a) Left: A time-resolved XMCD-STXM image at **t = 0 ns** showing the relaxed onion state after saturation with a uniform external magnetic field, H (red arrow), along the symmetrical axis of the ring (3π/4). The vortex core polarity of both vortex domain walls ($\boldsymbol{p = +1}$) is indicated in blue (head-to-head) and red (tail-to-tail). This image visualizes the magnetization state just before the start of the automotion. The yellow arrows indicate the direction of the magnetization. **Right:** Domain wall velocities plotted as a function of the azimuthal angle. **(b) Left:** A time-resolved XMCD-STXM snapshot at **t = 86 ns** showing the vortex state (clockwise) after the annihilation process of the domain walls. Red & blue lines illustrate the trajectory of the domain wall center, extracted from the time resolved movie. White (black) contrast corresponds to magnetization pointing to the right (left). **Right:** Domain wall velocities plotted as a function of time.

In order to investigate the automotive dynamics of a single domain wall traveling a longer distance, along the half ring, we now study the approach of a vortex wall towards a second pinned wall in the narrowest part of 100 nm wide asymmetric ring structure. This provides a comparison to the previous measurement of two moving vortex domain walls and open up the possibility to learn more about the automotive domain wall propagation in different ring-width gradient.

The experiments employ a short unidirectional uniform magnetic field excitation along the symmetrical axis of the ring (i.e. ~ 3π/4 direction), with field strength of $\mathbf{B} \approx 9$ mT and pulse duration of ~ 25 ns. Figure 5.4a depicts the initial magnetic configuration and position of the two domain walls, at $t = 0\ ns$. We note the magnetic field pulse duration and strength are not enough to perfectly align both domain walls along the symmetrical axis of the ring, as seen in the figure. Similarly to the former nucleation process, both domain walls should have the same chirality. We can clearly observe that the tail-to-tail domain wall has a clockwise chirality ($c = -1$), whereas it is more difficult to easily identify the head-to-head chirality, due to the spatial resolution limitation at this narrowest part of the ring and the resulting small wall width.

The results of the automotive domain wall propagation in the 100 nm asymmetric ring geometry, are shown in Figure 5.4. This figure show the experimental velocity profile for both domain walls plotted as a function of the azimuthal angle around the ring, as well as a function of time. The tail-to-tail wall moves toward the second wall in the narrowest part before being annihilated. The duration of the full annihilation process of the domain wall, is roughly $86 \pm 2\ ns$.

The domain walls start to move spontaneously at $t < 2\ ns$, just after the unidirectional magnetic field is removed. The velocity profile in figure 5.4b clearly shows that the tail-to-tail domain wall (in red) accelerates first and reaches two local maximum velocity at $t = 14\ ns$ and $t = 32\ ns$, as at this part of the ring (widest part) the domain wall energy, *U*, is the highest. This velocity oscillation is explained by the interplay between the relevant forces that act on the wall and the local pinning potential resulting from extrinsic effects, such as defects and imperfections in the nanowires as explained above. At $t = 32\ ns$, the wall experiences a strong pinning effect thus the domain wall start to decelerate to a local minimum at $t = 46\ ns$. We note that again this is due to extrinsic pinning, since this drop of velocity was not observed at this position in different field sequence (not shown). Afterwards for $t > 46\ ns$ the tail-to-tail wall velocity increases since the wall is roughly at the highest ring-width gradient where the local forces, $\mathbf{F_U}$, resulting from the spatially dependent domain wall energy are expected to reach a maximum. Furthermore the long-range mutual interaction force becomes more significant since it is inversely proportional to the separation between the domain walls.

On the other hand, the head-to-head wall is initially placed close to the narrowest part of the ring (i.e $\pi/4$ offset). At this position the wall experience local forces, which drive the wall towards the narrowest part in such a way as to minimize its energy, before getting pinned at roughly $t = 36\ ns$. However we can clearly infer from the graphs in figure 5.4b that the velocity for the head-to-head wall, is initially higher than for the second wall. This is due to the fact that during the

nucleation process, the head-to-head wall was already driven toward the narrowest part before the unidirectional uniform magnetic field has been removed, whereas the tail-to-tail wall was driven towards the widest part (opposite to its automotion direction after removing the field).

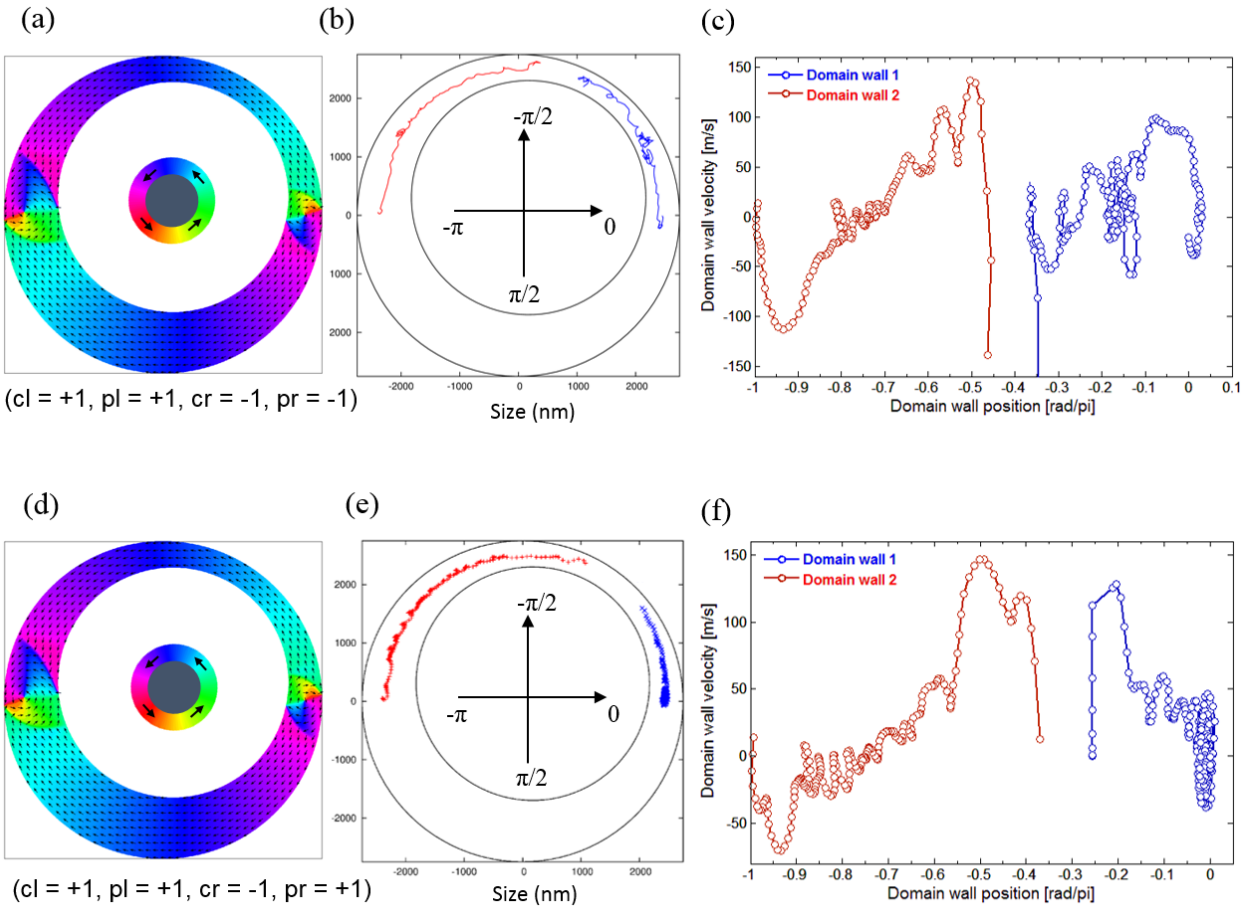

Figure 5.5: Micromagnetic simulations of domain wall dynamics at zero-field, comparing two different magnetic configurations where in both cases the domain walls have opposite chiralities. **Top**: domain walls with opposite chilarities and opposite polarity. **Bottom**: domain walls with opposite chilarities and same polarity ($\boldsymbol{p = +1}$). (cl = chirality of left domain wall, pl = polarity left, cr = chirality right, pr = polarity right). Head-to-head wall on the left and tail-to-tail wall on the right. Panels **(a)** and **(d)** show the spin structure of the 400 nm ring geometry. The color code represent the magnetization direction visualized by the small black arrows. Panels **(b)** and **(e)** show the trajectory of the vortex core extracted from the simulated movies, plotted in red and blue for the head-to-head and tail-to-tail domain wall, respectively. Panels **(c)** and **(f)** present the domain wall velocities plotted as a function of the azimuthal angle.

III.4. Micromagnetic simulation

In order to investigate the detailed intrinsic spin structure changes and their contribution to the domain wall dynamics at zero-field, such as the influence of the topology of the vortex wall, and compare with our experimental results, we performed a series of micromagnetic simulations using the MicroMagnum code [123]. This not only provides a quantitative determination of the energy contributions, but also opens up the possibility to learn more about the relevant energy landscape and the origin of the automotion process. The dimensions of the simulated asymmetric rings presented here are the same as in the experiment, (as discussed above in subsection III.2) with an outer diameter of 5.5 µm and non-centered inner diameter of 4 µm (400 nm in the narrowest part), a thickness of 30 nm and a cell size of $5 \times 5 \times 30\ nm^3$. We note that the proper dimension of the grid size is defined based on the so-called exchange length, $l_{ex} = \sqrt{2A/\mu_0 M_S^2}$, which depends on the magnetic properties. For instance, in our case the *exchange length*, $l_{ex} \geq 5\ nm$, which is typical for permalloy. The exchange length determines the characteristic length scale over which the exchange interaction is dominant. Thus, the magnetization is spatially uniform, over ~ l_{ex}. Therefore, the cell size, in a micromagnetic framework, has to be smaller than l_{ex} and at the same time not too small in order to reduce the simulation time and be consistent with the mesoscopic approximation of the model [125].

In general, tail-to-tail and head-to-head domain walls carry opposite magnetic charges [140]. They always attract each other when they are placed further apart than their width. Here the domain wall configuration under discussion is the vortex domain wall in the two-dimensional model [126]. This can be understood as a composite object composed of elementary topological defects [107], where the magnetization curls in-plane around the central vortex core (see chapter 1). These defects can be at the edges or within the interior of the nanowires. For a vortex domain wall, the edge defects have either - 1/2 or + 1/2 winding number, whereas the central defects have + 1 [30]. The total winding number or topological charge of a domain wall has always to be zero.

In this section we present a systematic micromagnetic simulation study of domain wall motion at zero-field in 400 nm asymmetric rings in the onion state. This allows us to investigate the spontaneous dynamics of domain walls in terms of their topological character. We vary the vortex chirality ($c = +1$ or $c = -1$) and the vortex core polarity p (anti-parallel ($p = -1$) or parallel ($p = +1$) to the z-direction) and we calculate domain wall automotion. From this we extract the propagation velocities, which is exactly what we measure experimentally. Both domain walls are initially placed along the in-plane angle (azimuthal axis) shifted ~ $\pi/4$ from the symmetrical axis of the ring, with the tail-to-tail wall closest to the narrowest part, similar to the experiment presented in figure 5.3. The position of the vortex core was extracted by fitting a Gaussian through the M_Z (out-of-plane) component of the magnetization. In general, such simulations of curved geometries lead to artifacts due to the cubic discretization of a curved surface that can entail artificial pinning at the edges of the nanoring which is detrimental to the domain wall automotion process. Therefore we define a smooth profile of the saturation magnetization along the edges of the nanoring to reduce this pinning.

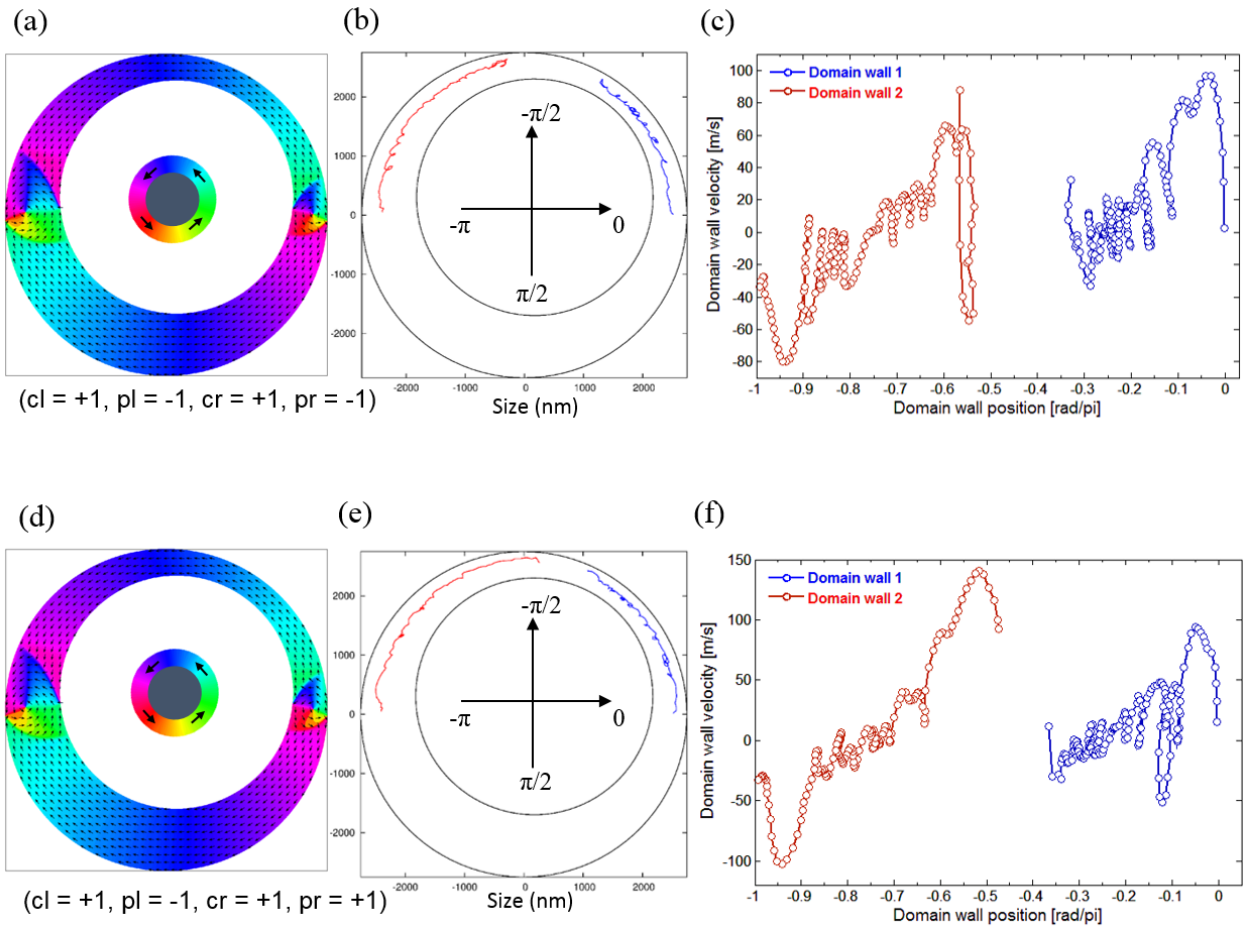

Figure 5.6: Micromagnetic simulations of domain wall dynamics at zero-field, comparing two different magnetic configurations where in both cases the domain walls have same chiralities ($\boldsymbol{c = +1}$). **Top**: domain walls with the same chilarities and the same polarities ($\boldsymbol{p = +1}$). **Bottom**: domain walls with the same chilarities and same polarity ($\boldsymbol{p = \pm 1}$). (cl = chirality of left domain wall, pl = polarity left, cr = chirality right, pr = polarity right). Panels **(a)** and **(d)** show the spin structure of the 400 nm ring geometry. The color code represents the magnetization direction visualized by the small black arrows. Panels **(b)** and **(e)** show the trajectory of the vortex core extracted from the simulated movies, plotted in red and blue for the head-to-head and tail-to-tail domain wall, respectively. Panels **(c)** and **(f)** present the domain wall velocities plotted as a function of the azimuthal angle.

Figure 5.5 presents the micromagnetic simulations of domain wall dynamics at zero-field, comparing two different magnetic configurations where in both cases the domain walls have opposite chiralities. In figure 5.5-bottom, the domain walls have the same polarities ($p = +1$) and opposite chilarities (this head-to-head wall: $c = +1$ and this tail-to-tail wall: $c = -1$), mirroring the experimental approach discussed in subsection III.2 and shown in figure 5.3. Thus by comparing both experimental (figure 5.3a) and simulated (figure 5.5f) results, we can clearly see that the domain wall automotion is seen in the micromagnetic simulations is in good qualitatively agreement with the obtained experimental results. The domain wall dynamics are

well reproduced even though the micromagnetic simulation is performed for different conditions than occur for the experiment, i.e. in a defect-free system and at zero Kelvin temperature. Moreover, the results shown in figure 5.5f clearly demonstrate that the walls experience a strong attractive interaction once they get very close to each other, as observed in the experiment. This effect manifests itself as a dramatic increase of the domain wall velocity just before the annihilation process occurs in the narrowest part of the ring. This is due to the attractive nature of the short-range exchange interaction force [140], resulting from the detailed topological nature of the walls with opposite chiralities, as mentioned above.

Figure 5.6 presents the micromagnetic simulations of domain wall dynamics at zero-field, comparing two different magnetic configurations where in both cases the domain walls have same chiralities $c = +1$. In (figure 5.6 top), the domain walls have the same polarities and chilarities (these head-to-head wall and tail-to-tail wall ($p = -1; c = +1$)) similar to the experimental approach discussed above in subsection III.1 and shown in figure 5.2. Here the studied geometry is a 400 nm asymmetric ring, whereas it is a 500 nm asymmetric ring with a positive polarity for both domain walls in the experiment. However as discussed above, we can expect both ring structures to have the same geometrical contribution to the magnetization dynamics. Thus on comparing both results we can in general find qualitative good agreement. Moreover, the results shown in figure 5.6f clearly demonstrate that the walls experience a short-range repulsive interaction once the walls get very close as in experiment. This is due to the repulsive nature of the short-range interaction force, resulting from the detailed topological nature of the walls with the same chiralities [140]. This effect lead to a slow decrease of the velocity of the tail-to-tail domain wall just before the annihilation process in the narrowest part of the ring. This result is in contrast to the previous case shown in figure 5.5f, confirming our experimental results qualitatively shown in figure 5.2b at $t = 30\ ns$.

In order the investigate the automotion of domain walls in terms of their detailed topological nature and to provide a further understanding of the internal spin structure dynamics at zero field, figure 5.7 presents a comparison between two other magnetic configurations. Again, in both cases the domain walls have opposite chiralities and varying polarities. The results shown in figure 5.7f clearly demonstrate that the walls experience a strong attractive interaction once the walls get very close to each other (as discussed above), which roughly reproduces the results in figure 5.5f and similar to the experimental results where domain walls have the same chirality (in term of the velocity increase of the walls when they approach to each other).

There are clearly several other effects going on concerning the detailed automotive vortex domain wall propagation while varying their topological character such as the vortex chirality and core polarity, which we do not focus on here. For example the detailed feature in the wall velocity when varying their polarities. However, the main message is that the domain wall automotion locally depends on the detailed topological nature of the walls, without inhibiting, globally, the annihilation of domain wall, which always occurs in our studied system because of the relevant forces on the vortex domain wall spin structure, as discussed below in section IV. Therefore by varying the detailed topological parameters we could observe small differences in

the domain wall velocities and trajectories as well as the duration and exact position of the annihilation (figure 5.5, 5.6 and 5.7). For example the topological defects influence the domain wall propagation dynamics by accelerating or decelerating the switching process between the two different ordered states: onion and vortex state.

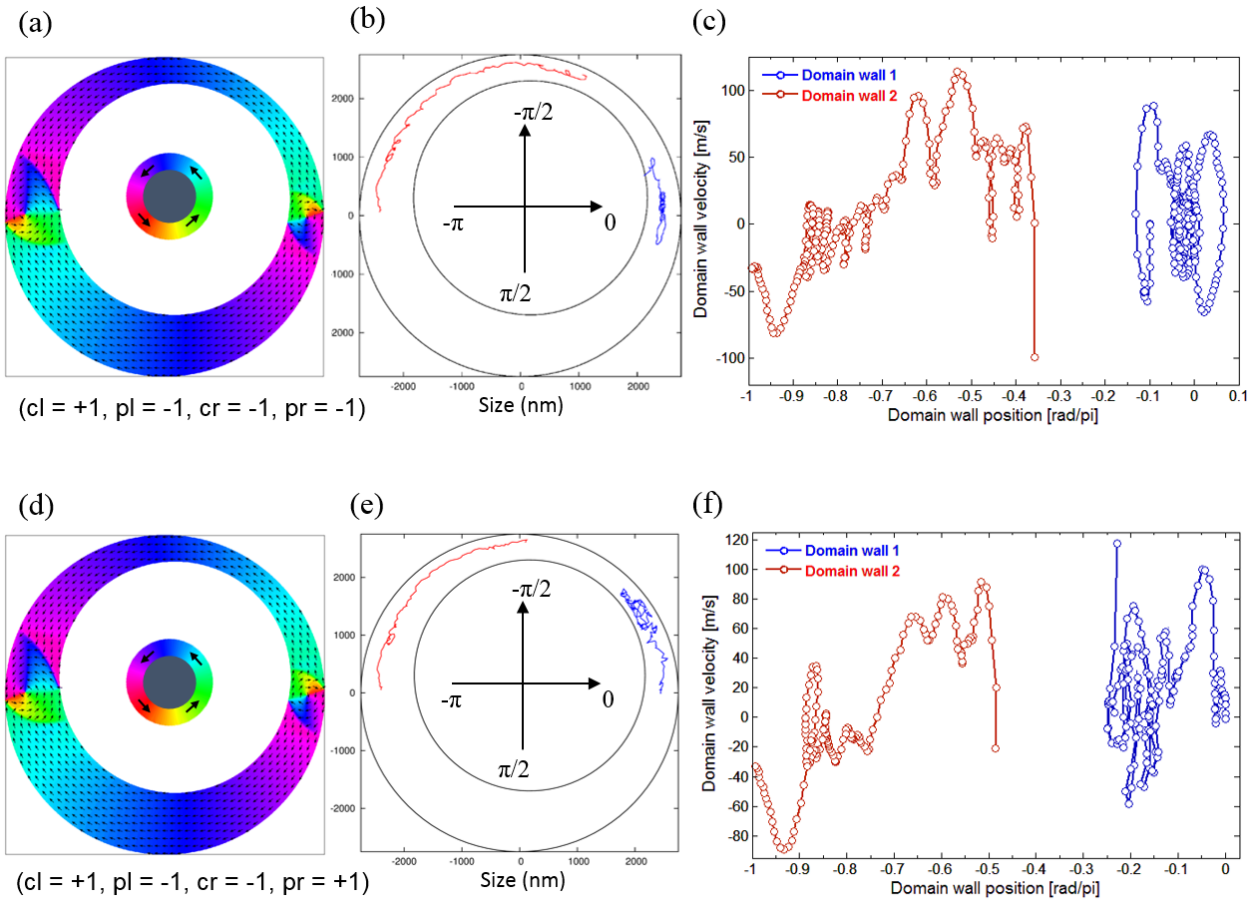

Figure 5.7: Micromagnetic simulations of domain wall dynamics at zero-field, comparing two different magnetic configurations where in both cases the domain walls have opposite chiralities. **Top**: domain walls with opposite chilarities and same polarity ($\boldsymbol{p = -1}$). **Bottom**: domain walls with opposite chilarities and opposite polarity ($\boldsymbol{p = \pm 1}$). (cl = chirality of left domain wall, pl = polarity left, cr = chirality right, pr = polarity right). Head-to-head wall on the left and tail-to-tail wall on the right. Panels **(a)** and **(d)** show the spin structure of the 400 nm ring geometry. The color code represent the magnetization direction visualized by the small black arrows. Panels **(b)** and **(e)** show the trajectory of the vortex core extracted from the simulated movies, plotted in red and blue for the head-to-head and tail-to-tail domain wall, respectively. Panels **(c)** and **(f)** present the domain wall velocities plotted as a function of the azimuthal angle.

IV. Discussion:

Our first surprising experimental observation of domain wall automotion (with an averaged velocity of ~ 60 m/s), in which the wall inertia is able to overcome the repulsive topological force between the walls with the same chirality, as well as the barrier potential resulting from the unavoidable sample imperfection that pin the wall, has not been previously observed. We explain the underlying mechanisms of this behavior by considering the forces that act on the vortex domain wall spin structure.

For sake of simplicity we consider the domain wall as a point-particle behavior, and, consequently described by one single coordinate like the vortex core position (as described in the 1D model (see chapter 1 - subsections II.1 and II.2). There are four forces acting on the vortex domain wall, one of which is a radial restoring force and the other three are tangential forces, which act as an azimuthal driving force.

Firstly the long-range attractive interaction between the walls, at large separation, is purely magnetostatic and largely independent of the chiral character of the domain walls. In nanowires, domain walls in the long distance limit can be considered as free magnetic monopoles carrying a single magnetic charge, with adjacent walls always having opposite charges.

Thus, the two walls always experience an attractive force (similar to the Coulomb force), pushing the walls towards each another, as is clear from the electrostatic analogy [107]. The relevant energy is mainly determined by the magnetic charge of the domain walls which serve as sources for stray fields. Moreover, the interaction between walls (through stray fields) has a dipole nature with the energy decreasing monotonically when the walls start to move towards one another. Hence, the resulting force is inversely proportional to the separation ($\propto 1/d$) [140].

The second force that acts on the domain wall is the force resulting from the asymmetrical shape of our ring structure, $\mathbf{F_U} = -grad\ U$. As mentioned above this force results from the spatially inhomogeneous potential landscape of the domain wall energy, U, in the asymmetric ring landscape with a minimum in the narrowest part. The domain wall potential landscape has a spatial dependence due to the exchange and dipolar energy variations in the domain wall spin structure and thus it depends on the local ring width. This is demonstrated in Figure 5.8, where we show the contribution to the domain wall energy at zero field in 500 nm asymmetric rings. At zero field the domain wall energy, $U = E_{ex} + E_d$, consists only of the sum of the exchange energy (E_{ex}) and dipolar energy (E_d). The energies are obtained from micromagnetic calculations, by propagating the domain wall along the ring at different directions. These energies allow the calculation of the local forces acting on the domain wall due to the potential landscape, which are directed to the narrowest part of the ring. We can clearly infer from the graphs in figure 5.8 that the domain walls' energy scales with the width of the structure, demonstrating that the potential landscape can be tailored by the geometry. This force is therefore classified as a local and short range-force, proportional to the width-gradient in the ring.

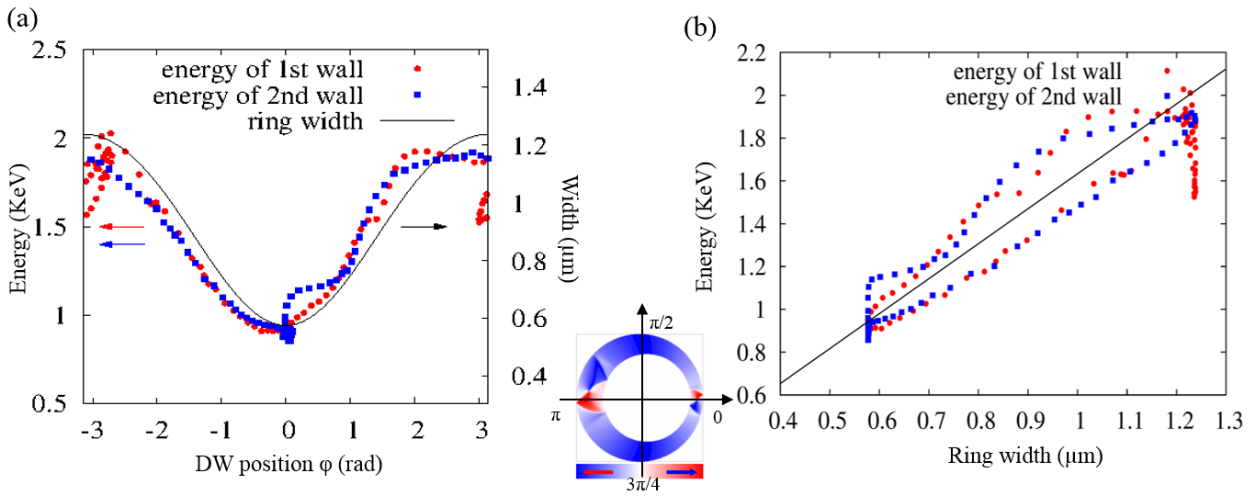

Figure 5.8: Contributions to the domain wall energy at zero field (exchange + magnetostatic energies) in 500 nm asymmetric rings. The red and blue curves correspond to the head-to-head (left) and tail-to-tail (right) vortex domain wall, respectively, as shown in the inset. The energies are obtained from micromagnetic calculations, by propagating the domain wall along the ring with a field pointing along different directions. **(a)** Domain wall potential landscape plotted as a function of domain wall position, **(b)** and as function of the ring width. These calculations has been obtained with the help of Dr. B. Krüger.

The third force that acts on the domain wall is the force resulting from the short-range interactions, arising when the separation distance, *d*, between domain walls become small. Contrary to the long-range attractive interaction force, this force depends on the detailed topological nature of the domain walls (chirality) [140]. This leads to a repulsive or attractive interaction whether the two vortex walls have the same or opposite chirality, respectively. This effect can be understood by considering the spin structure of the vortex walls, as discussed in Ref. [140, 141]. For instance, in vortex domain walls with the same chirality the spins between the two walls cannot continuously rotate, since the spins at both sides of the domain are anti-parallel. This leads to an increase of the exchange energy which opposes a further approach of both walls toward each another. Whereas for vortex walls carrying opposite chirality the magnetization can rotate continuously, because spins at both sides of the domain are parallel. Therefore these interaction forces are a consequence of topological edge defects that keep the total winding number of a domain wall equal to zero.

Finally the radial force that acts on the vortex wall is the restoring force, $\mathbf{F_{res}}$, resulting from the shape anisotropy, which pushes the vortex core toward the center of the nanowire and depends on the radial vortex core position as well as the ring width and material (see chapter 4 - subsection III.2).

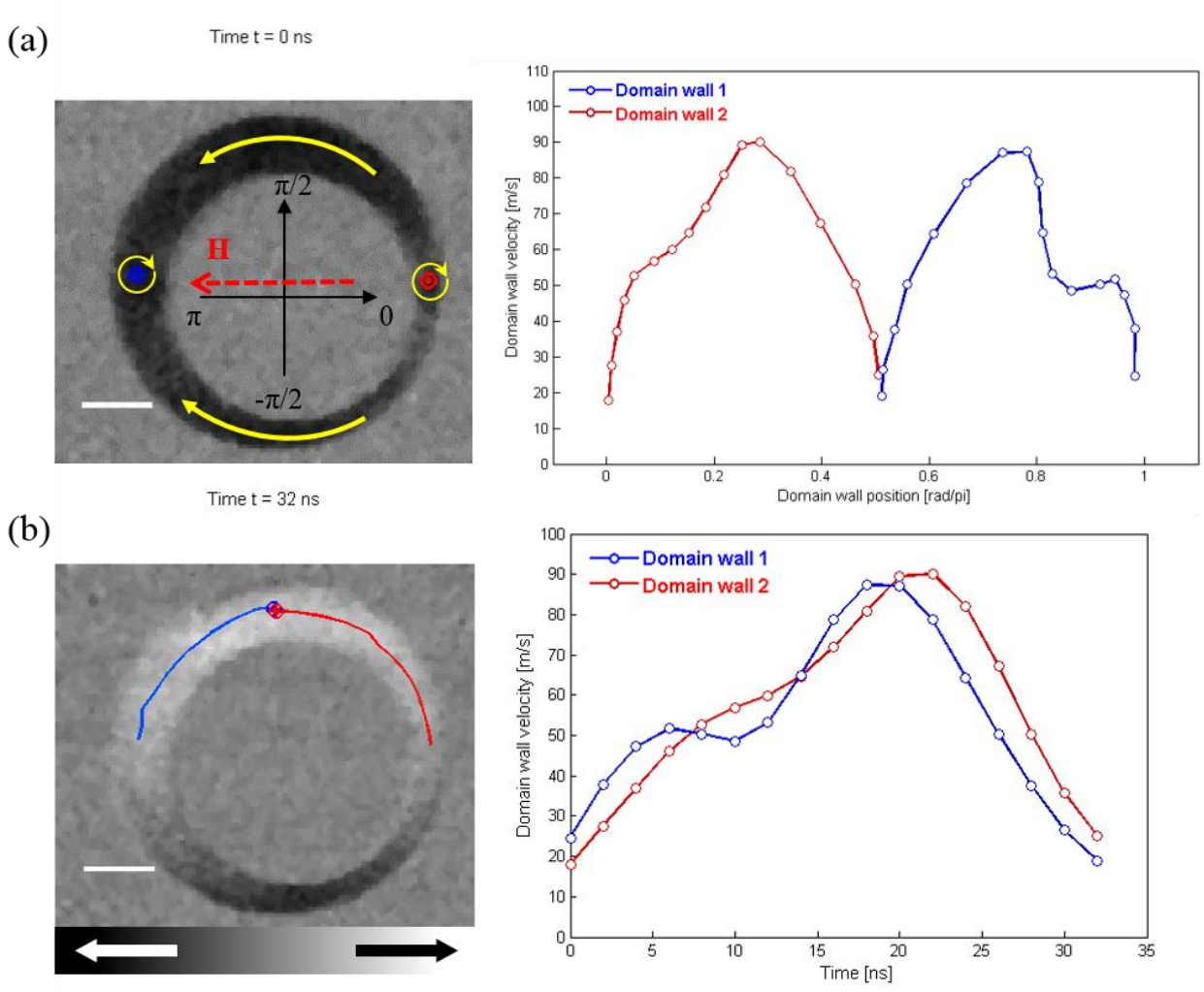

Figure 5.9: Automotive domain wall propagation in an asymmetric ring (300 nm): (a) Left: A time-resolved XMCD-STXM image at **t = 0 ns** showing the relaxed onion state after saturation with a uniform external magnetic field H (red arrow). The vortex core polarity of both vortex domain walls ($\boldsymbol{p = +1}$) is indicated in blue (head-to-head) and red (tail-to-tail). This image visualizes the magnetization state just before the start of the automotion process. The yellow arrows indicate the direction of the magnetization. **Right:** Domain wall velocities plotted as a function of the azimuthal angle. **(b) Left:** A time-resolved XMCD-STXM snapshot at **t = 32 ns** showing the vortex state (clockwise) after the annihilation process of the domain walls. Red and blue line illustrates the trajectory of the domain wall center, extracted from the time resolved movie. White (black) contrast corresponds to magnetization pointing to the right (left). Scale bar indicates a distance of 1µm. **Right:** Domain wall velocities plotted as a function of time.

We now compare the domain wall velocities found experimentally for different magnetic configurations. In particular we compare the results obtained for the both cases of automotive propagation of multiple vortex walls with the same chirality (Figure 5.2) and opposite chirality (Figure 5.3). For instance by considering the tail-to-tail wall velocity plotted in blue in the graph

of figure 5.2b, we can clearly see that the second peak in velocity is lower than the first one, whereas in figure 5.3b the second peak in velocity of the same wall (tail-to-tail wall) is higher than the first one. We attribute this to the short-range exchange interaction force which is a repulsive force in the first case (same chirality) and attractive in the second one (opposite chirality), as the domain walls move close to each other (as discussed above). Moreover by comparing the timing between these two local velocities (the second peak in velocity) and the domain wall annihilation, we find that in the second case (figure 5.3b) the annihilation occur sooner (~ 14 ns) than the first case (~ 24 ns) (shown in figure 5.2b). This further demonstrates the significant contribution of the short-range interaction force to the dynamics. Additionally this result is qualitatively in good agreement with our micromagnetic results, as described above in subsection III.5.

We note that in order to check the reliability and reproducibility of our experimental results the automotion experiment is repeated in several samples with almost the same geometry. Almost all samples reproduced similar results and showed similar physical behavior, with some examples discussed above. However it is worth mentioning that in very rare cases (in particular for the 300 nm geometry) we observe that domain walls, surprisingly, move towards the widest part of the asymmetric ring where they get annihilated (Figure 5.9). The domain walls propagation towards the widest part (highest energy) demonstrates that the local forces resulting from the width gradient do not always dominate. Thus this observation cannot be explained by the short-ranges forces, which usually push the walls towards the narrowest part of the ring, and only explained by the long-range dipolar interaction between walls which depends mostly on the magnetic charge of domain walls and the separation between walls, as discussed above.

V. Conclusion

In summary, we have directly imaged controlled domain wall automotion in asymmetric curved nanowires at zero field. We have demonstrated that automotive propagation occurs due to the influence of the demagnetization and exchange energy present in structures. This automotion is driven by the domain walls spin structure interaction, which depend on the topology of the system and by the energy gradient associated with the spin structure change when the geometry changes. Therefore the relaxation of the excited system from the onion state towards the potential well minimum, results in domain wall automotion. We used direct dynamic (time-resolved) imaging of the nanoscale spin structure that allows us for the first time to directly check previous predictions, which were quantitatively investigated and confirmed in our experimentally extracted domain wall velocities.

The pump and probe experiment of domain wall propagation at zero field showed, surprisingly, domain wall automotion with an average velocity of about ~ 60 m/s, which is a significant speed for spintronic devices based on domain wall dynamics. We demonstrate that the domain wall

inertia and the stored energy allows the walls to overcome both the local extrinsic pinning and the topological repulsion between domain walls carrying the same winding number (vortex chirality).

Furthermore we investigated the automotion mechanism in a series of samples having different widths in the narrowest part as well as different domain wall magnetic configurations. In particular we compare the results obtained for the automotive propagation of multiple vortex walls in the case of the same chirality and opposite chirality.

Finally, we presented a systematic micromagnetic simulation study of domain wall motion at zero-field in 400 nm asymmetric rings with the wall possessing different topological character. By performing a series of micromagnetic simulations on defect-free systems, we demonstrate that the domain wall automotion and annihilation is always present, and the results showed good quantitative agreement with our experimental results. Moreover we demonstrate that the detailed topological nature of the walls only influences the domain wall dynamics at a local scale without inhibiting the annihilation of domain walls through automotion. Thus in our system the influence of the topological defects is limited by locally modifying the domain wall propagation and the switching process between the two different ordered states.

Chapter 6

Domain wall pinning in ultra-narrow electro-migrated constriction

Abstract

One of the aims of the field of magnetism is to enable the continued realization of Moore's law by using new concepts and methods to build spintronic devices with feature sizes on the nanoscale. Therefore, in magnetic systems, studying the domain walls in confined geometries has recently been the focus of many research studies. However, dealing with super-miniature nanoscale systems is a major challenge due to geometrical effects which often dominate the measurement results and hide the intrinsic magnetic effects. In this chapter we discuss the evolution of domain wall pinning in an ultra-narrow ferromagnetic junction narrowed by electromigration. The magnetic junction was fabricated and eventually tailored in-situ in clean ultra-high vacuum conditions. This study was done on a Permalloy (Py) half-ring with a notch at the center. By using the advantage of a controlled in-situ electromigration process, which is able to tailor the nano-contact's width, we are able to probe the nanostructure device at different constriction widths. In agreement with the wall energy, which is reduced in narrower constrictions, we find that the domain wall pinning strength is increased on decreasing the contact width. Moreover, we measured the depinning field's angular dependence and symmetry in order to determine the complete domain wall pinning potential in a device with a narrow constriction.

This chapter is arranged as follows. In Section I we motivate the work by reviewing previous studies, which highlights a number of important open questions in this domain of study which we could potentially help to answer using our unique methods. In Section II we present and discuss our unique experimental approach and sample fabrication procedure and explain how we optimized in order to prevent experimental artefacts. Then in Section III we present the results of our depinning study and finally in Sections IV and V we discuss the results and summarize the work. The work in this chapter was carried out in collaboration and with the contribution of Dr. Robert M. Reeve and André Loescher who I acknowledge. The presented work is based on the results obtained during André Loescher's diploma thesis (which continued an initial measurement and characterization of such nanocontacts which was an initial focus of my PhD project). Therefore my contribution was in the following: sample fabrication, transport measurements and finally discussing the results and the data analysis. Part of this work has been published in Ref. [152].

I. Introduction:

Recently, the study of magnetic nanocontacts has started to draw the attention of numerous research efforts. In the case of the non-magnetic nanocontact junctions where the size of the contact width is reduced to be comparable to some physical material length scales, the transport properties can be qualitatively changed. However, in the case of magnetic systems, one needs to fundamentally understand additional effects which arise by comparing with the non-magnetic systems. The understanding of these additional effects, from an applications' point of view, may help to provide new devices which have better efficiencies and exciting functionalities [153]. Many new transport effects have been seen or predicted in magnetic nanojunctions. As examples, a modification of the quantized conductance levels has been reported in such systems due to the spin degeneracy lifting [154], as well as new magneto-resistance (MR) properties such as enhanced anisotropic magnetoresistance (AMR) in both tunneling and ballistic regimes [155-157] in addition to the so-called ballistic magnetoresistance (BMR) [158, 159] and finally, new Kondo properties in the nanoscale ferromagnetic systems [160, 161].

The study of magnetic domain walls in the magnetic nanocontacts is a particularly interesting field of research. Nowadays it is well known that the material's conductivity is modified due to the presence of a magnetic domain wall and these effects usually increase on decreasing the contact size [162]. So far there are several models which explain this domain wall resistivity, however, they differ significantly in the magnitude and even in the sign of the predicted effects [163-167], and similarly a variety of experimental measurements have been reported [163, 168–177].

Obviously there are many important factors behind these contradictions in the reported studies. Firstly, as mentioned above, the behavior will be dominated by different transport effects depending on the size scale of the structure. For instance, by changing the transport from the diffusive to ballistic regime, it is expected that a qualitative change in properties will take place. Comparing different experimental results it is also necessary to remember that these experiments have been done under different experimental conditions (temperature, materials, methods, *etc*), which must be taken into account in addition to the dimensionality. This makes the comparison difficult and means it can be difficult to disentangle whether the dimension parameter is the main factor responsible for the disparate observations.

A second consideration when working with such tiny nanostructures is that it is crucial to control the structure very precisely in order to be sure that defects do not influence or dominate the physical effects at this regime scale. For instance, in a system where the interesting part consists of only a few atoms, it is enough to have just a small level of contamination in order to obtain large artefacts in the measurement [154, 178]. Furthermore, some local or extrinsic pinning can take place in the case of local oxidation in the system.

In the ferromagnetic system, additional effects which should be taken into account such as the magnetostriction effect, since big changes in the contact conductance can arise from the resulting changes in the junction geometry and not due to the magnetization spin structures of the nanocontact [179–183]. Therefore a key prerequisite for this field of study is the capability to disentangle the pure magnetic effects from such artefact effects.

A new controlled experimental technique has been developed in our group in order to overcome, these issues. This experimental procedure enables the magnetic nanocontact fabrication and subsequent investigation of the transport measurement *in-situ* in the same ultra-high vacuum (UHV) environment [184]. This approach uses a double resist layer mask which results a significant undercut through which the material is deposited. In this way we ensure that the magnetic nanostructure and the surrounding metal film are disconnected which permits the transport measurement *in-situ*, without taking the sample out from the (UHV) deposition chamber. Moreover, the nancontacts can be tailored in a controlled way, *in-situ*, by using the electrical current-narrowing technique at low temperature. This is based on electromigration of the contact atoms via a computer-controlled process. The tailoring procedure starts with an initial junction state with a constriction cross-section of few tens of nanometers and can lead to a cross-section of a few atoms at the junction constriction or even fabrication a small gap. In order to rule out or minimize all undesired artifact errors, such as the magnetostriction effect, in addition to providing the spin control of the structure, we have carefully chosen the material, the nanocontact geometry and measurement schemes. Thus, in this way it is possible to investigate the magneto-transport properties for different resistance levels, by tailoring the contact width, in the same sample, while keeping fixed measurement conditions.

Using this measurement system in our group we have previously studied the domain wall magnetoresistance (DWMR) in half-ring nanocontacts made of Permalloy where three distinct regimes of behavior have been observed [184].

a) Initial low resistance regime:

The presence of a domain wall in a nanocontact with a size on the order of a few tens of nanometers, which is considered here a relatively wide contact, is reported to result in a decrease of the structure resistance [134, 185-187]. This change in resistance is however, a small effect (smaller than 1%), which can be explained by the anisotropic magnetoresistance (AMR) effect. This latter effect arises due to the spins within the domain wall which have a perpendicular direction or angle with respect to the electron current flow along the junction.

b) Middle resistance regime:

By performing electromigration the nanocontact cross-section is reduced to a few nanometers. Yet, when the transport is still in the diffusive regime, we recently observed an additional contribution to the DWMR. This latter contribution is positive in sign [152]. In this regime the effect is also small, however it increases on reducing the size of the contact.

c) Third or high resistance regime:

Finally in the case of the so-called ballistic regime, where the contacts have atomic dimensions, much larger DWMR signatures are observed, up to 50% [184].

Moreover, in this high resistance regime, the DWMR effect is observed to have a critical dependence on the precise arrangements of the atoms of the contact [184, 187].

For applications based on domain walls [71, 73], it should be possible to selectively control the domain wall propagation within the nanostructure, and in order to make use of the large DWMR effects in applications one needs to be able to achieve such domain wall control in ultra-narrow wires.

An intuitive method for controlling the domain wall position is the introduction of artificial pinning sites within the nanocontacts, where by consequence a pinning potential landscape is generated around the introduced constriction or notch [66].

As shown in chapter 1, at the nanoscale there are two main stable domain wall magnetization configurations in soft magnetic materials nanowires; the transverse and the vortex domain wall. The transverse is energetically favored in narrow wires, whereas the vortex domain wall has the lower energy in wider wires [66]. Thus, by tuning the thickness and the width, the magnetic structure will have a preference for either vortex or transverse domain walls. Since the domain wall energy scales with its length, this mean in order to minimize the total energy, the domain wall will preferentially move towards constrictions within the structure. Since this constriction create a potential well for the domain wall. In a first approximation, the depth of this potential well is obtained by measuring the energy difference between the wall inside and away from the constriction. However, in order to obtain a full characterization of the potential well landscape it is necessary to take into account the spin structure of the domain wall inside the notch as well. It was found that the transverse walls are attracted towards the center of the notch, whereas the vortex walls are pushed out from the central area and are instead pinned at an adjacent position to the constriction, where in this case this domain wall position results in a minimum energy for the associated stray field induced from the spin configuration of the vortex domain wall [110]. A classical way to investigate the height of the potential barrier is through the measurement of the magnetic field strength needed to depin or move the domain wall away from the potential trap. Once the magnetic field is applied an additional energy contribution to the domain wall arises (Zeeman energy), which is proportional to the external magnetic field amplitude. In this way previous experiments has been performed that characterize the depth and the shape of the potential well in relation to the width [110, 188, 189] and geometry of the constriction [189–191], as well as the spin structure configuration of the domain wall [132, 150, 190, 192], which provides a customization of the domain wall potential.

Several studies have investigated such pinning in top-down patterned contacts with a minimum width higher than 20 nm. Indeed many such studies have been performed previously in our group

where we determined all the characteristic and physical properties of the potential landscape generated by notches within a magnetic structure. For instance the previous work in the group has established the width [132, 134, 192], depth [110, 134, 192] and curvature [193] of the pinning potential well.

However, due to the challenging fabrication technical difficulties, domain wall pinning studies at the extreme nanoscale have received comparatively little attention, even though, from the technological application point of view, this regime is expected to become very important, e.g. due to the continued need for the miniaturization of the technological devices while keeping, or even increasing, their efficiency. Secondly, this regime is of particular interest because of the DWMR effects, which become more significant at this scale.

So far it has not been possible to produce such narrow constriction within the contact by using the conventional lithography state-of-art, nevertheless by using the electromigration break-junction technique we can reach this regime.

A key consideration for controllable pinning is stochastic effects since a multiplicity of potential domain wall spin structures surrounding the notch [189] and thermal fluctuations [194] can result in to changeable behavior of the device. Higher pinning potentials could be used to solve the undesired thermal switching problems, which influence as well the efficiency operation of the devices. In the case of requiring bidirectional of domain wall motion, one may need a perfectly symmetric pinning potential, whilst in order to fix a preferential direction for the domain wall motion an asymmetric pinning potential is needed. This latter can provide a magnetic domain wall ratchet effect [191].

In order to investigate these unresolved open questions, in this study we use our methods reported in previous work [184] which permit us to prepare high quality magnetic nanostructures in order to discuss the evolution of domain wall pinning at notches which are subsequently thinned and engineered with the use of the *in-situ* electromigration break junction technique. This technique paves the path to the study of domain wall pinning in a new regime of ultra-narrow constrictions, by keeping a high quality and cleanliness of the nanocontacts which guarantees that measured physical effects, such as the pinning potential, are fully dominated by the extrinsic effects resulting from the geometry only. Furthermore we are able to determine the asymmetry of the pinning potential and investigate the dependence of the domain wall pinning field strength on the constriction width. Moreover we determine the pinning potential landscape width. Finally, by direct observation of the system using our scanning electron microscopy with polarization analysis system (SEMPA), we explain how the spin structure configuration of the complete system influences the given switching field.

II. Experimental

II.1. Sample preparation

Our samples consist of half-ring nanocontacts made of Permalloy. The nanocontacts are fabricated using electron-beam lithography (EBL). The Permalloy material was thermally evaporated through electron-beam evaporation.

In general the devices fabrication was done in three steps using a Si/SiO2 substrate (375 μm thick), as in general described in chapter 2 – section II, however a summary of this fabrication process as well as a specific description in each step are presented below.

First step:

The first step consists of the preparation of Cr(5 nm)/ Au(55 nm) contact pads. These were prepared by lift off processing using a PMMA positive mask resist after pattering pads by the electron-beam of the lithography system at our institute. In the same pattering step alignment marker we prepared as well in order to use them in the next lithography step. The contact pads material deposition was done via direct current sputtering. The chromium is used here as an adhesion buffer layer, since the direct growth of Au on Si/SiO2 shows poor adhesion [195].

Second step:

At this step one needs to prepare a resist mask of the nanocontacts, including the contact pads as well, in order to ensure a continuous connection between the pads and the junction, before mounting the sample inside the deposition/measurement chamber for the Py material deposition and subsequently carrying the experiments *in-situ.* In order to do that, first of all we spin coat a double positive polymer resist layer with components of different thickness and sensitivity, which is required to produce a shadow-mask with a significant a undercut, ensuring the nanostructure is electrically disconnected from the surrounding metal film and that transport measurements can be performed *in-situ* without any short-circuit issues. To this end the mask consists of a thick MMA and PMMA double layer, where the PMMA is on top of the MMA. Two electron-beam lithography exposure steps with two different writing field parameters are employed for the resist in order to ensure the best results from the time and fabrication resolution standpoints. The first step is for the magnetic nano-contact exposure in the area between the pre-existing contact pads and the second step consists of re-exposing the contact pads in order to allow a good continuous electrical connection of the sample as mentioned above.

At each lithography step many specific parameters (electron beam exposure parameters, resist parameters and thickness) have been used, which were determined after several dose tests in order to ensure the highest quality and possible precision of the device.

Third step:

At this stage the sample can be mounted onto the sample holder, and by using the mechanical wire-bonder we connect the contact pads of the sample with these of the sample holder, with a micro metallic wire such as aluminum or gold. Afterwards the sample is loaded into the UHV deposition molecular beam epitaxy (MBE) and measurement chamber. The deposition of the magnetic material is done by thermal evaporation with the base pressure of the chamber in the regime of $5 \cdot 10^{-10}$ mbar and the deposition rate fixed to be around 4 nm/hour. This procedure provides us with a very high quality and clean nanocontact. In these experiments we chose Permalloy due to its soft magnetic properties and low magnetostriction. The shadow mask plays two important roles, which arise from the big undercut due to the double resist layer:

- ✓ Firstly it provides electrical isolation between the Py nanocontact and the Py evaporated above the resist, which is very important, since without doing lift-off, it allows *in-situ* transport measurements.
- ✓ Secondly, it helps with the achievement of a very small notch in the ring, which is usually not easy to gets due to the proximity effect. However when making the evaporation under an oblique angle in the presence of the undercut, it is possible [196].

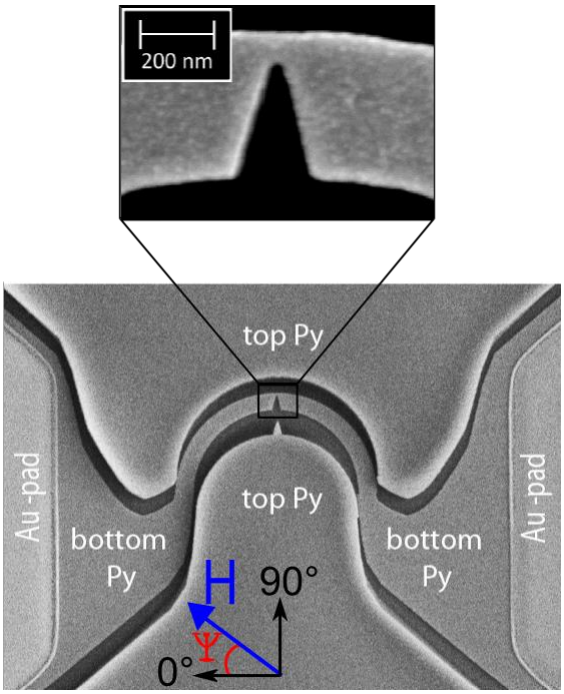

Figure 6.1: Scanning electron microscope image of a notched Py half ring located in-between two contact pads. The radius of the half ring is 2.5 µm, its width is 400 nm and the size of the constriction is ~ 70 nm. The top image shows a magnification of the area around the notch. The inset highlights the angle relation of the magnetic field to the sample's geometry [152].

An example of our sample geometry is shown in the scanning electron microscopy (SEM) image (Figure 6.1). It is clearly seen that there is a pronounced separation between the two Py layers. This SEM image represents the top view observation of the sample; therefore the undercut is not directly observed, however a side view image shows how the Py material on top of the mask resist and the nanocontact (which is directly in contact with the substrate) are in fact disconnected [184].

We also show a magnified view of the constriction area of the contact in the figure 6.1 inset. The overall width of the junction is around 400 nm and at the narrowest part, the notch size has only 70 nm width. The nominal thickness of the Py film is 23 nm, where the thickness was controlled using a calibrated quartz microbalance inside the chamber.

II.2. Measurement schemes

The transport and magnetic measurement in addition to the electromigration of the sample inside the chamber can be performed at 80 K since the sample holder is attached to a liquid nitrogen cryostat. The characterization of the magnetic properties of the sample is carried out *in-situ* with the aid of a 2D-vector magnet which surrounds the sample holder. This electromagnet can generate in-plane fields up to 150 mT [197].

The domain wall presence in the ring can be detected by measuring the sample resistance. Since the resistance of the junction is different depending on whether the domain wall is present within the contact or not, due to the magnetoresistance effect which is associated with the domain wall presence [185].

By using half-ring nanocontact's geometry, as seen in Figure 6.1, and taking the advantage of the small magnetocrystalline anisotropy of Permalloy (soft magnetic material), we can control the position of the domain walls in the contacts. The magnetic spin structure is mainly dominated by the shape anisotropy of the contact. In such a geometry there are two main expected magnetization states which depend on the magnetic history of the sample. The magnetization configuration can be either a state including a single head-to-head or tail-to-tail domain wall, or a quasi-uniform state where the spin structure direction is continuously following the contact shape, similar case to the reported onion or vortex states in the full ring geometry [65].

By applying an initializing saturation magnetic field along different chosen angular directions the domain wall can be nucleated at a desired point in the ring, and therefore we obtain a state with a single head-to-head or tail-to-tail domain wall. However, by applying the initializing saturation magnetic field along the horizontal axis of the sample, which corresponds to $\psi = 0°$ or 180°, (see inset of Figure 6.1), the quasi-uniform state will form. By applying the nucleation field close enough to the notch, the domain wall will be influenced by the potential well created by the notch and get trapped. Based on these facts it therefore possible to investigate and determine the energy landscape of the system by using our previous employed measurement techniques from our group.

First of all, we can determine the pinning potential width or extent by measuring the remanent resistance state of the nanocontact following to the initial saturation field of the nancontact spin structure at different angles by scanning ψ (which here represents the angle of the saturation field direction) from 0° to 360°. This kind of measurement is called "mode étoile" measurement [185, 134, 132].

Secondly using a new measurement scheme which is presented here, we evaluate the nature of the pinning potential asymmetry, by nucleating a domain wall at different angular positions in the wire (ψ going from 0° to 360°), and compare the measured difference in depinning fields for opposite directions, ±90°, from each nucleated domain wall angular position.

Finally, we can determine and measure the strength of the full potential landscape with the following measurement scheme: we nucleate the domain wall at the constriction in the nanocontact and measure the required depinning field amplitude from the notch as function of each applied depinning field angle (scanning the depinning field angle going from 0° to 360°) [193].

II.3. Electromigration process

The main and final key component in our measurement method is the capacity to change the constriction properties (width, shape, etc) *in-situ,* without moving the sample and retaining the sample cleanliness. This is very important in order to be able to investigate the evolution in the properties by changing the width of the contact system with a single set of samples.

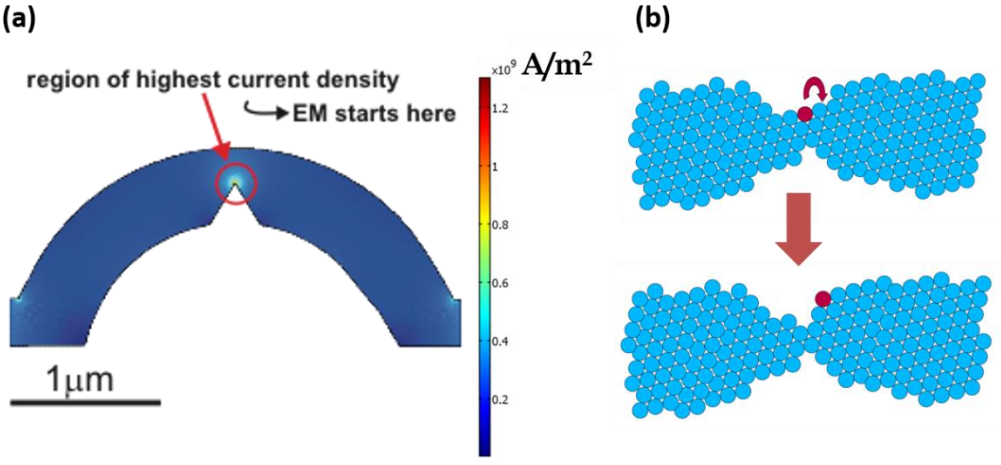

Figure 6.2: (a) simulated current distribution prior to electromigration (EM). **(b)** Schematic depicting atomic hopping during electromigration.

Therefore after each full set of measurements or magnetic characterization of the system, we use our controlled electromigration methodology for tailoring the constriction width has schematically illustrated in Figure 6.2b. In the metal system a thermally activated diffusion of atoms occurs in a specific direction under the influence of the electromigration forces due to the

high critical density (which is maximal at the constriction). The first force or so-called wind force arises from the momentum transfer from the flow of electrons to the cores of atoms. The second force arises from the electrostatic field. By using appropriate experimental conditions, this electromigration effect can be used to controllably thinning the nanocontact at the notch position [198]. We note that the highest current densities happen at the notch area of the contact since it is the narrowest part of the junction. Consequently, the notch position will exhibit the highest temperature and thus the electromigration effect is preferentially begins at this position in the contact.

By using a carefully computer controlled feed-back cycle for the electromigration process, (implemented in LabView), the dissipated power can be measured and limited in order to manipulate the temperature of the nanocontact and in turn the rate of atom migration [199, 200].

The contact tailoring procedure starts follows:

We initially start the electromigration procedure by applying a voltage, V_0, across the contact, where we are sure that this voltage is not enough to start the electromigration. We subsequently, step by step, increase the applied voltage until the threshold in temperature for electromigration is reached. This is indicated by a faster increase in resistance because of the increase in temperature. In this manner, we control the local temperature at the notch, and we avoid the thermal runaway and catastrophic damage to the contact.

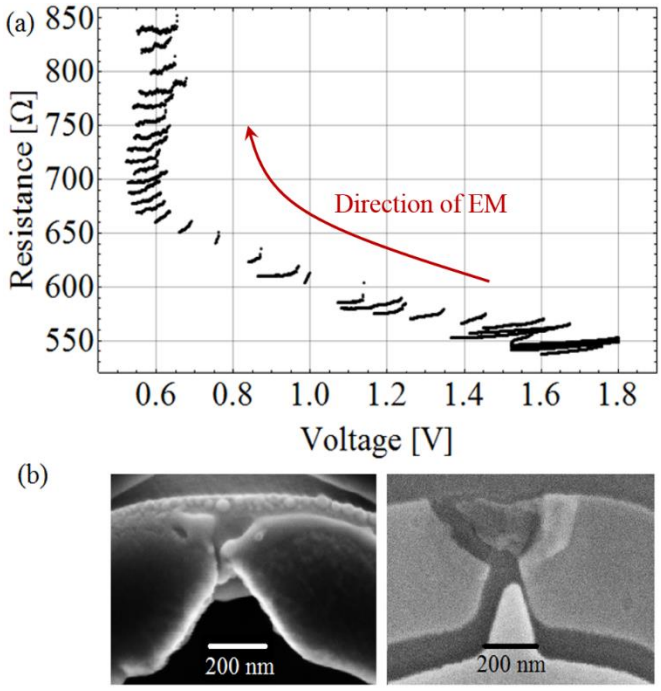

Figure 6.3: (a) Evolution of the electrical resistance during electromigration (EM) as a function of applied voltage, initially becoming appreciable at 1.8V. Computer controlled reduction of the applied voltage prevents destruction of the sample. **(b)** SEM micrographs of two contacts following electromigration made from Permalloy (left) and Cobalt (right) [152].

When the increase in resistances of the junction reaches a pre-chosen threshold, one completes a so-called electromigration cycle. Then the voltage, and thus the power dissipated at the contact is decreased by the program and a new voltage ramp cycle is begun [200, 201].

There are, additionally, two further parameters controlling the process. The first is a break off threshold, G_{BO}. If this chosen resistance level is reached the program completely stops the electromigration process at the contact. The second parameter is the target voltage, V_T, which is the voltage limit on a given ramp cycle. If V_T is reached before the pre-chosen threshold of the resistance has been reached the software automatically switches back to the input voltage to V_0 and new ramp begins. This parameter is indispensable to limit the scale of the voltage scans and helps provide a further electromigration control.

A typical electromigration process is shown through the evolution of the electrical resistance in Figure 6.3. Here we show an example of an electromigration process for a 23 nm thick Py nano-contact with a resistance below 1 KΩ, which is the regime of the present study.

Intuitively the resistance of a given sample depends on the width of the initial constriction, the thickness and the nanocontact width. In the case presented in Figure 6.3 the initial resistance is ~ 550 Ω. We observe that an appreciable electromigration first sets in at a voltage of 1.8 V due to a significant heating at this voltage. Therefore the overall resistance increases. The following electromigration cycles set at lower voltages, as can be observed in the figure which correspond to the same power dissipation in the constriction, due to the resistance increment [200].

The electromigration process is then stopped at a chosen resistance level in order to perform again a new magnetic characterization and transport measurement for the new nanocontact configuration. This step can be followed by resuming the electromigration in order to reach the subsequent desired resistance level point. Depending on the requirements of the measurement, this complete procedure can be stably repeated until the resistance becomes unstable due to the atomic hops, where the nancontact consists of just a few atoms, or even until a small gap is opened up [198, 201].

This described electromigration process can be applied at several variety of conductors and transition metals such as Au [198–201] and Pd [201], alloys [184, 185, 202] and graphene [203]. In Figure 6.2 we show two SEM images of a typical contact subsequent electomigration status of two different metals: Permalloy and Cobalt.

Usually we keep measuring the sample until the gap is completely opened, before removing the sample from the UHV chamber. Therefore, both contact materials, showed in Figure 6.2b, present an opened gap in the contact within the notch area.

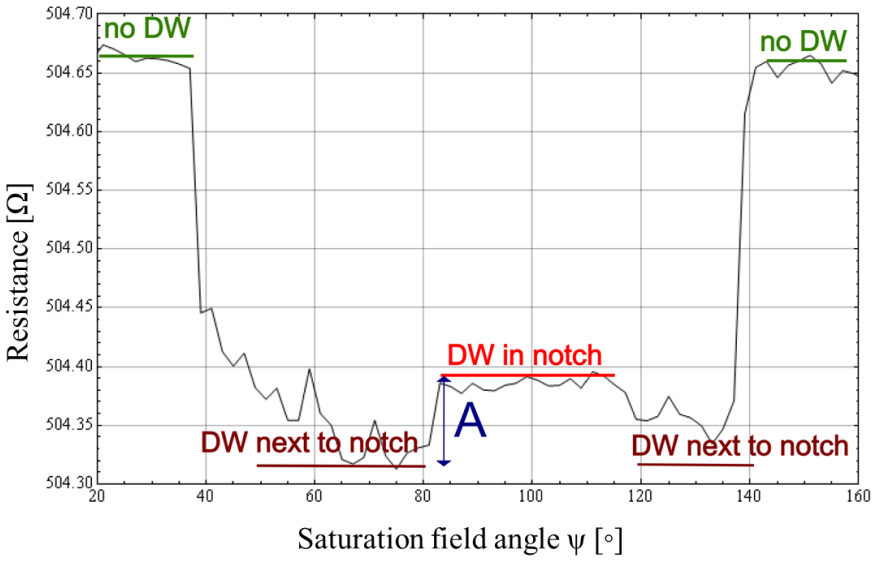

Figure 6.4: Mode étoile curve at **R = 505 Ω** showing the angular range between **20°** and **160°.** Green lines give the range for the absence of a domain wall in the contact while the red lines illustrate the level of a domain wall depending on the position to the notch. The blue arrow "A" shows the difference in resistance between the state with the domain wall in the notch and that with domain wall in the ring but not in the notch [186].

III. Results

In this section, we present the experimental results of the evolution of the domain wall pinning potential in the system. In the following, all experimental results and transport measurement data correspond to a single Permalloy nanocontact (half-ring geometry shape) of 23 nm thickness, with an initial resistance of ~ 440 Ω prior to any electromigration process.

Before starting to study the evolution of the domain wall pinning potential for different resistance regimes, we check first our capacity to controllably nucleate a domain wall in the half ring.

In order to do that, we apply an initial saturation field along a specific angle and then measure the remanent resistance of the structure ("mode étoile" measurement), similar to previous work [185, 134, 132]. In this resistance regime the DWMR is dominated by the AMR effect, thus the domain walls have been observed to lower the overall resistance. This resistance would be slightly different between states with domain walls inside and next to the notch, as can is sometimes be observed (Figure 6.4). This difference in resistance arises from the spin structure difference between the domain wall states in and next to the notch, and since this area of the contact has the contribution to the total resistance [184, 185].

We now start with the potential well investigation. In order to characterize the asymmetry and the size of the potential well, we perform the following steps:

1) We nucleate a domain wall at different points within the nanocontact by applying saturating field pulses along varying angles.
2) Subsequently we try to depin the domain wall, by applying gradually incremented fields with an orientation of ±90° to this angle as shown in the sketch in Figure 6.5a.
3) We measure the resistance of the structure, thus being able to detect the depinning field strength for each domain wall position in the half-ring, as explained below. The obtained angular dependence of the depinning fields for our nanocontact is shown in Figure 6.5b.

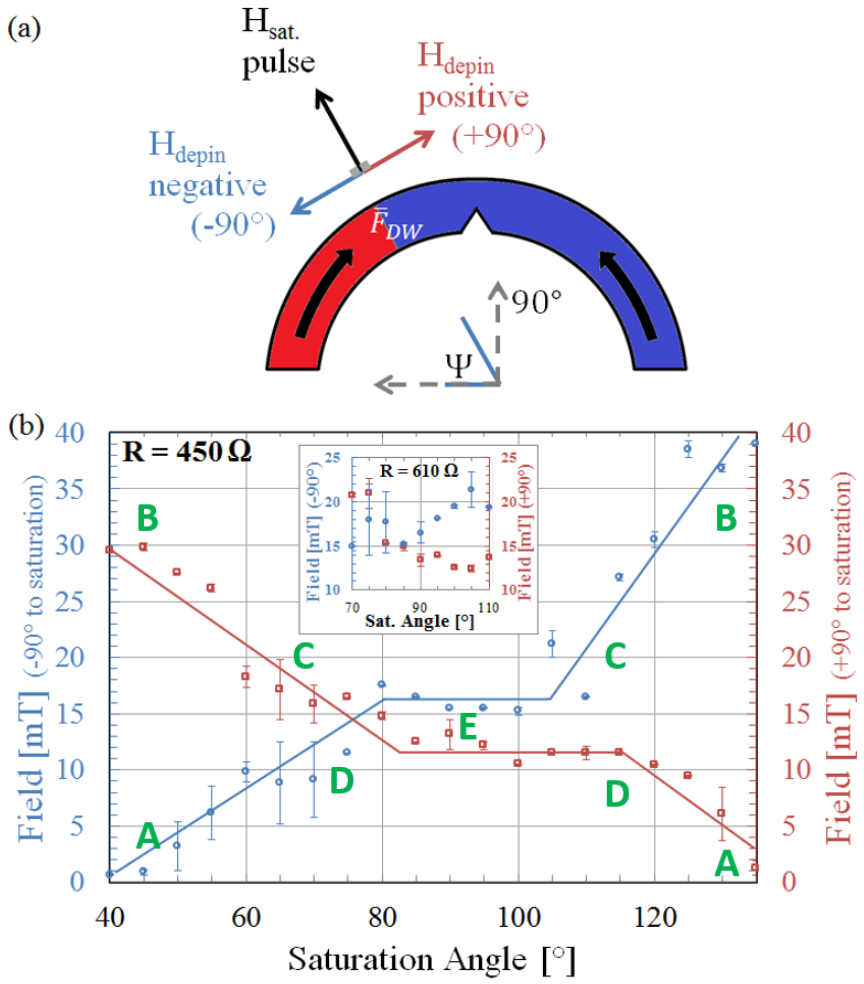

Figure 6.5: (a) Sketch depicting the measurement scheme, indicating the relation between the direction of a representative saturation field pulse (H_{sat}) and the two opposing depinning fields (H_{depin}). The resulting force on the DW F_{DW} is also shown. **(b)** The depinning fields for DWs nucleated in different positions of the ring as determined by the initializing saturation field pulse direction. The left (blue)/right (red) axes correspond to the depinning fields in the negative/positive perpendicular directions to this saturation field. The resistance of the contact is 450 Ω and the lines are guides for the eye. The inset shows the corresponding data in the vicinity of the notch for the 610 Ω resistance state of the contact. The letters (**A-E**) indicate the regimes discussed in Section **IV.** Adapted from [152].

As mentioned above in the experimental section, the measurement is done at 80 K, which is made possible by the nitrogen cryostat, implemented into our UHV chamber.

Even at this low temperature there is still an influence from thermal effects and thus there can be some stochasticity in the depinning fields [191, 204]. In order to quantify this stochasiticity, each point represents an average of few repeat measurements of the depinning fields with the spread in results indicated by the error bars (see Figure 6.5b).

Finally, we turn to the to the potential well strength characterization. In order to do that we proceed with the following steps:

- ✓ We nucleate a domain wall at the constriction position with an initializing saturation field pulse along $\psi = 90°$.
- ✓ Next we measure the magnetic field strength needed to depin the domain wall from the notch, when applying (gradually increasing) the magnetic field along different angles until the domain wall is pushed out from the notch.

Figure 6.6 shows an example of such a measurement for the initial contact state before performing any electromigration. We clearly observe a sudden large increase in the resistance, as the depinning field is increased. These resistance jumps can be explained by the fact that the domain wall is being removed from the notch, as an opposite effect to the lowering of the resistance after nucleating a domain wall within the contact, as explained above.

The field value at which this occurs is denoted as the depinning field. The changes in spin structures of the domain wall also lead to changes in resistance. However, this is a much smaller effect in this resistance regime [134, 110], therefore these larger jumps in resistance are only expected to be due to the domain wall depinning effect.

The depinning field is varied depending on the orientation of the applied field, i.e. whether it is easier or harder to depin the domain wall along to the field angles, as one can observe by comparing the traces for $\psi = 0°$ and 25°. In Figure 6.4b we present the full angular dependency of the depinnig field for four resistance states of the nanocontact.

IV. Discussion

Firstly let us discuss the experimental results from the measurement of the asymmetry and size of the domain wall pinning potential. In Figure 6.4b, the data range of the graph consist the range of the saturation angles where the relaxed state contains a domain wall in the contact, as shown in the initial characterization. We can distinguish between five different situations:

A. Domain wall placed at the contact edges and H_{depin} pointed away from the notch:

At the contact (half ring) edges the nucleated domain wall, due to the saturation field pulse, is quite far from the constriction. Thus the domain wall will not feel, or be attracted by, the

potential well surrounding the notch area. Therefore the domain wall will stay in the contact lead at the position of a local extrinsic pinning site due to natural edge roughness or due to a defect resulting from the sample fabrication. However these natural pinning sites are much smaller than the notch pinning potential, consequently one needs a very small field strength to drive the domain wall to another position or even expel the domain wall completely from the contact, away from the constriction. As we can see, for instance, in the graph (Figure 6.4b) for saturation angles >110° (red line, positive H_{depin}) and < 80° (blue line, negative H_{depin}), where we observe very small depinning fields of only a few mT.

B. Domain wall placed at the contact edges and H_{depin} pointing toward the notch:

However, in the opposite direction for saturation angles >110° (blue line, negative H_{depin}) and <80° (red line, positive H_{depin}), in order to depin the domain wall a much larger depinning field is required. This is because in this case the domain wall is first driven toward the constriction, where it becomes pinned and afterwards should be depinned from it.

C. Domain wall placed closer to the notch and H_{depin} pointed toward the notch:

For the angular range where the domain wall is placed near the notch (center of the half-ring), the required field to depin the domain wall, passing through the notch, decreases in comparison with case "**B**" . This can be explained by the fact that the depinnig field becomes more favorably aligned in relation to the geometry, since the depinning field has an increasingly larger component perpendicular to the constriction from where it should finally be depinned. This resulting feature is an additional demonstration that we are in fact measuring the domain wall being pushed through the constriction and not some different effect.

D. Domain wall placed closer to the notch and H_{depin} pointed outward the notch:

Reciprocally, in order to depin a domain wall in the direction away from the notch, where up to a point the domain wall is initially placed nearer the center, the required depinning field is higher than the case "**A**". This increase of the required depinning field can analogously be linked to a small favorable geometrical alignment of the depinning field with respect to the edge roughness or extrinsic pinning at the other ends of the half-ring, before the wall is expelled.

E. Domain wall placed very close to the notch:

Finally, in the center region of the graph plot (Figure 6.5b), for saturation angles between 80° and 110° (blue/red line, negative/positive H_{depin}), one can observe a plateau in the depinning field results where there is a small variation in the curves. At this extent of saturation angles the domain wall is already influenced by the pinning potential well created by the notch and is pulled into the constriction at zero field.

As has been shown previously, it is possible for the potential well, generated by the notch, to pull the domain wall form a significant distance away from the notch position [134]. In Figure 6.5b,

the plateau area at the middle (the angles between 80° and 110°) correspond to an angular range of around 35° which is equivalent to a distance of~ ±750 nm away from the center of the potential well. It is worth mentioning that the domain wall is usually attracted into the notch even when the domain wall is nucleated at larger absolute angles from the notch position, due to the domain wall initialization technique used in the experiment, which involves the reduction of the field from saturation [134].

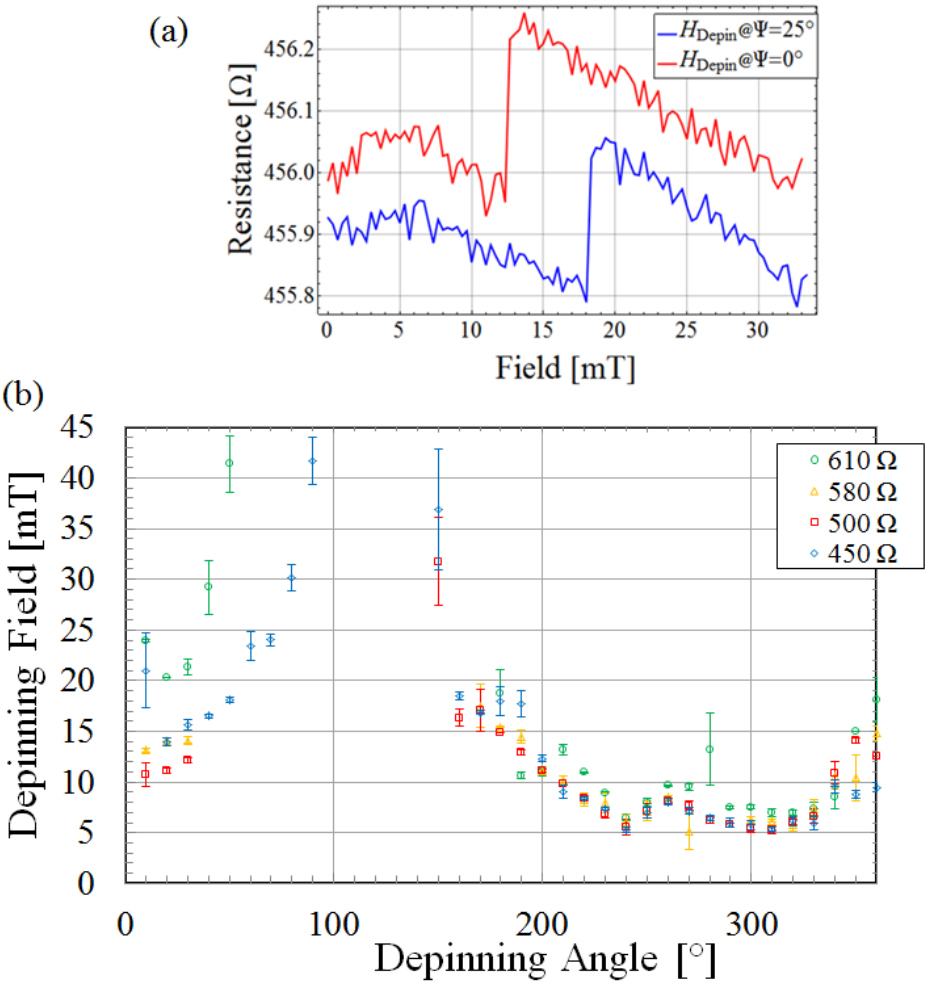

Figure 6.6: (a) The resistance as a function of the depinning field after DW nucleation at the notch position. The red curve represents a measurement where the DW is depinned with a field applied perpendicularly to the initializing nucleation field pulse (90°), requiring a field strength of 12 mT. For a depinning field that is closer to the angle of the initial nucleation pulse, however, a larger depinning field is required as demonstrated by the blue curve which reveals a depinning field of 18 mT for an angle of 25°. A small vertical offset has been added between the traces for clarity. **(b)** The field required to depin a DW from the notch for four different resistance states of the contact, as a function of the angle of the applied field. The overall trend is for the pinning to increase for increasing resistance, although local fluctuations are also seen [152].

In order to describe the asymmetry of the potential well, we should compare the depinning fields along the two orthogonal opposite directions to the nucleation field pulse, for the middle area where the domain wall is inside the potential well. We can clearly observe in Figure 6.5b that the potential is asymmetric, since there is a clear difference between both depinning fields $\pm H_{depin}$ (about 16 mT in the negative direction, $- H_{depin}$, compared to roughly around 12 mT in the positive direction, $+ H_{depin}$), although this difference is quite small compared to the asymmetry presented away from the notch. This can be explained by the fact that the notch geometry may itself exhibit small degree of asymmetry [134].

After electromigration, we do not observe significant consistent changes in the lateral extent of the potential well. The resulting depinning data for the highest resistance state, at the central region of interest, next to the constriction, is shown in the inset of Figure 6.5b. There is no considerable increase in the directional asymmetry of the potential. The observed results at this resistance level show us that the potential landscape has become more complicated than the lower resistance level, since for angles below 90° the depinning field is equal for both depinning directions, whereas for angles above 90° a slight difference in the depinning fields is seen, comparable to the results obtained at the previous resistance state. Finally, one can conclude that implementing our methodology it is possible to probe the asymmetries and the width of the potential well of the depinning resulting from the energy landscape created by the constriction.

Here we switch our attention to the angular dependence of the pinning potential well presented in Figure 6.6. In this figure we present the field required to depin a domain wall from the notch for four different resistance states in the contact, as a function of the applied depinning field angle ($\psi = 0° \rightarrow 360°$). It is clearly observed that the overall shape of the curves look very similar. This result is a further demonstration that we are capable to extract the details of the pinning potential from our measurements with a high reliability. In our experiment, we are able to reliably obtain a well-defined domain wall in the notch on relaxation from a saturated magnetization configuration, due to the geometry of our system in combination with our initialization procedure, which is not the case for some other studies [150, 189, 190].

In our case the stochasticity related to the transition of the domain wall into the notch and the spin structure variations during from the surrounding pad region [205] do not influence our measurement.

In order to explain the general shape of the graph in Figure 6.6, we take into account two main important regions of behavior. The first region is where the depinning field angle largely opposed to the direction of the initializing saturation field ($\sim\psi = 200°–340°$), where there is still a little difference between in the depinning field values for different resistance levels, shown in different color.

The second key region, is the part of the graph surrounding the nucleation field direction ($\psi = 90°$), where a more pronounced break between the curves is distinguished. It is obvious that the

lowest depinnig fields for the nanocontact are obtained in the first region (~ψ = 200°–340°). In this area, the ejection of the domain wall from the constriction can be expected to happen through the creeping of a reverse domain from the contact pad area at the end of the contact. As shown in Figure 6.1, the pads area of the structure is comparatively large, therefore the magnetization configuration is expected to be a complex multidomain state [205]. We note that the resulting domain wall type, after the initializing field pulse, is a head-to head domain wall. By applying a depinning field with in the angle range of (~ψ = 200°–340°), a tail-to-tail domain wall could thus propagate from one of the pads into the half-ring and end up at the constriction notch position, where it will annihilate with the initial head-to-head domain wall which remains pinned there. Since the pad area has a low resistance it must be not influenced by the electromigration and thus will have the same magnetization configuration for the different states. This is supported by the clear convergence of the plots for the different resistance states in this region of the graph.

In order to confirm this interpretation further we imaged the magnetic spin structure of a sample using the scanning electron microscopy with polarization analysis system (SEMPA) in our group. This was done after we finished all needed *in-situ* measurements on the sample. The imaging was proceeded by sample surface cleaning using a 1 kV Ar+ ion sputter gun, in order to remove any surface oxide layer formed during the *ex-situ* transfer of the sample between our UHV measurement and microscope chambers. The SEMPA setup is described in [206]. The obtained magnetic image, which show the magnetization configuration of the whole contact, is presented in Figure 6.7a in addition to a scanning electron microscope SEM image which is shown alongside (b) for comparison. Before imaging we saturated the sample in the notch by applying an initializing magnetic field pulse along the constriction, as was the case during the *in-situ* measurements, in order to get an identical magnetization configuration state within the sample exactly similar to what we had during our, previous characterization.

Firstly we can clearly observe that the magnetization configuration within the half-ring follows the contact edge, then at the contact center there is a change in contrast exactly at the constriction position which indicates that there is, as expected a nucleated a domain wall is presented at this contact point, Figure 6.7. However by looking at the two half-ring ends, it is clearly seen that a relatively complex domain configuration is formed. Specifically, in the bottom part of the left contact pad a big reversed domain (magnetic moment oriented in the opposite direction with respect to the saturated field pulse) can be observed in green as a portion of a vortex configuration. Subsequently, by applying a depinning field oriented along the spin structure within this domain, the domain will grow in size until pinned. One of the first intuitive pinning points is presented at the connection between the half ring and the pads due to the structure geometrical shape reduction at this region of the sample. However this pinning strength is expected to be much lower than the pinning at the central notch of the structure and will thus be overcome at lower fields. Then, the resulting opposing domain wall can creep up the side of the half-ring and approach to the notch site, where it will be annihilated with the other domain wall

presented at the central region of the contact and result in a quasi-uniform magnetized state within the half-ring.

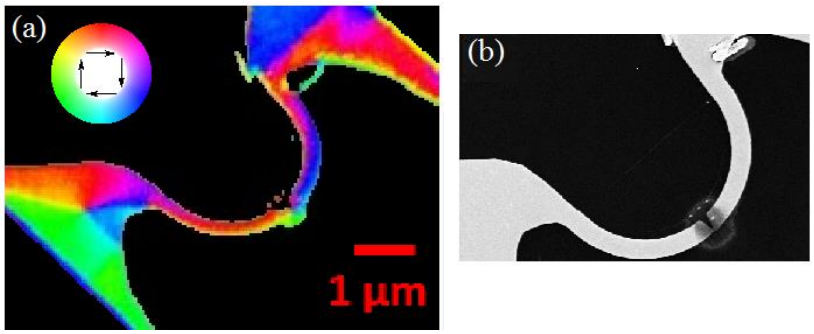

Figure 6.7: (a) SEMPA image depicting the magnetic domain configuration in the nanocontact, as indicated by the color disk. **(b)** An SEM image of the same region [152].

Using this hypothesis, we can therefore explain the peak in the depinning field around 270° as resulting from the angular dependence of the pinning of the magnetization in the pad area. Taking into account these considerations we deduce that the measured 'depinning-field' in, this region (~ψ = 200°–340°), does indeed constitute the injection field of a domain wall from the contact magnetic pad. Indeed, since the resulting domain wall annihilation process gives rise to a similar increase in the resistance to that of a domain wall depining from the constriction, both effects are difficult to be identified separately in the transport measurement. Although it should be kept in mind that in practice different effects will be happening depending on the measurement scheme, we keep using the terms depinning and depinning field as a general identification to these domain wall expulsion or annihilation procedures.

We now discuss area of the plots around ψ = 90°. This region is more interesting than the previous area for the present study since it can be direct related with true domain wall depinning from the constriction. As we can infer for the graph, in this region there are significant differences in depinning fields for the different resistance states (450 Ω, 500 Ω, 580 Ω and 610 Ω). Which indicate that the behavior must result from the changed pinning potential at this notch region, since this part of the contact is the only one which is modified with the electromigration process. At this region it can be observed, as expected, that one needs higher depinning fields in order to depin the domain wall along angles close to the half-ring center, since the component of the field oriented perpendicular to the constriction will have a sin(ψ) dependence. Moreover in the very close vicinity of the notch, the domain wall depinning is geometrically not allowed. According to the plot, it is obvious that the center of the potential is not symmetric at the center

of the half ring. The potential symmetry seems to be shifted to higher angles than ψ = 90°. This observed effect can be attributed to an angular shift in the narrowest part of the constriction geometry. It can result, for instance, from electromigration which did not happen symmetrically in the center of the constriction, analogous to the angular shift of the opened gap in the Co sample due to the electromigration in Figure 6.3b. Alternatively this shift maybe due to a small misalignment between the evaporator and the shadow mask during the initial material deposition. By making a comparison between the depinning measurements for different resistance states we could conclude that higher depinning fields are needed for smaller sized constrictions. In detail, a significant difference between the lowest and the highest resistance state can be clearly observed for angles between ψ (= 0° and 90°). However because of the changes in the nanocontact due to the electromigration, some local different preferred depinning direction maybe formed. This might explain the observed non-monotonous (for a specific angle) relation between the resistance and the depinning field, which leads to some additional fluctuations in the measurement.

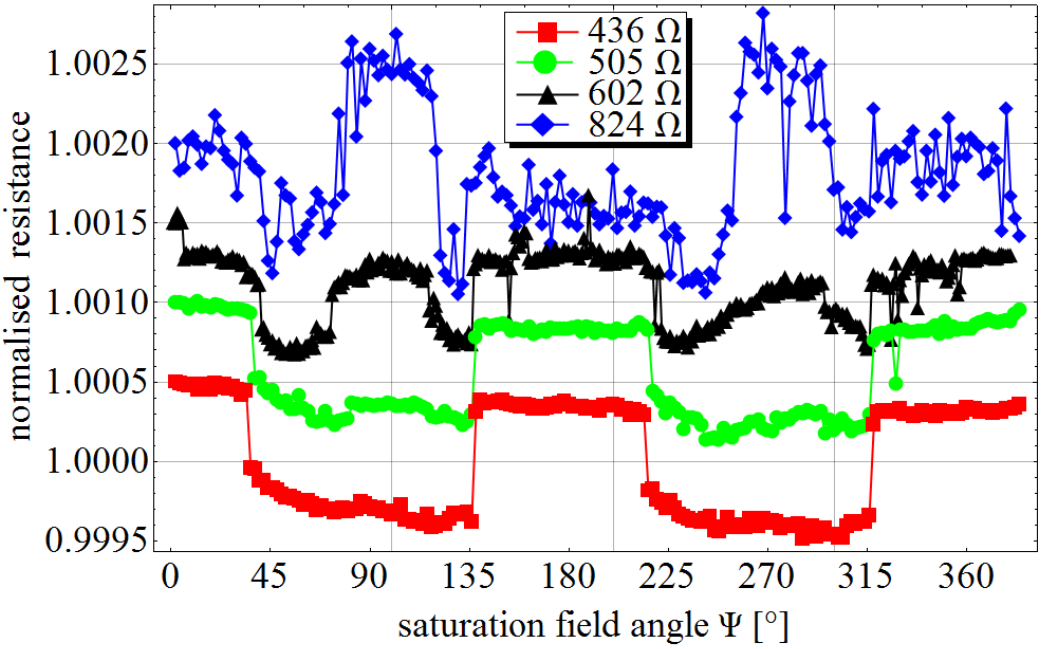

Figure 6.8: Mode étoile curves showing the resistance at remanence following saturation along the given angle, for different resistance states of the contact. Initially (red) two resistance states are observed corresponding to the presence (low R) or absence (high R) of a domain wall. For smaller contacts an increase in R around the notch (90/270°) is seen due to intrinsic DWMR. The data is normalized by its corresponding base resistance and for clarity separated by adding a small offset value [186].

We expect that the changes observed in the potential well of the domain wall are mainly correlated to the shape evolution of the contact size. Moreover, in addition to the geometrical

effects, there might be a local change of the material properties, during the electromigration process, which may lead to a local modification of the alloy composition, for instance. In general this can easily affect the measured depinning fields, for example due to the local changes of the saturation magnetization or the magnetic coercivity. However, in the periodic table the Ni and Fe are close therefore we anticipate the electromigration of these two materials to be similar [202] and thus no significant changes to the Ni/Fe stoichiometry are expected in the present studied regime. This would be expected to be more relevant when the single atom limit is reached, which is out of our focus in this study. Moreover, we expect a high localized temperature profile at the constriction leading to geometrical or compositional variation taking place at the constriction itself and not elsewhere in structure. This expectation is based on the fact that the notch is comparatively small in comparison to the standard grain size. Based on this, it is expected that some of the finer details and small fluctuation could arise from both local structure and material (composition) variations, but we expect that the larger effect should be dominated by the changes in the size of the constriction. In order to further investigate this, the spatial extent of the domain wall pinning potential is probed with mode étoile measurements presented in Figure 6.8.

This figure presents typical mode étoile curves for different resistance states. For the initial state of the contact (red squares) the resistance is 436 Ω and two different resistance levels at remanence can be discerned corresponding to the presence (low resistance) or absence (high resistance) of a domain wall in the half ring, due to the dominating AMR effect at this resistance regime, as previously explained. Since the measured signal is increasingly dominated by the notch, domain wall in the notch provides a high contribution to the total measured signal. These curves represent the evolution of the angular dependence after each electromigration step of the nanocontact and therefore decreasing the contact size. After several cycles of electromigration, the shape of the curve evolves at angles close to 90° (270°), which correspond to the constriction position.

By continuing with the electromigration we obtained the blue diamond curve in Figure 6.8, where the electrical resistance is roughly twice the starting value. Here, a domain wall at the constriction yields a resistance value higher than the state with no domain wall located in the nanostructure (see peaks at 90° (270°)) The height of the peak in relation to the base resistance (domain wall inside the half ring) gradually increases as the base resistance of the contact increases. This result is in contrast to the normal AMR effect in Permalloy, which leads to a resistance decrease in the curve at this position as was the case for the 436 Ω (red) curve. Hence, the peak can be unambiguously attributed to positive intrinsic MR produced by a domain wall located in the constriction. This peak in MR around the notch is seen to increase with decreasing contact size via electromigration. These measurements represent direct experimental evidence for a positive intrinsic DWMR contribution, where the resistance of the nanocontact is higher when a domain wall present in the constriction than the resistance without the domain wall. These results prove that the AMR effect is no longer the dominant effect at this resistance state contact size and another intrinsic contribution (*i.e.* DWMR) emerges.

In order to have a sense of the geometrical evolution of the nanocontact, it is possible to roughly estimate the contact size respecting the change in the resistance. An approximation of the contact size can be calculated using Wexler's formula [207] as reported in [185], which is valid between the diffusive and ballistic regime of conduction,

$$R_{contact} = \frac{4}{3\pi}\frac{\rho l}{r^2} + \gamma\frac{\rho}{2r} \quad , \quad \text{with } \gamma = \frac{1 + 0.83(l/r)}{1 + 1.33(l/r)}$$

Where ρ is the resistivity, l is the electron mean-free path, r is the contact radius. The effective radius of the contact can be calculated using an electron mean free path l = 1 nm [208], the Permalloy resistivity $\rho = 30\ \mu\Omega cm$ [209], correcting for a lead resistance of 440 Ω (obtained from the electromigration data) and a given $R_{contact}$.

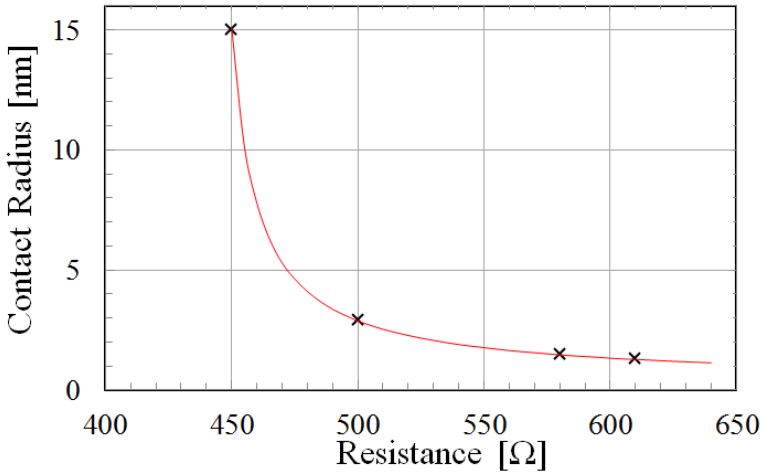

Figure 6.9: The relationship between the resistance of the nanocontact and the calculated contact radius at the notch position, as determined from Wexler's formula. The parameters used for the calculation are described in the text. The crosses in the figure, represent the contact radius for the four resistance states discussed in the present work [152].

The obtained calculation is given in Figure 6.9 where the estimated contact radii for the four resistances of interest to this study are indicated with crosses. We observe in the figure that the 610 Ω state is correlated to a nanocontact with the smallest radius (~1 nm) at the constriction position, which is a large difference from the initial width of the contact (~20 -15 nm). However, this calculation is only a low limit estimate of the contact radius, since these values assume a constant lead resistance and constant resistivity. To be more precise, for instance, the constant lead resistance hypothesis is valid only when the thinning of the contact by the electromigration is localized only on the constriction position. In general the calculated values from Wexler's formula can be considered a lower bound on the nanocontact magnitude. Furthermore as we could see, in Figure 6.3, which shows the SEM images of the nanocontacts after the completed electromigration at the end of the measurement, some transformation of the leads in the

proximity of the constriction may occur, even though the largest changes are confined to a narrow channel. This still suggests that the main contribution to the resistance change is changes to the junction region itself. In Figure 6.9 the initial deep slope of the resistance dependence of the contact radius demonstrates that only a small change in the resistance leads to major reduction in the size of the nanocontact area.

V. Conclusion

To summarize this chapter, we have studied the domain wall depinning, under clean UHV conditions, in nanocontacts made of Permalloy and thinned by the electromigrated break-junctions procedure.

We show that our carefully chosen structure and unique experimental methodology allow us to prevent many strong artefacts in the measurement, for instance local oxidation. This provides us with a high precision of controlling the magnetic configurations and properties of the structures, which is vital for such a measurement.

We demonstrate and we investigate the width of the potential well created by the constriction, and the asymmetry of the pinning potential that results from the asymmetry of the energy landscape of the system. These latter measurements have been done by measuring the depinning field along the two orthogonal directions to the domain wall positioned at different regions in the half-ring. In the proximity of the constriction position we found a low asymmetry in the pinning potential landscape. By positioning the domain wall at the constriction, we demonstrate that the pinning strength increases on decreasing the width of the constriction.

Moreover, in the domain wall expulsion/annihilation process or switching, we distinguished between the domain walls being annihilated by the propagation of a reversed domain to the one present at the notch, and simple depinning processes in relation to the field direction (ψ) with respect to the notch.

We show, using the mode étoile measurement technique, that for the low resistance diffusive transport regime the MR signal is initially dominated by AMR and the domain wall pinning potential is seen to increase with decreasing contact size. However for smaller contacts, a positive intrinsic DWMR contribution to the MR emerges.

Finally we confirm the expected spin structure configuration by direct imaging using (SEMPA) high resolution magnetic microscopy. This observed symmetry of the depinning fields combined with the observed tailoring of the pinning potential can auger well for applications. For example, the possible use of tailored nanocontacts where one is able to control the domain wall pinning in nanosystems down to a few atoms at the contact. This regime of study has not yet been reached by the top-down patterning techniques but might become more interesting in the future due to the continued need for the miniaturization of the technological devices while keeping, or even increasing, their efficiency.

Summary and Outlook

The overall aim of this work was to study the controlled propagation of magnetic domain walls in ferromagnetic nanowire made of Permalloy ($Ni_{80}Fe_{20}$), including curved geometries, with varying width (asymmetric rings). The investigation include both domain wall motion driven by fast rotating magnetic field pulses, as well the automotive propagation of domain walls in nanoscale spintronic devices. Additionally we accomplished a major breakthrough in the development of methods of information processing in spintronics, by successfully demonstrating a scheme that can induce synchronous motion of in-plane domain walls in ferromagnetic nanowires using perpendicular field pulses. The direct visualization of the domain wall spin structure in all experiments was performed employing the time resolved scanning transmission X-ray microscopy, which combines the requisite temporal and lateral resolution needed in our measurements. Furthermore, part of the research activities are based on the magneto-transport characterization of magnetic nanocontacts in order to understand the interaction between spin polarized charge carriers and magnetization on the nanoscale. In particular, the evolution of the domain wall magneto-resistance was investigate in electromigrated ferromagnetic nanocontact fabricated in ultra-high vacuum conditions.

In this thesis we discussed four specific subjects as follows:

- ✓ **Synchronous precessional motion of multiple domain walls in a ferromagnetic nanowire by perpendicular field pulses.** We proposed a radically different approach to domain wall motion using perpendicular field pulses which could provide the necessary paradigm shift to obtain the synchronous motion of multiple domain walls driven by magnetic fields, as required for devices such as the Racetrack memory. This is an efficient alternative to the current induced domain wall motion. We demonstrated that we can displace in-plane transverse walls by perpendicular magnetic field pulses. This achievement provides the required functionality for nonvolatile domain wall-based shift register devices. The experimental demonstration was supported by an extended analytical model (based on the one-dimensional model), and by micromagnetic simulations. The experimental observations showed a qualitative agreement with our analytical and numerical results, which confirm and demonstrate the viability of our proposed novel mechanism approach for domain wall motion. The transverse wall motion direction relies only on the chirality ($c = \pm 1$) of the transverse wall and the field direction. Analytically we showed, using the 1D collective coordinate domain wall profile model that the displacement of the transverse wall happens during the non-equilibrium dynamics when

the pulse is active. The net transverse wall displacement is obtained over a few hundred of nanometers with a high velocity, where the backward motion is suppressed using asymmetric field pulses and including periodic pining centers.

- ✓ **Local domain wall velocity engineering via tailored potential landscapes in asymmetric rings.** We have directly imaged controlled domain wall propagation in an asymmetric ring structure driven by rotating magnetic fields. The relevant forces acting on the domain wall are proportional to the applied field and the geometry of the inhomogeneous ring which leads to a spatially dependent domain wall potential landscape with a minimum domain wall energy, *U*, in the narrowest part of the ring and maximum velocity in the widest part. We demonstrate that the observed oscillatory velocity profile can be tailored by variations of the domain wall potential landscape, leading to a global maximum velocity in the widest part of the ring. Furthermore, the inhomogeneous domain wall potential landscape stabilizes the radial motion of the vortex core in the wall, keeping the internal spin structure constant and leading to the observed circular trajectory of the vortex core. We conclude that the oscillations must result from the variation of the ring width which is related to the varying tangential force arising from the non-zero phase difference, since the radial forces acting on the domain wall can be excluded and only the tangential forces should be considered. This is an important result since the latter effects, which in our case lead to these domain wall oscillations, can be extrinsically tailored and controlled by the geometry of the structure. The minimum of the domain wall energy landscape presented in the narrowest part of the ring leads to the spatial synchronization of domain wall velocities. Finally, we have demonstrated additionally that all micromagnetic simulation results are consistent with the experimental observations and explain the velocity oscillations as arising from the energetics of the asymmetric potential landscape.

- ✓ **Domain wall automotion induced by geometrical effects in asymmetric ferromagnetic rings.** We have directly imaged controlled domain wall automotion in asymmetric curved nanowires at zero field. We have demonstrated that automotive propagation occurs due to the influence of the demagnetization and exchange energy present in the structures. This automotion is driven by the domain wall spin structure interactions, which depends on the topology of the system and by the energy gradient associated with the spin structure change when the geometry changes. The pump and probe experiment of domain wall propagation at zero field showed, surprisingly, domain wall automotion with an average velocity of about ~ 60 m/s, which is a significant speed for spintronic devices based on domain wall dynamics. We demonstrate that the domain wall inertia and the stored energy allows the walls to overcome both the local extrinsic pinning and the topological repulsion between domain walls carrying the same winding number (vortex chirality). Furthermore we investigated the automotion mechanism in a series of samples having different widths in the narrowest part as well as different domain wall magnetic configurations. In particular we compare the results obtained for the automotive propagation of multiple vortex walls in the case of the same chirality and opposite chirality. Finally, we presented a systematic micromagnetic simulation study of domain wall motion at zero-field in 400 nm asymmetric rings with the wall possessing

different topological character. By performing a series of micromagnetic simulations on defect-free systems, we demonstrate that the domain wall automotion and annihilation is always present, and the results showed good quantitative agreement with our experimental results. Moreover we demonstrated that the detailed topological nature of the walls only influences the domain wall dynamics on a local scale without inhibiting the annihilation of domain walls through automotion. Thus in our system the influence of the topological defects is limited by locally modifying the domain wall propagation and the switching process between the two different ordered states.

- ✓ **Domain wall pinning in ultra-narrow electro-migrated constriction.** We have studied the domain wall depinning, under clean UHV conditions, in nanocontacts made of Permalloy and thinned by the electromigrated break-junctions procedure. We show that our carefully chosen structure and unique experimental methodology allow us to prevent many strong artefacts in the measurement, for instance local oxidation. This provides us with a high precision of controlling the magnetic configurations and properties of the structures, which is vital for such a measurement. We demonstrate and we investigate the width of the potential well created by the constriction, and the asymmetry of the pinning potential that results from the asymmetry of the energy landscape of the system. Moreover, in the domain wall expulsion/annihilation process or switching, we distinguished between the domain walls being annihilated by the propagation of a reversed domain to the notch, and simple depinning processes of domain walls from the notch. We show, using the mode étoile measurement technique, that for the low resistance diffusive transport regime the MR signal is initially dominated by AMR and the domain wall pinning potential is seen to increase with decreasing contact size. However for smaller contacts, a positive intrinsic DWMR contribution to the MR emerges. Finally we confirm the expected spin structure configuration by direct imaging using (SEMPA) high resolution magnetic microscopy. This observed symmetry of the depinning fields combined with the observed tailoring of the pinning potential can auger well for applications. For example, the possible use of tailored nanocontacts where one is able to control the domain wall pinning in nanosystems down to a few atoms at the contact. This regime of study has not yet been reached by the top-down patterning techniques but might become more interesting in the future due to the continued need for the miniaturization of the technological devices while keeping, or even increasing, their efficiency.

In addition to the wealth of knowledge and the new results achieved in this work, there are several new ideas developed which not yet have been investigated and which can be considered as an outlook for this thesis. For example, experimentally investigating the influence of the domain wall potential landscape on its propagation at different driving speeds in asymmetric rings with locally varying ring width. This includes gradually changing widths yielding constant potential gradients and abrupt changes induced by notches. Moreover in this proposed experiment we will start with the domain wall at different positions, and observe the wall getting pinned by and depinned from the notch as a function of wall velocity and distance of the starting point from the notch. The observation of these processes would allow one to tailor the motion of domain walls to eventually

allow for a deterministically displacement. (Depending on the change in the domain wall spin structure, the pinning will have a different strength). The understanding of such mechanisms would potentially allow for further deterministic control of the domain wall propagation.

Another interesting area of study is the dynamics of the switching process from the vortex to the onion states of rings during the nucleation of domain walls.

Initial results in this area for asymmetric structures have been obtained which are not reported in this thesis, but which have just been submitted for publication [210]. Here we show that the vortex state in the ring structure is particularly resistant to the rotating field pulse when the sense of rotation is opposite to the spin structure direction in the initial vortex state. The direct visualization of the domain wall spin structure shows that the switching process from the vortex to the onion state is done through creation of transient ripple-like magnetization patterns during the nucleation of the domain walls. This is found to be highly reproducible and characterized by a relatively long life time which determines the overall time of this switching process. We experimentally demonstrated that this reproducible nucleation process depends on the details of the external field and on the shape/width of the ring structure. By performing micromagnetic simulations we showed that the nucleation event occurs in the energetically unfavorable half-ring and its position is determined by stray fields emerging from sample shape. These factors play a major role in the prediction and engineering of novel spintronic devices employing switching process.

Furthermore for high densities of nanowires, as required in high density storage and memory devices, we have to take into account the mutual interaction of domain walls and the effect of these interactions on the domain wall dynamics. Thus we developed a new experimental system using curved magnetic nanowires (see Figure 2.17) in order to determine domain wall velocity variations due to interactions of domain walls in neighboring wires, which is expected to depend on the pinning potential generated by the neighboring domain wall stray field that acts as an energy barrier. Previous work has studied such domain wall interactions statically and by theoretical calculations, but the vital dynamic imaging is currently lacking. Here, the idea is to dynamically image the domain wall spin structure and determine the domain wall velocity, since the energy barrier, in particular, depends on the domain wall spin structure and the changing domain wall velocity is a direct measure of the potential depth.

Overall, our exciting new results obtained in the scope of this thesis, pave the way for the development of a new generation of non-volatile spintronic components, which could be implemented in a wide range of applications for logic, sensing as well as data storage devices based on the reliable and reproducible manipulation of the domain wall.

Bibliography

[1] S. Blundell. Magnetism in Condensed Matter. *Oxford Master Series in Condensed Matter Physics* (2001).

[2] P. Weiss. La variation du ferromagnétisme avec la temperature. *Compt. Rend.* **143**, 1136 (1906).

[3] P. Weiss. L'hypothèse du champ moléculaire et la propriété ferromagnétique. *J. Phys.* **6**, 661 (1907).

[4] E. C. Stoner, E. P. Wohlfarth. A Mechanism of Magnetic Hysteresis in Heterogeneous Alloys. *Trans. Roy. Soc. A* **240**, 599 (1948).

[5] O. Boulle, G. Malinowski, M. Kläui. Current-induced domain wall motion in nanoscale ferromagnetic elements. *Materials Science and Engineering R* **72**, Issue 9, 159 –187 (2011).

[6] A. Hubert, R. Schäfer, Magnetic Domains - The Analysis of Magnetic Microstructures, Springer, Berlin, Heidelberg, New York (1998).

[7] L. D. Landau, E. Lifshitz, *Phys. Z. Sowjetunion* **8**, 153–169 (1935).

[8] F. Bloch. Zur Theorie des Austauschproblems und der Remanenzerscheinung der Ferromagnetika. *Z. Phys. A* **74**, 295–335 (1932).

[9] H. Kronmüller, M. Fähnle, Micromagnetism and the Microstructure of Ferromagnetic Solids, Cambridge University Press, Cambridge, (2003).

[10] M. Kläui, C. A. F. Vaz, H. Kronmüller, S. S. P. Parkin. Handbook of Magnetism and Advanced Magnetic Materials, Volume **2**, John Wiley and Sons, Chichester, (2007).

[11] R. D. McMichael and M. J. Donahue. Head to head domain wall structures in thin magnetic strips *IEEE Trans. Magn.* **33**, 4167–4169 (1997).

[12] E. Feldtkeller and H. Thomas. Struktur und Energie von Blochlinien in dünnen ferromagnetischen Schichten. *Z. Phys. B Cond. Mat.* **4**, (1965).

[13] S. Jamet, N. Rougemaille, J. -C. Toussaint, O. Fruchart. Head-to-head domain walls in one-dimensional nanostructures: an extended phase diagram ranging from strips to cylindrical wires. **arXiv:1412.0679** [cond-mat.mes-hall] (2014).

[14] Y. Nakatani, A. Thiaville, and J. Miltat. Head-to-head domain walls in soft nano-strips: a refined phase diagram. *Journal of Magnetism and Magnetic Materials* **290-291(1)**, 750-753 (2005).

[15] M. Laufenberg, D. Backes, W. Bührer, D. Bedau, M. Kläui, U. Rüdiger, C.A.F. Vaz, J. A. C. Bland, L. J. Heyderman, F. Nolting, S. Cherifi, A. Locatelli, R. Belkhou, S. Heun, and E. Bauer. Observation of thermally activated domain wall transformations. *Appl. Phys. Lett.* **88**, 052507 (2006).

[16] J. K. Ha, R. Hertel and J. Kirschner. Micromagnetic study of magnetic configurations in submicron permalloy disks. *Phys. Rev. B* **67**, 224432 (2003).

[17] J. Stöhr and H. C. Siegmann. Magnetism: From Fundamentals to Nanoscale Dynamics (Springer, Berlin, 2006).

[18] A. Aharoni. Introduction to the theory of ferromagnetism. 2nd. Oxford, (2000).

[19] M. E. Fischer. Magnetism in one-dimensional systems - The Heisenberg model for infinite spin. *Am. J. Phys.* **32**, 343–346 (1964).

[20] W. F. Brown. Micromagnetics (Krieger, New York, 1963).

[21] L. Landau and E. Lifshitz. On the theory of the dispersion of magnetic permeability in ferromagnetic bodies. *Phys. Zeitsch. Sow.* **8**, 153–169 (1935).

[22] T. L. Gilbert. A lagrangian formulation of the gyromagnetic equation of the magnetic field. *Phys. Rev.* **100**, 1243 (1955).

[23] G. S. D. Beach, M. Tsoi, and J. L. Erskine. Current-induced domain wall motion. *J. Magn. Magn. Mater.* **320**, 1272 (2008).

[24] A. Bisig, M. Stärk, M. -A. Mawass, C. Moutafis, J. Rhensius, J. Heidler, F. Büttner, M. Noske, M. Weigand, S. Eisebitt, T. Tyliszczak, B. V. Waeyenberge, H. Stoll, G. Schütz and M. Kläui. Correlation between spin structure oscillations and domain wall velocities. *Nat. Commun* **4**, 2328 (2013).

[25] A. P. Malozemoff and J. C. Slonczewski. Magnetic domain walls in bubble material. *Academic, New York* (1979).

[26] B. Hillebrands, A. Thiaville (Eds.): Spin dynamics in confined magnetic structure III. Chapter: Domain wall dynamics in nanowires and nanostrip. A. Thiaville, Y. Nakatani. *Topics Appl. Physics* **101**, 161-205 (2006). (Springer-Verlag, Berlin Heidelberg, 2006).

[27] N. L. Schryer, L. R. Walker. The motion of 180° domain walls in uniform dc magnetic fields. *J. Appl. Phys.* **45**, 5406 (1974).

[28] A. Mougin, M. Cormier, J. P. Adam, P. J. Metaxas and J. Ferré. Domain wall mobility, stability and Walker breakdown in magnetic nanowires. *Europhys. Lett.* **78**, 57007 (2007).

[29] J. Yang, C. Nistor, G. Beach, and J. Erskine. Magnetic domain-wall velocity oscillations in permalloy nanowires. *Phys. Rev. B* **77**, 014413 (2008).

[30] D. J. Clarke, O. A. Tretiakov, G. -W. Chern, Ya. B. Bazaliy, O. Tchernyshyov, Dynamics of a vortex domain wall in a magnetic nanostrip: Application of the collective-coordinate approach. *Phys. Rev. B* **78**, 134412 (2008).

[31] L. F. Yin, D. H. Wei, N. Lei, L. H. Zhou, C. S. Tian, G. S. Dong, X. F. Jin, L. P. Guo, Q. J. Jia, and R. Q. Wu. Magnetocrystalline anisotropy in permalloy revisited. *Phys. Rev. Lett.* **97**, 067203 (2006).

[32] P. M. Tedrow and R. Meservey. Spin polarization of electrons tunneling from films of fe, co, ni, and gd. *Phys. Rev. B* **7**, 318–326 (1973).

[33] R. J. Soulen, J. M. Byers, M. S. Osofsky, B. Nadgorny, T. Ambrose, S. F. Cheng, P. R. Broussard, C. T. Tanaka, J. Nowak, J. S. Moodera, A. Barry, J. M. D. Coey. Measuring the spin polarization of a metal with a superconducting point contact. *Science* **282**, 85–88 (1998).

[34] A. F. Mayadas, J. F. Janak and A. Gangulee. Resistivity of permalloy thin films. *J. Appl. Phys.* **45**, 2780–2781 (1974).

[35] S. Kasai, Y. Nakatani, K. Kobayashi, H. Kohno and T. Ono. Current-Driven resonant excitation of magnetic vortices. *Phys. Rev. Lett.* **97**, 107204 (2006).

[36] J. Stöhr. X-ray magnetic circular dichroism spectroscopy of transition metal thin films. *J. Electron Spectrosc.* **75**, 253–272 (1995).

[37] M. Hatzakis. Electron beam processing systems (a state of the art review). *Polymer Engineering and Science* **14**, (1974).

[38] Raith GmbH. Raith PIONEER data sheet. URL http://www.raith.com.

[39] MicroChem. NANO™PMMA and Copolymer, data sheet, (2001).

[40] Rainer Behrisch. Sputtering by particle bombardment. *Topics in applied physics*. Springer, Berlin (2007).

[41] Krishna Seshan. Handbook of thin-film deposition processes and techniques. *Noyes Publications*, (2002).

[42] E. Beaurepaire, H. Bulou, F. Scheurer and J.-P. Kappler. Magnetism: A Synchrotron Radiation Approach (Springer, Berlin, 2006).

[43] G. Schütz, W. Wagner, W. Wilhelm, P. Kienle, R. Zeller, R. Frahm, and G. Materlik. Absorption of circularly polarized x rays in iron. *Phys. Rev. Lett.* **58**, 737–740 (1987).

[44] T. Warwick *et al.* A scanning transmission x-ray microscope for materials science spectromicroscopy at the advanced light source. *Review of Scientific Instruments*, **69(8)**: 2964-2973, (1998).

[45] P. Fischer, T. Eimüller, G. Schütz, M. Köhler, G. Bayreuther, G. Denbeaux and D. Attwood. Study of in-plane magnetic domains with magnetic transmission x-ray microscopy. *J. Appl. Phys.* **89**, 7159-7161, (2001).

[46] S. Anders *et al*. Photoemission electron microscope for the study of magnetic materials. *Review of Scientific Instruments*, **70(10)**:3973-3981, (1999).

[47] S. Eisebitt *et al.* Lensless imaging of magnetic nanostructures by x-ray spectroholography. *Nature* **432**, 885–888 (2004).

[48] B. Hillebrands, K. Ounadjela (Eds.): Spin Dynamics in Confined Magnetic Structures II, *Topics Appl. Phys.* **87**, 155–185 Springer-Verlag Berlin Heidelberg (2003).

[49] http://neel.cnrs.fr/

[50] J. Stöhr, Y. Wu, in: A.S. Schlacter, F.J. Wuilleumier (Eds.), New Directions in Research with Third-Generation Soft X-Ray Synchrotron Radiation Sources, Kluwer, Amsterdam, (1994).

[51] H. Wende and C. Antoniak. X-ray magnetic dichroism. In E. Beaurepaire, H. Bulou, F. Scheurer and K. Jean-Paul (eds.) Magnetism and Synchrotron Radiation (Springer, Berlin, 2010).

[52] M. Blume, Doone Gibbs. *Phys. Rev. B* **37**, 1779. (1988).

[53] E. Beaurepaire, F. Scheurer, G. Krill, J.-P. Kappler (Eds.) Magnetism and synchrotron Radiation; LNP; Springer. Chapter: Dichroism in X-ray Absorption, Maurizio Sacchi and Jan Vogel.

[54] http://www.synchrotron-soleil.fr/

[55] M. Abo-Bakr. Bunch length measurement at bessy. In Proceedings of the 2003 Particle Accelerator Conference, (2003).

[56] A. L. D. Kilcoyne *et al.* Interferometer-controlled scanning transmission x-ray microscopes at the advanced light source. *Journal of Synchrotron Radiation*, **10**:125-136, (2003).

[57] P Horowitz. Scanning X-Ray Microscope Using Synchrotron Radiation. *Science*, **178**, (4061):608 - &, (1972).

[58] U. Wiesemann *et al.* First results of the new scanning transmission X-ray microscope at BESSYII. *Journal de physique IV* **104**: 95-98, (2003).

[59] A. L. D. Kilcoyne *et. al. Journal of synchrotron radiation* **10**(Pt 2), 125-136 (2003).

[60] W. L. Chao, B. D. Harteneck, J. A. Liddle, E. H. Anderson, and D. T. Attwood. Soft X-ray microscopy at a spatial resolution better than 15nm. *Nature*, **435**:1210-1213 (2005).

[61] Helmholz Zentrum Berlin - http://www.helmholtz-berlin.de/.

[62] J. Rhensius, M. Kläui, L. Heyne. Imaging of domain wall inertia in permalloy Half-Ring nanowires by Time-Resolved photoemission electron microscopy. *Phys. Rev. Lett.* **104**, 067201 (2010).

[63] H. E. Knoepfel. Magnetic Fields: A Comprehensive Theoretical Treatise for Practical Use. *ohn Wiley & Sons*, **Science** 643 (2008).

[64] M. Kläui, C. A. F. Vaz, L. Lopez-Diaz and J. A. C. Bland. Vortex formation in narrow ferromagnetic rings. *J. Phys.: Condens. Matter* **15**, 985 (2003).

[65] J. Rothman, M. Kläui, L. Lopez-Diaz, C. A. F. Vaz, A. Bleloch, J. A. C. Bland, Z. Cui, and R. Speaks. Observation of a Bi-Domain state and nucleation free switching in mesoscopic ring magnets. *Phys. Rev. Lett.* **86**, 1098–1101 (2001).

[66] M. Kläui. Head-to-head domain walls in magnetic nanostructures. *J. Phys. Condens. Mat.* **20**, 313001 (2008).

[67] M. Negoita, T. J. Hayward and D. A. Allwood. Controlling domain walls velocities in ferromagnetic ring-shaped nanowires. *Appl. Phys. Lett.* **100**, 072405 (2012).

[68] A. O. Adeyeye et al. Size dependence of the magnetoresistance in submicron FeNi wires. *J. Appl. Phys.* **79**, 6120–6122 (1996).

[69] M. Curcic, H. Stoll, M. Weigand, V. Sackmann, P. Juellig, M. Kammerer, M. Noske, M. Sproll, B. V. Waeyenberge, A. Vansteenkiste, G. Woltersdorf, T. Tyliszczak and G. Schütz. Magnetic vortex core reversal by rotating magnetic fields generated on micrometer length scales. *Phys. Status Solidi B* **248**, 2317–2322 (2011).

[70] J. -S. Kim, M. -A. Mawass, A. Bisig, B. Krüger, R. Reeve, T. Schulz, F. Büttner, M. Weigand, H. Stoll, J. Yoon, C. -Y. You, G. Schütz, H. J. M. Swagten, B. Koopmans, S. Eisebitt and M. Kläui. *Nat. Commun*. **5**, 3429 (2014).

[71] D. A. Allwood, G. Xiong, C. C. Faulkner, D. Atkinson, D. Petit, and R. P. Cowburn Magnetic domain-wall logic. *Science* **309**, 1688-1692 (2005).

[72] S. S. P. Parkin. Shiftable magnetic shift register and method of using same. US patent 6,834,005 (2004).

[73] S. S. P. Parkin, M. Hayashi and L. Thomas. Magnetic domain-wall racetrack memory. *Science* **320**, 190–194 (2008).

[74] P. Xu, K Xia, C. Gu, L. Tang, H. Yang, J. Li. An all-metallic logic gate based on current-driven domain wall motion. *Nat. Nanotech.* **3**, 97–100 (2008).

[75] M. Diegel, S. Glathe, R. Mattheis, M. Scherzinger and E. Halder. A new four bit magnetic domain wall based multiturn counter. *IEEE Trans. Magn.* **45**, 3792–3795 (2009).

[76] D. Atkinson, D. A. Allwood, G. Xiong, M. D. Cooke, C. C. Faulkner and R. P. Cowburn. Magnetic domain-wall dynamics in a submicrometre ferromagnetic structure. *Nat. Mater.* **2**, 85–87 (2003).

[77] G. S. D. Beach, C. Nistor, C. Knutson, M. Tsoi, J. L. Erskine. Dynamics of field-driven domain-wall propagation in ferromagnetic nanowires. *Nat. Mater.* **4**, 741–744 (2005).

[78] M. Hayashi, L. Thomas, Y. B. Bazaliy, C. Rettner, R. Moriya, X. Jiang, and S. S. P. Parkin. Influence of current on field-driven domain wall motion in permalloy nanowires from time resolved measurements of anisotropic magnetoresistance. *Phys. Rev. Lett.* **96**, 197207 (2006).

[79] D. Ilgaz, M. Kläui, L. Heyne, O. Boulle, F. Zinser, S. Krzyk, M. Fonin, U. Rüdiger, D. Backes and L. J. Heyderman. Selective domain wall depinning by localized Oersted fields and Joule heating. *Appl. Phys. Lett.* **93**, 132503 (2008).

[80] R. P. Cowburn *et al.* Data storage device and method. Patent WO/2007/132174 (2007).

[81] J. H. Franken, H. J. M. Swagten and B. Koopmans. Shift registers based on magnetic domain wall ratchets with perpendicular anisotropy. *Nat. Nanotech.* **7**, 499–503 (2012).

[82] A. Yamaguchi, T. Ono, S. Nasu, K. Miyake, K. Mibu, and T. Shinjo. Real-space observation of current-driven domain wall motion in submicron magnetic wires. *Phys. Rev. Lett.* **92**, 077205 (2004).

[83] M. Kläui, P. -O. Jubert, R. Allenspach, A. Bischof, J. A. C. Bland, G. Faini, U. Rüdiger, C. A. F. Vaz, L. Vila, and C. Vouille. Direct observation of domain-wall configuration transformed by spin currents. *Phys. Rev. Lett.* **95**, 026601 (2005).

[84] J. Grollier *et al.* Switching a spin valve back and forth by current-induced domain wall motion. *Appl. Phys. Lett.* **83**, 509–511 (2003).

[85] C. -Y. You, I. -M. Sung, and B. -K. Joe. Analytic expression for the temperature of the current-heated nanowire for the current-induced domain wall motion. *Appl. Phys. Lett.* **89**, 222513 (2006).

[86] C.-Y. You and Ha, S.-S. Temperature increment in a current-heated nanowire for current-induced domain wall motion with finite thickness insulator layer. *Appl. Phys. Lett.* **91**, 022507 (2007).

[87] I. M. Miron, K. Garello, G. Gaudin, P. -J. Zermatten, M. V. Costache, S. Auffret, S. Bandiera, B. Rodmacq, A. Schuhl and P. Gambardella. Perpendicular switching of a single ferromagnetic layer induced by in-plane current injection. *Nature* **476**, 189–193 (2011).

[88] L. Liu, C. -F. Pai, Y. Li, H. W. Tseng, D. C. Ralph, R. A. Buhrman. Spin-torque switching with the giant spin Hall effect of tantalum. *Science* **336**, 555–558 (2012).

[89] P. P. J. Haazen, *et al.* Domain wall depinning governed by the spin Hall effect. *Nat. Mater.* **12**, 299–303 (2013).

[90] J. -Y. Lee, K. -S. Lee and S. -K. Kim. Remarkable enhancement of domain-wall velocity in magnetic nanostripes. *Appl. Phys. Lett.* **91**, 122513 (2007).

[91] A. Kunz and S. C. Reiff. Fast domain wall motion in nanostripes with out-of-plane fields. *Appl. Phys. Lett.* **93**, 082503 (2008).

[92] S. Zhang and Z. Li. Roles of nonequilibrium conduction electrons on the magnetization dynamics of ferromagnets. *Phys. Rev. Lett.* **93**, 127204 (2004).

[93] A. Thiaville, Y. Nakatani, J. Miltat and Y. Suzuki. Micromagnetic understanding of current driven domain wall motion in patterned nanowires. *Europhys. Lett.* **69**, 990–996 (2005).

[94] G. Tatara and H. Kohno. Theory of current-driven domain wall motion: spin transfer versus momentum transfer. *Phys. Rev. Lett.* **92**, 086601 (2004).

[95] L. Thomas, M. Hayashi, X. Jiang, R. Moriya, C. Rettner and S. S. P. Parkin. Oscillatory dependence of current-driven magnetic domain wall motion on current pulse length. *Nature* **443**, 197–200 (2006).

[96] H. W. Schumacher, C. Chappert, P. Crozat, R. C. Sousa, P. P. Freitas, J. Miltat, J. Fassbender, and B. Hillebrands. Phase coherent precessional magnetization reversal in microscopic spin valve elements. *Phys. Rev. Lett.* **90**, 017201 (2003).

[97] M. Muñoz and J. L. Prieto. Suppression of the intrinsic stochastic pinning of domain walls in magnetic nanostripes. *Nat. Commun.* **2**, 562 (2011).

[98] T. A. Moore *et al.* Magnetic-field-induced domain-wall motion in permalloy nanowire with modified Gilbert damping. *Phys. Rev. B* **82**, 094445 (2010).

[99] L. Bocklage, B. Krüger, T. Matsuyama, M. Bolte, U. Merkt, D. Pfannkuche and G. Meier Dependence of magnetic domain-wall motion on a fast changing current. *Phys Rev. Lett.* **103**, 197204 (2009).

[100] S. -M. Ahn, K. -W. Moon, D. -H. Kim and S. -B. Choe. Detection of the static and kinetic pinning of domain walls in ferromagnetic nanowires. *Appl. Phys. Lett.* **95**, 152506 (2009).

[101] S. -M. Ahn, D. -H. Kim and S. -B. Choe. Kinetic and static domain-wall pinning at notches on ferromagnetic nanowires. *IEEE Trans. Magn.* **45**, 2478–2480 (2009).

[102] D. Bedau, M. Kläui, M. T. Hua, S. Krzyk, U. Rüdiger, G. Faini, and L. Vila. Quantitative determination of the nonlinear pinning potential for a magnetic domain wall. *Phys. Rev. Lett.* **101**, 256602 (2008).

[103] P. -O. Jubert, M. Kläui, and A. Bischof. Velocity of vortex walls moved by current. *J. Appl. Phys.* **99**, 08G523 (2006).

[104] L. Heyne, J. Rhensius, A. Bisig, S. Krzyk, P. Punke, M. Kläui, L. J. Heyderman, L. L. Guyader and F. Nolting. Direct observation of high velocity current induced domain wall motion. *Appl. Phys. Lett.* **96**, 032504 (2010).

[105] R. J. Soulen Jr., J. M. Byers, M. S. Osofsky, B. Nadgorny, T. Ambrose, S. F. Cheng, P. R. Broussard, C. T. Tanaka, J. Nowak, J. S. Moodera, A. Barry, J. M. D. Coey. Measuring the spin polarization of a metal with a superconducting point contact. *Science* **282**, 85–88 (1998).

[106] G. Nahrwold, L. Bocklage, J. M. Scholtyssek, T. Matsuyama, B. Krüger, U. Merkt and G. Meier. Current-induced domain-wall depinning in curved Permalloy nanowires. *J. Appl. Phys.* **105**, 07D511 (2009).

[107] O. Tchernyshyov and G. -W. Chern. Fractional vortices and composite domain walls in flat nanomagnets. *Phys. Rev. Lett.* **95**, 197204 (2005).

[108] J. -G. Zhu, Y. Zheng, G. A. Prinz, Ultrahigh density vertical magnetoresistive random access memory. *J. Appl. Phys.* **87**, 6668 (2000).

[109] A. Imre, L. Zhou, A. Orlov, G. Csaba, G.H. Bernstein, W. Porod, V. Metlushko. Application of mesoscopic magnetic rings for logic devices. *4th IEEE Conference on Nanotechnology*, **137**, (2004).

[110] M. Kläui, H. Ehrke, U. Rüdiger, T. Kasama, R. E. Durin-Borkowski, D. Beckes, L. J. Heyderman, C. A. F. Vaz, J. A. C. Bland, G. Faini, E. Cambril, W. Wernsdorfer. Direct observation of domain-wall pinning at nanoscale constrictions. *App. Phys. Lett.* **87**, 102509 (2005).

[111] H. Y. Yuan, X. R. Wang, Domain wall pinning in notched nanowires. *Phys. Rev. B* **89**, 054423 (2014).

[112] D. Petit, A. -V. Jausovec, D. Read, R. P. Cowburn. Domain wall pinning and potential landscapes created by constrictions and protrusions in ferromagnetic nanowires. *J. Appl. Phys.* **103**, 114307 (2008).

[113] O. A. Tretiakov, Y. Liu, A. Abanov. Domain-wall dynamics in translationally nonivariant nanowires: Theory and Applications. *Phys. Rev. Lett.* **108**, 247201 (2012).

[114] K. Richter, A. Krone, M. -A. Mawass, B. Krüger, M. Weigand, H. Stoll, G. Schütz, and M. Kläui. Local Domain-Wall Velocity Engineering via Tailored Potential Landscapes in Ferromagnetic Rings. *Phys. Rev. Applied* **5**, 024007 (2016).

[115] A. Goldman, A. S. Licht, Y. Sun, Y. Li, N. R. Pradhan, T. Yang, M. T. Tuominen, and K. E. Aidala. Multiple 360° domain wall switching in thin ferromagnetic nanorings in a circular magnetic field. *J. Appl. Phys.* **111**, 07D113 (2012).

[116] L. Heyne, J. Rhensius, D. Bedau and S. Krzyk. Geometry-dependent scaling of critical current densities for current-induced domain wall motion and transformations. *Phys. Rev. B* **80**, 184405 (2009).

[117] L. Thomas, R. Moriya, C. Rettner and S. S. P. Parkin. Dynamics of magnetic domain walls under their own inertia. *Science* **330**, 1810–1813 (2010).

[118] A. Bisig, M. A. Mawass, M. Stärk, C. Moutafis, J. Rhensius, J. Heidler, S. Gliga, M. Weigand, T. Tyliszczak, B. V. Waeyenberge, H. Stoll, G. Schütz, M. Kläui. Dynamics domain wall chirality rectification by rotating magnetic fields. *Appl. Phys. Lett*. **106**, 122401 (2015).

[119] Y. Nakatani, A. Thiaville and J. Miltat. Faster magnetic walls in rough wires. *Nat. Mater*. **2**, 521–523 (2003).

[120] E. R. Lewis, D. Petit, L. O'Brien, A. Fernandez-Pacheco, J. Sampaio, A. -V. Jausovec, H. T. Zeng, D. E. Read and R. P. Cowburn. Fast domain wall motion in magnetic comb structures. *Nat. Mater* **9**, 980 (2010).

[121] A. Thiele. A Steady-state motion of magnetic domains. *Phys. Rev. Lett.* **30**, 230–233 (1973).

[122] D. L. Huber. Dynamics of spin vortices in two-dimensional planar magnets. *Phys. Rev. B* **26**, 3758–3765 (1982).

[123] http://micromagnum.informatik.uni-hamburg.de/

[124] T. A. Moore, M. Kläui, L. Heyne, P. Möhrke, D. Backes, J. Rhensius, U. Rüdiger, L. J. Heyderman, J. -U. Thiele, G. Woltersdorf, C. H. Back, A. Fraile Rodriguez, F. Nolting, T. O. Mentes, M. A. Nino, A. Locatelli, A. Potenza, H. Marchetto, S. Cavill, and S. S. Dhesi. Scaling of spin relaxation and angular momentum dissipation in permalloy nanowires. *Phys. Rev. B* **80**, 132403 (2009).

[125] Klaus D. Sattler (Eds.): Handbook of Nanophysics: Nanoelectronics and Nanophotonics. *CRC Press*- **Science** - 779 pages, (Sep 17, 2010).

[126] J. He, Z. Li, and S. Zhang. Current-driven vortex domain wall dynamics by micromagnetic simulations. *Phys. Rev. B* **73**, 184408 (2006).

[127] A. Wachowiak, J. Wiebe, M. Bode, O. Pietzsch, M. Morgenstern, and R. Wiesendanger. Direct observation of internal spin structure of magnetic vortex cores. *Science* **298**, 577 (2002).

[128] F. Q. Zhu, G. W. Chern, O. Tchernyshyov, X. C. Zhu, and C. L. Chien. Magnetic Bistability and Controllable Reversal of Asymmetric Ferromagnetic Nanorings. *Phys. Rev. Lett.* **96**, 027205 (2006).

[129] S. McVietie, G. S. White, J. Scott, P. Warin, and J. N. Chapman. Quantitative imaging of magnetic domain walls in thin films using Lorentz and magnetic force microscopies. *J. Appl. Phys*. **90**, 5220 (2001).

[130] P. -O. Jubert, R. Allenspach, and A. Bischof. Magnetic domain walls in constrained geometries. *Phys. Rev. B* **69**, 220410 (2004).

[131] P. Bruno. Geometrically Constrained Magnetic Wall. *Phys. Rev. Lett.* **83**, 2425 (1999).

[132] M. Kläui, C. A. F. Vaz, W. Wernsdorfer, E. Bauer, S. Cherifi, S. Heun, A. Locatelli, G. Faini, E. Cambril, L. J. Heyderman, and J. A. C. Bland. Domain wall behaviour at constrictions in ferromagnetic ring structures. *Physica B* **343**, 343 (2004).

[133] C. A. F. Vaz, L. Lopez-Diaz, M. Kläui, T. L. Monchesky, J. Unguris, Z. Cui, and J. A. C. Bland. Direct observation of remanent magnetic states in epitaxial fcc Co small disks. *Phys. Rev. B* **67**, 140405 (2003).

[134] M. Kläui, C. A. F. Vaz, J. Rothman, J. A. C. Bland, W. Wernsdorfer, G. Faini, and E. Cambril. Domain Wall Pinning in Narrow Ferromagnetic Ring Structures Probed by Magnetoresistance Measurements. *Phys. Rev. Lett.* **90**, 097202 (2003).

[135] S. P. Li, D. Peyrade, M. Natali, A. Lebib, Y. Chen, U. Ebels, L. D. Buda, and K. Ounadjela. Flux Closure Structures in Cobalt Rings. *Phys. Rev. Lett.* **86**, 1102 (2001).

[136] V. P. Kravchuk, D. D. Sheka and Y. Gaididei. Notes on onion state (2013).

[137] E. Saitoh, M. Kawabata, K. Harii, and H. Miyajima. Manipulation of vortex circulation in decentered ferromagnetic nanorings. *J. Appl. Phys.* **95**, 1986 (2004).

[138] D. K. Singh, T. Yang, and M. T. Tuominen. Magnetization vorticity and exchange bias phenomena in arrays of small asymmetric magnetic rings. *Physica B* **405**, 4377 (2010).

[139] F. Giesen, J. Podbielski, B. Botters, and D. Grundler. Vortex circulation control in large arrays of asymmetric magnetic rings. *Phys. Rev. B* **75**, 184428 (2007).

[140] L. Thomas, M. Hayashi, R. Moriya, C. Rettner and S. Parkin. Topological repulsion between domain walls in magnetic nanowires leading to the formation of bound states. *Nat. Commun.* **3**, 810 (2012).

[141] E. -M. Hempe, M. Kläui, T. Kasama, D. Backes, F. Junginger, S. Krzyk, L. J. Heyderman, R. Dunin-Borkowski and U. Rüdiger. Domain walls, domain wall transformations and structural changes in permalloy nanowires when subjected to current pulses. *phys .sat. sol.* (a) **204**, No. 12, 3922 – 3928 (2007).

[142] S. A. Wolf, D. D. Awschalom, R. A. Buhrman, J. M. Daughton, S. von Molnár, M. L. Rourkes, A. Y. Chtchelkanova, and D. M. Treger. Spintronics: A spin-based electronics vision for the future. *Science* **294**, 1488 (2001).

[143] J. -Y. Lee, K. -S. Lee, S. Choi, K. Y. Gueslienko, and S. -K. Kim. Dynamics transformation of the internal structure of a moving domain wall in magnetic nanostrips. *Phys. Rev. B* **76**, 184408 (2007).

[144] G. Meier, M. Bolte, R. Eiselt, B. Kraeuger, D. -H. Kim, and P. Fisher. Direct imaging of stochastic domain-wall motion driven by nanosecond current pulses. *Phys. Rev. Lett.* **98**, 187202 (2007).

[145] R. Varga, A. Zhukov, J. M. Blanco, M. Ipatov, V. Zhukova, J. Gonzalez, and P. Vojtaník. Fast magnetic domain wall in magnetic nanowire. *Phys. Rev. B* **74**, 212405 (2006).

[146] D. Djuhana, H. -G. Piao, J. -H. Shim, S. -H. Lee, S. -H. Jun, S. -C. Yu, S. K. Oh and D. -H. Kim. Spontaneous Domain wall motion at zero external magnetic field in ferromagnetic nanowire. *IEEE Trans. Magn.* **46** No. 2, 217 - 219 (2010).

[147] J. -Y. Chauleau, R. Weil, A. Thiaville, and J. Miltat. Magnetic domain walls displacement: Automotion versus spin-transfer torque. *Phys. Rev. B* **82**, 214414 (2010).

[148] X. H. Wang, W. K. Peng and W. S. Lew. Flux-closure chirality control and domain wall trapping in asymmetric magnetic ring. *J. Appl. Phys.* **106**, 043905 (2009).

[149] D. E. Nikonov, S. Manipatruni, and I. A. Young. Automotion of domain walls for spintronic interconnects. *J. Appl. Phys.* **115**, 213902 (2014).

[150] M. Hayashi, L. Thomas, C. Rettner, R. Moriya, X. Jiang, and S. S. P. Parkin. Dependence of Current and Field Driven Depinning of Domain Walls on Their Structure and Chirality in Permalloy Nanowires. *Phys. Rev. Lett.* **97**, 207205 (2006).

[151] X. Jiang, L. Thomas, R. Moriya, M. Hayashi, B. Bergman, C. Rettner and S. S. P. Parkin. Enhanced stochasticity of domain wall motion in magnetic racetracks due to dynamic pinning. *Nat. Commun.* **1**, 25 (2010).

[152] R. M. Reeve, A. Loescher, M. -A. Mawass, R. Hoffmann-Vogel and M. Kläui. Domain wall pinning in ultra-narrow electromigrated break junctions. *J. Phys.: Condens. Matter* **26**, 474207 (2014).

[153] N. Agraït, A. L. Yeyati and J. M. van Ruitenbeek. Quantum properties of atomic-sized conductors. *Phys. Rep.* **377**, 81–279 (2003).

[154] C. Untiedt, D. M. T. Dekker, D. Djukic and J. M. van Ruitenbeek. Absence of magnetically induced fractional quantization in atomic contacts. *Phys. Rev. B* **69**, 081401 (2004).

[155] D. Jacob, J. Fernández-Rossier and J.J. Palacios. Anisotropic magnetoresistance in nanocontacts. *Phys. Rev. B* **77**, 165412 (2008).

[156] M. Viret, M. Gabureac, F. Ott, C. Fermon, C. Barreteau, G. Autes and R. Guirado-Lopez. Giant anisotropic magneto-resistance in ferromagnetic atomic contacts. *Eur. Phys. J. B: Condens. Matter Complex Syst*. **51**, 1–4 (2006).

[157] K. I. Bolotin, F. Kuemmeth and D. C. Ralph. Anisotropic Magnetoresistance and Anisotropic Tunneling Magnetoresistance due to Quantum Interference in Ferromagnetic Metal Break Junctions. *Phys. Rev. Lett.* **97**, 127202 (2006).

[158] H. D. Chopra, M. R. Sullivan, J. N. Armstrong and S. Z. Hua. The quantum spin-valve in cobalt atomic point contacts. *Nature Mater*. **4**, 832 (2005).

[159] M. Viret, S. Berger, M. Gabureac, F. Ott, D. Olligs, I. Petej, J. F. Gregg, C. Fermon, G. Francinet and G. Le Goff. Magnetoresistance through a single nickel atom. *Phys. Rev. B* **66**, 220401 (2002).

[160] M. R. Calvo, J. Fernandez-Rossier, J. J. Palacios, D. Jacob, D. Natelson and C. Untiedt. The Kondo effect in ferromagnetic atomic contacts. *Nature* **458**, 1150 (2009).

[161] A. N. Pasupathy, R. C. Bialczak, J. Martinek, J. E. Grose, L. A. K. Donev, P. L. McEuen and D. C. Ralph. The Kondo effect in the presence of ferromagnetism. *Science* **306**, 86 (2004).

[162] C. H. Marrows. Spin-polarised currents and magnetic domain walls. *Adv. Phys.* **54**, 585 (2005).

[163] M. Viret, D. Vignoles, D. Cole, J. M. D. Coey, W. Allen, D. S. Daniel and J. F. Gregg. Spin scattering in ferromagnetic thin films. *Phys. Rev. B* **53**, 8464 (1996).

[164] P. M. Levy and S. Zhang. Resistivity due to Domain Wall Scattering. *Phys. Rev. Lett.* **79**, 5110 (1997).

[165] R. P. van Gorkom, A. Brataas and G. E. W. Bauer. Negative Domain Wall Resistance in Ferromagnets. *Phys. Rev. Lett.* **83**, 4401 (1999).

[166] C. Wickles and W. Belzig. Electronic transport in ferromagnetic conductors with inhomogeneous magnetic order parameter and domain-wall resistance. *Phys. Rev. B* **80**, 104435 (2009).

[167] G. Tatara and H. Fukuyama. Resistivity due to a Domain Wall in Ferromagnetic Metal. *Phys. Rev. Lett.* **78**, 3773 (1997).

[168] S. J. C. H. Theeuwen, J. Caro, K. I. Schreurs, R. P. van Gorkom, K. P. Wellock, N. N. Gribov, S. Radelaar, R. M. Jungblut, W. Oepts, R. Coehoorn and V. I. Kozub. Negative resistance contribution of a domain-wall structure in a constricted geometry. *J. Appl. Phys.* **89**, 4442 (2001).

[169] T. Taniyama, I. Nakatani, T. Namikawa, and Y. Yamazaki. Resistivity due to Domain Walls in Co Zigzag Wires. *Phys. Rev. Lett.* **82**, 2780 (1999).

[170] U. Ruediger, J. Yu, S. Zhang, A. D. Kent and S. S. P. Parkin. Negative Domain Wall Contribution to the Resistivity of Microfabricated Fe Wires. *Phys. Rev. Lett*. **80**, 5639 (1998).

[171] K. Miyake, K. Shigeto, K. Mibu, T. Shinjo and T. Ono. Geometrical confinement of a domain wall in a nanocontact between two NiFe wires. *J. Appl. Phys.* **91**, 3468 (2002).

[172] U. Ebels, A. Radulescu, Y. Henry, L. Piraux and K. Ounadjela. Spin Accumulation and Domain Wall Magnetoresistance in 35 nm Co Wires. *Phys. Rev. Lett.* **84**, 983 (2000).

[173] S. G. Kim, Y. Otani, K. Fukamichi, S. Yuasa, M. Nyvlt and T. Katayama. Magnetoresistivity of micron size (10·0) epitaxial Co wires. *IEEE Trans. Magn.* **35**, 2862 (1999).

[174] S. G. Kim, Y. Otani, K. Fukamichi, S. Yuasa, M. Nyvlt and T. Katayama. Magnetic and transport properties of epitaxial Fe/MgO(0 0 1) wires. *J. Magn. Magn. Mater*. **198-199**, 200-203 (1999).

[175] N. García, M. Muñoz and Y. W. Zhao. Magnetoresistance in excess of 200% in ballistic Ni nanocontacts at room temperature and 100 Oe. *Phys. Rev. Lett.* **82**, 2923 (1999).

[176] O. Céspedes, A. R. Rocha, S. Lioret, M. Viret, C. Dennis, J. F. Gregg, S. van Dijken, S. Sanvito and J. M. D. Coey. *J. Magn. Magn. Mater*. **272**, 1571 (2004).

[177] S. Khizroev, Y. Hijazi, R. Chomko, S. Mukherjee, R. Chantrell, X. Wu, R. Carley and D. Litvinov. Focused-ion-beam-fabricated nanoscale magnetoresistive ballistic sensors. *Appl. Phys. Lett*. **86**, 042502 (2005).

[178] K. Yoshida, A. Umeno, S. Sakata and K, Hirakawa. Importance of moisture control in formation of nanogap electrodes by electrical break junction method. *Japan. J. Appl. Phys.* **48**, 120216 (2009).

[179] B. Doudin and M. Viret. Ballistic magnetoresistance?, *J. Phys.: Condens. Matter* **20**, 083201 (2008).

[180] M. Müller, R. Montbrun, M. Marz, V. Fritsch, C. Sürgers and H. V. Löhneysen. Switching the conductance of Dy nanocontacts by magnetostriction. *Nano Lett.* **11**, 574 (2011).

[181] J. J. Mallett, E. B. Svedberg, H. Ettedgui, T. P. Moffat and W. F. Egelhoff. Absence of ballistic magnetoresistance in Ni contacts controlled by an electrochemical feedback system. *Phys. Rev. B* **70**, 172406 (2004).

[182] W. F. Egelhoff, L. Gan, H. Ettedgui, Y. Kadmon, C. J. Powell, P. J. Chen, A. J. Shapiro, R. D. McMichael, J. J. Mallett, T. P. Moffat, M. D. Stiles and E. B. Svedberg. Artifacts in ballistic magnetoresistance measurements. *J. Appl. Phys.* **95**, 7554 (2004).

[183] L. De Los Santos Valladares, A. Bustamante Dominguez, J. Albino Aguiar, R. M. Reeve, T. Mitrelias, R. M. Langford, Y. Azuma, C. H. W. Barnes, Y. Majima. Reorientation

Response of Magnetic Microspheres Attached to Gold Electrodes Under an Applied Magnetic Field. *Braz. J. Phys*. **43**, 209-13 (2013).

[184] A. Von Bieren, A. K. Patra, S. Krzyk, J. Rhensius, R. M. Reeve, L. J. Heyderman, R. Hoffmann-Vogel and M. Kläui. Domain-wall induced large magnetoresistance effects at zero applied field in ballistic nanocontacts. *Phys. Rev. Lett.* **110**, 067203 (2013).

[185] A. K. Patra A, A. von Bieren, S. Krzyk, J. Rhensius, L. J. Heyderman, and M. Kläui. Magnetoresistance measurement of tailored Permalloy nanocontacts. *Phys. Rev. B* **82**, 134447 (2010).

[186] A. Loescher, Diploma Thesis, *Johannes Gutenberg-Universität Mainz* (2013).

[187] S. Achilles, M. Czerner and I. Mertig. Tailoring magnetoresistance through rotating Ni particles. *Phys. Rev. B* **84**, 054418 (2011).

[188] C. C. Faulkner, M. D. Cooke, D. A. Allwood, D. Petit, D. Atkinson and R. P. Cowburn. Artificial domain wall nanotraps in Ni81Fe19 wires. *J. Appl. Phys.* **95**, 6717 (2004).

[189] M. -Y. Im, L. Bocklage, P. Fischer and G. Meier. Direct observation of stochastic domain-wall depinning in magnetic nanowires. *Phys. Rev. Lett.* **102**, 147204 (2009)

[190] L. K. Bogart, D. Atkinson, K. O'Shea, D. McGrouther and S. McVitie. Dependence of domain wall pinning potential landscapes on domain wall chirality and pinning site geometry in planar nanowires. *Phys. Rev. B* **79**, 054414 (2009).

[191] A. Himeno, S. Kasai and T. Ono. Depinning fields of a magnetic domain wall from asymmetric notches. *J. Appl. Phys.* **99**, 08G304 (2006).

[192] D. Bedau, M. Kläui, U. Rüdiger, C. A. F. Vaz, J. A. C. Bland, G. Faini, L. Vila and W. Wernsdorfer. Angular dependence of the depinning field for head-to-head domain walls at constrictions. *J. Appl. Phys.* **101**, 09F509 (2007).

[193] D. Bedau, M. Kläui, S. Krzyk, U. Rüdiger, G. Faini, L. Vila. Detection of current-induced resonance of geometrically confined domain walls. *Phys. Rev. Lett.* **99**, 146601 (2007).

[194] P. Lendecke, R. Eiselt, G. Meier and U. Merkt. Temperature dependence of domain-wall depinning fields in constricted Permalloy nanowires. *J. Appl. Phys.* **103**, 073909 (2008).

[195] G. Böhme, P. Hohn, H. Krupp, H. Rabenhorst, W. Schnabel and G. Walter. Adhesion of gold particles to silicon and gold substrates in ultrahigh vacuum. *J. Appl. Phys.* **44**, 3914 (1973).

[196] Z. Yao, H. Yang, W. Li, J. Li, A. Cui and C. Gu. Fabrication of Sub-20 nm Width Ferromagnetic Nanocontact Structures by Shadow Evaporation. *J. Nanosci. Nanotechnol.* **13**, 1199–202 (2013).

[197] S. Krzyk, A. Schmidsfeld, M. Kläui and U. Rüdiger. Magnetotransport effects of ultrathin Ni80Fe20 films probed in situ. *New J. Phys.* **12**, 013001 (2010).

[198] H. Park, A. K. L. Lim, A. Paul Alivisatos, J. Park and P. L. McEuen. Fabrication of metallic electrodes with nanometer separation by electromigration. *Appl. Phys. Lett.* **75**, 301–3 (1999).

[199] G. Esen and M. S. Fuhrer. Temperature control of electromigration to form gold nanogap junctions. *Appl. Phys. Lett.* **87**, 263101 (2005).

[200] R. Hoffmann, D. Weissenberger, J. Hawecker and D. Stöffler. Conductance of gold nanojunctions thinned by electromigration. *Appl. Phys. Lett.* **93**, 043118 (2008).

[201] D. Stöffler, S. Fostner, P. Grütter and R. Hoffmann-Vogel. Scanning probe microscopy imaging of metallic nanocontacts. *Phys. Rev. B* **85**, 033404 (2012).

[202] R. P. Gupta, Y. Serruys, G. Brebec and Y. Adda. Calculation of the effective valence for electromigration in niobium. *Phys. Rev. B* **27**, 672–7 (1983).

[203] F. Prins, A. Barreiro, J. W. Ruitenberg, J. S. Seldenthuis, N. Aliaga-Alcalde, L. M. K. Vandersypen and H. S. J. van der Zant. Room-temperature gating of molecular junctions using few-layer graphene nanogap electrodes. *Nano Lett.* **11**, 4607–11 (2011).

[204] E. Martinez, L. Lopez-Diaz, O. Alejos, L. Torres and C. Tristan. Thermal effects on domain wall depinning from a single notch. *Phys. Rev. Lett.* **98**, 267202 (2007).

[205] M. T. Bryan, P. W. Fry, T. Schrefl, M. R. J. Gibbs, D. A. Allwood, M. Y. Im and P. Fischer. Transverse Field-Induced Nucleation Pad Switching Modes During Domain Wall Injection. *IEEE Trans. Magn.* **46**, 963–7 (2010).

[206] R. M. Reeve, C. Mix, M. König, M. Foerster, G. Jakob and M. Kläui. Magnetic domain structure of La0.7 Sr0.3 MnO3 thin-films probed at variable temperature with scanning electron microscopy with polarization analysis. *Appl. Phys. Lett.* **102**, 122407 (2013).

[207] G. Wexler. The size effect and the non-local Boltzmann transport equation in orifice and disk geometry. *Proc. Phys. Soc. Lond.* **89**, 927 (1966).

[208] D. Y. Petrovykh, K. N. Altmann, H. Höchst, M. Laubscher, S. Maat, G. J. Mankey and F. J. Himpsel. Spin-dependent band structure, Fermi surface, and carrier lifetime of permalloy. *Appl. Phys. Lett.* **73**, 3459–61 (1998).

[209] L. K. Bogart and D. Atkinson. Domain wall anisotropic magnetoresistance in planar nanowires. *Appl. Phys. Lett.* **94**, 042511 (2009).

[210] K. Richter, A. Krone, M. -A. Mawass, B. Krüger, M. Weigand, H. Stoll, G. Schütz, and M. Kläui. Time-resolved observation of localized domain wall nucleation dynamics in asymmetric ferromagnetic rings. Submitted to *Nano letters* (2016).

Acknowledgments

Aus Datenschutzgründen entfernt / Removed due to data privacy

Aus Datenschutzgründen entfernt / Removed due to data privacy

Curriculum Vitae

Aus Datenschutzgründen entfernt / Removed due to data privacy

Aus Datenschutzgründen entfernt / Removed due to data privacy

List of publications

Journal Articles

- **M. -A. Mawass**, A. Bisig, B. Krüger, R. M. Reeve, K. Richter, A. Krone, H. Stoll, G. Schütz, and M. Kläui. Domain wall automotion induced by geometrical effects in asymmetric ferromagnetic rings. *To be submitted* (2016).

- K. Richter, A. Krone, **M. -A. Mawass**, B. Krüger, M. Weigand, H. Stoll, G. Schütz, and M. Kläui. Localized domain wall nucleation dynamics in asymmetric ferromagnetic rings revealed by direct time-resolved magnetic imaging. *Phys. Rev. B* **94**, 024435 (2016).

- S. Woo, K. Litzius, B. Krüger, M. -Y. Im, L. Caretta, K. Richter, M. Mann, A. Krone, R. Reeve, M. Weigand, P. Agrawal, I. Lemesh, **M. -A. Mawass**, P. Fischer, M. Kläui, G. S. D. Beach. Observation of room-temperature magnetic skyrmions and their current-driven dynamics in ultrathin metallic ferromagnets. *Nat. Mater.* **15**, 501–506 (2016).

- K. Richter, A. Krone, **M. -A. Mawass**, B. Krüger, M. Weigand, H. Stoll, G. Schütz, and M. Kläui. Local domain wall velocity engineering by tailored potential landscapes. *Phys. Rev. Applied* **5**, 024007 (2016).

- A. Bisig, **M. -A. Mawass**, M. Stärk, C. Moutafis, J. Rhensius, J. Heidler, S. Gliga, M. Weigand, T. Tyliszczak, B. V. Waeyenberge, H. Stoll, G. Schütz, M. Kläui. Dynamic domain wall chirality rectification by rotating magnetic fields. *Appl. Phys. Lett* **106**, 122401 (2015).

- S. Rao, J. Rhensius, A. Bisig, **M. -A. Mawass**, M. Weigand, M. Kläui, C. S. Bhatia and H. Yang. Time-resolved imaging of microwave-assisted magnetization reversal in patterned structures. *Sci. Rep*. **5**, 10695 (2015).

- J. -S. Kim, **M. -A. Mawass**, A. Bisig, B. Krüger, R. M. Reeve, T. Schulz, F. Büttner, J. Yoon, C. -Y. You, M. Weigand, H. Stoll, G. Schütz, H. J. M. Swagten, B. Koopmans, S. Eisebitt, M. Kläui. Synchronous precessional motion of multiple domain walls in a ferromagnetic nanowire by perpendicular field pulses. *Nat. Commun*. **5**, 3429 (2014).

- R. M. Reeve, A. Loescher, **M. -A. Mawass**, R. H.-Vogel, M. Kläui. Domain wall energetics in ultra-narrow electromigrated break junctions. *J. Phys.: Condens. Matter* **26**, 474207 (2014).

- S. Finizio, M. Foerster, B. Krüger, C. A. F. Vaz, T. Miyawaki, **M. -A. Mawass**, L. Peña, L. Méchin, S. Hühn, V. Moshnyaga. Domain wall transformations and hopping in La0.7Sr0.3MnO3 nanostructures imaged with high resolution x-ray magnetic microscopy. *J. Phys.: Condens. Matter* 26 456003 (2014).

- A. Bisig, M. Stärk, **M. -A. Mawass**, C. Moutafis, J. Rhensius, J. Heidler, F. Büttner, M. Noske, M. Weigand, S. Eisebitt, T. Tyliszczak, B. V. Waeyenberge, H. Stoll, G. Schütz and M. Kläui. Correlation between spin structure oscillations and domain wall velocities. *Nat. Commun.* **4**, 2328 (2013).

- S. Finizio, M. Foerster, C.A.F. Vaz, C. Mix**, M. -A. Mawass**, A. Tkach, G. Jakob and M. Kläui M. Buzzi and F. Nolting T. Miyawaki J. Hockel and G.P. Carman S. Valencia and F. Kronast. Electrical-field control of magnetism mediated by strain in Ni nanostructures fabricated on pre-poled PMN-PT (011). *SPIN* **3**, 1340008 *World Scientific Publishing Company* (2013).

- T. Miyawaki, M. Foerster, S. Finizio, C. A. F. Vaz**, M. -A. Mawass**, K. Inagaki, N. Fukatani, L. Le Guyader, F. Nolting, K. Ueda, H. Asano, and M. Kläui. The effect of magnetocrystalline anisotropy on the domain structure of patterned Fe2CrSi Heusler alloy thin films. *J. Appl. Phys.* **114**, 073905 (2013).

Conference Paper

- K. Richter, **M. -A. Mawass**, A. Krone, B. Krüger, M. Weigand, H. Stoll, G. Schütz, and M. Kläui. Automotive domain wall propagation in ferromagnetic rings. *Magnetics Conference (INTERMAG)*, IEEE (2015). DOI: 10.1109/INTMAG.2015.7157563

- K. Richter**, M. -A. Mawass**, A. Krone, B. Krüger, M. Weigand, H. Stoll, G. Schütz, and M. Kläui. Local control of domain wall dynamics in ferromagnetic rings. *Magnetics Conference (INTERMAG)*, 2015 IEEE (2015). DOI: 10.1109/INTMAG.2015.7157065

- A. Bisig, M. Stärk, **M. -A. Mawass**, C. Moutafis, J. Rhensius, J. Heidler, F. Büttner, M. Noske, M. Weigand, S. Eisebitt, T. Tyliszczak, B. V. Waeyenberge, H. Stoll, G. Schütz and M. Kläui. Correlation between spin structure oscillations and domain wall velocities

(presentation video). *Proc. SPIE* 9167, Spintronics VII, 91671Y (August 28, 2014); doi:10.1117/12.2060802

- C. Moutafis, F. Büttner, A. Bisig, B. Krüger, C. A. F. Vaz, M. Foerster, **M. -A. Mawass**, M. Schneider, C. Gunther, J. Geilhufe, C. V. K. Schmising, J. Mohanty, B. Pfau, S. Schaffert, T. Schulz, M. Weigand, H. J. M. Swagten, J. Raabe, M. Kläui and S. Eisebitt. Dynamics and topological mass of skyrmionic spin structures (presentation video). Proc. SPIE 9167, Spintronics VII, 91670W (August 28, 2014); doi:10.1117/12.2065838

- M. Foerster, C.A.F. Vaz, L. Pena, S. Finizio, L. Mechin, **M. -A. Mawass**, A. Bisig, F. Büttner, M. Kläui. Imaging current induced magnetic domain wall motion in La0.7 Sr0.3 MnO3 nanowires by XMCD-PEEM. *MMM 2013 (The 12th Joint MMM/Intermag Conference)*, Jan 2013, Chicago, United States. <hal-00979458>.

External Talks

- **M. -A. Mawass**, A. Bisig, J. -S. Kim, H. Stoll, G. Schütz and M. Kläui. Domain wall dynamics probed by Scanning Transmission X-ray Microscopy. *Invited talk* at Innovations for High Performance Microelectronics (IHP), Materials Research Department, (2016), Frankfurt (Oder), Germany.

- **M. -A. Mawass**, A. Bisig, J. -S. Kim, H. Stoll, G. Schütz and M. Kläui. Domain wall dynamics probed by Scanning Transmission X-ray Microscopy. *Invited talk* at Humboldt Universität zu Berlin, Department of Physics (2015), Berlin, Germany.

- **M. -A. Mawass**, A. Bisig, J. -S. Kim, H. Stoll, G. Schütz and M. Kläui. Domain wall dynamics probed by Scanning Transmission X-ray Microscopy. *Invited talk* at Deutsches Elektronen-Synchrotron (DESY) (2015), Hamburg, Germany.

- **M. -A. Mawass**, J. -S. Kim, A. Bisig, B. Krüger, R. Reeve, T. Schulz, F. Büttner, J. Yoon, C. -Y. You, M. Weigand, H. Stoll, G. Schütz, H. J. M. Swagten, B. Koopmans, S. Eisebitt and M. Kläui. Synchronous precessional motion of multiple domain walls in a ferromagnetic nanowire by perpendicular field pulses. DPG Spring Meeting (2014), Dresden, Germany.

- **M. -A. Mawass**, A. Bisig, A. Axt, M. Stärk, C. Moutafis, J. Rhensius, M. Noske, M. Weigand, T. Tyliszczak, B. V. Waeyenberge, H. Stoll, G. Schütz and M. Kläui. Universal correlated velocity and domain wall spin structure oscillations probed by direct dynamic imaging. DPG Spring Meeting (2013), Regensburg, Germany.

Posters

- K. Richter, **M. -A. Mawass**, A. Krone, B. Krüger, M. Weigand, H. Stoll, G. Schütz, and M. Kläui. Automotive domain wall propagation in ferromagnetic rings. The IEEE International Magnetics Conference, INTERMAG (2015), Beijing, China.

- K. Richter, **M. -A. Mawass**, A. Krone, B. Krüger, M. Weigand, H. Stoll, G. Schütz, and M. Kläui. Local control of domain wall dynamics in ferromagnetic rings. The IEEE International Magnetics Conference, INTERMAG (2015), Beijing, China.

- R. Reeve, A. Löscher**, M. A. Mawass**, A.von Bieren, R. Hoffman-Vogel, M. Kläui. Domain wall magnetoresistance in clean point contacts from the diffusive to the ballistic transport regime. The IEEE International Magnetics Conference, INTERMAG (2014), Dresden, Germany.

- **M. -A. Mawass**, K. Richter, A. Krone, A. Bisig, B. Krüger, A. Axt, M. Stärk, M. Weigand, H. Stoll, G. Schütz, M. Kläui. Magnetic domain wall dynamics in confined geometries imaged by high resolution microscopy. Institutstreff (2014), Institut für Physik, Mainz, Germany.

- A. Krone, **M. -A. Mawass**, K. Richter, B. Krüger, M. Stärk, M. Weigand, H. Stoll, G. Schütz and M. Kläui. Magnetic domain wall dynamics in asymmetric ferromagnetic rings. The 3rd German-Russian-Swedish Workshop on Ordering and Dynamics in Magnetic Nanostructures (2014), Schloß Maurach, Germany.

- **M. -A. Mawass**, A. Bisig, B. Krüger, A. Axt, M. Stärk, H. Stoll, G. Schütz, M. Kläui. Correlation between spin structure oscillations and domain wall velocities. The IEEE Magnetics Society Summer School (2013), Assisi, Italy.

- A. Axt, **M. -A .Mawass**, A. Bisig, B. Krüger, C. Moutafis, J. Rhenasius, J. Heidler, F. Büttner, M. Curcic, E. Prabu, M. Noske, M. Weigand, T. Tyliszczak, B. van Waeyenberge, H. Stoll, G. Schütz, M. Kläui. Spin-dynamics of Nanostructures on Membranes, 526. WE-Heraeus-Seminar (2013), Bad Honnef, Germany. (***Award best poster prize***)

- A. Loescher, **M. -A. Mawass**, R. M. Reeve, A. von Bieren, J. Heildler, J. Rhensius, L. J. Heyderman, R. Hoffmann and M. Kläui. Domain Wall Induced Magneto-resistance in Electromigrated Magnetic Nanocontacts. DPG Spring Meeting (2013), Regensburg, Germany.
- S. Finizio, M. Foerster, C. A. F. Vaz, F. Büttner, **M. -A. Mawass**, R. Lo Conte, T. Miyawaki, A. Bisig, L. Méchin, F. Nolting and M. Kläui. Current-induced domain wall motion at low current densities in La0.7Sr0.3MnO3 nanostructures. DPG Spring Meeting (2013), Regensburg, Germany.

- **M. A. Mawass**, A. Bisig, M. Stärk, H. Stoll, G. Schütz and M. Kläui. Direct imaging of processional Domain Wall Propagation in Ferromagnetic rings induced by circular magnetic fields. DPG Spring Meeting (2012), Berlin, Germany.

- **M. A. Mawass**, R. Reeve, R. H. -Vogel, M. Kläui. Domain wall dependent magneto-resistance at zero field electromigrated ferromagnetic nanocontacts. DPG Spring Meeting (2012), Berlin, Germany.

Internal Talks

- **M. A. Mawass**. Domain wall Dynamics probed by Scanning Transmission X-Ray Microscopy. Seminar Festkörper- und Grenzflächenphysik KOMET – experimentell, Institut für Physik, Mainz (2015).

- **M. A. Mawass**. Ultrafast magnetization dynamics of copper-doped FePt. Best of DPG Spring Meeting, internal group meeting (2014), Institut für Physik, Mainz, Germany.

- **M. A. Mawass**. Magnetic domain wall dynamics in asymmetric ferromagnetic rings, Progress report talk (2014), Institut für Physik, Mainz, Germany.

- **M. A. Mawass**. Control of domains and domain walls by thermal gradients. Best of DPG Spring Meeting, internal group meeting (2013), Institut für Physik, Mainz, Germany.

- **M. A. Mawass**. Domain wall Dynamics probed by Scanning Transmission X-Ray Microscopy. PhD Status talk (2013), internal group meeting, Institut für Physik, Mainz.

- **M. A. Mawass**. Electronic transport in one atom contact. Best of DPG Spring Meeting, internal group meeting (2012), Institut für Physik, Mainz, Germany.

- **M. A. Mawass**. Domain wall dependent magnetoresistance at zero field in electromigrated ferromagnetic nanocontacts. Group retreat (2012), Idar Oberstein, Germany.

- **M. A. Mawass**, A. Bisig. Direct imaging of processional domain wall propagation in ferromagnetic rings induced by circular magnetic fields. Group retreat (2012), Idar Oberstein, Germany.

Experimental Beamtimes

- 2nd June 2014 – 9th June 2014. Domain wall dynamics in asymmetrical rings. Synchrotron BESSYII, STXM beamline (MAXYMUS), Berlin, Germany. (***Main experimentalist***).

- 5th - 12th of May 2014. Domain wall dynamics in asymmetrical rings. Synchrotron BESSYII, STXM beamline (MAXYMUS), Berlin, Germany. (***Main experimentalist***).

- 13th - 16th of February 2014. Bubble Dynamics in out of plan magnetized samples. Synchrotron BESSYII, STXM beamline (MAXYMUS), Berlin, Germany. (***Main experimentalist***).

- 20th of January 2014 – 2nd of February 2014. Domain wall automotion in asymmetrical ferromagnetic rings. Synchrotron BESSYII, STXM beamline (MAXYMUS), Berlin, Germany. (***Main experimentalist***).

- 1st - 7th of July 2013. Synchronous precessional motion of multiple domain walls in a ferromagnetic nanowire by perpendicular field pulses. Synchrotron BESSYII, STXM beamline (MAXYMUS), Berlin, Germany. (***Main experimentalist***).

- 1st - 7th of April 2013. Direct imaging of microwave assisted reversal in nano-elements. Synchrotron BESSYII, STXM beamline (MAXYMUS), Berlin, Germany.

- 22nd - 31st of March 2013. Electrical-field control of magnetism mediated by strain in Ni nanostructures. Synchrotron SLS, PEEM beamline at PSI, Villigen, Switzerland.

- 21st - 27th of January 2013. Field induced domain wall motion in ring structure. Synchrotron BESSYII, STXM beamline (MAXYMUS), Berlin, Germany. (***Main experimentalist***).

- 08th – 14th October 2012. Holography imaging employing STXM. Synchrotron BESSYII, STXM beamline (MAXYMUS), Berlin, Germany.

- 20th – 27th April 2012. Current-induced domain wall motion at low current densities in La0.7Sr0.3MnO3 nanostructures. Synchrotron SLS, PEEM beamline at PSI, Villigen, Switzerland.

- 13th – 19th of March 2012. Field induced dynamics in ferromagnetic dot structures with a perpendicular magnetic anisotropy. Synchrotron BESSYII, STXM beamline (MAXYMUS), Berlin, Germany.

- 08th – 13th of March 2012. Field induced domain wall motion in ring structure. Synchrotron BESSYII, STXM beamline (MAXYMUS), Berlin, Germany. (***Main experimentalist***).

- 30th of October - 15th of November 2011. Field induced domain wall motion in ring structure. Synchrotron BESSYII, STXM beamline (MAXYMUS), Berlin, Germany.

Eidesstattliche Erklärung

Hiermit erkläre ich an Eides statt, dass ich meine Dissertation selbständig und ohne fremde Hilfe verfasst und keine anderen als die von mir angegebenen Quellen und Hilfsmittel zur Erstellung meiner Dissertation verwendet habe. Die Arbeit ist in vorliegender oder ähnlicher Form bei keiner anderen Prüfungsbehörde zur Erlangung eines Doktorgrades eingereicht worden.

Mainz, den

Mohamad Assaad Mawass